NTNU
Norwegian University of
Science and Technology

A study of the Dynamic Properties of Quick Clay from Flotten NGTS

with Particular Interest in Anisotropy and
Stress Relief During Unloading

Amy Beeston

Norwegian University of Science and Technology
Department of Civil and Environmental Engineering

NORWEGIAN UNIVERSITY OF SCIENCE AND TECHNOLOGY
DEPARTMENT OF CIVIL AND ENVIRONMENTAL ENGINEERING

Report Title: **A study of the Dynamic Properties of Quick Clay from Flotten NGTS - with Particular Interest in Anisotropy and Stress Relief during Loading**	Dato: **11.06.2018**	
	Number of pages: **238**	
	Master Thesis	x
Name: Amy Beeston		
Professor in charge/supervisor: Gudmund Eiksund		
Other external professional contacts/supervisors: Arnfinn Emdal		

Abstract:

The stiffness of a soil is of great importance in many areas of geotechnical engineering. It forms the link between strain and stress, which is crucial in incremental numerical modelling. More specific to this study, the maximum shear stiffness (G_{max}) is the primary parameter used in small shear strain models, earthquake engineering and vibration assessments. G_{max} is also used, in recent studies, to determine sample quality and is an important aspect for understanding what happens to a soil sample when it is unloaded and removed from its in-situ environment. Acquiring accurate values of G_{max} is problematic, particularly in the laboratory where reduced stiffness is thought to be due to stress relief during unloading, which affects sample quality.

In this study bender element testing was carried out using mini-block samples taken from the Flotten quick clay NGTS near Trondheim. Tests were carried out on unconfined trimmed triaxial samples and consolidated samples at different orientations to assess anisotropy in shear stiffness. Vertical shear stiffness results were compared to in-situ results from a seismic dilatometer test. Shear wave velocity was also measured during unloading to try to imitate and understand unloading effects during sampling.

Strong anisotropy was found in the samples and due to relationships with clay content and behaviour during unloading, it is concluded that this anisotropy would be expected in-situ. Anisotropy was found between rotations in the vertical plane, which is not possible according to a model based on a cross-anisotropic elastic medium. Therefore, the application of equations derived for wave propagation from such a model is brought into question. During unloading it is found that samples with no access maintain their stiffness compared to those whom have access to water where stiffness drops dramatically.

Keywords:

1. Small Strain Shear Stiffness
2. Bender Element Testing
3. Flotten Quick Clay
4. Shear Stiffness Anisotropy

NTNU
Faculty of Engineering Science and Technology
Institute of Civil and Environmental Engineering

MASTER DEGREE THESIS
Spring 2018
for
Student: Amy Beeston

A Study of the Dynamic Properties of Quick Clay from Flotten NGTS - with Particular Interest in Anisotropy and Stress Relief during Unloading

BACKGROUND
The stiffness of a soil is of great importance in many areas of geotechnical engineering. It forms the link between strain and stress, which is crucial in incremental numerical modelling. More specific to this study, the maximum shear stiffness (G_{max}) is the primary parameter used in small shear strain models, earthquake engineering, vibration assessments, and for immediate working load settlement predictions. G_{max} is also used, in recent studies, to determine sample quality and is an important aspect for understanding what happens to a soil sample when it is unloaded and removed from its in-situ environment. Acquiring accurate values of G_{max} is problematic, particularly in the laboratory where reduced stiffness is thought to be due to stress relief during unloading, which affects sample quality.

TASK
To determine small strain shear stiffness moduli and the presence of anisotropy for quick clay from Flotten NGTS, using a bender element triaxial system.

Task description
Triaxial samples were trimmed from mini-block samples in three orientations for each depth (one vertical and two horizontal) to determine the small strain stiffness modulus in the vertical and horizontal planes. The samples were tested unconfined and then consolidated to equal effective confining stresses for each depth. They were then unloaded, some with access to water and some without. Consolidated results were compared to supplied in-situ vertical shear wave velocity results from a seismic dilatometer test and to index test results that were also carried out on the mini-block samples.

Objective and purpose
The main objectives were to determine the presence of anisotropy in the small strain shear stiffness and understand the effects of stress relief during unloading of the samples.

Subtasks and research questions
Many subtasks were identified throughout this study such as the suitability of a cross-anisotropic elastic material model to calculate shear stiffness from a triaxial bender element system, the influence of sample dimensions on the "near-field" effect, the problem of estimating small strain shear stiffness from effective stresses and index parameters, the reliability of sample quality techniques and the use of P-waves to determine the constrained modulus and elastic parameters of the clay.

Professor in charge:
Prof. Gudmund Eiksund

Department of Civil and Transport Engineering, NTNU
Date: 09.06.2017, (revised: dd.mm.yyyy)

Gudmund Eiksund

Professor in charge (signature)

Preface

This study was performed as a Master Thesis as part of the MSc in Geotechnics and Geohazards and was written at the Geotechnical Division of the Department of Civil and Transport Engineering at the Norwegian University of Science and Technology (NTNU).

The study was performed during the spring semester over the period of 20 weeks.

The main supervisor for the study was Gudmund Eiksund with a secondary supervisor, Arnfinn Emdal with input from Steinar Nordal and Gustav Grimstad.

My interest in dynamic properties of soil and the availability of mini-block samples were the catalyst of the project, which evolved as interesting findings came about.

Trondheim, June 2018

Amy Louise Beeston Heritage

Acknowledgement

Summary and Conclusions

The stiffness of a soil is of great importance in many areas of geotechnical engineering. It forms the link between strain and stress, which is crucial in incremental numerical modelling. More specific to this study, the maximum shear stiffness (G_{max}) is the primary parameter used in small shear strain models, earthquake engineering and vibration assessments and for immediate working load settlement predictions. G_{max} is also used, in recent studies, to determine sample quality and is an important aspect for understanding what happens to a soil sample when it is unloaded and removed from its in-situ environment. Acquiring accurate values for G_{max} is problematic, particularly in the laboratory. Reduces stiffness is thought to be due to stress relief during unloading, which affects sample quality.

This study utilised mini-block samples taken from the Flotten quick clay at a Norwegian geotechnical test site near Tiller, Trondheim. Seven sample depths were tested with a bender element (BE) triaxial system to determine the shear stiffness properties in both the horizontal and vertical planes. The samples were tested before and during sample consolidation and during unloading to try to imitate the sampling process. Index parameters and grain size distributions were also determined for each mini-block sample. In addition, P-wave velocity was measured for one vertical sample and two horizontal samples from the same depth to determine the constrained modulus and hence elastic parameters of the clay, and S-wave velocity measurements were taken on unconfined half mini-blocks to determine effects of sample proportions. Vertical shear wave velocity results were supplied from a seismic dilatometer test (SDMT) carried out next to the sample hole. During the study many limitations were realised, but strong relationships in the results found.

The main limitation in this study comes from the accuracy of the shear wave and P-wave velocity output from the bender element system. It samples at a rate of 20 kHz, which results in a time resolution of 0.05 ms. The accuracy is studied and found to create maximum errors between 3 and 15 % for the shear modulus and between 7 and 150 % for the constrained modulus, increasing with shear velocity and P-wave velocity respectively. It was found that the errors in the shear modulus were overcome by the trend in the results, whilst the constrained modulus was deemed unusable but still formed some discussions.

The concept of the "near-field" effect was tested using half mini-block samples with a portable bender element set-up for S-wave propagation. The near-field effect is caused by the interference of P-waves due to transverse directivity between the sender and receiver elements. It was found that even when the ratio between sample height and wavelength (d/λ) was kept

below the suggest threshold of 2 (Sanchez-Salinero, Roesset, & Stokoe, 1986), there were still strong "near-field" effects deeming the results unusable. This "near-field" effect threshold was also checked for the triaxial samples by varying the input frequency and hence wavelength. It was found that even with a high ratio (d/λ = 3.6) interference from P-waves was absent. Therefore, a hypothesis is proposed that sample dimension ratio (d/w) has more influence and in this case 2:1 was suitable and 2:2 was not.

The bender element results showed strong anisotropy in the unconfined samples and after consolidation. This increased with consolidation suggesting an increase with effective confining pressure. After consolidation, small-strain shear stiffness in the horizontal plane (G_{hh}) was between 39 % and 72 % higher than in the vertical plane (G_{vh}). The origin of this anisotropy is considered, and it is concluded that whilst there is some influence by sample unloading (stress induced anisotropy) that there is also a relationship with clay content and the structure of the clay (inherent anisotropy) plays a significant role. As such, it seems reasonable to transfer this anisotropy from the BE results to the SDMT results.

The suitability of applying a cross-anisotropic elastic material model to a bender element test is brought into question in this study. In such a model the stiffness in the vertical plane should be equal ($G_{vh} = G_{hv}$) since there is no resistance to rotations in the vertical plane. However, it is found that there is a difference between stiffnesses in these orientations with G_{hv} 7-18 % lower than G_{vh}. It is concluded that since the shear wave comes from a point source and the shear wave is not transferred equally through the cylindrical sample that the cross-anisotropic elastic model is not suitable. A monoclinic material model is proposed which accounts for coupling effects from stiffnesses in other directions. The application of such a model is complex and beyond the scope of this study.

Relationships proposed in the literature between G_{max} with effective stress (p') and index parameters were applied to the BE and SDMT results. Whilst the relationships fit well and confirm high dependence on void ratio, it is challenging to determine correct stress exponents and soil characteristic parameters and as such using these in prediction of stiffness remains problematic. The effect of geological age was applied to the BE results and found to give good approximations to the SDMT results.

Unloading of the samples was carried out to try to imitate the effects of sampling procedures on the clay. One sample was allowed access to water on unloading and returned to its original state as was expected. The sample was allowed to take in more water than was expelled in the consolidation phase and its shear stiffness reduced further. A second sample was allowed to take in only half the expelled water. Even so the stiffness dropped almost back

to its original unconfined value. Several samples were closed to water immediately after unloading and the stiffness was found to remain much higher. This concludes water access during sampling plays a huge role in sample quality.

Sample quality was determined for the triaxial samples in this study based on the three techniques: change in volumetric strain ($\Delta\varepsilon_{vol}$) proposed by Andresen and Kolstad (1979), change in void ratio ($\Delta e/e_0$) proposed by Lunne, Berre, Andersen, Strandvik, and Sjursen (2006) and ratio of shear velocity measured on a sample in the field to the in-situ measurement ($v_{S,vh}/v_{SCPTU}$) proposed by Landon, DeGroot, and Sheahan (2007). All but three samples were found to be poor to very poor quality. The three samples at 8.90 m were of acceptable quality and were imposed to stress conditions calculated using assumed hydrostatic pore pressure conditions and K_0 of 0.5, as opposed to the in-situ under-hydrostatic pore pressure measurements and K_0 of 0.7 used for other samples. The consolidation rate was also found to influence the amount of water expelled from the clay. It is suggested that since there are many subjective choices in the consolidation phase of a triaxial test that techniques based on expelled water should be used with caution. The technique using shear wave velocities appears more suitable. Samples were also classified as poor using this technique, but the unconfined measurements were taken on trimmed triaxial samples, not straight out of the ground and field measurements were based on seismic dilatometer test results, not seismic cone penetrometer test results. Variation of sample quality was found to be lower for samples taken from the top of a mini-block than those taken from the bottom, which is thought to be due to variations in stress relief throughout the mini-block sample.

P-wave velocity measurements were taken at one sample depth. The limitations from the accuracy of the bender element system and from the complexity of P-wave propagation through the sample deemed the results inconclusive.

Table of Contents

List of Figures for Results

List of Tables for Results

List of Symbols and Abbreviations

γ	Shear strain
$\gamma_{0.7}$	Shear strain at $G/G_{max} = 0.7$
$\dot{\gamma}$	Strain rate
γ	Unit weight
γ_s	Unit weight of solids
γ_w	Unit weight of water
λ	Wavelength
ν	Poisson's ratio
ρ	Bulk density
ρ_s	Density of solids/particles
ρ_w	Density of water
σ'_h	Effective horizontal stress
σ'_{h0}	In-situ effective horizontal stress
σ'_v	Effective vertical stress
σ'_{v0}	In-situ effective vertical stress
σ'_m	Effective average confining stress ($=p'$)
$\delta\boldsymbol{\varepsilon}$	Strain increment matrix
$\delta\varepsilon_{ii}$	Strain increment in the i direction
$\delta\gamma_{ij}$	Shear strain increment in the ij plane
$\delta\boldsymbol{\sigma}$	Stress increment matrix
$\delta\sigma_{ii}$	Stress increment in the i direction
$\delta\tau_{ij}$	Shear stress increment in the ij plane
ε_f	Failure strain
ε_{vol}	Volumetric strain
Δe	Change in void ratio
ΔG_{max}	Increase in G_{max} over one log cycle of time
ΔV	Change in volume of sample
A	Material constant
BE	Bender element
c	Cementation
CPT	Cone penetrometer test
CSW	Continuous surface waves
$\boldsymbol{D}$	Stiffness matrix
e_0	Initial void ratio
e	Void ratio
E	Youngs modulus
E_h	Youngs modulus in the horizontal direction
E_v	Youngs modulus in the vertical direction
EOP	End of primary consolidation
$EPMA$	Electron probe micro analyser
f	Frequency
$F(e)$	Void ratio function
g	Acceleration due to gravity
G	Shear strain modulus
G_{max}	Small strain shear modulus / Maximum shear strain modulus
$G_{max,0}$	Unconfined small strain shear modulus
$G_{max,vh}$	Small strain shear modulus for horizontal shear in the vertical plane

$G_{max,hh}$	Small strain shear modulus for horizontal shear in the horizontal plane
$G_{max,hv}$	Small strain shear modulus for horizontal shear in the vertical plane
$G_{max,SCPTU}$	Small strain shear modulus measured by SCPTU
$(G_{max})_{1000}$	Value of G_{max} 1000 minutes past the end of primary consolidation
G_s	Secant shear modulus
I_L	Liquidity index
I_P	Plasticity index
k	OCR exponent
K	Bulk modulus
K_0	Coefficient of earth pressure at rest
m	Power exponent
m	Total wet mass
m_s	Dry mass
m_w	Mass of water
m_{wp}	Mass of the water filled pycnometer
m_{wps}	Mass of the pycnometer with sample and water
M	Constrained modulus
$MASW$	Multi-channel analysis of surface waves
n	Stress exponent
N_G	Rate of increase of G_{max} with geological time
$NGTS$	Norwegian geotechnical test site
NGI	Norwegian geotechnical institute
OCR	Over-consolidation ratio
p	Average confining pressure
p'	Average effective confining pressure
p_a	Atmospheric pressure
p_c'	Pre-consolidation stress
p_{ps}'	Theoretical effective confining pressure
p_r'	Residual effective confining pressure
$P1$	P-wave type 1
$P2$	P-wave type 2
$P3$	P-wave type 3
S	Soil characteristic parameter
$SASW$	Spectral analysis of surface waves
$SCPTU$	Seismic cone penetrometer test
$SDMT$	Seismic dilatometer test
$SDOF$	Single degree of freedom system
s_r	Remoulded shear strength
s_u	Undrained shear strength
S	Salinity
S_r	Degree of saturation
S_t	Sensitivity
t_g	Geological age
t_s	Shear wave travel time
u	Pore pressure
u_a	Air pressure in pores
u_{ps}	Theoretical pore pressure after unloading
u_r	Residual pore pressure
u_w	Water pressure in pores

V_0	Initial volume of sample
V_w	Volume of water
V_p	Volume of pores
$V_{s,vh}$	Shear wave velocity for vertical propagation and horizontal particle motion
$V_{s,hh}$	Shear wave velocity for horizontal propagation and horizontal particle motion
$V_{s,hv}$	Shear wave velocity for horizontal propagation and horizontal particle motion
V_P	P-wave velocity
w	Water content
w_L	Liquid limit
w_P	Plastic limit
w_S	Shrinkage limit
x	Power exponent

1. Introduction

1.1. Background

The stiffness of a soil is of great importance in many areas of geotechnical engineering. It forms the link between strain and stress, which is crucial in incremental numerical modelling. More specific to this study, the maximum shear stiffness (G_{max}) is the primary parameter used in small shear strain models, earthquake engineering and vibration assessments. As such, it is often referred to as a dynamic property of soil. G_{max} is also used, in recent studies, to determine sample quality and is an important aspect for understanding what happens to a soil sample when it is unloaded and removed from its in-situ environment. Acquiring accurate values of G_{max} is problematic, particularly in the laboratory where reduced stiffness is thought to be due to stress relief during unloading, which affects sample quality.

1.2. Objectives

The main objective of this study was to determine the dynamic properties of quick clay at the Flotten Norwegian geotechnical test site by carrying out bender element tests on triaxial samples trimmed from mini-block samples. The main objectives were as follows:

- To carry out index testing on the quick clay from the Flotten NGTS.
- To determine sample quality of the mini-block samples from the site.
- To determine the dynamic properties of the clay and the anisotropy of these properties.
- To compare these to in-situ G_{max} results.
- To verify relationships between G_{max}, index parameters and effective stress.
- To understand what happens to the dynamic properties when the clay is unloaded and the implications this has on sample quality.
- To determine the constrained modulus (M), bulk modulus (K), Young's modulus (E), Poisson's ratio (v) and hence the stiffness matrix (D).

Many other subtasks were identified throughout the study and looked in to. Such as:

- The suitability of a cross-anisotropic elastic material model for calculating small strain shear modulus from bender element tests.
- The influence of sample dimensions on "near-field" effects.

1.3. Limitations

Much more analysis could be done on these results with more time and the main limitation to the conclusions is based as such. More recent samples and field work, or more field results, would have added to the study, which again came down to time limitations.

1

In terms of the data, the main limitation is in the accuracy of the bender element system, which is analysed in some detail, but does not affect the overall conclusions.

1.4. Approach

Triaxial samples were trimmed from mini-block samples in three orientations for each depth (one vertical and two horizontal) to determine the small strain stiffness modulus in the vertical and horizontal planes. The samples were tested unconfined and then consolidated to equal effective confining stresses for each depth. They were then unloaded, some with access to water and some without. Consolidated results were compared to supplied in-situ vertical shear wave velocity results from a seismic dilatometer test and to index test results that were also carried out on the mini-block samples.

1.5. Structure of the report

The report is structured as follows:

- Chapter 1 outlines the objectives of the study
- Chapter 2 gives the theoretical background required to introduce the study.
- Chapter 3 introduces the background behind the quick clay site at Flotten and details of previous studies from this site.
- Chapter 4 outlines the procedures that were followed during the laboratory work.
- Chapter 5 gives a summary of the main result findings.
- Chapter 6 discusses the results in detail with suggested conclusions.
- Chapter 7 outlines the main conclusions and suggestions for further work.

2.   Theoretical Background

The stiffness of a soil is of great importance in many areas of geotechnical engineering. It forms the link between strain and stress, which is crucial in incremental numerical modelling. More specific to this study, the maximum shear stiffness, G_{max}, (also known as the small strain stiffness) is the primary parameter used in small shear strain models, earthquake engineering, vibration assessments and instantaneous working load settlement predictions. As such, it is often referred to as a dynamic property of soil. G_{max} is also used, in recent studies, to determine sample quality and is an important aspect for understanding what happens to a soil sample when it is unloaded and removed from its in-situ environment. All these areas are considered in this study and a brief overview of the theory is outlined in this chapter along with the specific application to quick clays. More detailed theory of geotechnical earthquake engineering, from a separate study, is given in APPENDIX E – Theory of Geotechnical Earthquake Engineering.

2.1.   Application of Small Strain Shear Stiffness, G_{max}

Stiffness is a key property of the soil when considering input parameters for geotechnical numerical modelling. The stiffness provides the link between strain increments, $\delta\boldsymbol{\varepsilon}$, and stress increments, $\delta\boldsymbol{\sigma}$, in numerical analysis model.

$$\delta\boldsymbol{\sigma} = \boldsymbol{D}\delta\varepsilon$$

[2.1]

where $\boldsymbol{D}$ is the stiffness matrix discussed in section 2.2.1.

It is a known that stress-strain behaviours of soil are non-linear, that is stiffness varies with strain level. Therefore, choosing the most appropriate stiffness parameter for a specific engineering problem is key in geotechnical numerical modelling. Figure 2.1 shows how the shear stiffness varies with strain level and how it is applicable to various engineering applications.
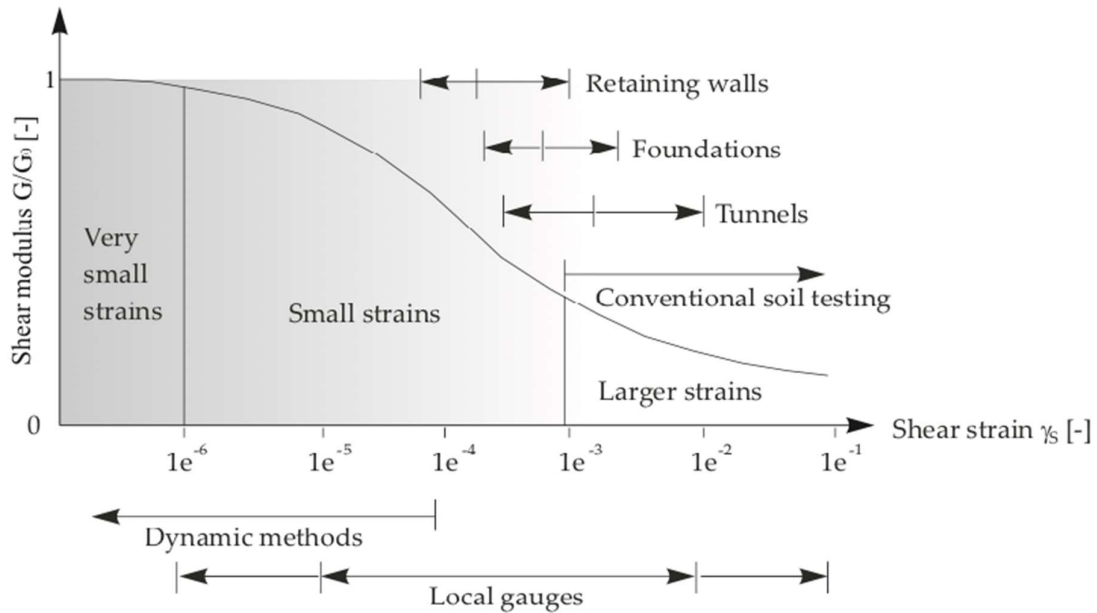
Figure 2.1: Relationship between normalised shear stiffness and strain level for various engineering problems (Figure 7.1 PLAXIS (2017) after Atkinson and Sallfors (1991))

It is generally accepted that at very small strains, truly elastic loading and unloading behaviour occurs and a linear stress-strain relationship with constant stiffness is acceptable. At slightly larger strains, nonetheless still small strains, it is important to consider a non-linear elastic relationship where the stiffness decays with increased strain.

A brief description of the geotechnical significance of G_{max} is given below regarding earthquake engineering, vibration assessments and settlement predictions. An introduction to how G_{max} can be used to assess sample quality is given in section 2.8.2.

2.1.1. *Earthquake Engineering and Vibration Assessments*

As seismic waves travel from the epicentre of an earthquake, the nature of these waves when they arrive at the surface is termed the ground surface motion. This is very hard to model particularly due to the soil layer, since wave propagation through soil shows much variation. Many design standards have been developed around the world to guide engineers in such processes. Eurocode 8 is one such standard that is followed in Norway. It supplies tools called response spectra that allow engineers to easily predict the response of a structure due to an earthquake and the forces that will be applied to the structure. The type of response spectra used depends on the ground type, which is determined by the shear velocity of the top 30 m of ground. In Eurocode 8 there are response spectra supplied for 5 ground types, but when a soil becomes too soft the response becomes too hard to predict. In such cases, such as a sensitive clay site, a detailed site response analyses are required.

The fundamentals of vibration assessments are as with earthquake engineering are based on wave propagation through an elastic medium and the response of the soil as a degree of freedom system (DOF). The stiffness of the soil is one of the freedoms of the system and is therefore vital in these predictions along with damping, Possion's ratio and density (the latter 2 of less importance). Since the strain induced by wave propagation is so small it is the small-strain stiffness (G_{max}) that is most relevant.

2.1.2. Settlement Predictions

Consolidation settlements, in soils under foundations, come about by the dissipations of pore pressures created by the added load. We know that soil stiffness controls the strains that develop as a result of the increased pore pressure. Therefore, estimates of settlements can be based on estimates of the increased pore pressure and the stiffness of the soil. Therefore, choosing a correct stiffness value is a fundamental step in settlement predictions. Recent developments in numerical modelling have incorporated the use of small-strain stiffness to estimate instantaneous settlements during working load conditions such as the Hardening Soil Small-Strain stiffness model used in PLAXIS (2017). This model uses a non-linear elastic stress-strain relationship. It uses the input parameters G_{max} and the secant shear modulus G_s at the strain level $\gamma_{0.7}$, which is about 70% of G_{max}.

Sensitive clays pose particular problems when it comes to the prediction of settlements as described later in section 2.7.

2.2. Shear Stiffness in an Elastic Medium

According to Hooke's law, an element of isotropic elastic material, unconstrained laterally, can be described by a direct stiffness, the Young's modulus E, and the Poisson's strain ratio v, which make up the stiffness matrix as described in the next section 2.2.1.

Hooke's law also relates the Youngs modulus to the shear modulus, G, and the bulk modulus, K, and the constrained modulus, M (also known as the oedometer modulus, E_{oed}) by the following equations, respectively:

$$G = \frac{E}{2(1 + v)}$$

[2.2]

$$K = \frac{E}{3(1 - 2v)}$$

[2.3]

$$M = \frac{E(1-v)}{(1+v)(1-2v)} = K + \frac{4}{3}G$$

<div align="right">[2.4]</div>

It can be seen from equations [2.2], [2.3] and [2.4] that if any two moduli of a material are known the Poisson's ratio and Youngs modulus of the material can be determined.

2.2.1. *Stiffness Anisotropy and the Stiffness Matrix*

All soils, due to their deposition structure (inherent anisotropy) and historical loading (induced anisotropy), are by nature structurally anisotropic. The inherent structural anisotropic nature is described further in section 2.5. As such, soils often display anisotropic stiffness properties, which can be illustrated by a stiffness matrix.
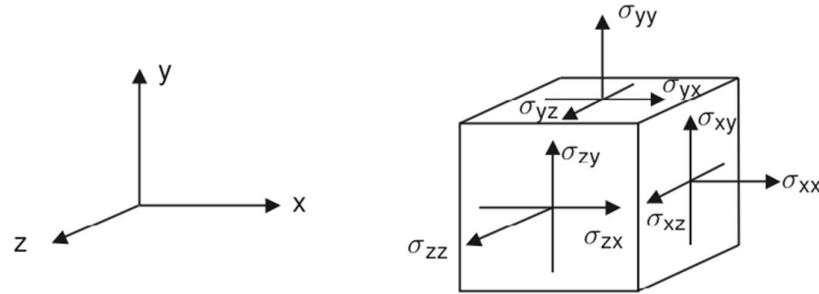
Figure 2.2: Illustration of a 3-dimensional stress system (Figure 2.1, PLAXIS (2017))

Based on Hooke's law for an element of isotropic elastic material, unconstrained laterally with 6 general stress and strain components as illustrated in Figure 2.2, the stiffness matrix for an isotropic, linear elastic material can be described:

$$\begin{pmatrix} \delta\sigma'_{xx} \\ \delta\sigma'_{yy} \\ \delta\sigma'_{zz} \\ \delta\tau'_{yz} \\ \delta\tau'_{zx} \\ \delta\tau'_{xy} \end{pmatrix} = \frac{E}{(1+v)(1-2v)} \begin{pmatrix} 1-v & v & v & 0 & 0 & 0 \\ v & 1-v & v & 0 & 0 & 0 \\ v & v & 1-v & 0 & 0 & 0 \\ 0 & 0 & 0 & 1/2-v & 0 & 0 \\ 0 & 0 & 0 & 0 & 1/2-v & 0 \\ 0 & 0 & 0 & 0 & 0 & 1/2-v \end{pmatrix} \begin{pmatrix} \delta\varepsilon_{xx} \\ \delta\varepsilon_{yy} \\ \delta\varepsilon_{zz} \\ \delta\gamma_{yz} \\ \delta\gamma_{zx} \\ \delta\gamma_{xy} \end{pmatrix}$$

<div align="right">[2.5]</div>

where the stiffness matrix is defined by the Young's modulus and the Poisson's ratio. It is the symmetric nature of the matrix that describes the elastic compliance.

An alternative and perhaps better visual display of the stiffness matrix (Yamashita, Hori, & Suzuki, 2006), which complies to the form in equation [2.1] for an elastic cross-anisotropic material symmetric about the vertical axis, such as soil:

$$\begin{pmatrix} \delta\varepsilon_{xx} \\ \delta\varepsilon_{yy} \\ \delta\varepsilon_{zz} \\ \delta\gamma_{yz} \\ \delta\gamma_{zx} \\ \delta\gamma_{xy} \end{pmatrix} = \begin{pmatrix} 1/E_h & -v_{hh}/E_h & -v_{vh}/E_v & 0 & 0 & 0 \\ -v_{hh}/E_h & 1/E_h & -v_{vh}/E_v & 0 & 0 & 0 \\ -v_{hv}/E_h & -v_{hv}/E_h & 1/E_v & 0 & 0 & 0 \\ 0 & 0 & 0 & 1/G_{hv} & 0 & 0 \\ 0 & 0 & 0 & 0 & 1/G_{vh} & 0 \\ 0 & 0 & 0 & 0 & 0 & 1/G_{hh} \end{pmatrix} \begin{pmatrix} \delta\sigma'_{xx} \\ \delta\sigma'_{yy} \\ \delta\sigma'_{zz} \\ \delta\tau'_{yz} \\ \delta\tau'_{zx} \\ \delta\tau'_{xy} \end{pmatrix}$$

[2.6]

where E_v and E_h are the vertical and horizontal Young's moduli; v_{vh}, v_{hh} and v_{hv} are the Poisson's Ratios, G_{vh}, G_{hh} and G_{hv} are the shear moduli. The three shear moduli are illustrated with reference to an element of soil with shear applied in Figure 2.3.
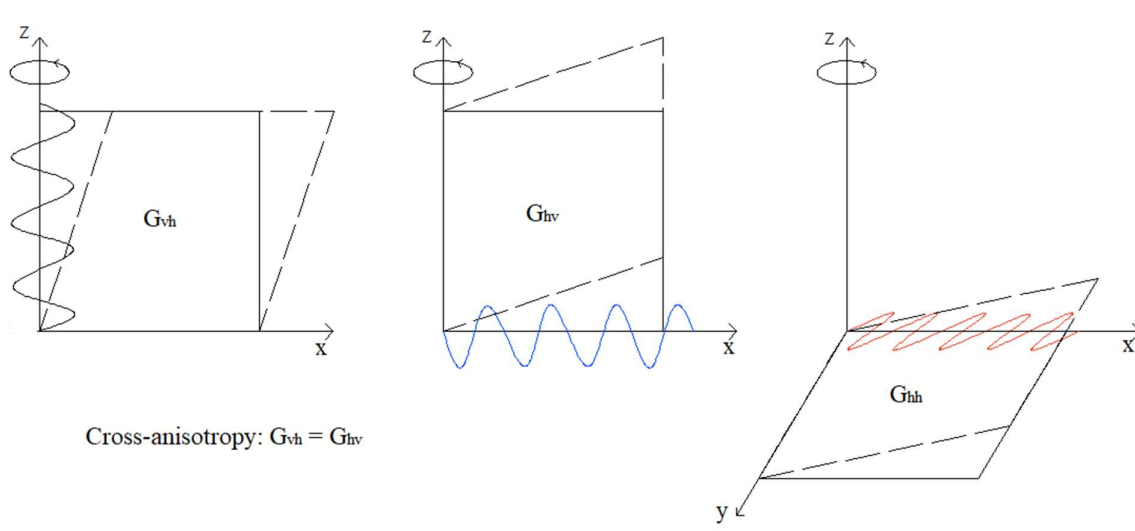
Figure 2.3: Three shear stiffness moduli for a cross-anisotropic element of soil

Yamashita et al. (2006) state also that from the symmetry of the matrix and the isotropy in the horizontal plane, the following equations can be obtained:

$$\frac{v_{vh}}{E_v} = \frac{v_{hv}}{E_h}$$

[2.7]

$$G_{hh} = \frac{E_h}{2(1 + v_{hh})}$$

[2.8]

Of course, the above is based on reduction of a fully anisotropic matrix, given by 21 independent material properties to a cross-anisotropic (also referred to as transverse isotropic) matrix, which is represented by five independent elastic properties, E_v, E_h, v_{vh}, v_{hh}, G_{vh}. To comply with this model G_{vh} must equal G_{hv}, since one is purely a rotation of the other and there is no resistance to rotation in the vertical plane. However, in the literature differences are reported between G_{vh} and G_{hv} using bender element (BE) testing. Pennington, Nash, and Lings

7

(2001) suggest that this may be due to the non-point like source of the S-waves at the BE contact with the specimen. Arroyo (2001) suggests that in addition there are likely influences from the way in which the shear waves are transmitted through the cylindrical sample.

2.3. Measurement of G_{max}

As introduced the use of G_{max} in geotechnical engineering design is widespread and as such it is crucial to acquire accurate values. Furthermore, L'Heureux and Long (2017) have shown that shear velocity in soils can be correlated with soil properties and as such, if measured well can be used as a first order estimate of soil properties in site investigations.

G_{max} is effectively the in-situ shear modulus of the material and can be measured directly in the field by measuring shear velocity and density of the soil, and using techniques in the laboratory, although these are affected by sample disturbance. All techniques are based on equation [2.9], which comes from the theory of wave propagation through an isotropic elastic medium.

$$G_{max,ij} = \rho V_{s,ij}^2$$

[2.9]

Figure 2.4 illustrates these three shear moduli in relation to shear wave propagation through a soil specimen which has cross-anisotropic properties, where $G_{vh}=G_{hv}$.
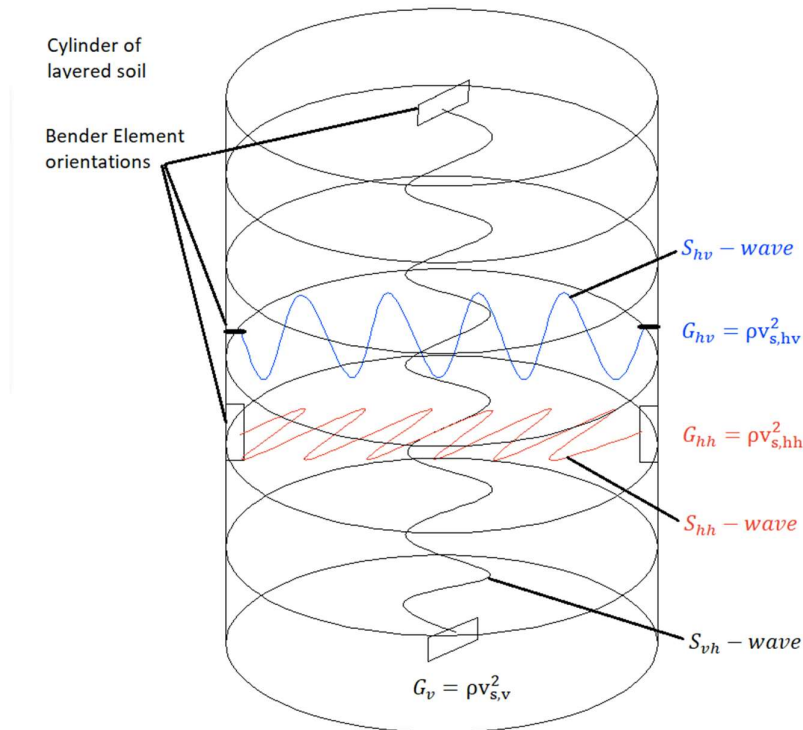
Figure 2.4: Illustration of G_{vh} an, G_{hh} and G_{hv} from a soil specimen

The constrained modulus, M can be calculated in the same way from the compressional wave velocity (P-wave velocity), V_p:

$$V_P = \sqrt{\frac{M}{\rho}}$$

<div align="right">[2.10]</div>

The bulk modulus of the material, K, can be measured from the compressional wave velocity (P-wave velocity), V_p if the shear modulus is known:

$$V_P = \sqrt{\frac{K + \frac{4}{3}G}{\rho}}$$

<div align="right">[2.11]</div>

The use of P-waves is discussed further in section 2.6.

2.3.1. *Overview of field and lab techniques*

Field Techniques

Non-intrusive techniques are in theory the most accurate techniques for determining the in-situ G_{max} values. Examples of such techniques are spectral analysis of surface waves (SASW), multi-channel analysis of surface waves (MASW), continuous surface waves (CSW), seismic reflection and seismic refraction. The most commonly used technique is MASW, which involves the use a seismic source and an array of geophones as illustrated in Figure 2.5.

Intrusive techniques are also quite common in field investigations, but the possibility of soil disturbance brings into question their accuracy. Common techniques include, down-hole or up-hole logging, cross-hole logging, seismic cone penetration tests (SCPTU) and seismic dilatometer tests (SDMT), some of which are illustrated in Figure 2.5.
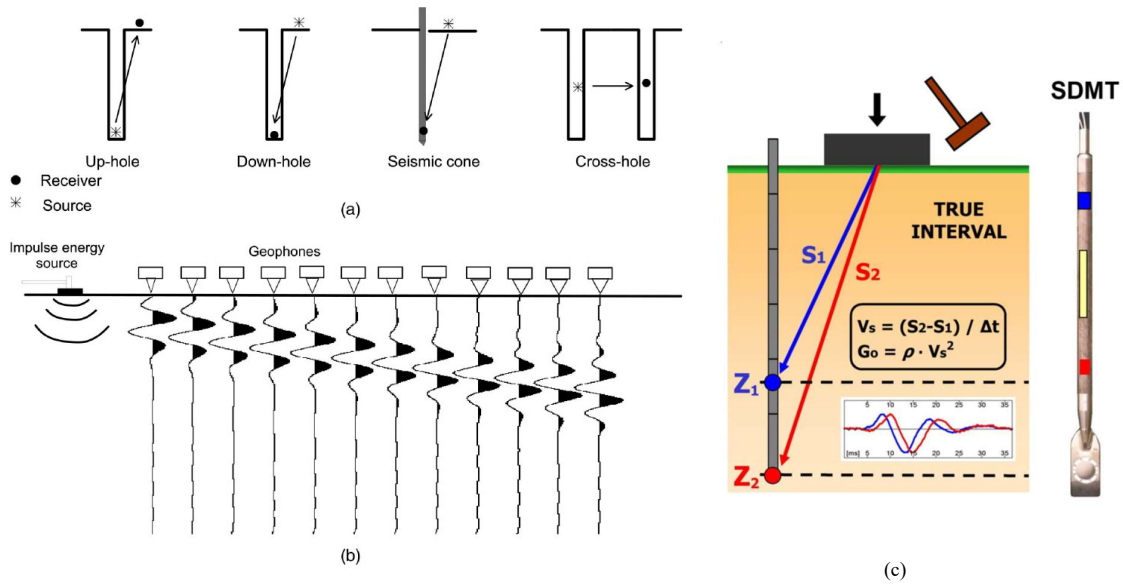
Figure 2.5: Illustration of (a) various intrusive field techniques and (b) multi-channel analysis of surface waves (MASW) (Figure 1, L'Heureux and Long (2017)) and (c) seismic dilatometer test (SDMT) (NGI, 2017)

The SDMT technique as shown in Figure 2.5c is a modification of a standard dilatometer, which is a stainless-steel blade with a flat, circular steel membrane mounted flush on one side (NGI, 2017). It is pushed into the ground with a push rig such as with a CPT and measures every 20 cm to determine relative strength and stiffness of the subsurface soils. The seismic module can be attached to the instrument and has two geophones as illustrated in Figure 2.5c. Shear waves are created at the ground surface by hitting an anchored plate horizontally with a sledgehammer. The vertical shear wave travel time (t_s) between the two geophones can be measured and hence the vertical shear wave velocity (V_s).

Laboratory Techniques

Resonant Column tests and Bender Element tests are the most common techniques for determining G_{max} from samples in the laboratory, but as with any laboratory test the problem of sample disturbance brings in significant uncertainties and it has been shown the G_{max} is significantly reduced when measured by such techniques. Therefore, they cannot be relied upon alone. Nonetheless they are commonly used as additional measurements when other laboratory tests are required.

2.3.2. *Measurement Using Bender Element Tests*

Bender element testing was first introduced into soil testing by Shirley and Hampton (1978) and later Dyvik and Madshus (1985) showed good agreement of G_{max} measurements with those of Resonant column tests.

A bender element system, as illustrated in Figure 2.6, consists of piezoelectric elements, which create voltage readings when pressure is applied, mounted in the standard inserts of a triaxial cell. One element is the sender element and the other the receiver element. An electric current is applied to the sender element, which causes it to contract on one side and expand on the other such that it bends and applies pressure to the soil it is contact with and thus creating a shear wave through the material. In the opposite way, the shear wave that has travelled through the material will apply a pressure to the receiver element that will create an electric current that is recorded by the system and thus gives a delay time and measurement of the shear wave velocity of the material.
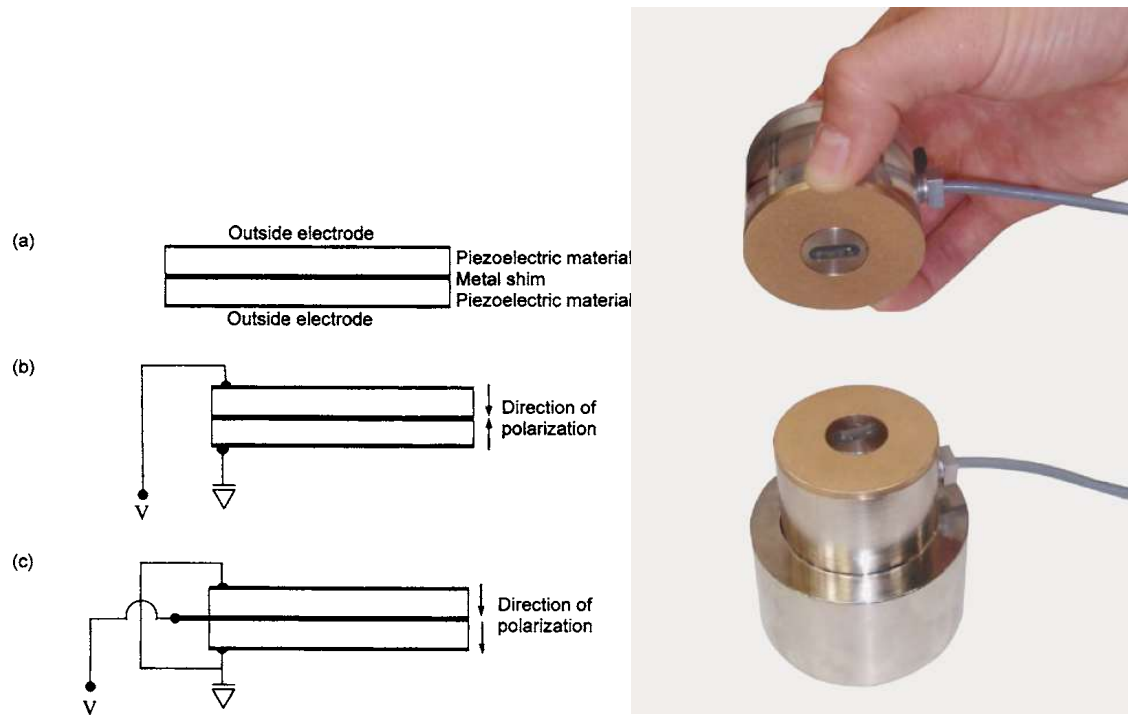
Figure 2.6: Schematic representation of bender elements. A) materials b) series type, c) parallel type. (Figure 1, Lee and Santamarina (2005)) and an image of the GDS Bender Element system (GDS)

There are 2 types of bender elements: series and parallel (Lee & Santamarina, 2005). The parallel type, in which the 2 piezoelectric layers have the same polling direction, gives twice the displacement as the series type in which the layers have the opposite polling direction. Using parallel type bender elements as sender and receiver minimises electromagnetic coupling effects in soils with high electric conductivity (Lee & Santamarina, 2005).

Interference of P-waves

When an S-wave set-up is used for the bender element test, P-waves will still be created horizontally through the sample from the sender element as shown in Figure 2.7. When these P-waves reach the side of the sample, a free-surface, they will be reflected and reach the

receiver. P-waves are faster than S-waves so depending on the properties of the soil and the size of the sample they will often interfere with the S-wave arrival signal. This is determined by the ratio between the velocities, which is related to the Poisson's ratio:

$$\frac{V_P}{V_S} = \approx \sqrt{\frac{1(1-v)}{1-2v}}$$

For a dry, unsaturated soil $v \approx 0.1$ so $V_P/V_S \approx 1.5$. However for saturated soils V_P/V_S is stress dependant and for soils subjected to low effective stresses, may exceed 20 (Sanchez-Salinero et al., 1986). It is in such cases that the near-field effect is important. Sanchez-Salinero et al. (1986) show that samples with a ratio of at least $d/\lambda > 2$ are required to eliminate this problem, where d is the distance between the sender and receiver and λ is the shear wavelength. Therefore, the input frequency is important ($\lambda = v/f$) when approaching this suggested limit. An increase in frequency will increase the distance to wavelength ratio.
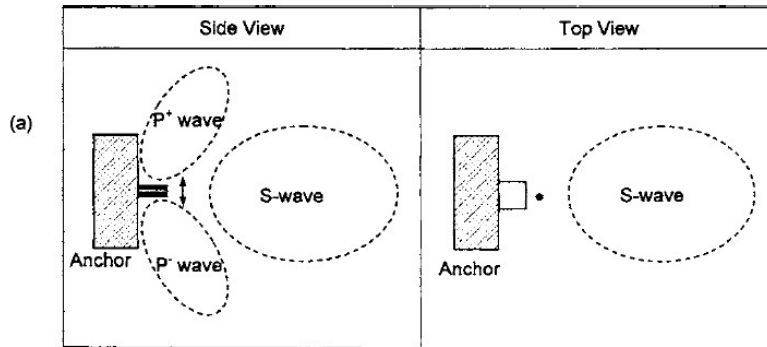
Figure 2.7: Illustration of "near field" effect created by P-waves (taken from Lee and Santamarina (2005))

Travel Distance and Picking of Travel Time

In the study by Lee and Santamarina (2005), they found that the correct distance to use in the calculations of G_{max} is tip to tip of the BEs. They also compare various techniques for picking the first arrival of S-waves. By analysing the 1st and 2nd S-wave arrival events they conclude that point C in Figure 2.8 is correct. This was termed the first zero cross-over method by Kawaguchi, Mitachi, and Shibuya (2001).
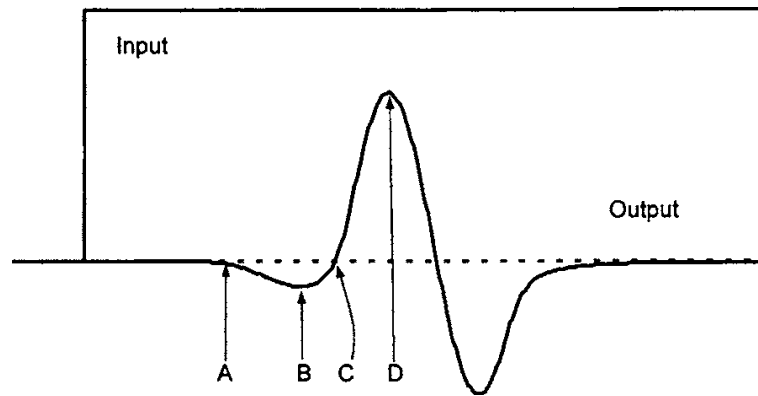
Figure 2.8: Picking of travel time from wave form (Lee & Santamarina, 2005)

2.4.   Factors Influencing G_{max}

As described by equation [2.9], the small strain shear stiffness is a product of the shear velocity and density of the soil at none to very small strains. There are many factors and soil properties that effect G_{max} as summarised in Table 2.1. Each factor is discussed briefly in this chapter.

Table 2.1: Summary of factors influencing G_{max} (modified (*) from table 6-7, S. Kramer (2017))

Increasing Factor	Effect on G_{max}
Effective confining pressure, p'	Increases
Void Ratio, e	Decreases
Overconsolidation Ratio, OCR	Increases (only significant for high OCR)*
Plasticity Index, I_P	Increases (only significant for high OCR)*
Strain Rate, $\dot{\gamma}$	Increases for plastic soils
Geological age, t_g	Increases
Cementation, c	Increases
Degree of Saturation, S_r	Decreases *

Hardin (1978) proposed a relationship to estimate G_{max} incorporating some of the parameters above:

$$G_{max} = A\, F(e)\, (OCR)^k (\sigma'_m)^n p_a^{(1-2n)}$$

where A is a material constant dependant on the soil and reference stress (A=625 is commonly used for atmospheric pressure (S. L. Kramer, 1996)), $F(e)$ is the void ratio function, OCR the overconsolidation ratio, k an OCR exponent dependant on the plasticity index (I_P), σ'_m is the effective average confining stress, n is the stress exponent and p_a is atmospheric pressure.

Leroueil and Hight (2003) also developed an empirical equation to describe the influencing factors on G_{max}:

$$G_{max} = S\,F(e)(\sigma_v'\sigma_h')^n p_a^{(1-2n)}$$

where S is a dimensionless soil characteristic parameter, σ'_v and σ'_h are the effective vertical and horizontal stresses. Donohue and Long (2010) and L'Heureux et al. (2013) have shown previously that the above equation works well for Norwegian clays when S is taken in the range 500-700, $F(e) = 1/e^{1.3}$ (where e is the void ratio), $K_0 = 0.5$ and n=0.25.

It can then be seen from these relationships that the primary factors influencing G_{max} are the void ratio, the effective confining pressure ($p' = (2\sigma_h' + \sigma_v')/3$) and OCR.

2.4.1. Confining Effective Pressure, p'

At large strains a power law relationship was proposed by Janbu (1963) and has been shown to be similar at small strains:

$$G_{max} \propto p'^m$$

Where p' is the average confining stress and m is a power exponent. This exponent shows great variation in the literature between 0.4 and 1.0 (Benz, 2007). An example of proposed relationships for clays is given in Figure 2.9.
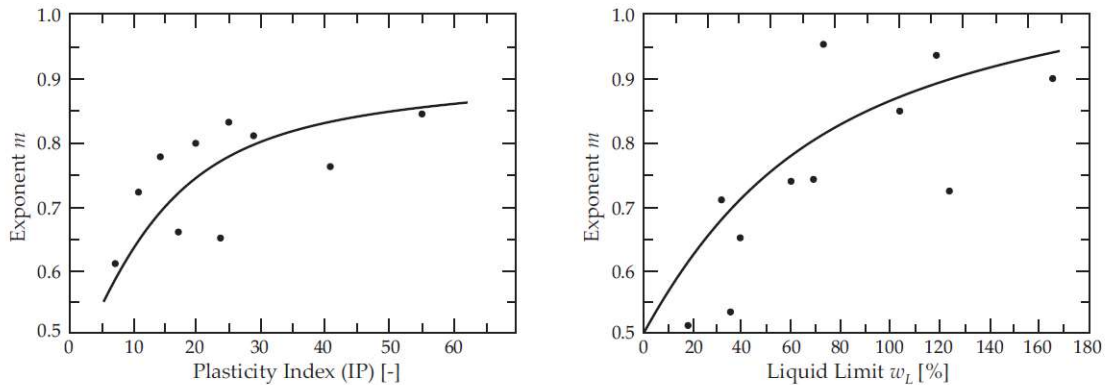
Figure 2.9: The power law exponent m as a function of plasticity index (I_P) and liquid limit, (w_L) (Figure 3.6, Benz (2007))

2.4.2. Void Ratio

In basic terms, a soil with a higher void ratio (e) indicates more contact between grains, hence denser and therefore stiffer. Common relationships between void ratio and G_{max} in the literature follow the form:

$$G_{max} \propto e^{-x}$$

where x is an exponent that varies dependant on the soil type and has been shown by Presti, Pallara, Lancellotta, Armandi, and Maniscalco (1993) to be between 1.1 and 1.5 for various clays. This form of the relationship is also accounted for in equations [2.13] and [2.14] in the void ratio function ($F(e)$).

Hardin and Richart (1963) found the following relationship works for clays with low surface activity:

$$G_{max} \propto \frac{(2.97 - e)^2}{(1 + e)}$$

[2.17]

For clays with high surface activity, which would be expected in a quick clay, the coefficient *2.97* should be replaced by a higher one.

2.4.3. OCR and Plasticity Index

It is known that OCR and plasticity of a clay can affect the modulus reduction curve (the reduction of G with increasing strain), which is very important for cyclic loading and earthquake response. This is illustrated in Figure 2.10.
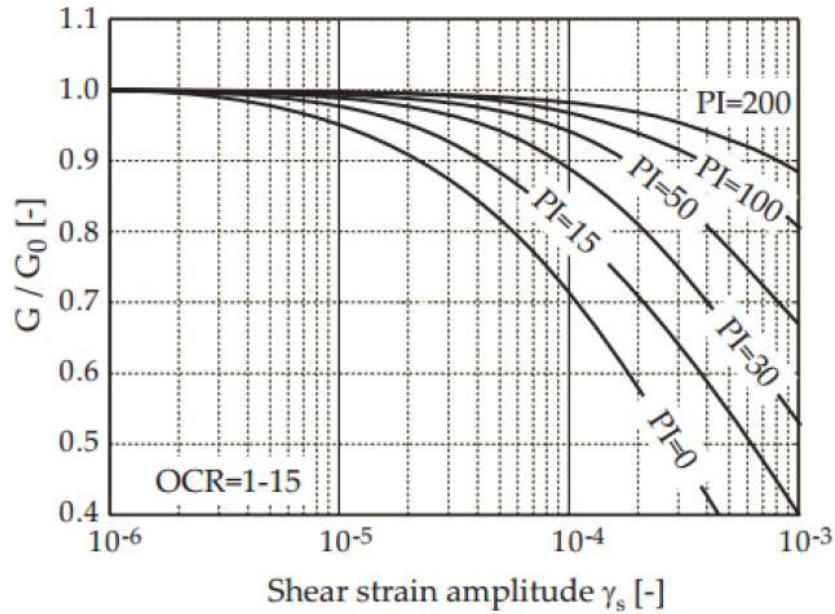
Figure 2.10: Stiffness reduction curve for soils of different plasticity (Vucetic & Dobry, 1991)

When just considering G_{max}, it can also be illustrated by equation [2.13], that for high OCR and OCR exponent (k), which increases with increasing plasticity as shown in Table 2.2, there should be an increase in G_{max}. Later research, for example by Shibuya et al. (1993), have shown that for low OCR, the influence of both factors is negligible as long as correct factors for stress and void ratio are applied.

Table 2.2: OCR exponent (k) with Plasticity Index (I_P) (Hardin & Drnevich, 1973)

Plasticity Index	k
0	0.00
20	0.18
40	0.30
60	0.41
80	0.48
≥100	0.50

2.4.4. Strain Rate

Strain rate becomes significant when comparing shear wave velocity measurements (or G_{max}) from the field with laboratory data, since they are measured with slightly different frequencies and hence strain rate. It has been shown that G_{max} can increase up 10% per tenfold increase in strain rate (S. L. Kramer, 1996).

2.4.5. Geological age effects

After primary consolidation, shear wave velocity (or G_{max}) increases approximately linearly with logarithmic time (S. L. Kramer, 1996) and can be described by:

$$\Delta G_{max} = N_G (G_{max})_{1000}$$

[2.18]

where ΔG_{max} is the increase in G_{max} over one log cycle of time and $(G_{max})_{1000}$ is the value of G_{max} 1000 minutes past the end of primary consolidation. N_G has been shown to increase with plasticity index (I_P) and for normally consolidated clays can be estimated from the relationship

$$N_G \approx 0.027\sqrt{I_P}$$

[2.19]

It has been shown that N_G can be used to correct G_{max} values measured in the laboratory to estimate more realistic in-situ values.

2.4.6. Degree of Saturation

Since S-waves only travel through the soil skeleton there should be no effect by the degree of saturation. However as Leong and Cheng (2016) discuss, a reduction in saturation can lead to increased matrix suction (illustrated in Figure 2.11), which is analogous to increasing effective stress and thus increases stiffness.
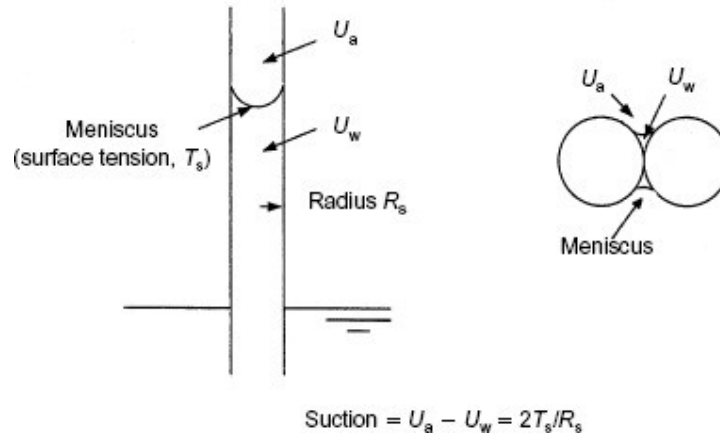
Figure 2.11: Illustration of matrix suction (Ridley, Dineen, Burland, & Vaughan, 2003)

2.5. Anisotropy of G_{max}

The anisotropic nature of soil properties can come from in-situ stress conditions (induced anisotropy) and the structure of the soil fabric (inherent anisotropy). Course silt, sand or gravel will tend to show less inherent anisotropy than a dense lacustrine clay due to the orientation and structure of the grains and illustrated in Figure 2.12.
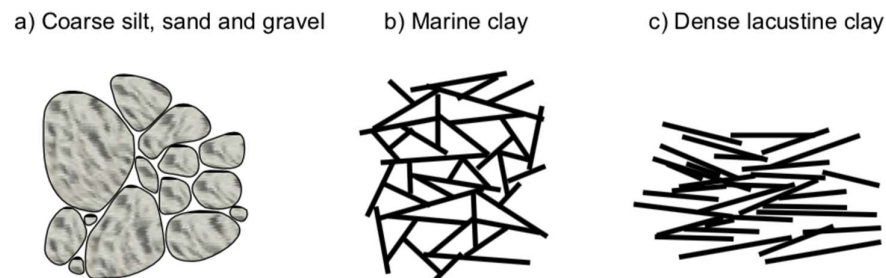
Figure 2.12: Examples of grain structures in various soils (Janbu, 1978)

Lacustrine clay is inherently anisotropic in nature due to its internal structure that was created during deposition. Clay particles by their planar nature, orientate horizontally and tend to be densely packed with face-to-face alignment (Wang, Lo, Yan, & Dong, 2007) as shown in Figure 2.13, due to the low number of ions in the fresh pore water (NTNU, 2015).

In marine clays the soil fabric structure is determined by the interaction of the clay minerals with the ions in the saline pore water. This creates a flocculated structure. It is therefore expected that marine clays show less anisotropic properties than lacustrine clays, but due to the presence of some horizontal orientation and the presence of anisotropic stress conditions, there is expected to be some anisotropic effect.

17
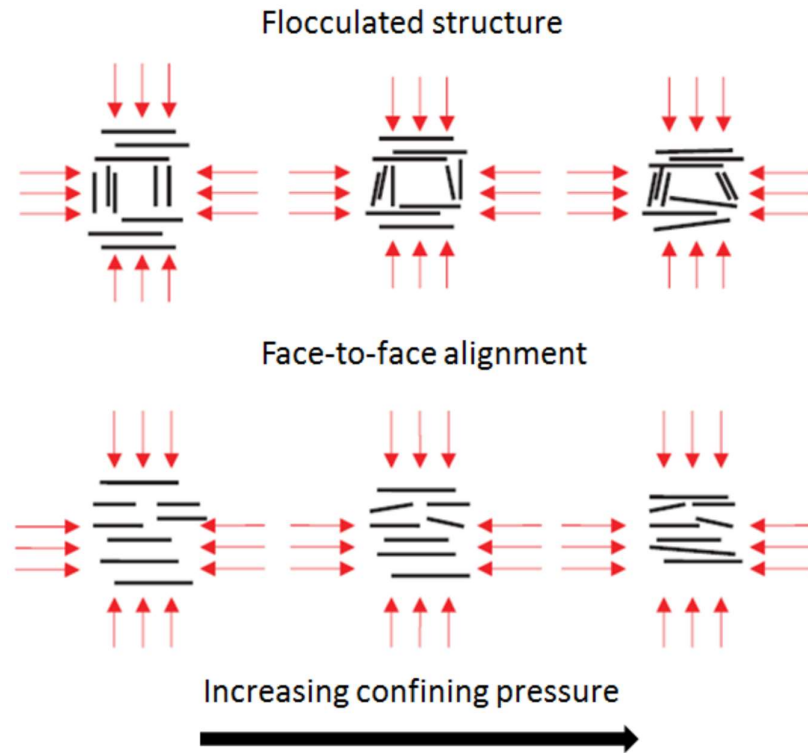
Figure 2.13: Illustration of volume-change mechanisms for soils of flocculated and face-to-face alignment (Wang et al., 2007)

L'Heureux and Long (2017) found that small strain-stiffness was largely isotropic for several soft clays tested throughout Norway using various techniques and directions of propagation and polarisation. However, Yamashita et al. (2006) carried out tests using a bender element system on reconstituted clay samples and found that horizontal shear wave velocities with the particle motion also parallel to the bedding planes ($V_{s,hh}$) is much greater (G_{max} greater) than when the particle motion is perpendicular to the bedding plane ($V_{s,vh}$.and $V_{s,hv}$). They also found that anisotropy in the elastic moduli of the clay became lower with increase in strain level and consolidation stress.

2.6.   P-wave propagation through Soil

The behaviour of P-waves differs from S-waves in saturated materials such as soils. S-waves only travel through the soil skeleton so are directly affected by changes in effective stress and void ratio as seen previously. However, P-waves travel through the soil skeleton and water, so are highly dependent on degree of saturation between 90-100%. At full saturation P-waves velocity remains constant even with increasing effective stress. As such it has been proposed that P-waves can be used to measure the degree of saturation more accurately than Skempton's B-value (Leong & Cheng, 2016).

According to Hooks'law for an element of isotropic elastic material, the constrained modulus can be calculated directly from the P-wave velocity as in equation [2.10]. However, the literature shows many different factors that influence the travel time of P-waves and it appears this becomes very complex problem for soils with potential anisotropy and/or varying saturation, and for application to triaxial samples using a bender element system.

Yang (2000) models P-waves through a partially saturated (< 90%) porous soil and finds two P-waves (P1 and P2) where both are frequency dependent and attenuated. P1 is fastest and associated with viscous coupling (in-phase movement) between solid and fluid and P2 shows more influence by degree of saturation, with out of phase movement of the soil skeleton and pore fluid. Other theories based on continuum mechanics conclude three types of P-waves (P1, P2 and P3) (Leong & Cheng, 2016), where P1 and P2 are as described previously and P3, which is the slowest and, due to its high attenuation, is difficult to detect and not well understood.

2.7. Quick Clays

Quick clays also referred to as sensitive clays are deposits of melt water sediments that were deposited in marine water during the last glaciation approximately 10,000 years ago. Due to the fast deposition process and flocculation due to the salt water, the clay particles are poorly sorted and therefore have high porosities of between 40-60% (A. S. Gylland, Rueslåtten, Jostad, & Nordal, 2013) and high-water contents. In their deposited state the structure of the soil is described as a 'card house structure' as seen in Figure 2.12 and Figure 2.13, with the phyllosilicates, which have a platy shape, bonded by van der Waals forces with end to surface bonds. Since isostatic rebound, the salt water content of the clays has been diluted by the infiltration of fresh water, resulting in repulsive forces on the mineral surfaces, which counter balance the van der Waals attractive forces. It is in this state that the clay is considered 'quick'. The in-situ structure is the same as before, but a slight disturbance can completely collapse the 'card house structure', resulting in decreased porosity and thus increased excess pore water and liquification.

Due to the similar latitude and geological processes these quick clays are common in Norway, Sweden, Canada and Japan. Not including Japan, who's quick clays are post-glacial, they all have similar mineralogy comprising mainly quartz, feldspars, amphiboles, mica and chlorites as well as iron oxide nanoparticles produced during grinding (Torrance, 2017). In Canada, quick clays are often cemented by carbonates, which increases their undisturbed strength.

The definition of a quick clay according to Norwegian standards (NGF, 2011) is when the remoulded shear strength of the clay (s_r) is less than 0.5 kPa and the sensitivity (S_t) is greater than 30. Quick clays are often also characterised by the following soil properties:

- Liquid limit, $w_L < w$, water content
- Salinity: < 2 g/l

It is well known that the resistance of clay against deformations for small load increments increases with age due to the development of cohesive bonds between the particles (Bjerrum, 1967). This is known as the aging effect and is seen in quick clays in Norway. There are 3 ways the cohesive bonds can be modified: cold-welding of mineral contact points between particles; exchange of cations; or precipitation of cementing agents. It is cation exchange that is the main process to have an influence on Norwegian clays. Since clay minerals have a net negative charge they attract cations to their surface. The majority of these cations will be sodium, (Na^+) in a marine clay. Over time, since isostatic rebound, the same leaching process that creates the quick clay properties, as described above, also reduces the pH levels of the porewater and starts disintegration of the feldspar, mica and chlorite minerals. This releases other cations into the pore water and since they are cations of a higher order, they exchange with the Na^+ ions on the surface of the clay minerals. It is known that the dominant cation to exchange in the early phases of this process in Norwegian clays is potassium, K^+. This has been shown to increase the plasticity index, I_p and remoulded shear strength, s_r as shown in Table 2.3.

Table 2.3: Common types of cation participating in ion-exchange phenomena in Norwegian clays (Bjerrum, 1967)

Type of cation	Origin or possible source	Effect on hydrous-mica/chlorite type clays	
		Plasticity index I_p	Remoulded shear strength s_u* ton/sq. m
H^+ pore water	Water, dissolved CO_2 decomposing organic matter	7·5	<0·01
Na^+	Seawater	16·4	0·11
Ca^{++}	Seawater, microfossils	16·7	0·15
Mg^{++}	Seawater, disintegrating chlorite	17·9	0·13
Al^{+++}	Disintegrated chlorite and felspar	21·6	0·42
$(Fe^{++}), Fe^{+++}$	Disintegrating chlorite	22·4	0·21
K^+	Seawater, disintegrating felspar and mica	22·7	0·29

* Tested at natural water content of clay, about 48%.

This process is essentially a weathering effect and is a commonly seen in soil profiles in Norway as illustrated in Figure 2.14. The upper 2-3 m are subjected to drying resulting in reduced water

content and increased shear strength. Below this, the soil shows no change in water content but there is additional shear strength when compared to the estimated original shear strength. This effect due to weathering diminishes with depth.
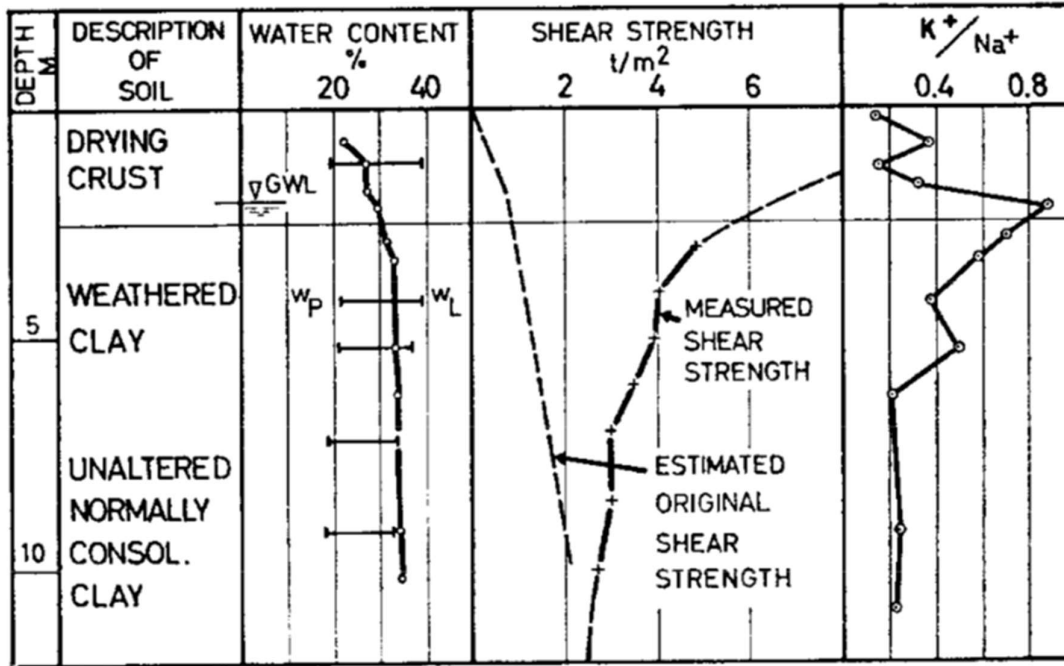
Figure 2.14: Geotechnical profile of typical Norwegian marine clay showing the effect of weathering on properties of clay ((Bjerrum, 1967)

In such a process the clay develops a critical pressure, which is comparable to a pre-consolidation pressure, pc' and displays the behaviour of an overconsolidated clay.

A. Gylland, Long, Emdal, and Sandven (2013) carried out a full study of a soil profile a quick clay NGTS at Tiller, Trondheim. They found that there were no significant changes in water content, salt content or porosity between non-sensitive and quick clay layers. This supports the theory that quick clay is an intermediate state in a geological process. Whilst initially the percolation of fresh water leaches sodium from the clay structure and creates quick clay properties in "young" marine clays, with more geological time it allows the development of strength through the process of cation exchange.

2.7.1. Dynamic Properties of Quick Clays

It is shown by L'Heureux and Long (2017) who studied shear velocity in clays at 28 sites in Norway, that there is a strong correlation between shear wave velocity and s_u with depth and that there is no difference between the quick clay site and normal clay sites. Therefore, V_s is independent of clay sensitivity.

21

2.8. Sampling and Sample Disturbance

Sample disturbance is particularly important for sensitive clays. It can occur in all steps of retrieving a sample including transport, storage, trimming and reconsolidation. When concerning Norwegian clays, the most significant effects of sample disturbance on laboratory tests is a reduction in the measured pre-consolidation stress (p_c') and peak undrained shear strength (s_u), a reduction in the initial/small-strain stiffness (G_{max}) and an increase in failure strain (ε_f) (A. Gylland et al., 2013; Karlsson, Emdal, & Dijkstra, 2016). Regarding the measurement of shear stiffness (G_{max}), there are many problems with determining an accurate value, which have been highlighted by variations between field and laboratory results. It is therefore important to understand the theory behind these differences in terms of the behaviour of the clay. Sample disturbance and stress relief due to unloading seem to be the main causes of such differences and it is these that shall be the focus of this study.

2.8.1. Sampling Techniques

Development of sampling over the years has found that block sampling is considered among the best methods for acquiring high quality samples, although even these must be handled and stored properly (Thakur, L'Heureux, & Locat, 2017). The Sherbrook block sampler, which takes samples 250 mm in diameter by 350 mm in height, has been developed in Norway since the 1980's and is well known to produce high quality samples (A. Gylland et al., 2013). However, the sampler has been found to be expensive and time consuming. Therefore, the Mini-block sampler has been developed in recent years at the geotechnical division of NTNU (Emdal, Gylland, Amundsen, Kåsin, & Long, 2016). A technical drawing is presented in Figure 2.15.
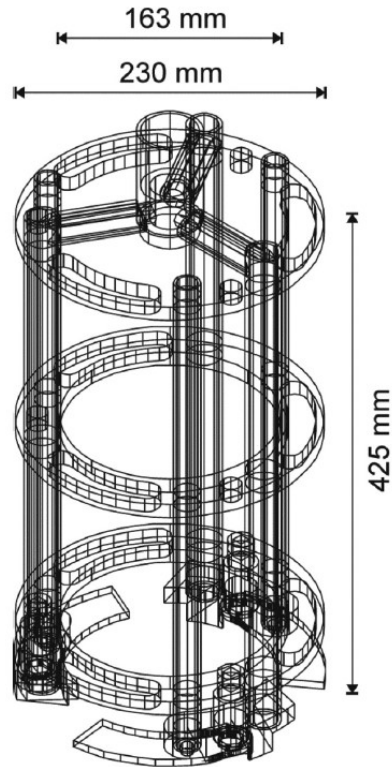
Figure 2.15: Technical drawing of the mini-block sampler (Emdal et al., 2016)

The main differences are a reduced sample size of 160 mm diameter and maximum sample height of 300 mm. The main purposes of reducing the size is to increase the efficiency of sample retrieval and handling. As shown by Karlsson et al. (2016), Rognlien (2017) also found that there is no difference in sample quality between Sherbrooke and Mini-block samples of quick clay taken from the NGTS at Tiller, Norway. Mini-block samples from the same site are used in this study.

2.8.2. *Measures of Sample Disturbance*

Andresen and Kolstad (1979) proposed a measure of sample disturbance that uses the volumetric strain during the consolidation phase of a triaxial and oedometer tests:

$$\varepsilon_{vol} = \frac{\Delta V}{V_0}$$

[2.20]

The criteria for this technique are shown in Table 2.4. The change in volume can be measured from the total water expelled during consolidation of a triaxial test and the deformation of an oedometer test.

Table 2.4: Criterion for sample disturbance described by Andresen and Kolstad (1979)

OCR [-]	Depth [m]	Perfect quality epsvol < [%]	Acceptable quality <epsvol < [%]	Disturbed quality eps vol > [%]
1 - 1.2	0 - 10	3.0	3.0 - 5.0	5.0
1.2 - 1.5	0 - 10	2.0	2.0 - 4.0	4.0
1.5 - 2	0 - 10	1.5	1.5 - 3.5	3.5
2 - 3	0 - 10	1.0	1.0 - 3.0	3.0
3 - 8	0 - 10	0.5	0.5 - 1.0	1.0

Lunne et al. (2006) found a clear relationship between the amount of water that is expelled during the consolidation phase of a triaxial test and the resulting properties that are measured during the shear phase of the triaxial test. They found that at small strains (<3-4%) the peak shear stress is smaller when more water is expelled during the consolidation stage, and at higher shear strains (~15%) the shear resistance is higher when more water is expelled. This is because sample disturbance at small strains results from the breakdown of the clay structure and at large strains from the reduction in water content. As such they proposed a measurement of sample disturbance:

$$\frac{\Delta e}{e_0}$$

[2.21]

where Δe is the change in pore volume and e_0 the initial pore volume. The proposed criteria are presented in Table 2.5.

Table 2.5: Proposed criteria for evaluation of sample disturbance as quantified by the value of $\Delta e/e_0$ (Lunne et al., 2006).

OCR	$\Delta e / e_0$			
	Very good to excellent quality (1)	Good to fair quality (2)	Poor quality (3)	Very poor quality (4)
1-2	<0.04	0.04-0.07	0.07-0.14	>0.14
2-4	<0.03	0.03-0.05	0.05-0.10	>0.10

This measurement should be used for samples that require the further measurement of mechanical properties. Also they are only relevant for marine clays with plasticity index 6-43%, water content 20-67 %, OCR 1-4 and depth below ground level 0-25 m (Lunne et al., 2006).

Both of the above measurements are taken after the sample has been trimmed (destructed) for laboratory testing. Landon et al. (2007) proposed a technique using a portable

bender element to take a shear wave velocity measurement as soon as a block comes out of the ground, i.e. non-destructive. This is compared to in-situ shear wave velocity values taken by seismic piezocone tests:

$$\frac{V_{S,vh}}{V_{SCPTU}}$$

<div align="right">[2.22]</div>

This technique allows for real time sample quality assessment in the field, so adjustments can be made and more effective selection of samples for laboratory testing. The criteria for the method are outlined in Table 2.6. The technique has been found to give good reliable measurements (Donohue & Long, 2010) but is not able to distinguish between very good to excellent quality (1) and fair to good quality (2) as defined by Lunne et al. (2006).

Table 2.6: Criteria for the non-destructive sample disturbance technique proposed by Landon et al. (2007) using shear wave velocity measurements compared to Lunne et al. (2006) criteria.

	Lunne, et al. (2006) criteria
$v_{S,vh} / v_{SCPTU} \geq 0.60$	1 and 2 (Fair to excellent quality)
$0.35 \leq v_{S,vh} / v_{SCPTU} < 0.60$	3 (Poor quality)
$v_{S,vh} / v_{SCPTU} < 0.35$	4 (Very poor quality)

Other developments have incorporated the use of suction (u_r) measurements on the unconfined samples normalised by the in-situ vertical effective stress (σ'_{v0}) (Tanaka, Sharma, Tsuchida, & Tanaka, 1996). Donohue and Long (2010) have further developed the following empirically derived normalised parameters:

$$L_{vs} = \frac{V_S\,in\,situ - V_{S0}}{V_S\,in\,situ - V_S remoulded}$$

<div align="right">[2.23]</div>

$$L_u = \frac{0.2\,\sigma'_{v0} - u_r}{0.2\sigma'_{v0}}$$

<div align="right">[2.24]</div>

As seen this technique incorporates the worst possible quality by inclusion of the remoulded shear velocity measurement. Again, this technique has advantage over the void ratio technique since it produces fast measurements in the field using a portable suction probe. The criteria for the classification of sample quality is presented in Figure 2.16. However, these are tentatively proposed based on samples from three sites in Norway.

Sample classification	L_{vs}	L_u
Very good to excellent	<0·65	<0·4
Good to fair	0·65–0·8	0·4–0·6
Poor	>0·8	>0·6
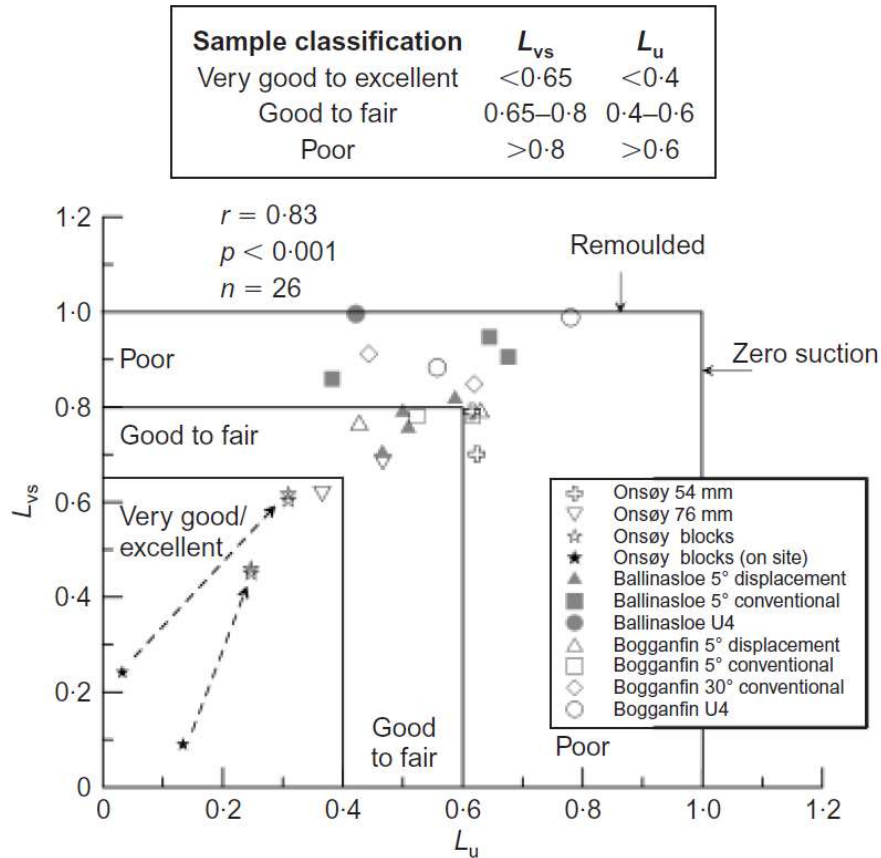
Figure 2.16: L_{vs} – L_u sample quality criterion proposed by Donohue and Long (2010).

2.8.3. Stress Relief due to Unloading

While considerable developments have been made to sampling techniques that have resulted in significant improvements in sample quality, the sample quality is still well below what is anticipated. It is widely accepted that the reduction of stresses to zero around a sample upon extrusion are what cause the reduction in sample quality, especially for low-plasticity sensitive clays (Amundsen, Jønland, Emdal, & Thakur, 2017). As considered by Donohue and Long (2010) levels of suction play a significant role during the sampling process. It is believed that this negative pore pressure creates a pressure gradient in the sample, which sucks water from the disturbed outer zone of the block sample to the intact clay in the centre (Amundsen et al., 2017). Theoretical pore pressure after unloading is defined by:

$$u_{ps} = -\frac{1}{3}(\sigma'_{v0} + 2\sigma'_{h0})$$

[2.25]

However residual pore pressure in low plasticity clays is found to be lower than the theoretical value ($|u_r|<|u_{ps}|$). Furthermore, any gases come out of solution creating an increase in pore volume and a reduction of residual effective stress ($p'_r<p'_{ps}$) which in turn causes the intact soil

26

to swell. Since block sampling does not constrict the sample during or after sampling this swelling is not constrained and therefore p'_r increases with time.

Amundsen et al. (2017) carried out a study to measure pore pressure development during the block sampling process. Figure 2.17 show the results of the study during sampling and after sampling. (9)-(10) was during the lifting of the sample. The sample was sealed at (11) and held in storage until (12) when it was transported and opened at (13).
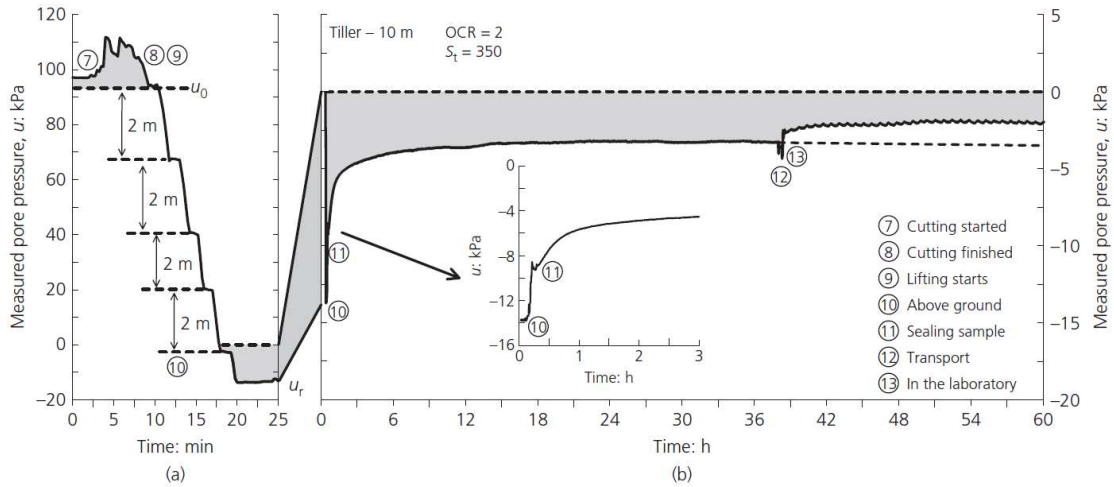
Figure 2.17: Pore pressures measured with a wireless piezometer inside a block sample during (a) sampling at 10m, (b) sealing, storage and transport of the sample (Fig.6. Amundsen et al. (2017))

The results show that residual pore pressure reduced rapidly during the 10 minutes before the sample was wrapped and that wrapping significantly reduced the rate of reduction. This rapid reduction in residual pore pressure confirms that it is swelling and water migration into the sample that keeps the residual effective stresses lower than the theoretical value (Amundsen et al., 2017).

3.   Location Specific Background

3.1.   Norwegian Geotechnical Test Sites (NGTS)

NGTS' are part of a research and development program supported by The Research Council of Norway Infrastructure program and led by the Norwegian Geotechnical Institute (NGI). There are 5 such sites in Norway (Figure 3.1) located near Oslo, Trondheim and Svalbard, which are chosen to represent 5 relevant soil types: soft clay, quick clay, silt, sand and permafrost.

Figure 3.1: Overview map of NGTS Locations

3.2.   Flotten Test Site

The quick clay for this study is from the Flotten NGTS at Tiller, Trondheim as shown in Figure 3.2. A number of research campaigns have been carried out at this site since 1982. The site is of interest since it is within a high risk quick clay hazard zone as shown in Figure 3.3. There was a major landslide event approximately 1 km north of the test site in 1816 involving 7,000,000 m^3 of soil and killing 15 people.
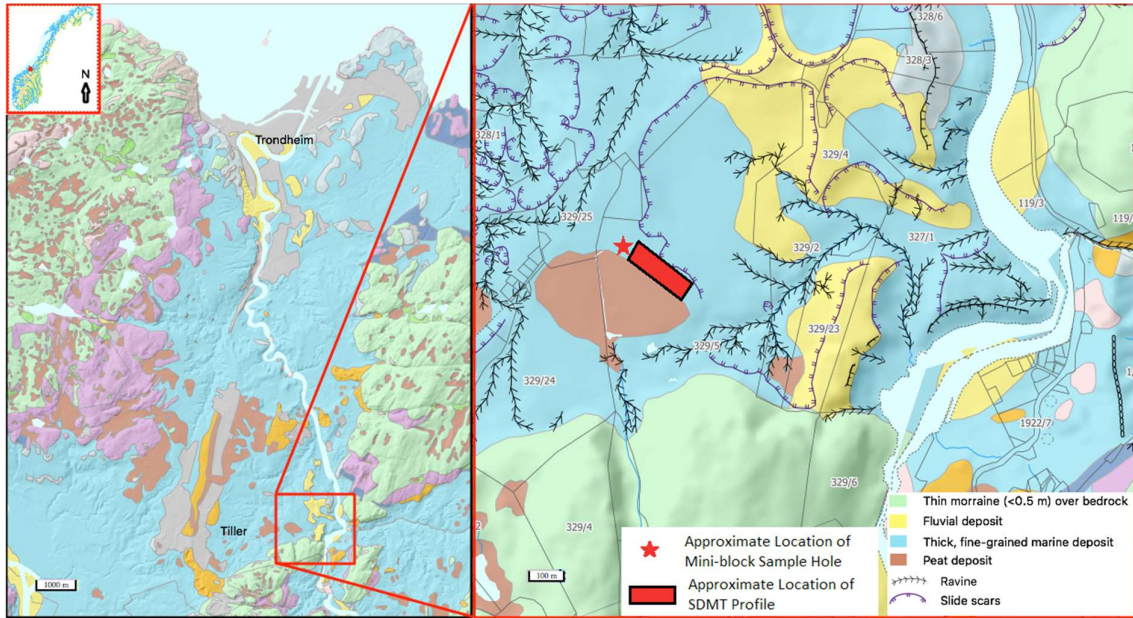
Figure 3.2: Location of the Flotten Quick Clay NGTS (NGU, 2018)
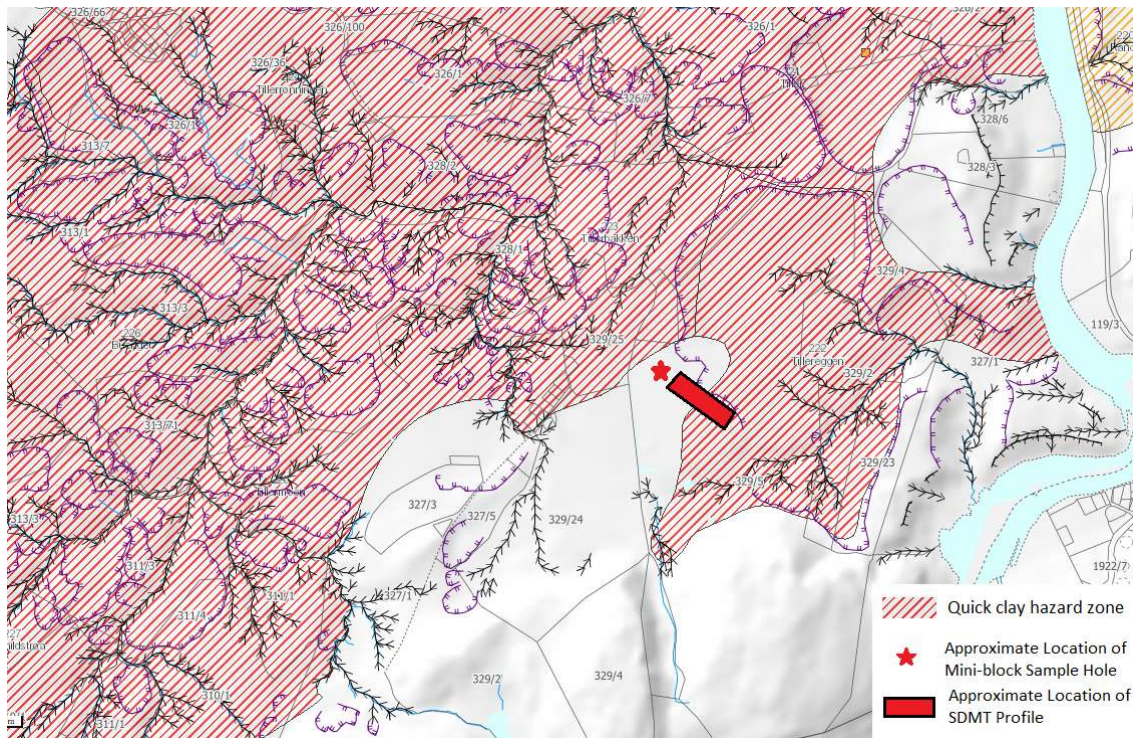

Figure 3.3: Quick Clay hazard zone at Tiller (NVE, 2018).

3.2.1. *Geological Setting*

A. Gylland et al. (2013) carried out a detailed study to characterise the engineering properties of the quick clay at Tiller from a location approximately 1.5 km west south-west of this study location. According to A. Gylland et al. (2013) and NGU (2018), as illustrated in Figure 3.2,

the site is covered by thick deposits of clay and the geomorphology of the area is defined by ravines and slide scars. The bedrock is dominated by greenstones, metasediments and volcanics that were metamorphosed and moved into place during the Caledonian orogeny. During the Younger Dryas between 10,800 and 10,500 year ago, the clay was deposited in sea water as the glacier retreated. The mineralogy of the clay is derived from the bedrock and the main components are quartz, feldspars, illite and chlorite with the latter phyllosilicates making up the majority of the clay fraction. Backscatter images shown in Figure 3.4 from an electron probe micro analyser (EPMA) scan illustrate the mineral content and structure of the Tiller clay (A. Gylland et al., 2013).
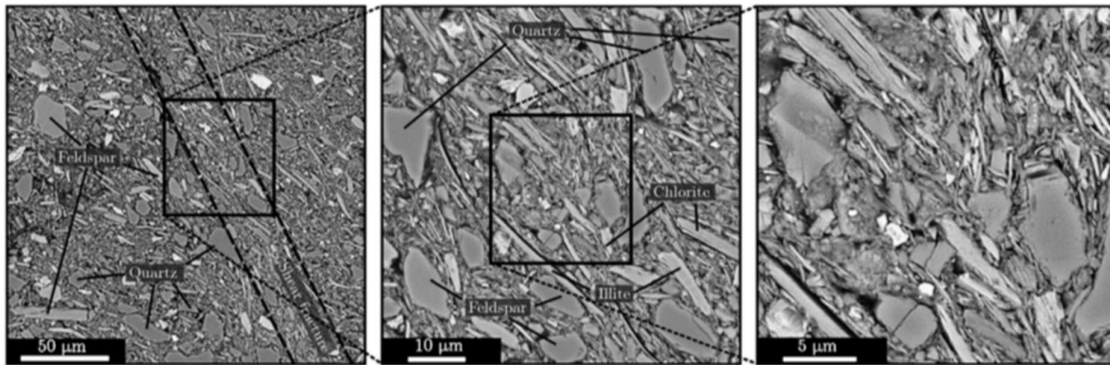
Figure 3.4: Backscatter image from EPMA scan illustrating mineral content and structure of the Tiller clay (A. Gylland et al., 2013)

3.2.2. Stress Conditions

Although there are no known historical loading situations, it has been shown (A. Gylland et al., 2013) that there is a pre-consolidation stress, p_c' well above the in situ vertical effective stress, σ_{v0}' based on a ground water level at 0.5 m and hydrostatic pore pressure. The corresponding over-consolidation ratio (OCR) were found to be between 3 at 5 m and 2 at 10m as shown in Figure 3.5.
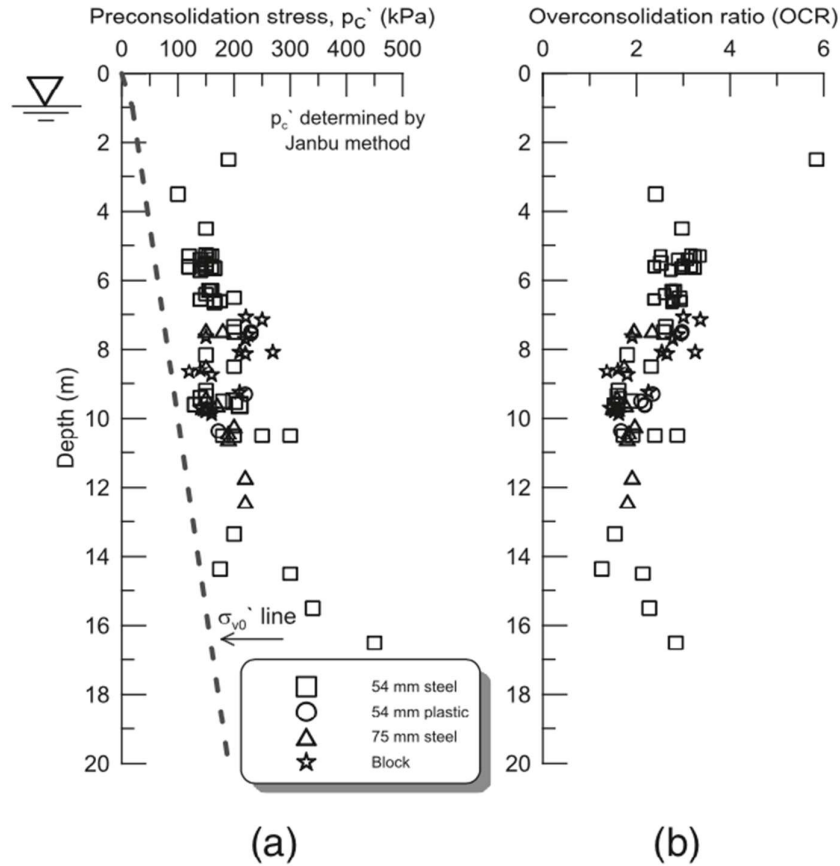
Figure 3.5: (a) Pre-consolidation stress and (b) OCR from the NGTS at Tiller (A. Gylland et al., 2013)

This presence of over-consolidation in what should be considered a normally consolidated soil has been referred to as a result of an aging effect or secondary/delayed compression a (Bjerrum, 1967) as described earlier in section 2.7, and is likely to be the contributing factor to what is seen in the Tiller clay.

Recent studies closer to the location of this study and within the Flotten clay, have shown a 2 m dry crust is underlain by a quite homogeneous plastic clay layer. There is a transition zone from about 8 m into the quick clay layer up to approximately 20 m, which is underlain by a coarser drained layer. Lindgård and Ofstad (2017) acquired piezometer results from this site, close to the location in this study (approximately 200 m southeast). They found the groundwater level at 1.5m depth and under-hydrostatic pore pressures with depth, as shown in Figure 3.6, thought to be due to the coarser underlying draining layer and the proximity to a stream to the east of the location.
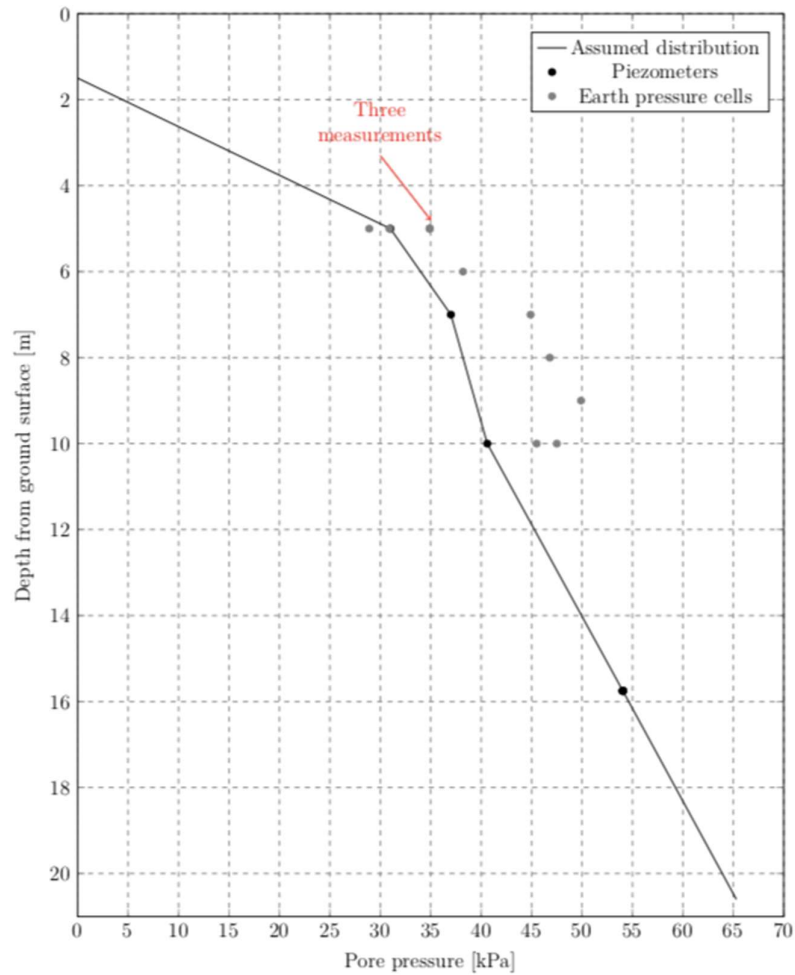
Figure 3.6: Overview of pore pressure measurements taken at Flotten (Lindgård & Ofstad, 2017)

Lindgård and Ofstad (2017) carried out an in-depth study of the problems of determining the coefficient of earth pressure at rest (K'_0) using samples from the Flotten site. The variation of results, presented in Figure 3.7, highlight the challenges in selection of a suitable K'_0 value.
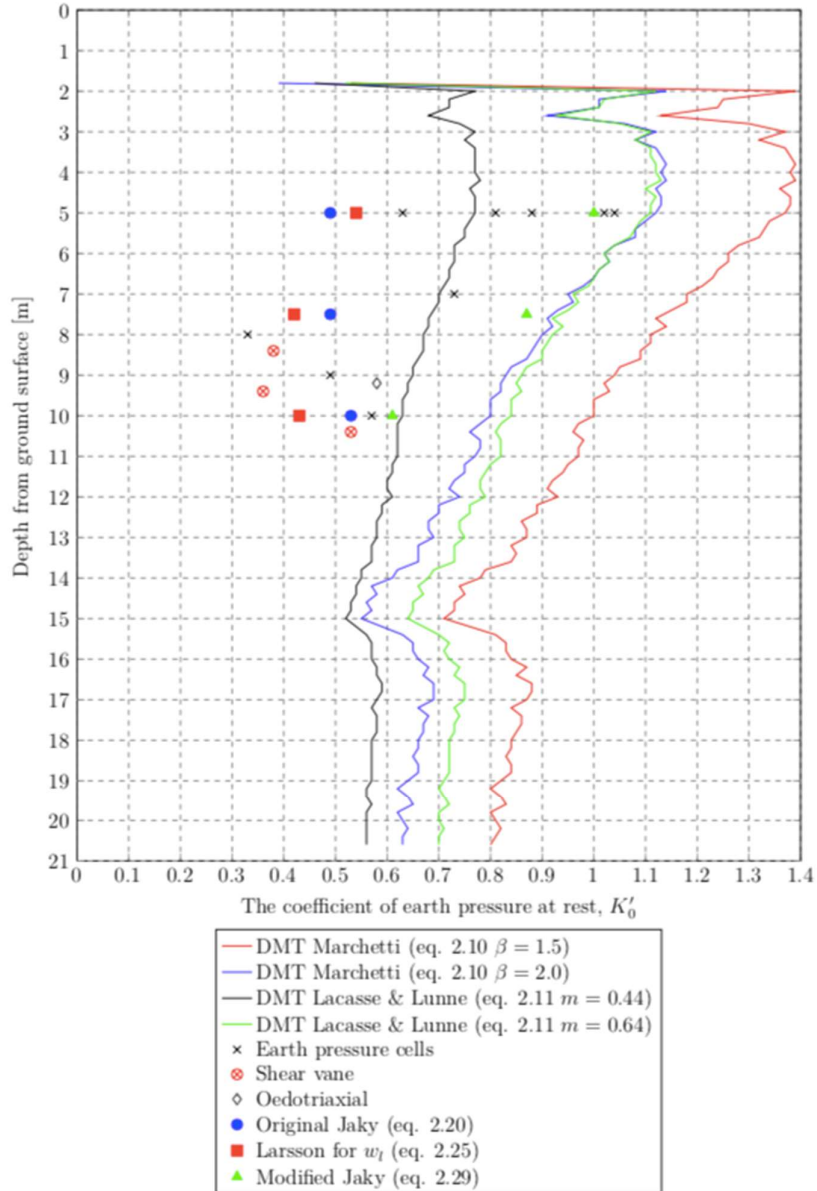
Figure 3.7: Comparison of different methods to determine K'₀ (Lindgård & Ofstad, 2017))

3.2.3. Shear Wave Velocity Measurements

A seismic dilatancy meter test profile was carried out for NGTS (NGI, 2017) very close to the sample location as shown in Figure 3.2. The results of the test are shown in Figure 3.8 and are compared and used as in-situ measurements for this study. As such the full results are included in APPENDIX D – SDMT Results.
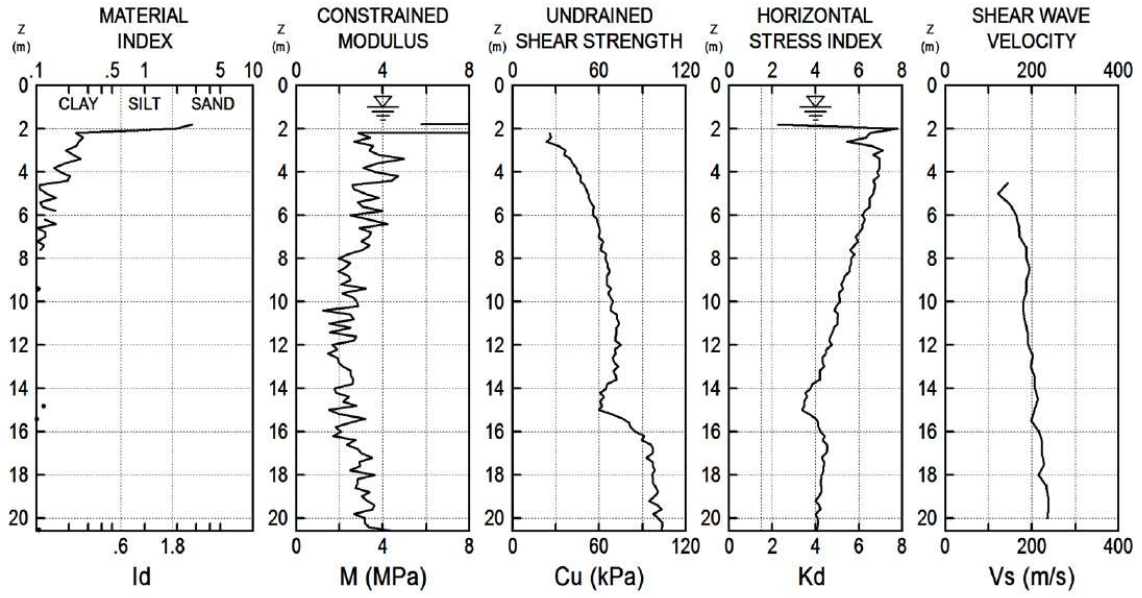
Figure 3.8: Results from an SDMT profile carried out by NGI NGI (2017)

4.   Laboratory Investigations

The following laboratory tests were carried out at the geotechnical division laboratory at NTNU, on samples taken from Flotten NGTS:

- Index tests

- Bender Element (BE) shear wave tests on unconfined half mini-block samples

- BE shear wave tests on unconfined trimmed triaxial samples

- BE shear wave tests on consolidated triaxial samples

- BE shear wave tests on/during unloading of triaxial samples

- BE P-wave tests on unconfined, consolidated and unloaded triaxial samples

The BE tests were carried out in both horizontal and vertical directions as described further in section 4.1.2, to determine anisotropic properties.

This chapter describes the procedures that were carried out for the laboratory tests.

4.1.   Sample Preparation

4.1.1. Sampling Procedure

Samples were taken using NTNU's mini-block sampler, from the Flotten NGTS, during September and October 2017, hence samples were 3-5 months old at the time of testing. According to Rognlien (2017), after removal from the ground, surface debris was removed, the block placed on a bottom plate, and the sample was wrapped in several layers of plastic film. The samples were placed in cylindrical plastic containers with a void between the sample and the container that was filled with styrofoam pellets to damp any vibrations during transportation. These were stored in a temperature regulated room at 4-5°C with high humidity.

4.1.2. Sample Division

For the purposes of this study six mini-block samples were utilised. These were divided into half lengthways. For four of these, only the bottom half was used, whilst another masters student used the top half. For two blocks the top half was also used for "extra tests" as described in section 4.4. It is expected that approximately 50 mm at the bottom of the mini-block is highly disturbed due to the cutting process and the pressures imposed during of lifting the sample out of the ground. Therefore, the sample is divided from the top to minimize disturbance effects in the final trimmed samples. Off-cuts from the top and centre were kept and wrapped immediately to be transferred to the laboratory for index testing.

Some half blocks were first tested using the portable bender element set-up if required (described in section 4.3.2), then divided into three slices in one of the two configurations shown in Figure 4.1. Configuration (a) was used for most tests to determine anisotropy in shear stiffness, where black is a vertical sample, red and blue are horizontal samples with different BE orientations to measure $G_{max,hh}$ and $G_{max,hv}$, respectively as was introduced in 2.3. Configuration (b) was used for one half mini-block to test influence of consolidation rate and salt at the BE contacts. Approximately 10 mm of the outer edges of the mini/block samples were found to be disturbed as illustrated in Figure 4.2. Therefore, it was important to divide the samples efficiently to avoid these areas.
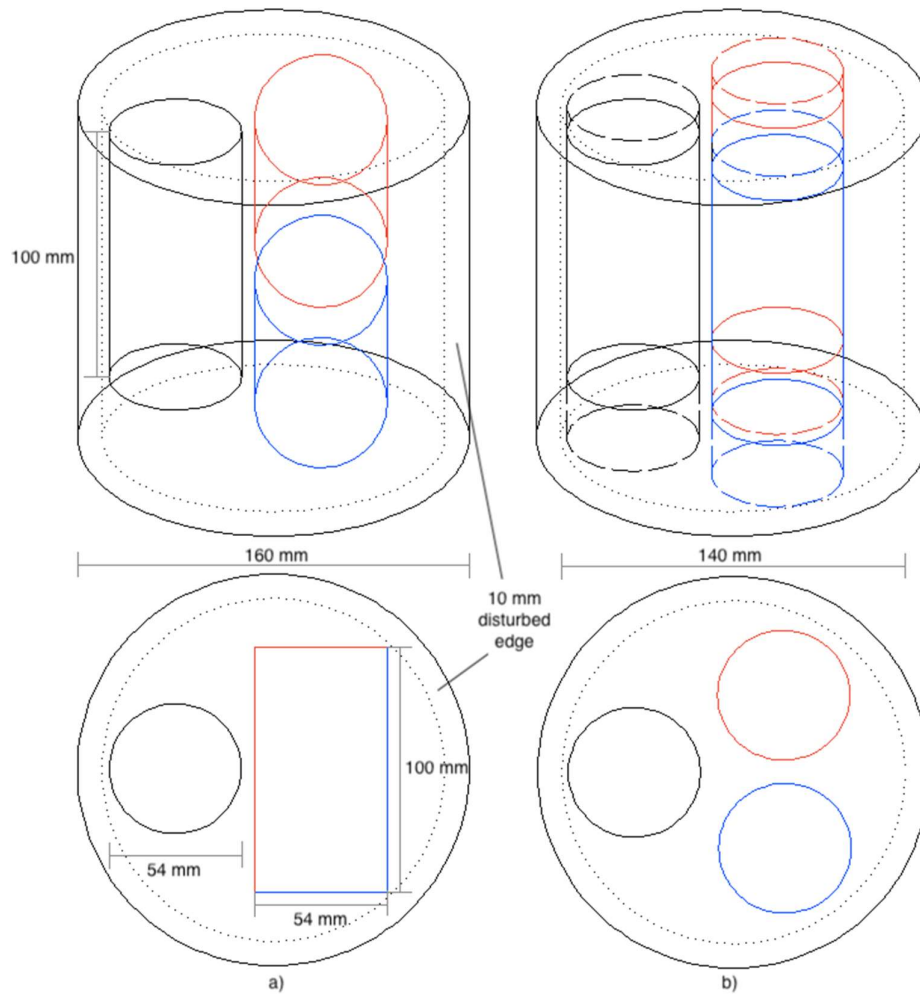
Figure 4.1: Subdivision of mini-black half sample (a) 3 vertical samples (b) 1 vertical, 2 horizontal samples
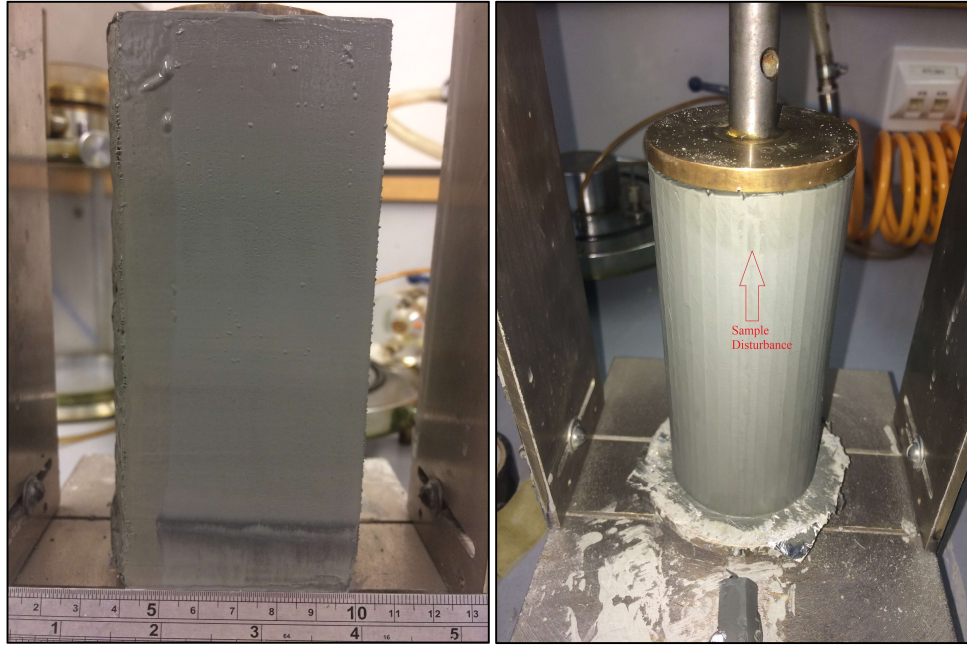
Figure 4.2: Image of disturbance at the edges of the mini-block samples seen in a vertical cut and horizontally trimmed sample.

On subdivision into slices, the top direction was clearly marked and then the samples were wrapped in several layers of plastic film. These were stored in an airtight container with a moist rag. BE tests were then carried out as soon as possible, being left in the storage room no more than 48 hours before being trimmed for testing.

4.2. Index Testing

Index testing is an important part of laboratory testing allowing the soil to be classified according to standard systems. The index parameters can be used for simple correlations with mechanical soil properties and measurements of some mechanical properties such as undrained shear strength (s_u) can be attained. The parameter can also be used for input parameters for ongoing laboratory tests, for example unit weight for calculations of in-situ stress conditions. The following index tests were carried out:

- Water Content
- Salinity
- Atterberg limits
- Bulk density
- Grain density
- Falling cone
- Grain size distribution

Unconfined compression tests and determination of organic content were not carried out for this study. A brief overview of the procedures is given in this chapter.

4.2.1. Water Content / Degree of Saturation

Water content was determined by drying a sample of the soil according to the standard ISO 17892-1 (ISO, 2014a). The water content is calculated in percent as follows:

$$w = \frac{m_w}{m_s} \cdot 100 = \frac{m - m_s}{m_s} \cdot 100 \quad [\%]$$

[4.1]

where m_w is the mass of water, m_s is the dry mass and m is the total wet mass.

4.2.2. Salinity

The sample was remoulded and mounted into apparatus that uses compressed air to pressurise and expel pore water from the sample. The electric conductivity was measured and used to determine the salt content.

4.2.3. Atterberg Limits

A fine-grained soil can exist in four states: hard (dry), firm or crumbling, plastic, and liquid. These are defined by the water content of the soil and as such the limits between the states occur at specific water contents. These limits are known as the Atterberg limits:

w_L = liquid limit (%)

w_P = plastic limit (%)

w_S = shrinkage limit (%)

To determine liquid limit of the clay a Casagrande test was carried out according to section 5.3 in NS8001 (Norge, 1982). The plastic limit was determined using procedures according to section 5.3 in ISO/TS 17892-12 (ISO, 2004a).

The plasticity index (I_P) and liquidity index can then be calculated as follows by equations [4.2] and [4.3], respectively.

$$I_P = w_L - w_P$$

[4.2]

$$I_L = \frac{w - w_P}{w_L - w_P}$$

[4.3]

Plasticity is classified as shown in Table 4.1.

Classification of material	Classification of plasticity	I_P (%)
Low plastic	Low plasticity	< 10
Medium plastic	Medium plasticity	10 - 20
Highly plastic	High plasticity	> 20

Most Norwegian clays tend to be of low plasticity (NTNU, 2015). Quick clay behaviour is indicated when the liquidity index is more than one ($I_L > 1$) or water content is more than the liquid limit ($w > w_L$).

4.2.4. Density

Bulk Density

The bulk density was determined according to section 5.1.4 in ISO 17892-2 (ISO, 2014b), using a small cylindrical ring of calibrated mass and internal volume, which pushed into a sample of clay. The bulk density is then calculated by equation [2.1] and the unit weight by equation [4.4].

$$\rho = \frac{m_s + m_w}{V} = \frac{m}{V} \qquad \left[\frac{g}{cm^3}\right]$$

[4.4]

$$\gamma = \frac{(m_s + m_w) \cdot g}{V} = \frac{m \cdot g}{V} \qquad \left[\frac{kN}{m^3}\right]$$

[4.5]

where m_s is the mass of the solid particles, m_s is the mass of water, V is the total volume, m is the total mass and $g = 9.81$ m/s^2.

Particle Density

The particle (grain) density was determined according to ISO 17892-3 (ISO, 2015) using a pycnometer with a volume of 100 ml. Equations [4.6] and [4.7] were used to calculate the grain density and unit weight of solids, respectively.

$$\rho_s = \frac{m_s}{m_{wp} + m_s - m_{wps}} \cdot \rho_w \qquad \left[\frac{g}{cm^3}\right]$$

[4.6]

$$\gamma_s = \rho_s \cdot g \qquad \left[\frac{kN}{m^3}\right]$$

[4.7]

where m_s is the mass of the dry solid particles, m_{wp} is the mass of the water filled pycnometer, m_{wps} is the mass of the pycnometer with sample and water, ρ_w is the density of water and $g = 9.81$ m/s^2.

4.2.5. Sensitivity

The falling cone method was used to determine undrained shear strength of both undisturbed and remoulded samples according to ISO 17892-6 (ISO, 2017). Soils strength is classified according to Table 4.2, and sensitivity was then calculated using equation [4.8] and classified according to Table 4.3.

$$S_t = \frac{s_u}{s_r} \qquad [-]$$

[4.8]

Table 4.2: Classification of soil strength according to undisturbed soil strength (NGF, 2011)

Classification of soil type	Classification of shear strength	s_u (kPa)
Very soft	Very low	< 12.5
Soft	low	12.5 – 25
Medium stiff	Medium high	25 – 50
Stiff	High	50 – 100
Very stiff	Very high	> 100

Table 4.3: Classification of soil according to sensitivity

Classification of soil type	Classification of sensitivity	S_t (-)
Low sensitive	Low	< 8
Medium sensitive	Medium	8 – 30
Highly sensitive	High	> 30

4.2.6. Grain Size Distribution

The grain size distribution was determined using hydrometer analysis according to NS8005 (Norge, 1990). The method is based on Stoke's law for sedimentation velocity of spherical grains in a liquid or gas. The equivalent spherical diameter is determined in this case for clay particles. A homogeneous suspension of the clay sample is created, and a dispersive matter is added to prevent particle flocculation.

4.2.7. Index Parameter Calculations

Degree of Saturation

Degree of saturation is calculated using equation [4.9].

$$S_r = \frac{V_w}{V_p} = \frac{w \cdot \gamma}{\gamma_w \left(1 + w - \dfrac{\gamma}{\gamma_s}\right)} \quad [-]$$

[4.9]

where V_w is the volume of water, V_p is the volume of voids and γ_w is the unit weight of water. For soils below the water table the degree of saturation should equal to 1 (100%).

Porosity

Porosity is a measure of the ratio between the volume of voids and total volume of the sample and is calculated using equation [4.10].

$$n = \frac{V_p}{V} = 1 - \frac{\gamma}{\gamma_s (1 + w)} \cdot 100 \quad [\%]$$

[4.10]

Void Ratio

For clays the void ratio, which is the ratio between the pore volume and the volume of solid particles, is commonly used. It is calculated using equation [4.11].

$$e = \frac{V_p}{V_s} = \frac{\gamma_s (1 + w)}{\gamma} - 1 \quad [-]$$

[4.11]

4.3. Bender Element Tests

The NTNU laboratories use a bender element system (BES) by GDS. Specifications of the system can be found in APPENDIX A – Bender Element Specifications. The element system can be added to a triaxial testing system as shown in Figure 4.3 or can be a stand-alone system by simple removal of the bottom cap from the triaxial bottom plate. Both set-ups are used for this study.
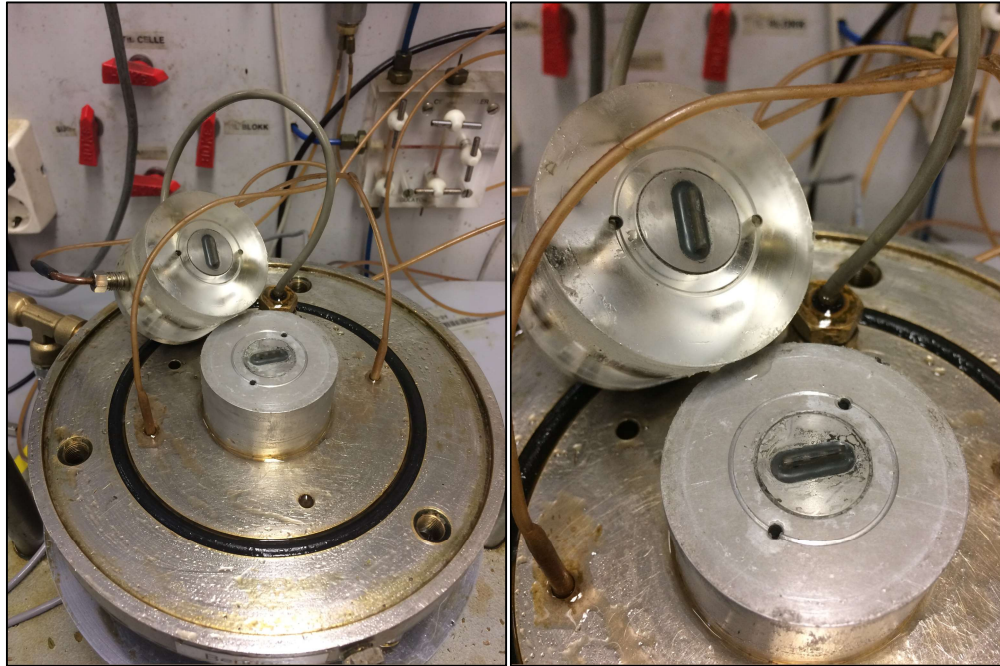
Figure 4.3: Bender element system set-up in a triaxial cell at NTNUs geotechnical laboratory

The elements can be easily set up in both in S-wave and P-wave configuration by a simple change of wiring. The input signal is created, and the interpretation of the return signal is carried out, using a LabVIEW program created by Per Asbjørn Østensen at NTNU. This uses a multifunction data acquisition (DAQ) device to send out a single sine signal in each measurement. In order to get a good output signal, the transmitter element and receiver element are connected to a power amplifier and voltage amplifier, respectively. The amplitude and frequency of the input signal can be varied to ensure a good output signal, but these were rarely changed from 5 V and between 0.6 and 2.0 kHz, respectively. The software uses cross-correlation (method of least squares) to match the shape of the output signal to the input signal in order to determine the travel time as illustrated in Figure 4.4, where white is the input signal, red is the received signal and green is the matched signal. The system records the received signal at a sampling rate of 20 kHz, so a time resolution of 0.5 ms. On set up of the project, each measurement had to be taken manually and only one output containing time, bender element delay (ms), effective height (mm) and received signal (mV) was recorded into a file. The program was later modified to run automatically at a user specified interval and to output an image of each measurement to allow quality control and back measurement if necessary.

Figure 4.4: Example of a measurement taken by the Bender Element LabVIEW program

4.3.1. Overview of Bender Element tests carried out

An overview of the Bender Element tests carried out for this study is given in Table 4.4. Tests were carried out in the displayed order and are described in such an order in this section so as to explain the development of the testing techniques. Shear wave and compression wave velocity measurements are given by V_s and V_p, respectively with the orientation indicated. Samples are named by depth and orientation. For example, Sample-890-Shh was taken from 8.90 m and tested with S-waves with horizontal propagation and particle movement.

Table 4.4: Overview of Bender Element tests carried out

Sample depth (m)	Unconfined and Consolidation Measurements	Unloading Measurements (burette open/closed)	Half mini-block Measurements	Other (K_0, consolidation rate, time left, salt used, etc)
8.90	V_{Sv}	V_{Svh} (closed)		$K_0 = 0.5$, 2kPa/2min
	V_{Shh}	V_{Shh} (closed)		$K_0 = 0.5$, 2kPa/2min
	V_{Shv}	V_{Shv} (closed)		$K_0 = 0.5$, 2kPa/2min
9.60	V_{Sv}	V_{Svh} (closed)		$K_0 = 0.7$, 2kPa/min
	V_{Shh}			$K_0 = 0.7$, 2kPa/min
	V_{Shv}	V_{Shv} (closed)		$K_0 = 0.7$, 2kPa/min
10.70	V_{Sv}	V_{Svh} (closed)	V_{Sv}	$K_0 = 0.7$, 2kPa/min
	V_{Shh}	V_{Shh} (closed)	V_{Shh}	$K_0 = 0.7$, 2kPa/min
	V_{Shv}	V_{Shv} (closed)	V_{Shv}	$K_0 = 0.7$, 2kPa/min
15.85	V_{Sv}	V_{Svh} (closed)	V_{Sv}	$K_0 = 0.7$, 2kPa/min
	V_{Shh}	V_{Shh} (closed)	V_{Shh}	$K_0 = 0.7$, 2kPa/min
	V_{Shv}	V_{Shv} (closed)	V_{Shv}	$K_0 = 0.7$, 2kPa/min
11.65	V_{Sv}	V_{Sv} (closed)	V_{Sv}	$K_0 = 0.7$, 2kPa/2min
	V_{Shh}	V_{Shh} (closed)	V_{Shh}	$K_0 = 0.7$, 2kPa/2min
	V_{Shv}	V_{Shv} (closed)	V_{Shv}	$K_0 = 0.7$, 2kPa/2min
15.70	V_{Sv1}	V_{Sv} (open/closed)		$K_0 = 0.7$, 5kPa/min Left for 10 days
	V_{Sv2}	V_{Sv} (closed)		$K_0 = 0.7$, 10kPa/min Salt on contacts
	V_{Sv3}	V_{Sv} (closed)		$K_0 = 0.7$, 10kPa/min
13.75	V_{Phv}	V_{Phv} (open)		$K_0 = 0.7$, 5kPa/min Closed and left over a weekend
	V_{Ph1}	V_{Ph1} (open)		$K_0 = 0.7$, 5kPa/min
	V_{Ph2}	V_{Ph2} (closed)		$K_0 = 0.7$, 5kPa/min
13.60	V_{Sv}	V_{Sv} (open)	V_{Sv}	$K_0 = 0.7$, 5kPa/min
	V_{Shh}	V_{Shh} (closed)	V_{Shh}	$K_0 = 0.7$, 10kPa/min
	V_{Shv}	V_{Shv} (closed)	V_{Shv}	$K_0 = 0.7$, 10kPa/min

4.3.2. Stand-Alone System on Half Mini-block Samples

The Bender elements are easily removed from the triaxial top and bottom plates to make a stand-alone "portable system". Before trimming some half mini-blocks were tested using this system only in the S-wave configuration. The hope was to confirm the "near-field" effect from P-wave interference and see if there was an influence by sample proportions (that is, half a mini-block has roughly 1:1 height to width ratio compared to 2:1 dimensions of a triaxial sample). The set-up and measurement directions are illustrated in Figure 4.5.
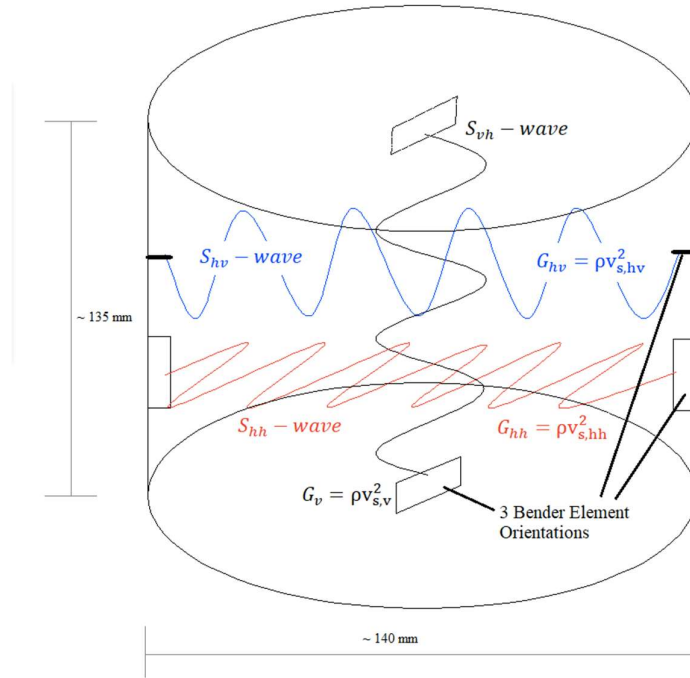

Figure 4.5: Measurement directions using the stand-alone system

4.3.3. Triaxial Testing System

Pre-cut slices, as described in 4.1.2, were taken from the cold storage room, trimmed to 54 mm diameter with a wire saw, cut to 100 mm height and mounted onto the triaxial rig as quick as possible. Filter paper was cut to anulus shape for the top and bottom. For the horizontal samples the bedding direction was marked on the paper to help with correct alignment of the bender elements. The sample was gently placed onto the bottom receiver element in the correct orientation. Filter paper was saturated and placed around the sample. Silicon grease was spread around the top and bottom caps where the rubber membrane is held on. The triaxial membrane was placed using the mounting cylinder. In this process the top cap with sending bender element was installed and held in place using four rubber rings. Images of these steps are used for illustration in Figure 4.6.
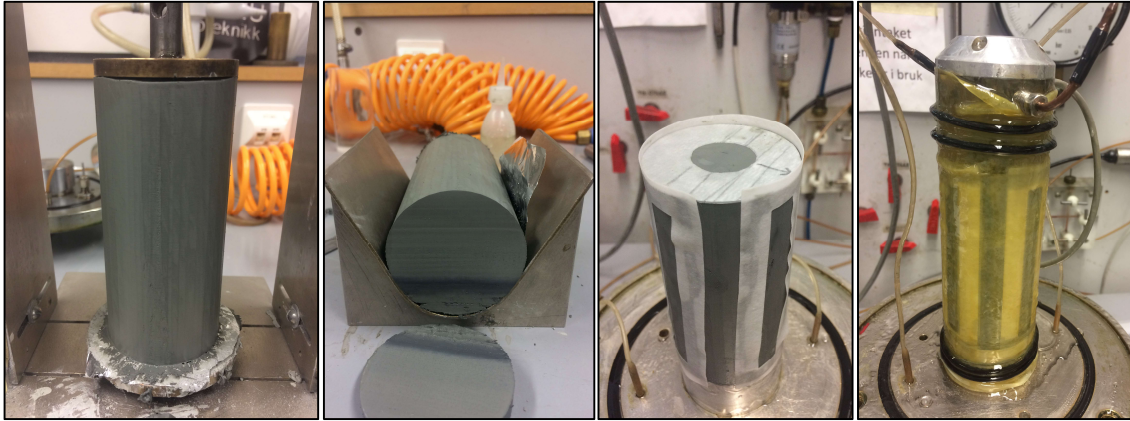
Figure 4.6: Sample trimming and preparation for triaxial bender element testing (different samples)

When the samples were fully mounted it was then that the first velocity measurements were taken. The triaxial cell was then installed and filled according to the equipment procedures. Once the cell was filled and the system checked for leaks the cell pressure was increased to 10 kPa, which was the start pressure of all the tests. Another reading was taken approximately 2 minutes after this and then the process of consolidation proceeded.

On starting the consolidation step, a 5 kPa vertical pressure was applied for all tests to maintain good contact between the bender elements and the sample. The cell pressure was then increased at a rate of between 1 kPa/min and 10 kPa/min. The cell pressure is considered applied in all three principle stress directions. As such, an additional vertical load was applied at the same rate thereafter for the vertical samples, which were consolidated to anisotropic conditions. The primary objective was to expose each sample from the same depth to the same average effective pressure (p'). Stress calculations and actual applied stresses are summarised in Table 4.5.

End of primary consolidation (EOP) is taken according to ISO (2004b), when the volume change is less than 0.1 % of the specimen volume per hour or 0.1 cm^3/hr (ml/hr), whichever is greater.

Velocity measurements were taken at pre-consolidation, during consolidation and after unloading. For some later tests, measurements were also taken during unloading with valves to the burette both open and closed to compare the effect of samples having access to water during unloading.

Details of the procedures for each sample are included in APPENDIX B – Details of Individual Bender Element Tests.

In-Situ Stress Calculations

Table 4.5 summarises the stress conditions calculated, and the actual applied stresses each sample. It should be noted that there were some mistakes in calculations at the start of the tests, which resulted in slightly higher average confining stress conditions and higher actual K_0 values. These effects will be discussed in section 0.

Table 4.5: Summary of calculated stress conditions and those applied to each sample

			Calculated Stress Levels									Appled Stress Levels			
Depth (m)	Sample Orientation	Unit weight (kN/m3)	Vertical total stress, σ_v (kPa)	Pore Pressure, u (kPa)	Additional modifications (kPa)	Vertical effective stress, σ'_v (kPa)	K_0	Horizontal effective stress, σ'_v (kPa)	Cell Pressure (kPa)	Additional Vertical Pressure (kPa)	Average Confining Pressure, p' (kPa)	Cell Pressure applied (kPa)	Vertical Pressure applied (kPa)	Average Confining Pressure, p' (kPa)	K_0
8.90	Vertical	19	169.1	89		80.1	0.5	40.1	40.1	40.1	53.4	53.4	26.7	62.3	0.67
8.90	Horizontal	19	169.1	89		80.1	0.5	40.1	53.4	5	53.4	53.4	5.0	55.1	
9.60	Vertical	18	172.8	40	-10	122.8	0.7	93.0	93.0	29.8	106.2	106.2	16.6	111.7	0.86
9.60	Horizontal	18	172.8	40	-10	122.8	0.7	93.0	106.2	5	106.2	106.2	5.0	107.9	
10.70	Vertical	18.5	198.0	42		156.0	0.7	109.2	109.2	46.8	124.8	124.8	30.7	135.0	0.80
10.70	Horizontal	18.5	198.0	42		156.0	0.7	109.2	124.8	5	124.8	124.8	5	126.5	
11.65	Vertical	18.5	215.5	44		171.5	0.7	120.1	120.1	51.5	137.2	119.9	56.6	138.8	0.68
11.65	Horizontal	18.5	215.5	44		171.5	0.7	120.1	137.2	5	137.2	152	5	153.7	
15.85	Vertical	18.5	293.2	54		239.2	0.7	167.5	167.5	71.8	191.38	167.5	76.7	193.1	0.69
15.85	Horizontal	18.5	293.2	54		239.2	0.7	167.5	191.4	5	191.38	191.5	5	193.2	
15.70	Vertical	18.5	290.5	54		236.5	0.7	165.5	165.5	70.9	189.16	165.6	71	189.3	0.70
13.75	Vertical	18.5	254.4	49		205.4	0.7	143.8	143.8	61.6	164.3	143.7	61.8	164.3	0.70
13.75	Horizontal	18.5	254.4	49		205.4	0.7	143.8	164.3	5	164.3	164.7	5	166.4	
13.60	Vertical	18.5	251.6	49		202.6	0.7	141.8	141.8	60.8	162.08	141.8	64.1	163.2	0.69
13.60	Horizontal	18.5	251.6	49		202.6	0.7	141.8	162.1	5	162.08	162.5	5	164.2	

4.3.4. Relevant Developments in Methodology

Samples 890 Sv, Shh and Shv

The first mini-block tests were consolidated to in-situ stresses that were calculated assuming hydrostatic pore water pressure and with an assumed K_0 value of 0.5. A unit weight of 19 kN/m³ was assumed. They were also consolidated in steps of 2 kPa per 2 minutes (1 kPa/min).

At this stage the bender element software only allowed velocity readings to be taken manually, so readings were taken at approximately four-minute intervals during application of pressure, then intervals were lengthened. It was also necessary to take snapshots of the readings/waveforms. This was both for quality control and to be able to manually pick the first arrivals. Manual picks were carried out for these first 3 tests. It was then realised that this was too big a task for whole project.

It was also realised that since the frequency changes during consolidation (as the sample becomes stiffer), even if an input frequency was chosen at the start of the test in order for the automatic picking to work this changed over the test. Therefore, the automatic picking had more limitations that originally thought. This is discussed in section 6.1.1.

Samples 960 Sv, Shh and Shv

On a review of literature from the area, it was decided that a unit weight of 18.0 kN/m3 would be more reasonable and a K_0 value of 0.7 more realistic based on previous studies. Also a K_0 value of 0.5 was thought to possibly cause higher level of shear than would exist in-situ. On the use of higher K_0 value, it was thought that the vertical stress should be reduced a little more by 10 kPa to avoid too high an average pressure. Pore pressures were taken from piezometer measurements (Lindgård & Ofstad, 2017).

The vertical sample was slightly over pressured in this test, but the overall average applied pressures for each sample were similar (within 5 kPa).

The bender element software was modified for sample 960 Shv, so that measurements could be taken automatically at set intervals and images of the output signals were saved for each measurement.

Samples 1070 Sv, Shh, Shv, 1165 Sv, Shh, Shv and 1585 Sv, Shh, Shv

As above, but a unit weight of 18.5 kN/m3 was used from hereon in. Overall average applied pressure for each sample were similar.

On unmounting of sample 1070 Shv, the sample was very disturbed down one side. Further measurements were taken out of interest.

These samples were used for comparison of various techniques on consolidation and unloading scenarios. This was the first top half of a mini-block to be tested. The bottom half was tested first so this was left in the storage room for an extra 3 days, although it was heavily wrapped and not sliced.

Sv1 was tested with the same consolidation rate of 5 kPa/min and was unloaded the same way as previous tests but was left over a weekend with the valves to the burette remaining closed. The triaxial program was stopped so no pore pressure measurements were made.

Sv2 was tested with salt at the BE contacts and with a higher consolidation rate of 10 kPa/min.

Sv3 was also consolidated at 10 kPa/min and was unloaded with the burette left open. The amount of water expelled was left to go into the sample whilst velocity measurements were also taken. Filter paper was also weighed after the tests from hereon in.

Samples 1375 Pv, Ph1, Ph2

The bottom half of this block was used to test P-wave velocity for calculation of the constrained modulus (*M*) and bulk modulus (*K*) both vertically and horizontally. Sample 1375 Pv was unloaded with the burette open to allow the volume of water expelled back into the sample. The burette was then closed, and the sample was left over a weekend.

Although there was expected to be no difference, the BE were rotated between Ph1 and Ph2 as they were for the S-wave samples.

Ph1 was consolidated at 5 kPa/min. The sample was unloaded the next day in two steps with the burette left open until the expelled water was back in the sample. The burette was then closed and the triaxial program was left running to try and record the pore pressure. The differential pressure is measured by a meter between the cell pressure and the water outlets from top and bottom caps. Hence,

$$u = cell\ pressure - diff.pressure$$

[4.12]

Although this is not expected to represent the true pore pressure within the sample and only at the edges of the sample, it was hoped it could indicate variations in pressure to help understand what occurs due to unloading during sampling techniques.

Ph2 was consolidated in the same way but after unloading the burette was closed whilst the triaxial program was left recording for approximately 1.5 hours to try to determine pore pressure changes.

For the final tests it was decided to look a bit further into what happens when the samples are unloaded. It should be noted that these S-wave tests were carried out on the top half of a mini-block sample when compared to the other S-wave tests.

Sv was loaded at 5 kPa/min to the calculated anisotropic conditions. After unloading only half the volume of expelled water was allowed back into the sample and then the burette was closed. The triaxial program was left to run to determine changes in the pore pressures. This sample was left for 10 days.

Shh and Shv were both consolidated at 10 kPa/min. They were unloaded the next day and the burette was immediately closed with pore pressure measurements left to record for between 1 to 1.5 hours.

4.4. Extra Tests

4.4.1. Consolidation Rate

As discussed above, the consolidation rate was varied between 5 kPa/min and 10 kPa/min on three vertical samples from the same depth (15.70 m) to see if there was an effect on sample quality and/or shear stiffness.

4.4.2. Salt on contacts

Although there had been no problems observed with the strength of the output signal, it had been suggested by some staff in the Geotechnical department at NTNU that the use of salt on the BE contacts can help with the measurements. This was tested on sample 1570 Sv2. A small amount was sprinkled on the bottom element before placing the sample, and the same amount on the top the sample before the top cap was installed as shown in Figure 4.7.
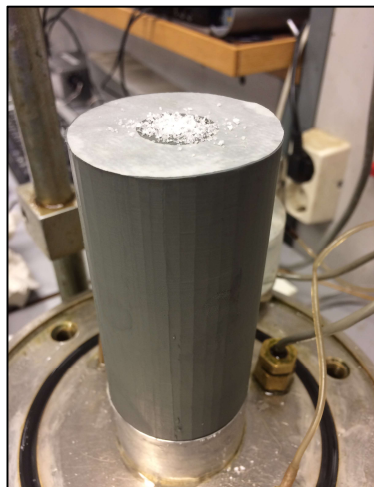

Figure 4.7: Sample Sv2 with salt on the contact with the top element

4.4.3. *Sample disturbance after triaxial testing*

Sample 1070 Shh was heavily disturbed along one side by accident during unmounting. Out of interest measurements were taken after this.

4.4.4. *Saturation of Filter Paper*

Quite early on it was noted on unmounting of the triaxial samples that the filter paper was dry around the middle parts of the sample as shown in Figure 4.8. In these cases, the samples were unloaded with the burette open, once the pressure was removed, the burette was closed, the cell drained and then the sample unmounted. Less than 5 minutes passed between closing the burette and unwrapping the samples. Therefore, in some tests the filter paper was weighed immediately after testing. This was also done for sample where the burette was left open after unloading to see if the same amount of water remained in the filter paper.
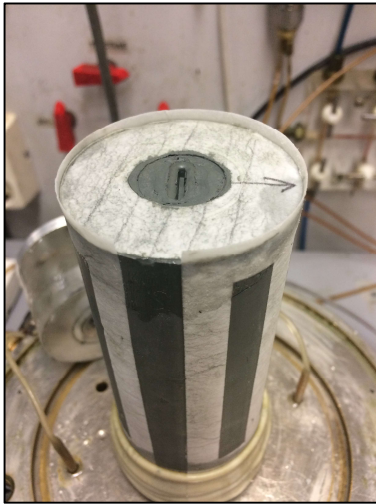

Figure 4.8: Example of drying filter paper immediately after unloading and removal of the rubber sleeve.

5.   Overview of Results

A summary of the main results is given in this section with detailed discussions in section 6.

5.1.   Index Test Results

A summary of index test results is presented in Table 5.1 and plotted in Figure 5.1.

Tests at all depths indicate the clay has quick properties, although 2 samples showed remoulded shear strength (s_r) only just over 0.5 kPa classification (NGF, 2011). At 8.90 m, this can be considered due to the proximity to the transition zone. At 15.80 m, all other properties indicate quick clay and with s_r at only 0.6 kPa, it seems reasonable to assume the whole profile is considered as quick clay.

It should be noted that the tests at 8.90 m were carried out first and are not considered to be accurate due to human errors. This is particularly highlighted by a degree of saturation greater than 1 and a higher void ratio as is discussed later.

Hydrometer analysis was carried out to determine the grain size distribution for a representative sample from each mini-block. These are presented in Figure 5.2 with percentage clay values included in Table 5.1. It should be noted that the test at 10.70 m is unreliable since too much material was used in the test, which makes the calculation of diameter size inaccurate. Interpolation was carried out but is not thought to be correct.

Table 5.1: Summary of Index Test Parameters

Sample Depth	Water Content, w	Density, ρ	Unit weight, γ	Dry Density, ρ_d	Grain Density, ρ_s	Unit weight of solids, γ_s	Plastic Limit, w_p	Plasticity Index, I_P	Liquid Limit, w_L	Liquidity Index, I_L
(m)	(%)	(g/cm^3)	(kN/m^3)	(g/cm^3)	(g/cm^3)	(kN/m^3)	(%)	(%)	(%)	(-)
8.75 - 9.05	47.2	1.83	18.0	1.29	2.82	27.7	24.9	9.8	34.6	2.3
9.40 - 9.75	46.2	1.78	17.4	1.20	2.85	27.9	24.5	11.1	35.6	2.0
10.45 - 10.80	40.9	1.80	17.7	1.25	2.87	28.2	25.2	7.1	32.3	2.2
11.45 - 11.75	42.5	1.84	18.0	1.29	2.86	28.1	25.4	5.7	31.1	3.0
13.50 - 13.85	41.6	1.82	17.9	1.26	2.83	27.8	25.0	6.0	31.0	2.8
15.60 - 15.95	39.8	1.83	18.0	1.30	2.86	28.1	25.5	6.4	31.8	2.2

| Sample Depth	Porosity, n	Void Ratio, e	Degree of saturation, S_r	Salt content, S	Undrained Shear Strength, s_u	Remoulded Shear Strength, s_r	Senstivity, S_t	Clay Content
(m)	(%)	(-)	(-)	(g/l)	(kPa)	(kPa)	(-)	(%)
8.75 - 9.05	55.9	1.27	1.05	1	38.7	0.66	59.0	72.6
9.40 - 9.75	57.3	1.34	0.98	0.9	52.6	0.42	124.3	45.6
10.45 - 10.80	55.6	1.25	0.94	1.3	49.7	0.29	169.5	64.3
11.45 - 11.75	55.0	1.22	1.00	0.8	54.0	0.29	186.1	40.2
13.50 - 13.85	54.6	1.20	0.98	0.8	40.8	0.26	157.1	57.1
15.60 - 15.95	54.2	1.18	0.96	1.3	40.5	0.56	72.8	57.5

Figure 5.1: Index Test Plot

57
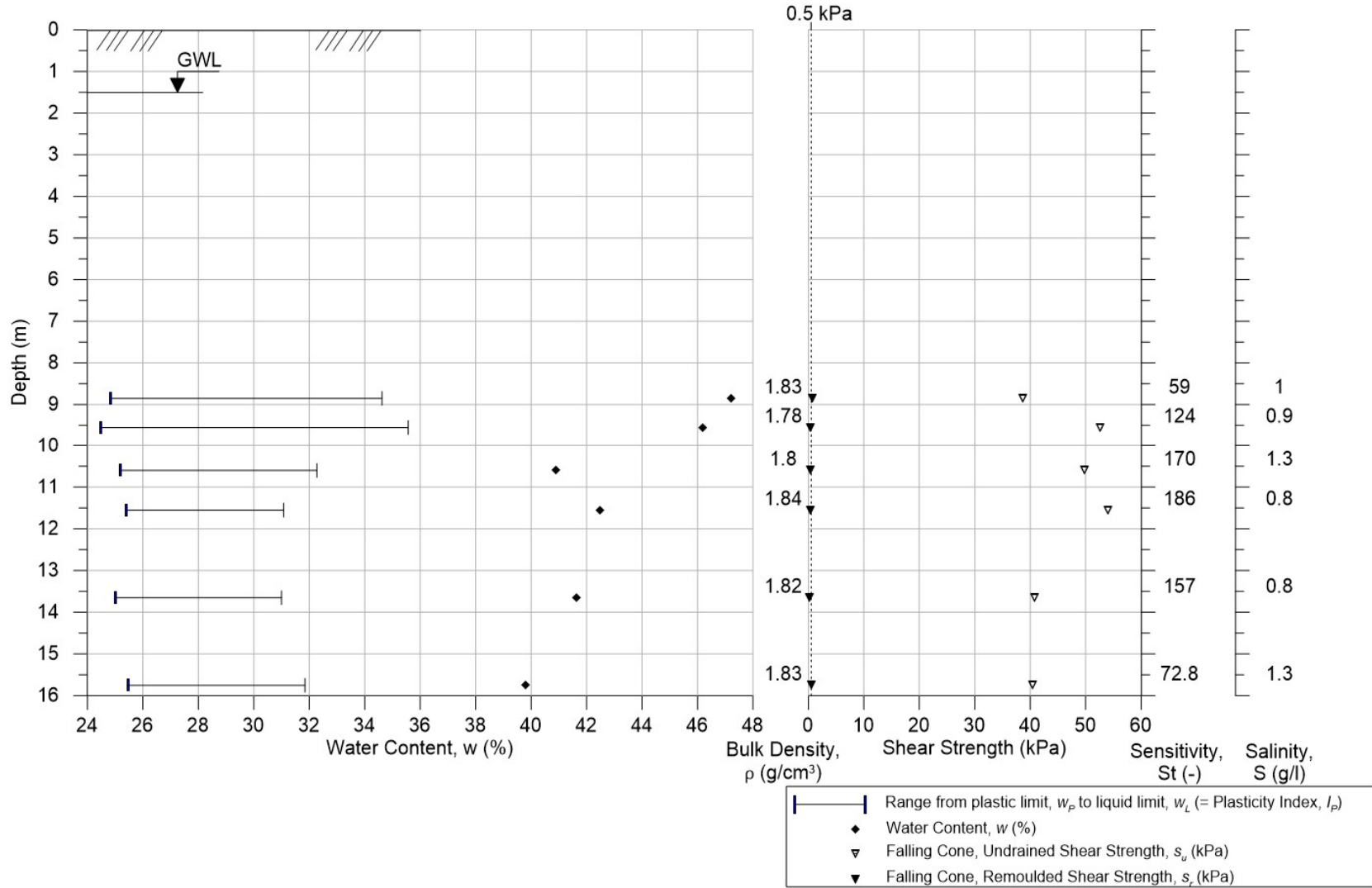
Figure 5.2: Hydrometer Results

58
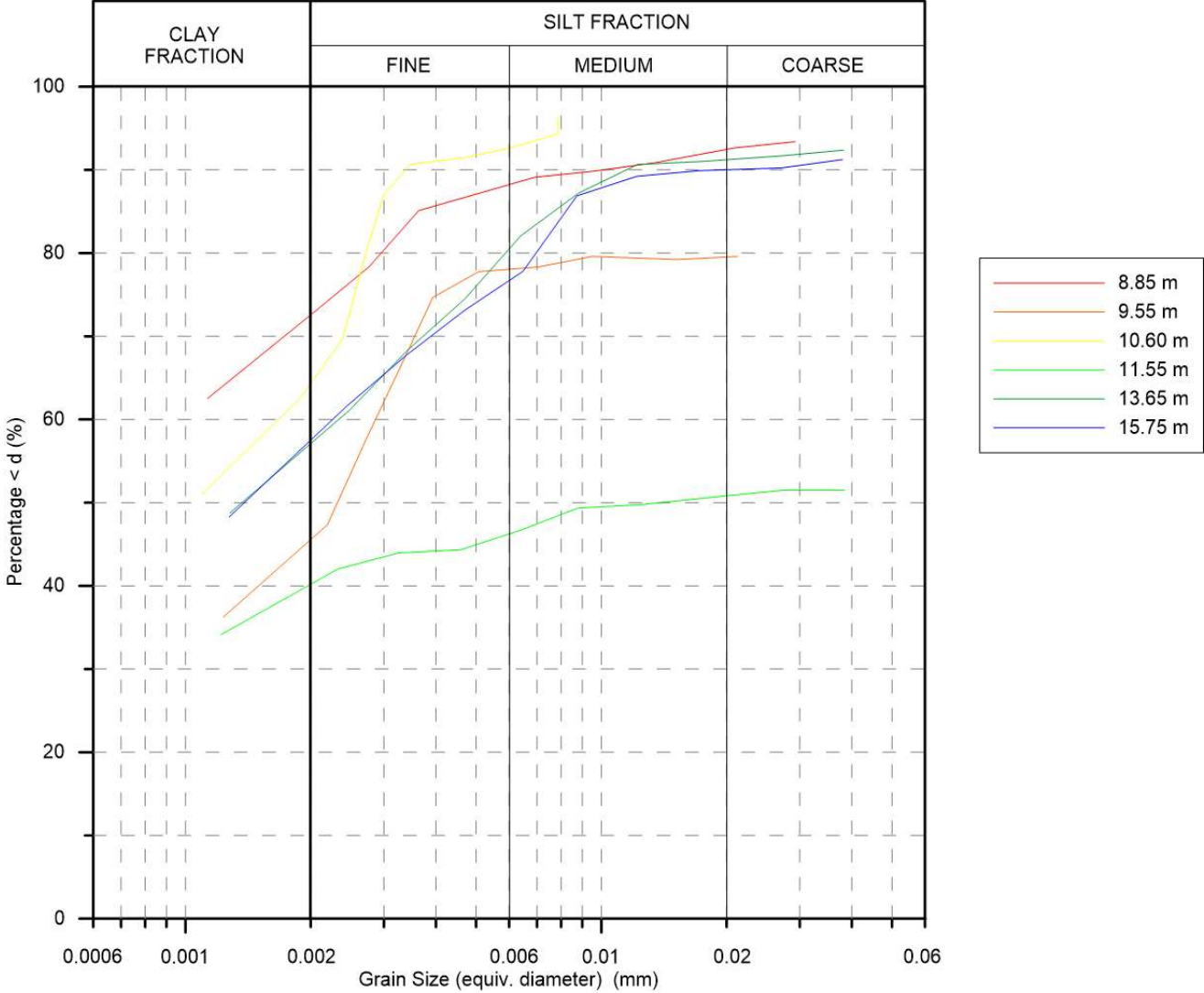
5.2. Results of Triaxial Bender Element System

5.2.1. Results of Individual Samples

All results were imported into Microsoft Excel and plotted using Golden Grapher software. The BE LabView program outputs data with:

- Time
- Bender delay (ms) (wave travel time)
- Effective height (mm)
- Received signal (mV peak)

These were imported into excel along with the triaxial results, which include:

- Time
- Deformation (mm)
- Load (N)
- Differential Pressure (kPa)
- Cell Pressure (kPa)
- Burette (ml)

Using time correlation, the relevant data from the triaxial file was aligned with the BE results. Shear wave (and P-wave) velocity were calculated:

$$V_{s,ij} = \frac{d_s - d_f}{t_s}$$

[5.1]

where d_s is the starting sample height (95 mm tip-tip), d_f is the deformation from the triaxial file ($d = d_s - d_f$) and t_s is the bender delay (shear wave travel time). The shear and constrained moduli were then calculated using for each sample:

$$G_{ij} = \rho V_{s,ij}^2$$

[5.2]

and

$$M_{ij} = \rho V_{P,ij}^2$$

[5.3]

respectively, where i is the wave propagation direction, j is the particle motion direction and ρ is the density taken from the index tests at that sample depth.

The results are plotted against time. Each plot includes the results of the 3 tests (1 vertical and 2 horizontal) from that depth. They are presented from Figure 5.3 to Figure 5.13. Included on the plots are:

- Average Applied Pressure, p (kPa) – it should be noted that this can only be considered average effective pressure, p' after primary consolidation has been reached (EOP)

- Small Strain Shear Stiffness, G_{max} (Constrained Modulus, M for 13.75 m)

- Expelled water, Burette (ml)

- Pore Pressure, u (kPa) - displayed when the burette is closed. It should be noted that this is not the pore pressure inside the sample, but a measure of the pressure at the top and bottom of the sample.

There are three main stages of the tests that are indicated by the increase and decrease in p:

1) Loaded (at the rate stated in Table 4.4) to the calculated effective stress, anisotropic for vertical samples and isotropic for horizontal samples

2) Consolidate overnight. End of primary consolidation (EOP) as defined by ISO (2004b) is marked.

3) Unloading

A summary of the unconfined (pre-consolidation), consolidated (after EOP) and unloaded shear stiffness values are summarised in Table 5.2. It should be noted that unloading procedures varied, with some samples having access to water and some not as marked. The detailed descriptions of the procedures and results for each test are found in APPENDIX B – Details of Individual Bender Element Tests. They are described if found relevant in this section.

It should be noted that steps in the stiffness moduli are as a result of the time resolution (sample rate) of the bender element system, which is discussed further in section 6.1.1. The initial intent was to interpret the first arrivals manually to achieve more accurate results. This was done for the first samples at 8.90 m depth. However, it became apparent that this was too large a task.

Table 5.2: Summary of shear stiffness results for unconfined, consolidated and unloaded samples. (* = access to water on unloading)

Depth (m)			(MPa)	
	Orientation	Pre-Cons $G_{max,0}$	Consolidated G_{max}	Unloaded $G_{max,u}$
8.90 Figure 5.3	vh	9.8	22.3	10.7
	hh	10.6	31.1	22.3
	hv	10.9	18.3	14.6
9.60 Figure 5.4	vh	7.6	27.1	18.8
	hh	11.1	43.8	-
	hv	7.6	24.5	21.7
10.70 Figure 5.5	vh	6.3	31.6	24.2
	hh	9.6	52.3	37.4
	hv	8.3	28.2	19.6
11.65 Figure 5.6	vh	8.5	37.6	17.6
	hh	9.1	64.5	44.7
	hv	9.1	44.5	28.1
13.60 Figure 5.7 Figure 5.8	vh *	6.4	36.5	8.4
	hh	9.0	36.5	24.5
	hv	6.4	44.5	19.6
15.70 Figure 5.11 Figure 5.12	v1	7.4	27.5	18.6
	v2	5.1	35.8	23.6
	v3 *	7.4	37.0	3.7
15.85 Figure 5.13	vh	10.6	47.5	-
	hh	10.6	70.7	24.9
	hv	9.1	40.8	17.2

Figure 5.3: Triaxial bender element S-wave results for samples at 8.90 m depth
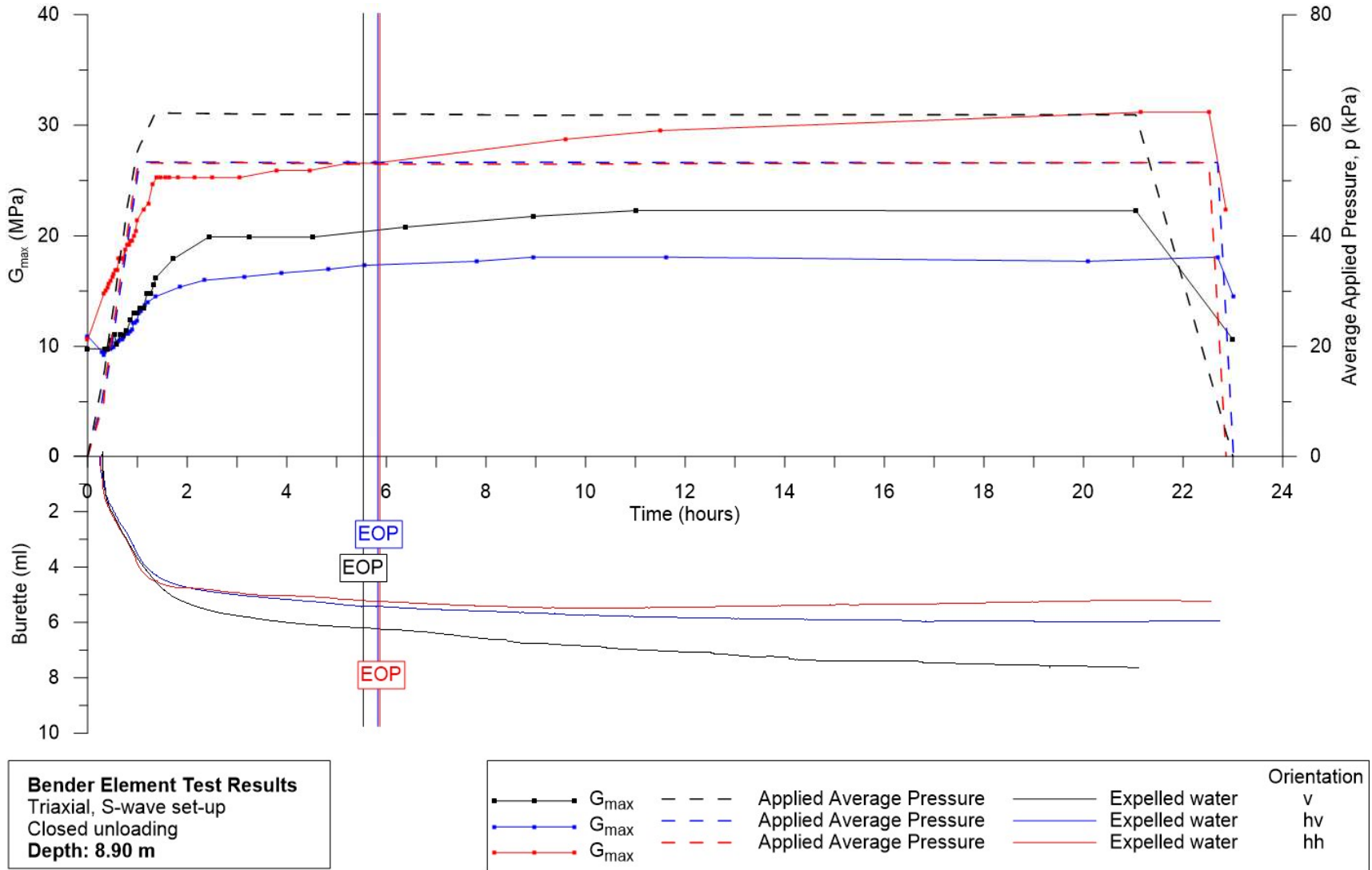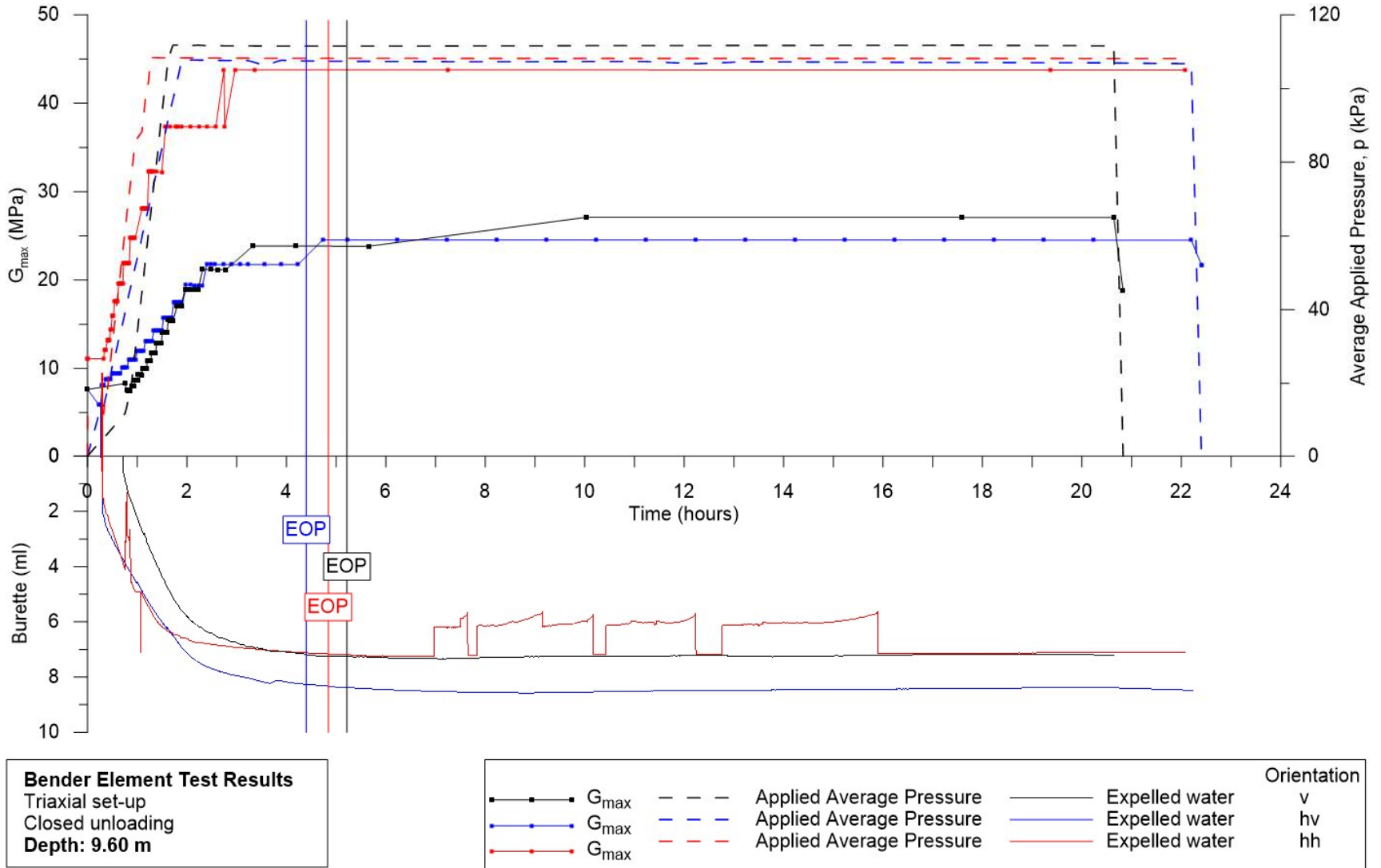
Figure 5.5: Triaxial bender element S-wave results for samples at 10.70 m depth
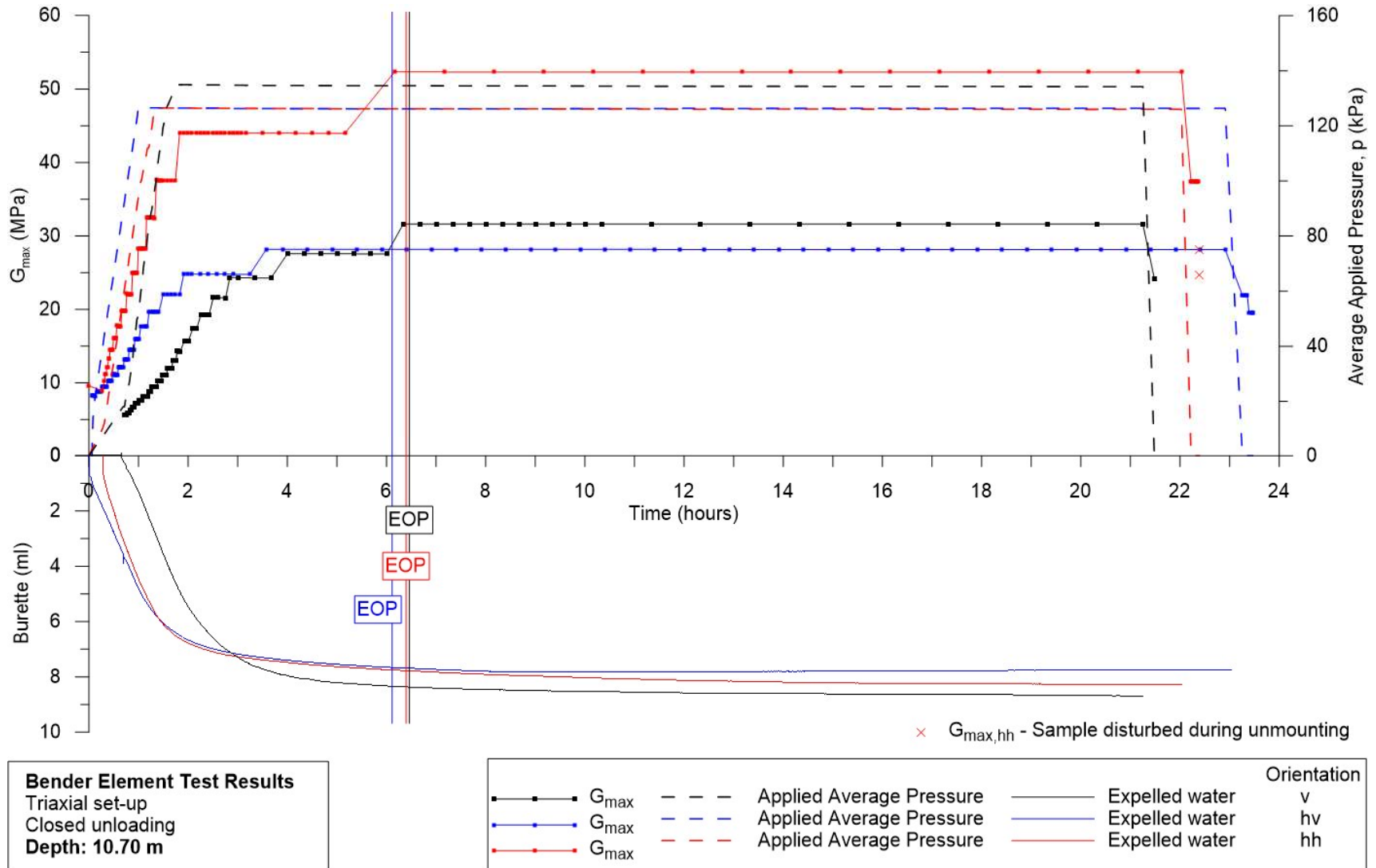
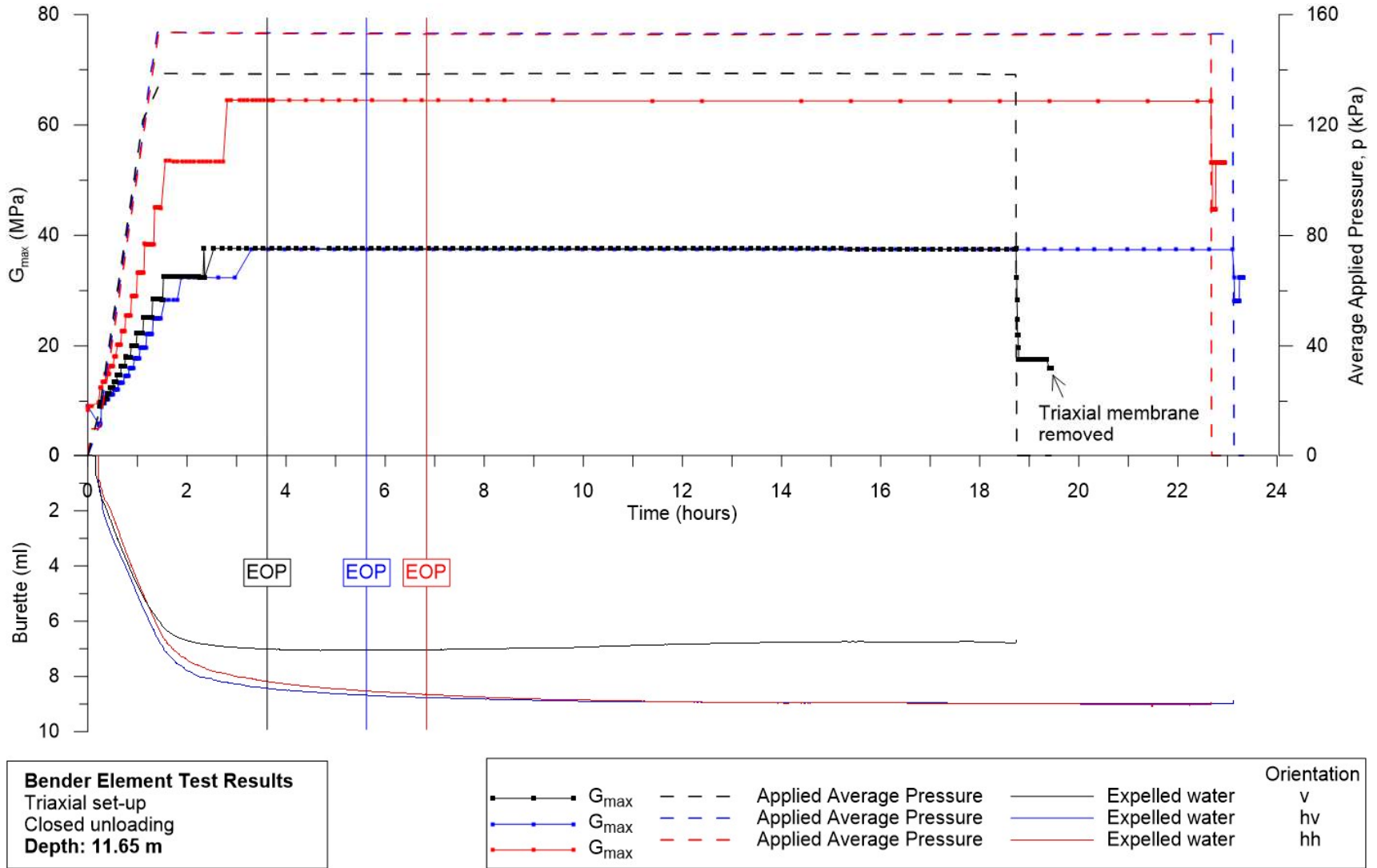*Figure 5.6: Triaxial bender element S-wave results for samples at 11.65 m depth*

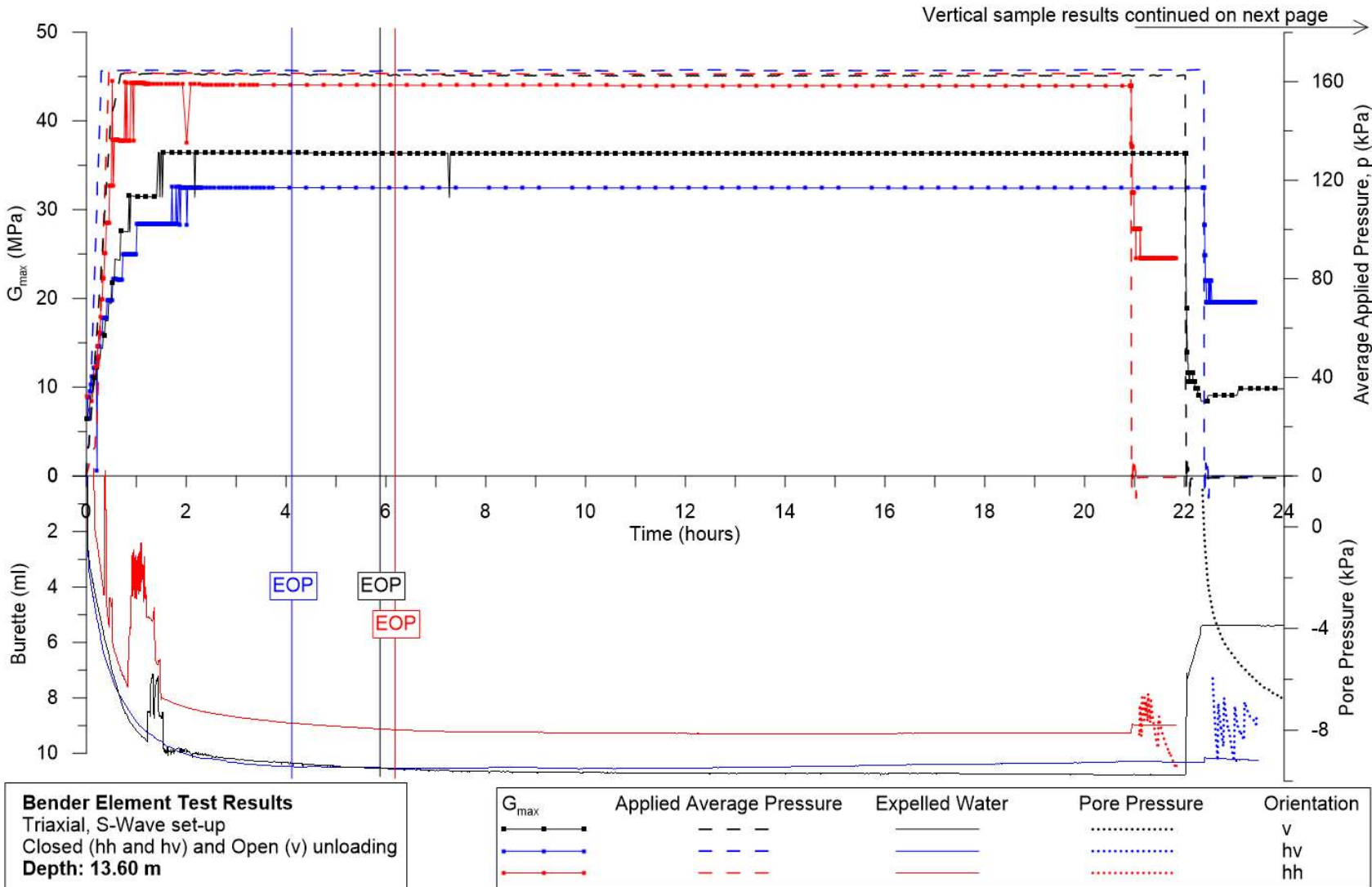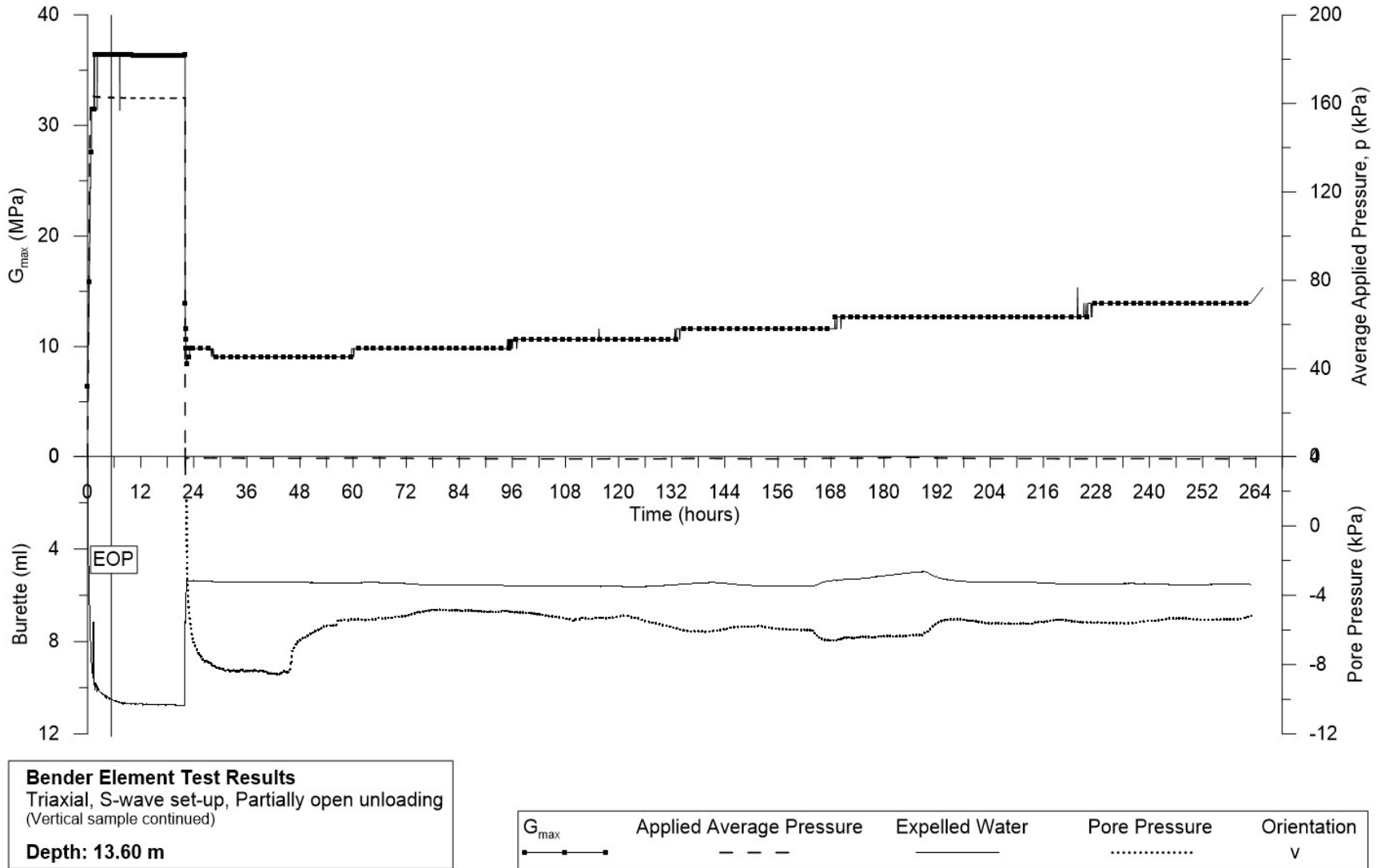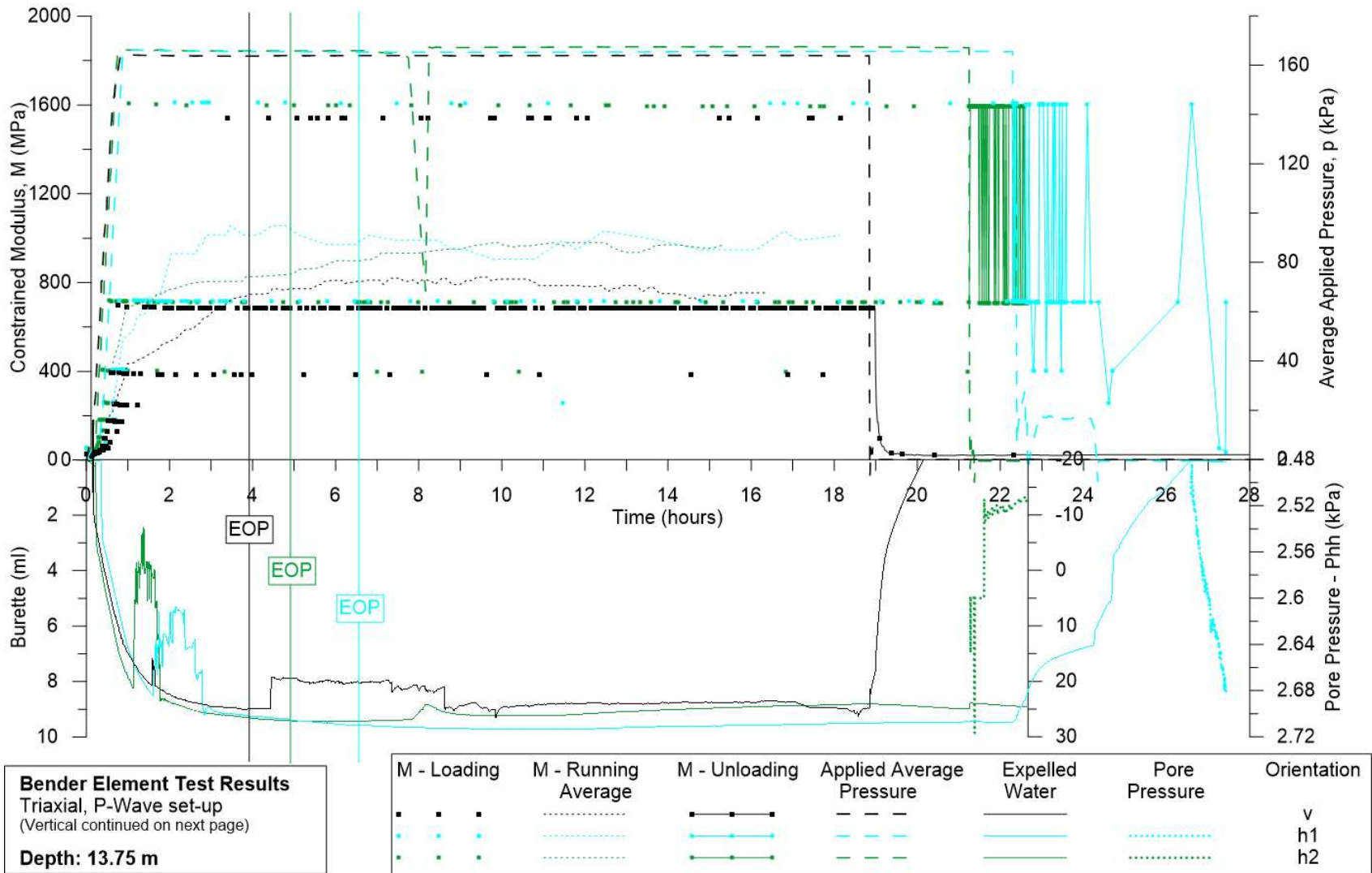*Figure 5.7: Triaxial bender element S-wave results for samples at 13.60 m depth*

66

Bender Element Test Results
Triaxial, S-wave set-up, Partially open unloading
(Vertical sample continued)

Depth: 13.60 m

G_{max}	Applied Average Pressure	Expelled Water	Pore Pressure	Orientation
■–■–■	– – –	———	············	v

Figure 5.9: Triaxial bender element P-wave results for samples at 13.75 m depth

68

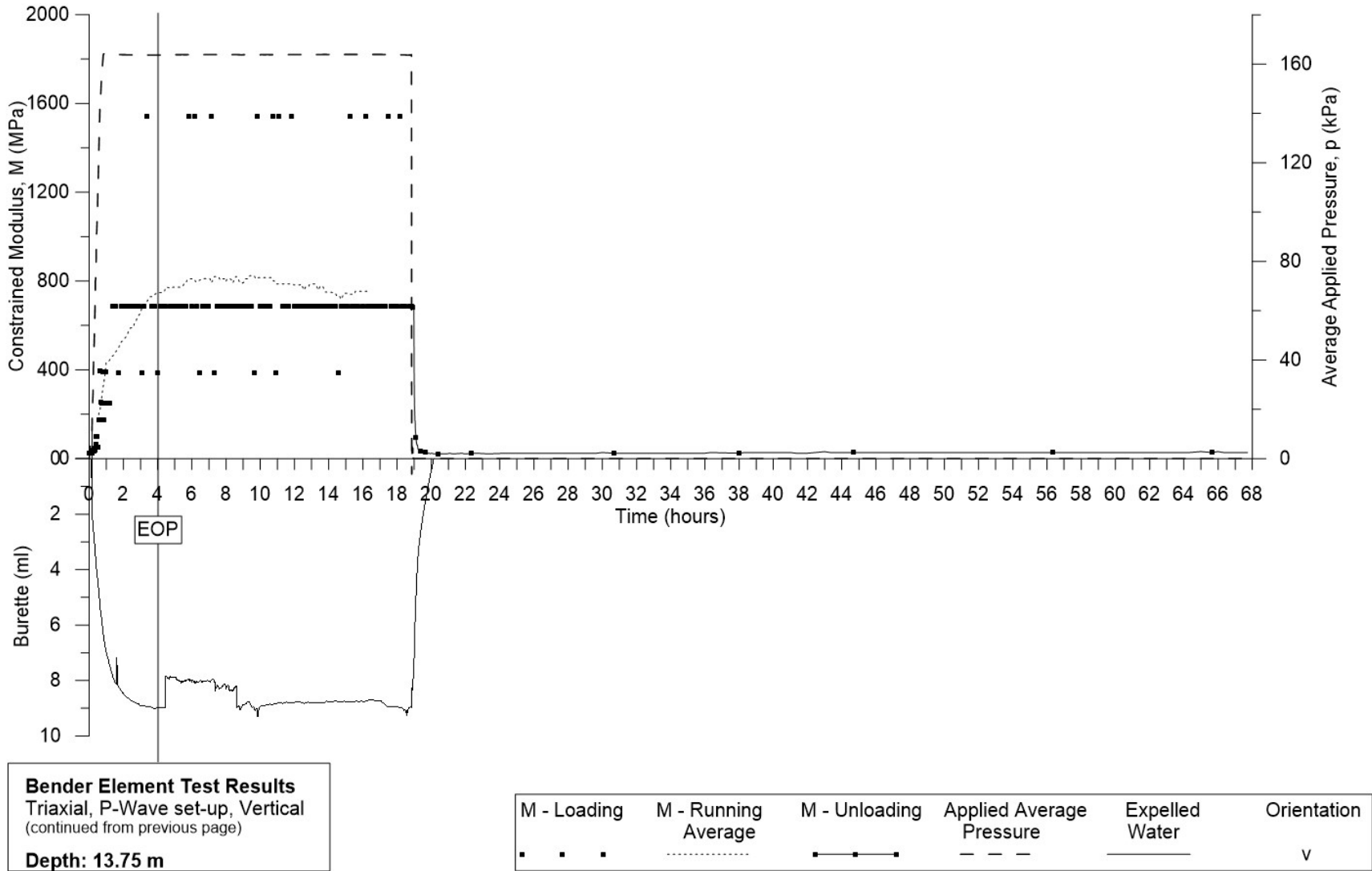*Figure 5.10: Triaxial bender element P-wave results for samples at 13.75 m depth continued*

69

Figure 5.11: Triaxial bender element S-wave results for samples at 15.70 m depth
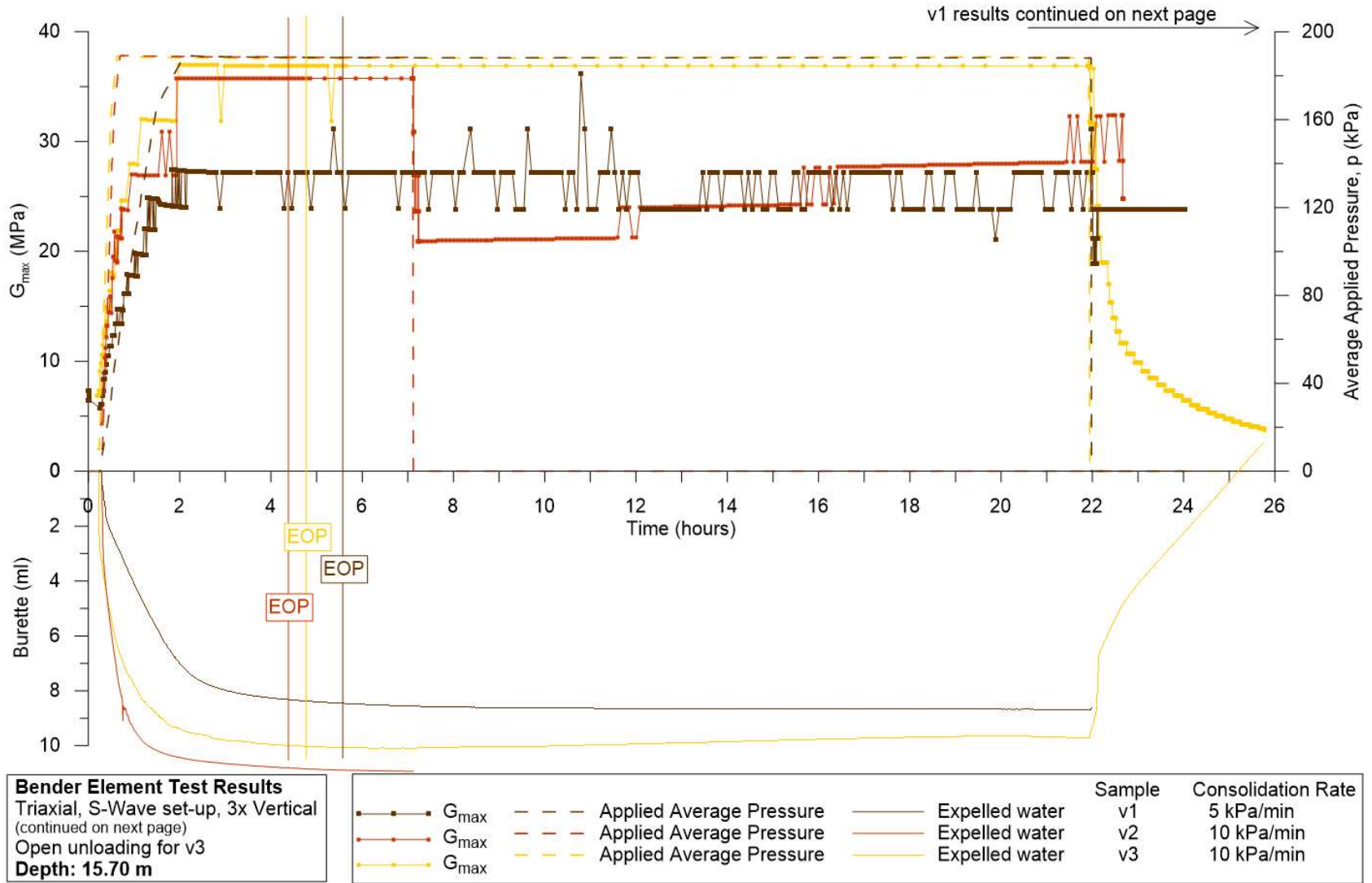
70

Bender Element Test Results
Triaxial, S-Wave set-up
(continued from previous page)

Depth: 15.70 m

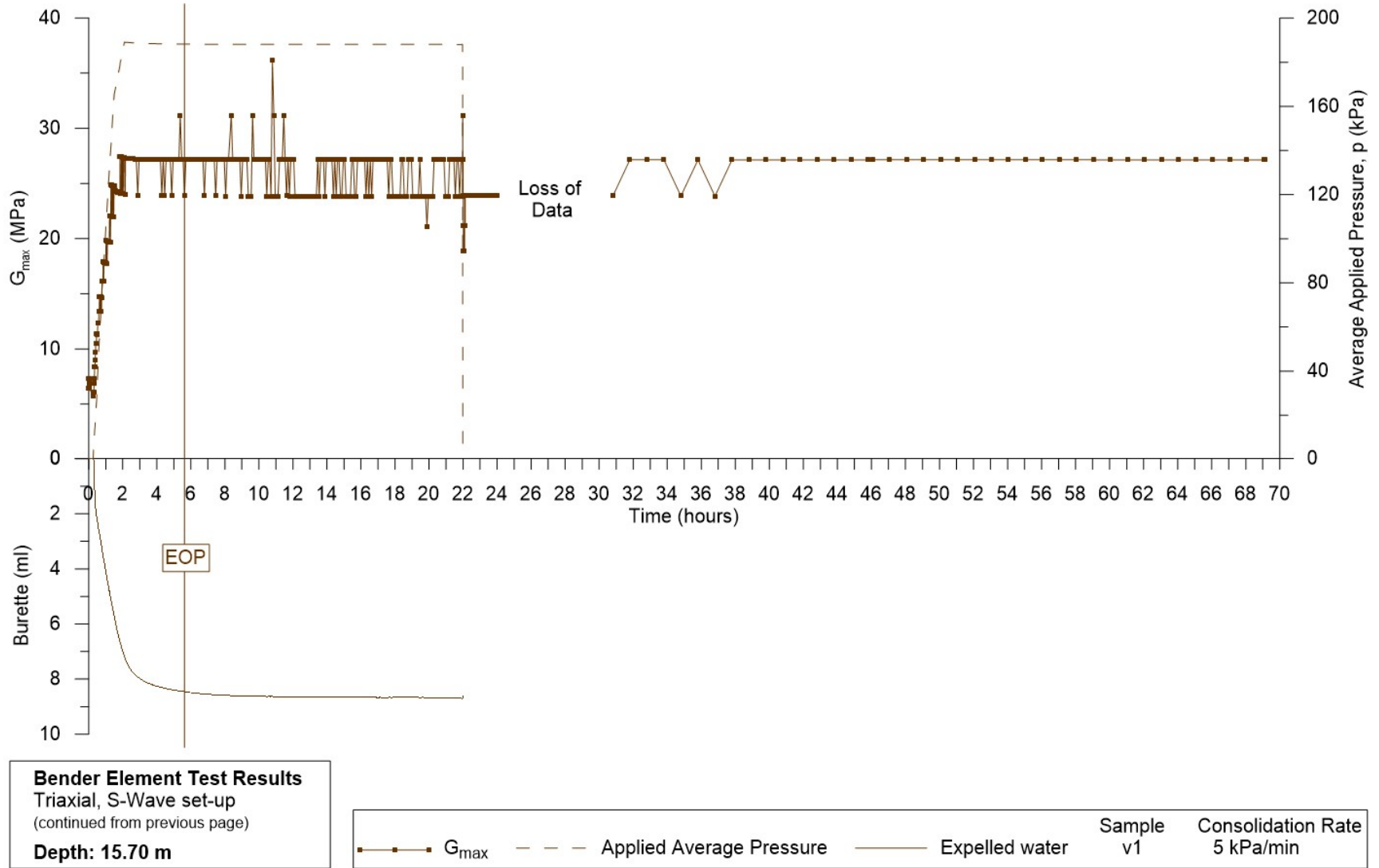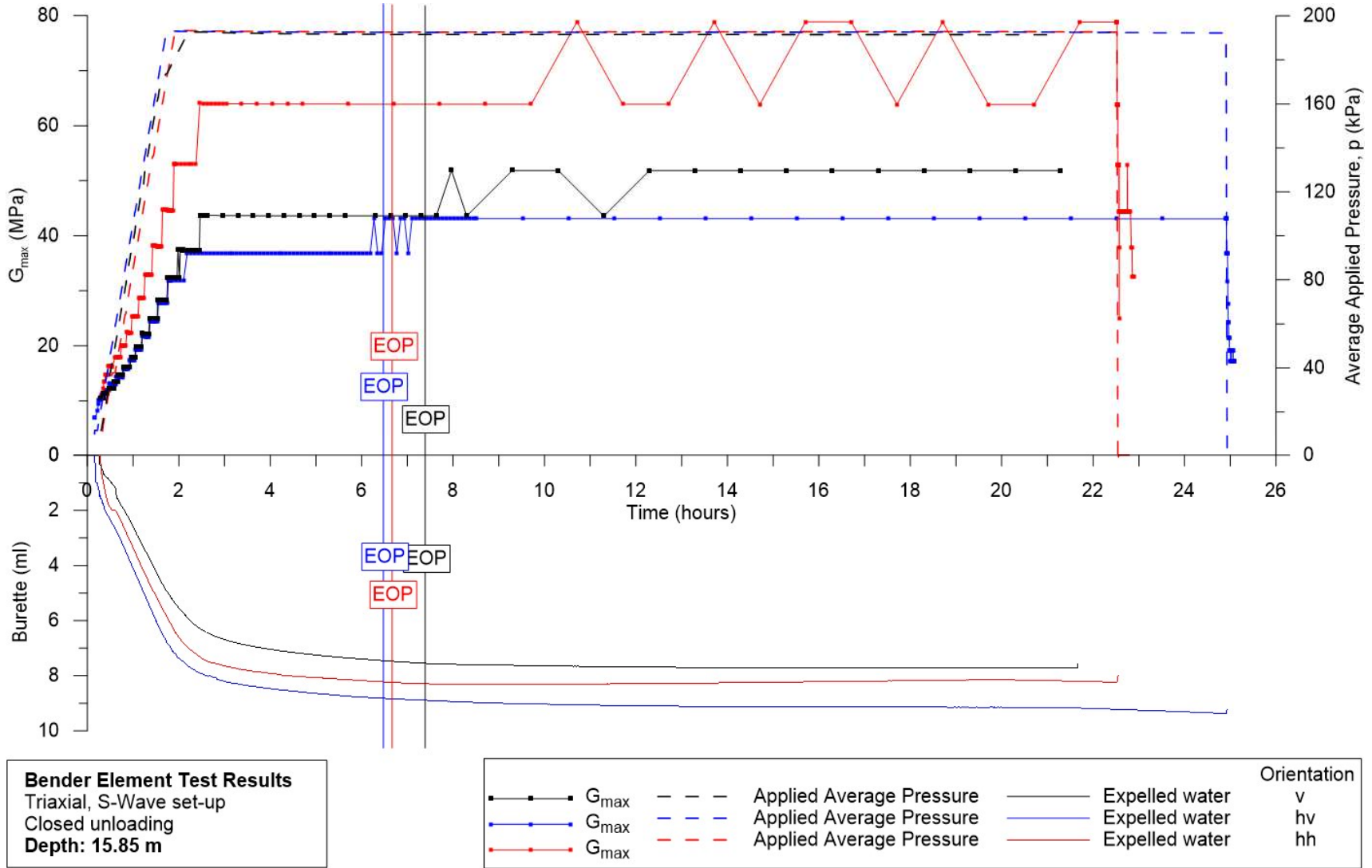|	Gmax	— — — Applied Average Pressure	—— Expelled water	Sample	Consolidation Rate
				v1	5 kPa/min

Figure 5.13: Triaxial bender element S-wave results for samples at 15.85 m depth

5.2.2. G_{max} with Depth

After EOP it is considered that the sample has reached its in-situ effective stress state. G_{max} is taken for each sample at this time (accuracy is explained in section 6.1.1). Figure 5.14 displays the increase of the small strain shear modulus with depth. Also plotted are the results from the external SDMT profile. The full results are included in APPENDIX D – SDMT Results..

The results show clear anisotropy particularly between $G_{max,v}$ and both $G_{max,hh}$ and $G_{max,hv}$ with the former being 39-71 % greater and the latter being 9-18 % less as shown in Table 5.3. The latter is not thought to be true anisotropy but is kept in the results for discussion in section 6.1.3. This anisotropy tends to increase with depth and as such the ratios are calculated. These anisotropic results are discussed in detail in section 6.2.2.

There is a clear discrepancy of the results from the top half of the mini-blocks (13.60 m and 15.70 m), so these are excluded from the analysis. This is discussed under sample quality in section 6.2.10.

Table 5.3: G_{max} results with depth and anisotropy ratios

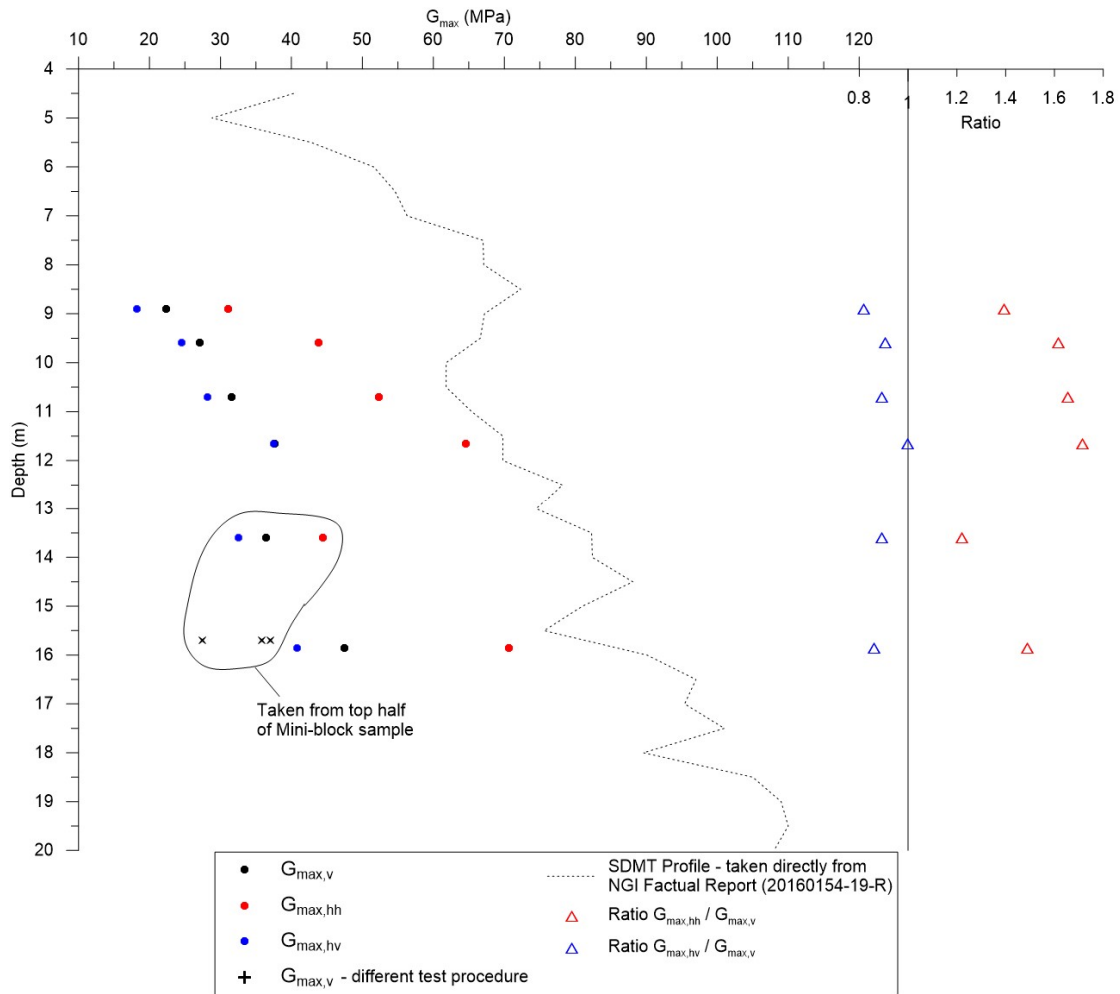| Depth (m)	$G_{max,v}$	$G_{max,hh}$	$G_{max,hv}$	$G_{max,hh}$ / $G_{max,v}$	$G_{max,hv}$ / $G_{max,v}$
8.90	22.3	31.1	18.3	1.39	0.82
9.60	27.8	43.4	24.5	1.56	0.88
10.70	32.3	52.3	28.2	1.62	0.87
11.65	37.6	64.5	37.5	1.71	1.00
13.60	36.5	44.5	32.5	1.22	0.89
15.70	27.5				
	35.8				
	37.0				
15.85	47.5	70.7	40.8	1.49	0.86
			Average Ratios:	1.57	0.89

Figure 5.14: Plot of G_{max} variation with depth including results from external SDMT Profile from NGI (2017) (Appendix D)

5.2.3. Sample Quality

End of primary consolidation (EOP) is taken according to ISO (2004b), when the volume change is less than 0.1 % of the specimen volume per hour or 0.1 cm^3/hr (ml/hr), whichever is greater. In this case the latter is greater and is used.

Sample quality is determined using the three techniques described in section 2.8.2 with the assumed OCR of 2-3. Results are shown in Table 5.4. The volume of water expelled during the consolidation phase is used to determine the change in volume. It should be noted that the measurements here for the Landon et al. (2007) technique are not taken as the procedure suggests and are purely out of interest. These results use the unconfined shear velocity ($V_{S0,vh}$) as measured on the trimmed triaxial sample compared to the SDMT test measurements ($V_{S,SDMT}$), as opposed to a measurement on the sample straight out of the ground compared to the SCPTU measurement. They are also only available for the vertical samples using S-wave velocity set-up.

Table 5.4: Sample quality results summary

Sample	Lunne et al. (2006)		Andresen and Kolstad (1979)		Landon et al. (2007)	
	$\Delta e/e_0$ [-]	Category	$\Delta \varepsilon_{vol}$ [%]	Category	$v_{S0,vh}$ / $v_{S,SDMT}$	Category
8.90 Sv	0.049	Good to fair	2.7	Acceptable	0.34	Very Poor
8.90 Shh	0.041	Good to fair	2.3	Acceptable		
8.90 Shv	0.042	Good to fair	2.4	Acceptable		
9.60 Sv	0.055	Poor	3.2	Disturbed	0.35	Poor
9.60 Shh	0.055	Poor	3.1	Disturbed		
9.60 Shv	0.063	Poor	3.6	Disturbed		
10.70 Sv	0.066	Poor	3.7	Disturbed	0.33	Very Poor
10.70 Shh	0.061	Poor	3.4	Disturbed		
10.70 Shv	0.060	Poor	3.3	Disturbed		
11.65 Sv	0.055	Poor	3.1	Disturbed	0.36	Poor
11.65 Shh	0.068	Poor	3.8	Disturbed		
11.65 Shv	0.068	Poor	3.8	Disturbed		
13.60 Sv	0.084	Poor	4.6	Disturbed	0.29	Very Poor
13.60 Shh	0.073	Poor	4.0	Disturbed		
13.60 Shv	0.084	Poor	4.6	Disturbed		
13.75 Pv	0.072	Poor	3.9	Disturbed		
13.75 Ph1	0.077	Poor	4.2	Disturbed		
13.75 Ph2	0.075	Poor	4.1	Disturbed		
15.70 Sv1	0.068	Poor	3.7	Disturbed	0.32	Very Poor
15.70 Sv2	0.087	Poor	4.7	Disturbed	0.27	Very Poor
15.70 Sv3	0.081	Poor	4.4	Disturbed	0.32	Very Poor
15.85 Sv	0.061	Poor	3.3	Disturbed	0.35	Poor
15.85 Shh	0.066	Poor	3.6	Disturbed		
15.85 Shv	0.071	Poor	3.8	Disturbed		

Nearly all samples are of poor to very poor quality, which is to be expected since they had been in storage for 3-5 months. The samples from 8.90 m are found to be fair to good quality. Most of the samples are only just over the limit into poor/disturbed category. Samples from depths 13.60 m and 15.70 m are further over the limit. These were taken from the top of a mini-block sample. These results are discussed in further detail in section 6.2.10.

6. Discussion

6.1. Accuracy

6.1.1. Bender Element System

Stiffness Steps due to Sampling Rate.

The steps in the stiffness moduli, seen in the results, are due to the sampling rate (time resolution) of the bender element system. The program uses a cross-correlation method (method of least squares) to match the shape of the received signal with the input signal and determine the travel time. The received signal is sampled at a rate of 20 kHz and hence a resolution of 0.05ms. Thus, the travel time is measured and output in milliseconds to the nearest 0.05 ms. An illustration of how this creates steps in the calculated shear wave velocity and shear modulus is presented in Figure 6.1. This covers the range of results for this study and gives a percentage error in shear modulus for each 0.05 ms step.
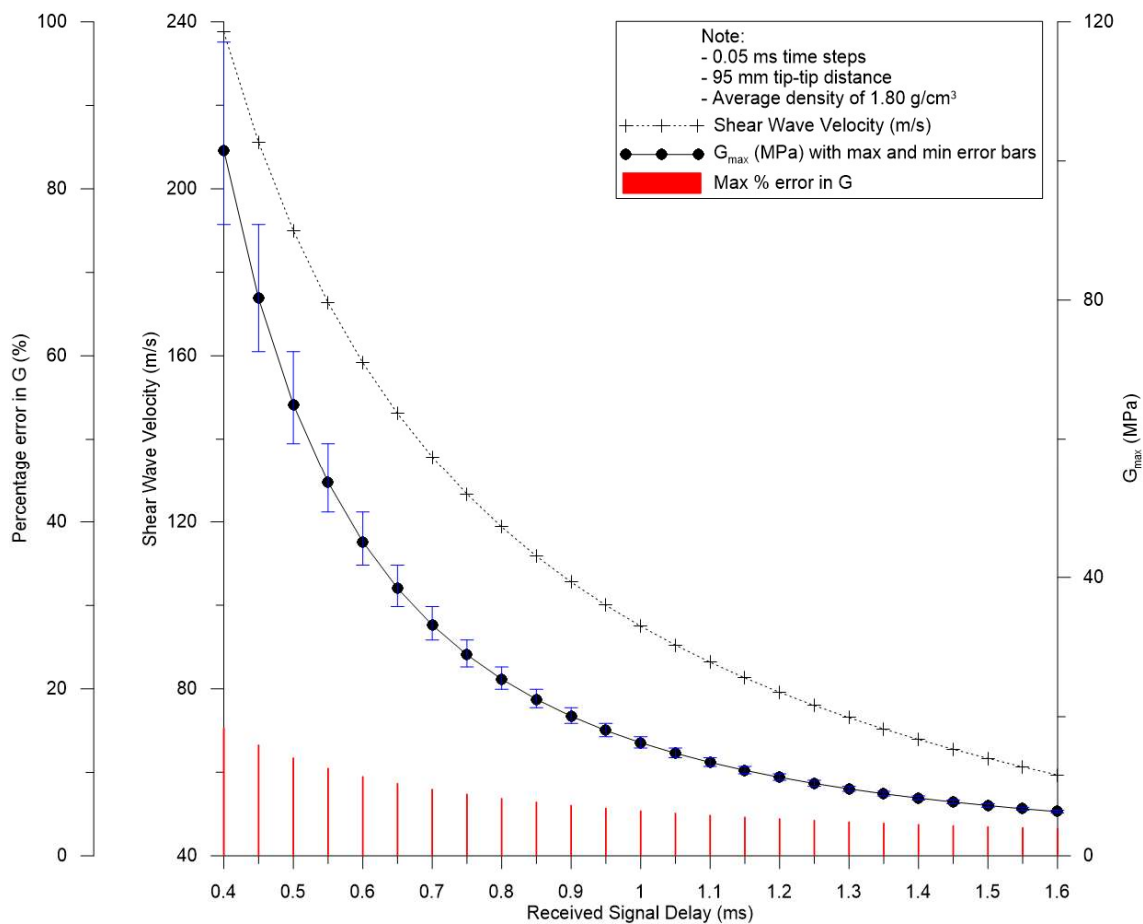

Figure 6.1: Illustration of how 0.05 ms resolution in received signal time delay affects the calculated shear wave velocity and shear modulus results (for tip-tip distance 95 mm and density 1.80 g/cm³)

The largest step is seen in the results for 1585 Shh, as shown in Figure 6.2a, where the step between 0.45 ms to 0.50 ms is equal to approximately 15 MPa difference in shear modulus.

Of course, the best way to overcome this problem is to manually interpret the first arrivals for each measurement. However, there would still be limitations by the sampling rate as interpretation would be based on interpolation between sampling points. This was done for the first three tests as described in the next section. However, it was quickly realised that this was far too big a task for the entire study.

At some depths, the accurate final EOP value is obviously between two step values and is therefore interpreted as shown in Figure 6.2a. In some ways this reduces the error as it is reasonable to assume the value is very close to midway between these steps, but the maximum error is still calculated based on the maximum and minimum step values using the appropriate value of density and adjusted sample height for each sample. For example, the maximum error for the interpreted value of sample 1585 Sv, in Figure 6.2a is found to be 11.4%. These interpreted values for sample 1585 are from heroin used in the analysis of the results.
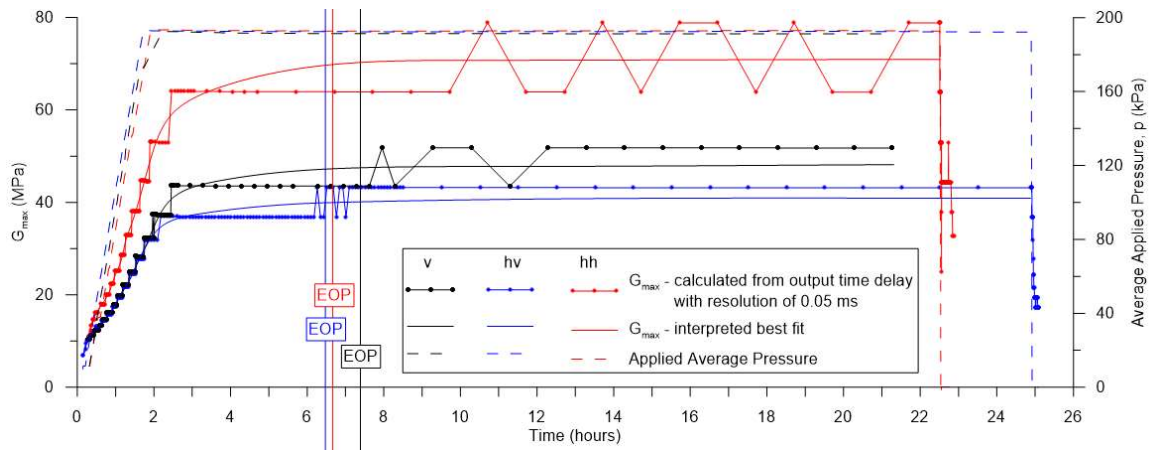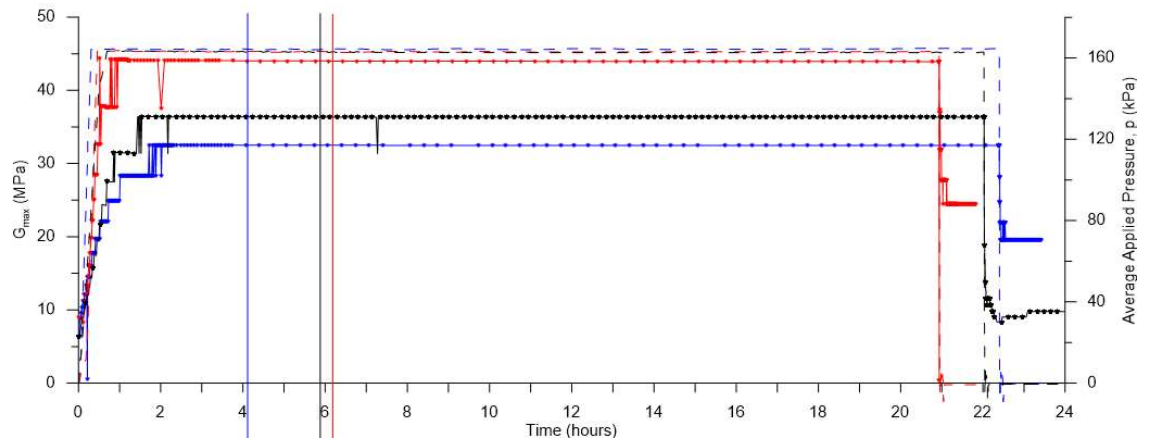
Figure 6.2: Illustration of approximate best fit line to estimate a more accurate G_{max} value. Results from a) sample 1585 Sv, Shh, Shv and b) 1360 Sv, Shh, and Shv.

78

For most sample results the EOP value settled at one step value as shown in Figure 6.2 b). In such cases it is harder to interpret a more accurate value, so the step values are taken with the possible error bars calculated from these. Sample 1585 Sv, Shh, and Shv are the only samples where an interpreted value is used.

A final plot of the interpreted values with their associated errors is presented in Figure 6.3. These values are used in further analysis and discussions.
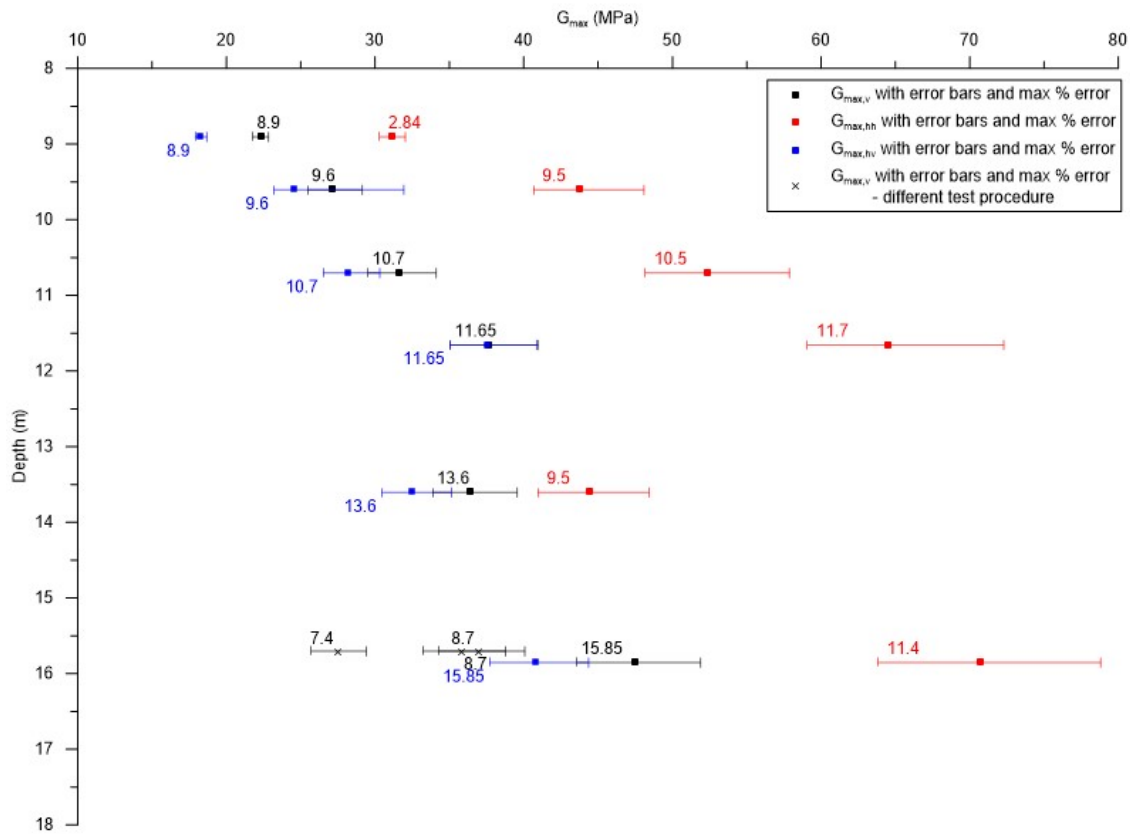

Figure 6.3: Plot of interpreted Gmax values with error bars and maximum percentage error indicated.

The same effect is seen in the P-wave results but due to the higher speed of P-waves and the fact that P-wave velocity highly influenced by the degree of saturation (discussed in the next section), the steps in the data are more severe and troublesome for interpretation of an accurate constrained modulus. The effects of the time delay resolution on P-wave velocity and constrained modulus are illustrated in Figure 6.4. This for the range of results in this study and the maximum percentage error for each 0.05 ms step is given.
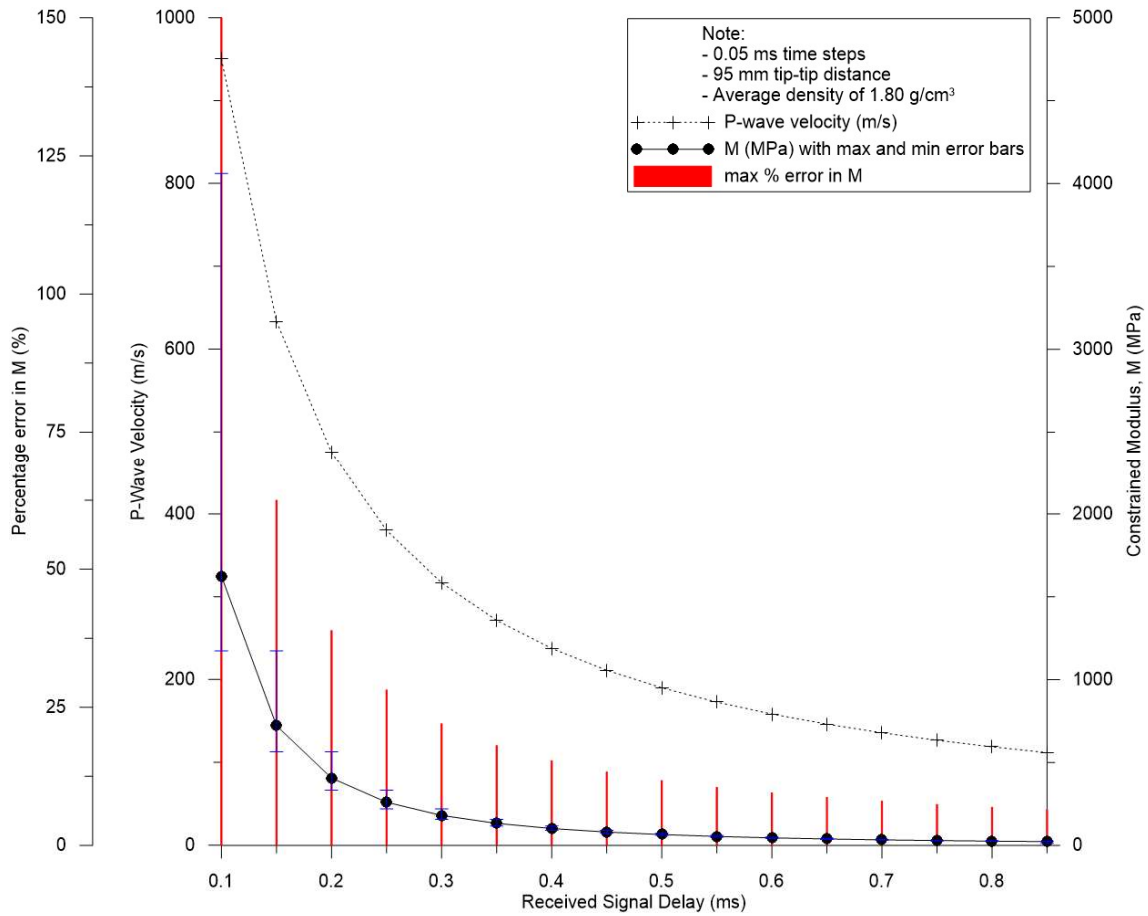
Figure 6.4: Illustration of how 0.05 ms resolution in received signal time delay affects the calculated P-wave velocity and constrained modulus results (for tip-tip distance 95 mm and density 1.80 g/cm³)

As shown in Figure 6.5, the largest step, seen in all three P-wave test samples (1375 Pv, Ph1 and Ph2), is between 0.10 ms to 0.15 ms, and is equal to approximately 900 MPa difference in the constrained modulus.
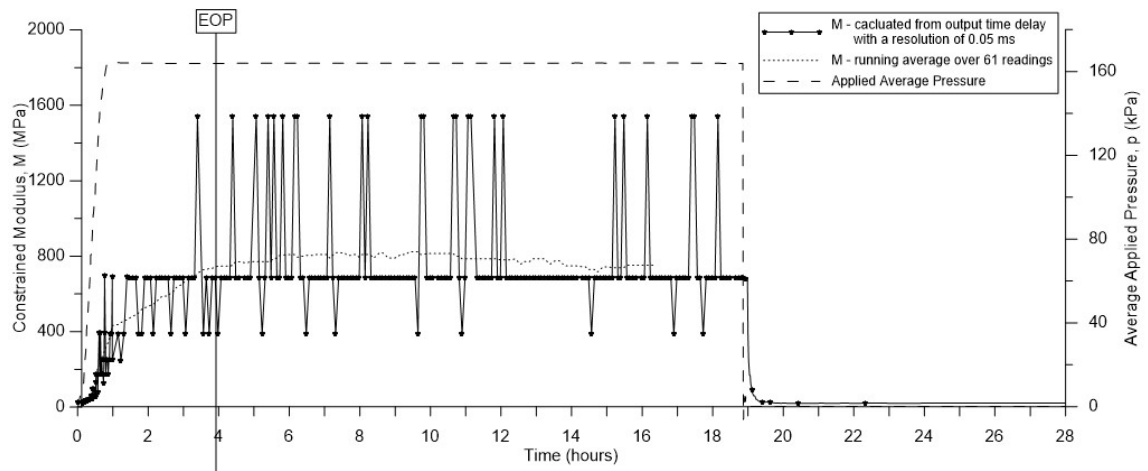

Figure 6.5: Illustration of running average fit line to estimate a more accurate M value. Results from sample 1375 Pv.

To estimate a more accurate/representative value for the constrained modulus after consolidation, based on the variance of that readings it seemed more appropriate to use a running average algorithm in the Grapher software. An example is shown for 1375 Pv in Figure 6.5. These interpreted values are with calculated errors are presented in Table 6.1.

Table 6.1: Interpreted Constrained Modulus Results

|		Interpreted best fit				
Depth (m)	Orientation	Constrained Modulus, M (MPa)	P-wave Velocity (m/s)	Minimum step value (MPa)	Maximum step value (MPa)	Maximum error (%)
13.75	Vertical	823	672	588	1232	49.7
13.75	Horizontal	1056	762	730	1659	57.2
13.75	Horizontal	980	734	685	1514	54.5

With these high errors, these results are deemed unreliable but are referred to in further discussions in section 6.2.8.

Manual picks versus automatic

Ideally one would manually interpret the wave first arrival (time delay) to resolve the data resolution problem. This was done for the first three tests as shown in Figure 6.6 and although the steps are quite small at these velocities, it illustrates that the shear modulus does increase more smoothly as expected. Although, of course such interpretations are based on interpolated presentation of the received waveform and are always subjective and human errors are present.
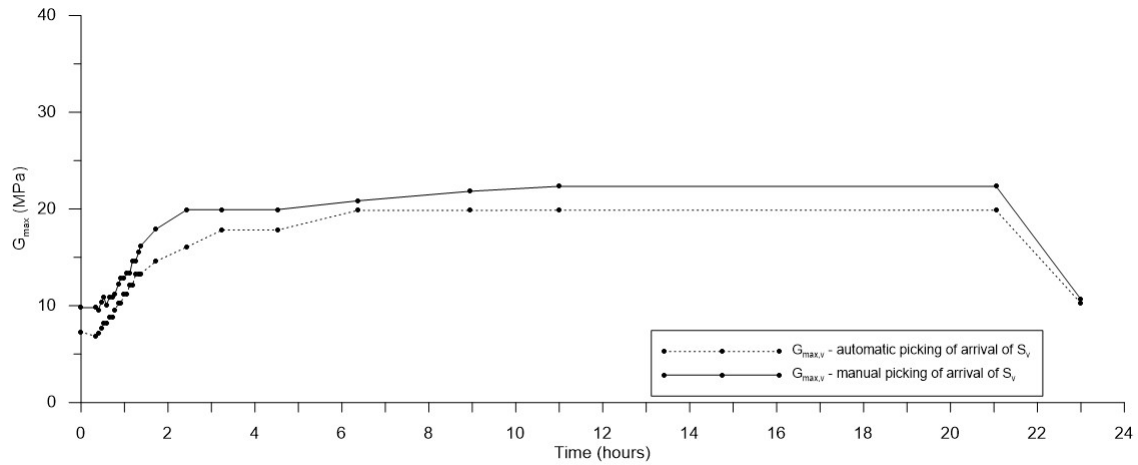
a)
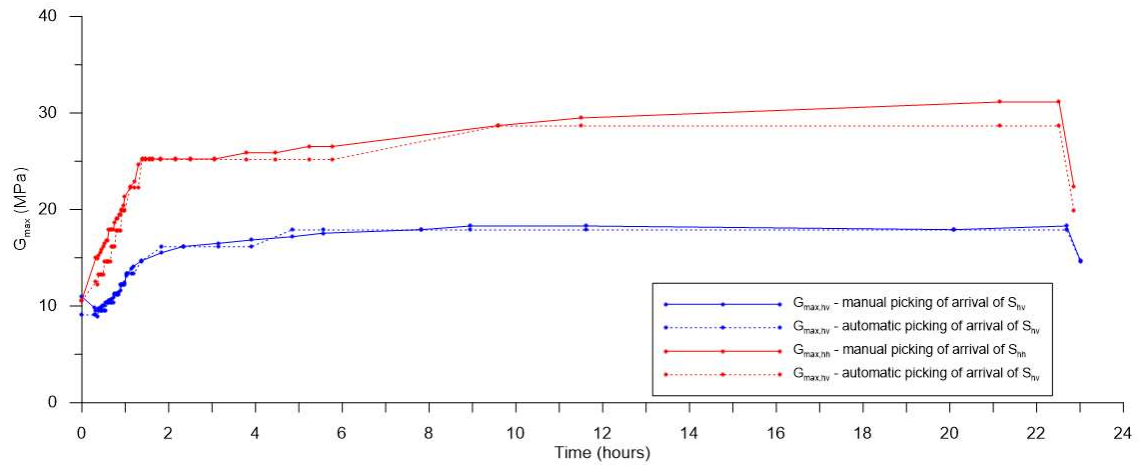
b)

Figure 6.6: Manual versus Automatic picking of S-wave arrival times at for a) Sample 890 Sv b) Samples 890 Shh and Shv.

It should be noted that Sample 890 Sv was the first test and the input frequency was not set-up correctly (discussed below), hence there is quite significant difference in the resulting G_{max} values. These manually interpreted values are used in further analysis of the results.

Input Frequency and Changes During the Tests

As seen in Figure 6.6a it is important that the initial input frequency is correctly chosen so that the input signal is a similar shape to the output signal. This is because the automated picking program uses a cross-correlation method to match the received signal and pick the first arrival time (time delay). If the input signal is not similar to the output signal, there will be errors in from using the automated system. This is illustrated by one of the first measurements as shown in Figure 6.7a. In this case the input frequency of 2 kHz is not suitable and results in a time delay that is approximately 0.2 ms too slow. At this stage in the test, 1.55 ms to 1.35 ms results in a difference in shear modulus of 2 MPa (approximately 24 % error).
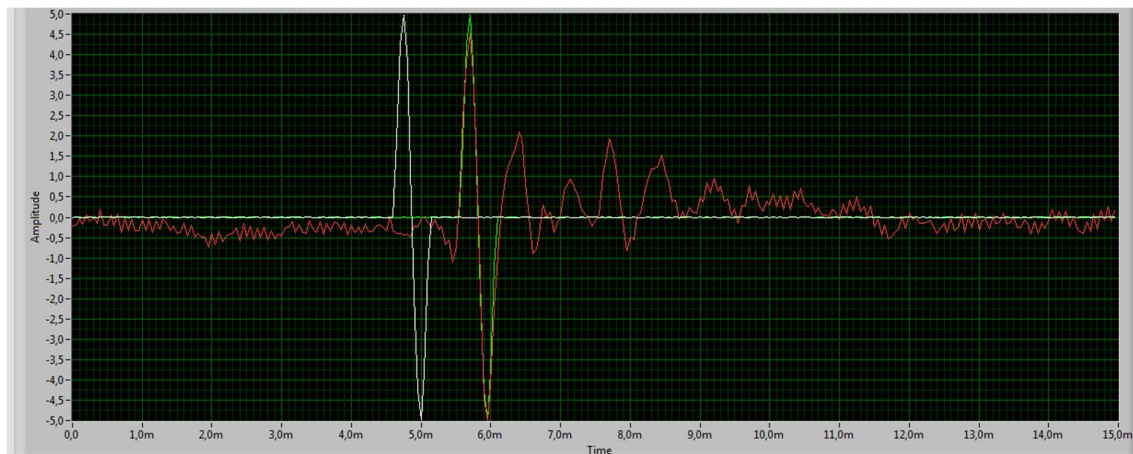
Figure 6.7: Illustration of the importance of the input signal frequency on the automatic picking of the program. Taken from Sample 890 Sv a) at the start of the consolidation process. 0.2 ms change in delay results in ~2MPa change in G_{max}. b) at the end of consolidation illustrating the change in frequency of the output signal during the test.

Throughout the study it was noted that the frequency of the received signal decreases over the duration of the test, as would be expected. This is illustrated by Figure 6.7b, which is taken from the same test but after the end of consolidation. It is seen that the output signal matches the input signal much better than at the start of the test.

It was found that a lower frequency of 0.6 kHz seemed to maintain its match throughout the test. This is illustrated in Figure 6.8 where the frequency was changed from 2 kHz (the default of the BE LabView program) to 0.6 kHz in the pre-consolidation tests. It shows that 0.6 kHz still gives a good match after consolidation. It should be noted that the high frequency noise is a result of the reduction in the voltage of the received signal, which is observed during the consolidation phase (discussed in section 6.2.11).
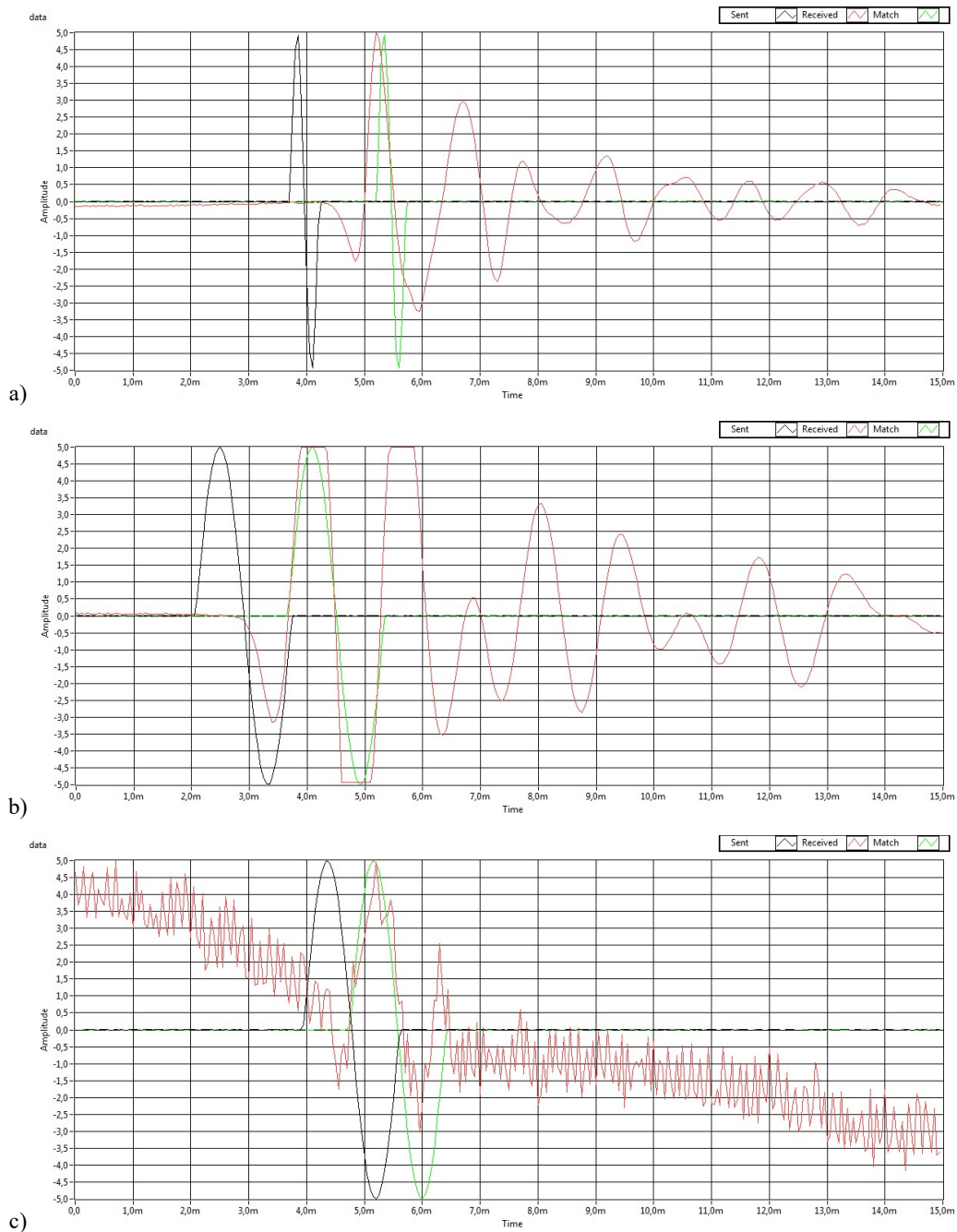

Figure 6.8: Illustration of influence of changing the input frequency from 2 kHz to 0.6 kHz from Sample 1570 Sv1. a) pre-consolidation using input frequency of 2 kHz. b) pre-consolidation using input frequency of 0.6 kHz. c) consolidated test using frequency of 0.6 kHz

The fact that 0.6 kHz is more suited is expected to result from the fact that the natural frequency of the system is closer to 0.6 kHz.

Sample length to wavelength guidelines suggested by Sanchez-Salinero et al. (1986) as discussed in section 2.3.2 ($d/\lambda > 2$) are evaluated and presented in Table 6.2. It is seen that using 2 kHz exceeds the limits where the interference of P-waves is a risk. However, this is not seen in the output waveform seen in Figure 6.8c.

Table 6.2: Evaluation of sample height to wavelength guidelines recommended by Sanchez-Salinero et al. (1986) for Sample 1570 Sv1 using input frequency of 0.6 kHz and 2.0 kHz.

| Test	Input frequency (kHz)	Measured Shear Velocity (m/s)	Wavelength, λ (mm)	Sample Height, d (mm)	d / λ
Pre-cons	2.0	59.38	29.7	95.0	3.20
Pre-cons	0.6	59.38	99.0	95.0	0.95
Post-cons	0.6	114.41	190.7	91.5	0.47

Based on the above, a frequency of 0.6 kHz was deemed appropriate. However, since the BE LabView program defaults to 2.0 kHz on restart, it is possible that this may have been occasionally used. Nonetheless, it is seen that after consolidation (the values that are of true interest) are not affected by this.

Interference from the Triaxial Anti-Friction Motor

The anti-friction motor is installed on the triaxial equipment to enable smooth application of vertical load via the load rod to the sample. As such it emits a vibration that interferes slightly with the bender element signals, usually as a low amplitude, low frequency interference. As such for most of the tests the motor was switched off after the appropriate vertical load was applied. In some cases, this was forgotten and Figure 6.9 illustrates the difference between the signals
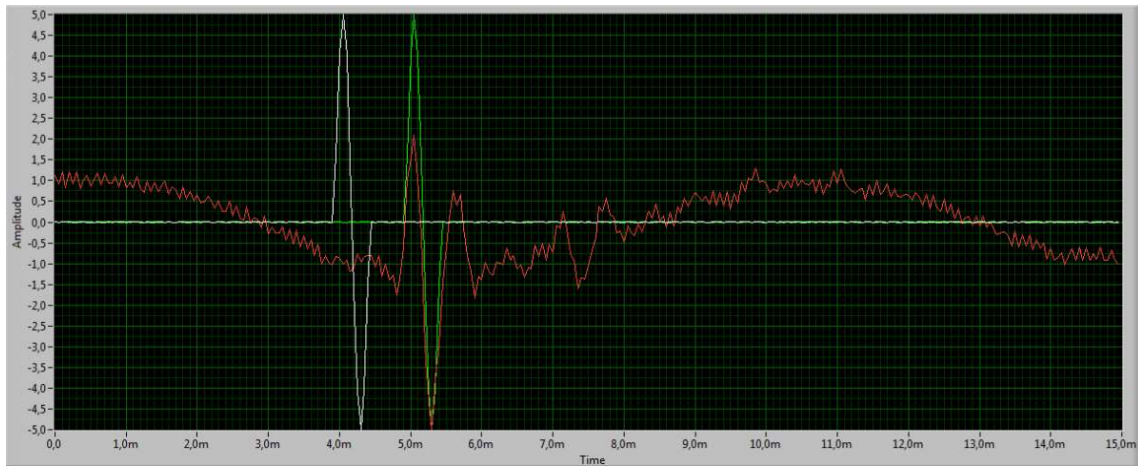
a)
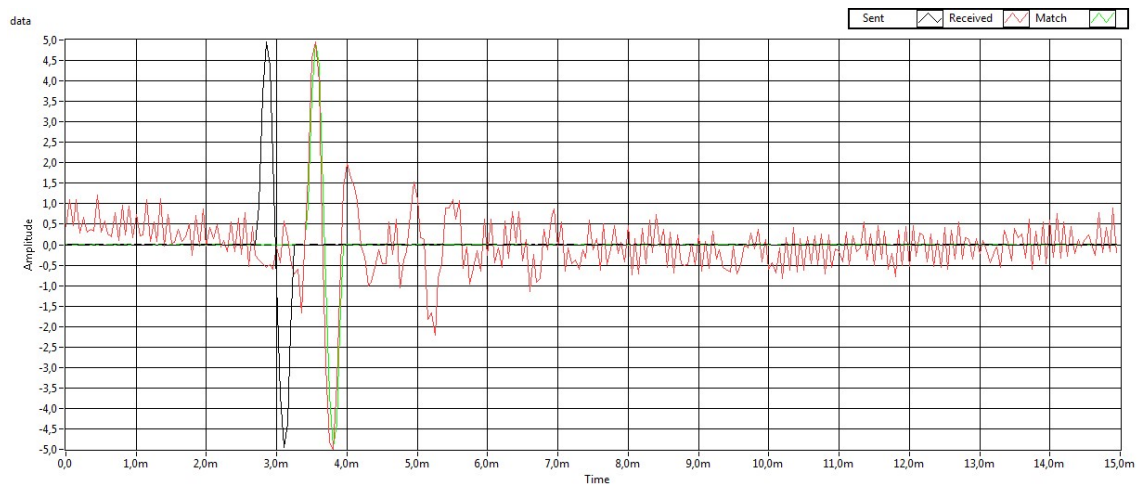
b)

Figure 6.9: Illustration of interference from the anti-friction motor a) motor on for sample 960 Sv b) motor off for sample 1165 Sv. Both images are from late in the consolidation process when received voltages were low

Since the program uses cross-correlation to match the signal shapes this does not actually affect the delay time that is picked and only the effect of frequency miss match affects the results. The motor interference would only be a problem if the zero cross-over method were used and is therefore thought to be insignificant in this case.

6.1.2. Triaxial System

There are many errors that can come about in the mounting of the sample and application of stresses to the sample during this study. These are perhaps not as critical as when the triaxial equipment is used for the purposes of measuring soil strength parameters but are nonetheless discussed briefly here.

As introduced in section 2.8.2, the amount of water that comes out of the sample during the consolidation phase can be used as a measure of sample quality. During this study it was found that 2 crucial factors can create significant errors in this process:

1. The correct choice of applied stresses to represent in-situ conditions.
2. How much water is added to the system via filter paper

It was noted previously that the first sample at 8.90 m was subjected to stresses calculated using hydrostatic water pressure and a K_0 value of 0.5, compared to 0.7 for the other samples and the lower than hydrostatic pore water pressures. It is seen that these are the only fair to good quality samples. Obviously more water will be expelled when higher stresses are applied, so it is important to be sure that these stresses are correct. The main problem in this case is the choice of K_0, which is hard to determine as discussed in section 3.2.2. For example, in the stress calculations for the samples at 15.85 m the difference between a K_0 value of 0.5 and 0.7 creates an average confining stress difference of 32 kPa (159 to 191 kPa), which is 20 % greater. Perhaps using 0.5 would have achieved better-quality samples.

When the triaxial sample is mounted, water is added to the filter paper at the top bottom and around the edge. It was noted that for several tests that after unloading and unmounting, which usually only took 5 minutes, the filter paper around the sample was found to almost dry. Of course, some of this drying is likely to be due to suction after unloading (section 0), but out of interest, the filter paper was weighed after the tests. It was first measured how much water is held by the filter paper as shown in Figure 6.10.
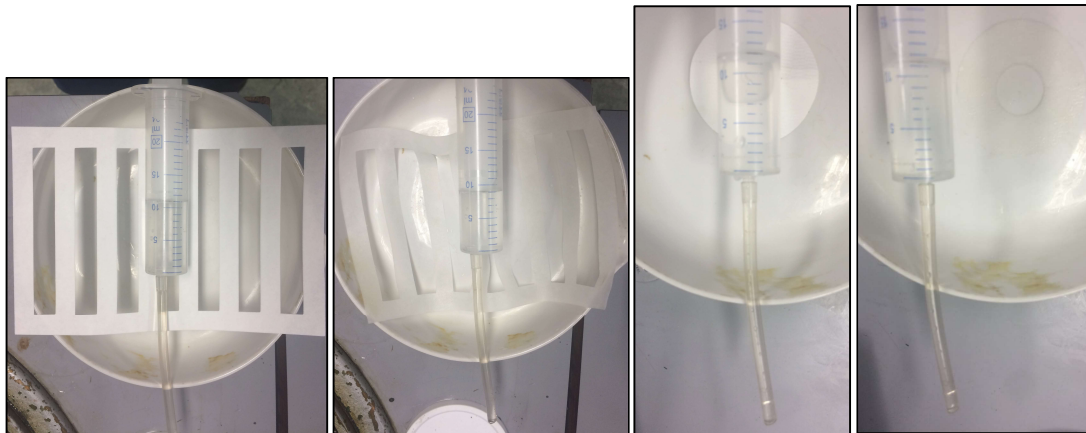

Figure 6.10: Amount of water in saturated filter paper

It was found that the saturated filter paper held 2 ml (cm^3 or g) in the edge paper and 0.5 ml in the top and bottom, a total of 3 ml. The amount of water in the filter paper after the tests was measured for some samples with the results presented in Table 6.3.

Table 6.3: Amount of water in the filter paper after the tests

Sample	Water in filter paper (ml, cm³, g)	Comments
1570 Sv2	1.96	Burette was left open during unloading and total expelled water was allowed back into the sample
1375 Pv	1.15	Unloaded, burette closed and unmounted within 5 min
1375 Ph2	0.52	Unloaded, burette closed and unmounted within 5 min
1360 Shh	0.73	Unloaded, burette closed and unmounted within 5 min
1360 Shv	0.64	Unloaded, burette closed and unmounted within 5 min

There are two important findings here. Firstly, and most importantly for this discussion, the sample with the open burette (1570 Sv2) shows that even when suction has been resolved in the sample, with all expelled water back into the clay, 1 ml (cm³) of that water is missing from the filter paper. As such it would be reasonable to say that 1 ml of the expelled water during consolidation is actually from the filter paper itself. Secondly there are implications to suction effects during unloading, which are discussed further in section 6.2.7.

Consolidation rate

It was considered from the start of this study that the rate of consolidation of the sample would have an influence on the sample quality as it seems intuitive that applying a stress in large loads such as 10 kPa may disturb the sample. As such an increase of 2 kPa per minute seemed reasonable. This was tested further for three vertical samples from the same depth at 15.70 m. The results are presented in Figure 5.11. The first sample was consolidated in steps of 5 kPa/min whilst the others at 10 kPa/min. One would expect the samples with the higher rate to be more disturbed and hence show lower stiffness. What is surprising is that the first sample with the slower rate shows the lower final stiffness. On inspection of the expelled water, less water was expelled from this sample. It could be that in using a higher consolidation rate, there is perhaps some effect on the structure of the clay. The pore pressure gradient may be high enough to pull the clay particles together causing a reduction in void ratio, which would result in higher stiffness.

A consolidation rate of 10 kPa/min was also used for samples 1360 Shv and Shh shown in Figure 5.7 and Figure 5.8. It is not really possible to see the effects of this since the samples were cut in different orientation so cannot be directly compared. Less water was expelled from sample Shh. These were also, from the top of a mini-block sample, which seem to display lower shear stiffness values as discussed in section 6.2.10.

To conclude, the consolidation rates could be considered a significant limitation to this study, although most were kept below 5 kPa/min.

6.1.3. Anisotropy

Use of Elastic Cross-Anisotropic Theory

The elastic cross-anisotropic stiffness matrix described in section 2.2.1 includes parameters that act infinitely in a 3D elastic material. When shear wave is sent from a point source and travels through a cylindrical sample the shear is not transferred infinitely in the lateral direction through the material. Hence, whilst the shear velocity is a correct measured value, the use of the equation:

$$G_{max,ij} = \rho \cdot V_{ij}^2$$

<div align="right">[6.1]</div>

may not give the true shear stiffness value. It is thought this is why the results show a difference between G_{vh} and G_{hv} when they should be equal. As discussed in section 2.2.1, previous theories suggest this difference is due to the non-point like source of the S-wave and influences in the way the shear wave travels through the cylindrical sample. It is likely that the latter is of most importance and that there is a coupling effect from stiffnesses in other directions that create resistance in the vertical plane. As such a monoclinic type stiffness matrix (still symmetric in the vertical plane) with 13 elastic constants is suggested to be more appropriate for bender element testing:

$$\begin{bmatrix} d_{11} & d_{12} & d_{13} & 0 & 0 & d_{16} \\ d_{12} & d_{22} & d_{23} & 0 & 0 & d_{26} \\ d_{13} & d_{23} & d_{33} & 0 & 0 & d_{36} \\ 0 & 0 & 0 & d_{44} & d_{45} & 0 \\ 0 & 0 & 0 & d_{45} & d_{55} & 0 \\ d_{16} & d_{26} & d_{36} & 0 & 0 & d_{66} \end{bmatrix}$$

<div align="right">[6.2]</div>

For the purposes of this study the cross-anisotropic model is used and hence differences in G_{vh} and G_{hv} are presented in the results and discussed in further detail in section 6.2.2. As such, the coupling effects are ignored and G_{vh} is considered as the vertical stiffness.

Orientation of horizontal samples

Since is seems there is a coupling effect between stiffnesses in other directions, the orientation of the samples becomes even more important. Cutting of the samples was carried out orthogonal to the base of the mini-block sample, so if this was not truly horizontal errors in the alignment of the triaxial samples with occur. An example is shown in Figure 6.11 taken from sample 1585

Shh. This could be a contributing factor to the difference between G_{vh} and G_{hv}. It is not possible to quantify these errors, but for further studies it should be considered in design of the tests.
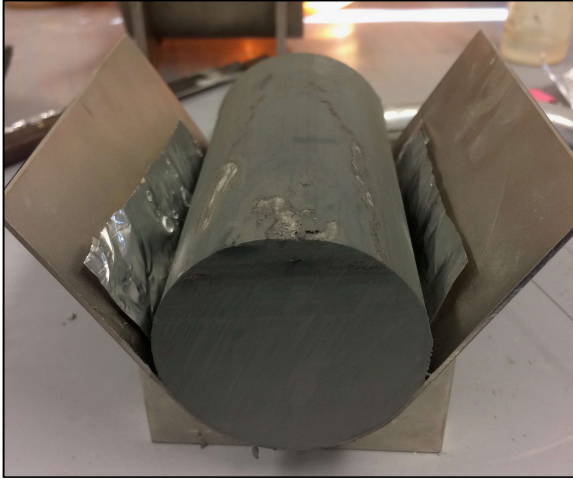

Figure 6.11: Example of a misaligned horizontal sample, with layering not exactly 90° to sample axis.

6.2. Analysis and Discussion of Results

6.2.1. G_{max} with Depth

As summarised in section 5.2, G_{max} was taken for each sample after EOP in order to estimate the in-situ stiffness. However, it is known that laboratory techniques do not achieve accurate (high enough) values for in-situ G_{max} and they are expected to be even lower in this case since the samples had been in storage for 3-5 months. Therefore, results from a SDMT survey are utilised here for comparison and interpretation (NGI, 2017). This profile is shown in Figure 6.12. In calculation of this profile, they use estimated values for density between 1.89 and 1.95 g/cm^3. In order to compare to the results from this study, the results were re-calculated using an average density of 1.80 g/cm^3 from the index test results. A polynomial fit line was calculated from this profile for further analysis and comparison with soil properties.

As expected the vertical G_{max} values from this study are less than the SDMT profile in the order of between 35-57% as shown in Table 6.4.

Table 6.4: Comparison of $G_{max,v}$ BE results with SDMT results

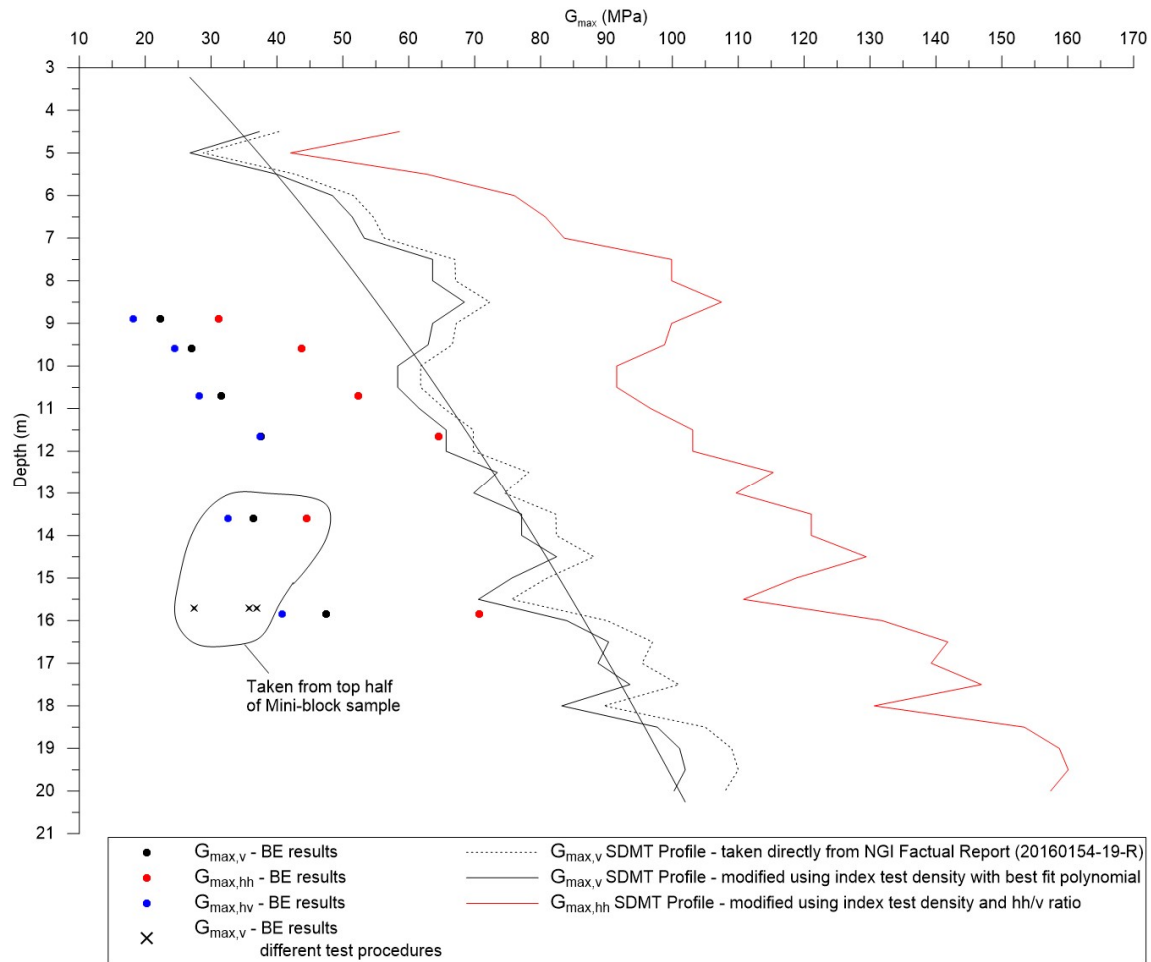| Depth (m)	$G_{max,v}$ - Triaxial	G_{max} – SDMT Profile (closest depth to 0.5m)	$G_{max,v}$ Triax / SDMT (%)
8.90	22.3	63.6	35
9.60	27.8	62.9	44
10.70	32.3	58.3	55
11.65	37.6	65.7	57
13.60	36.5	77.1	47
15.70	27.5	70.6	39
15.85	47.5	84.0	57

Figure 6.12: Plot of G_{max} variation with Depth with modified SDMT profile

6.2.2. *Anisotropy*

The SDMT technique measures the vertical shear wave velocity only. It is clear from the BE results that there is high anisotropy in the shear stiffness of the clay samples when they are consolidated, with $G_{max,vh}$ 39-71 % greater than $G_{max,hh}$. It seems reasonable to apply the same average ratio (*hh/vh*) to the SDMT profile. Note that the ratio (*hv/vh*) is not applied as discussed below. These results are also presented in Figure 6.12. However, this transfer of the anisotropy from the BE to the SDMT results should be used highly tentatively since it is not known if this anisotropic nature comes from the effects of unloading on the sample.

It is found that the anisotropy in the shear stiffness of the unconfined samples ($G_{max,0}$) is less but still present, with $G_{max,hh,0}$ between 7 - 51 % greater than $G_{max,vh,0}$ as shown in Figure 6.13. It is therefore reasonable to conclude that the degree of anisotropy increases with an increase in effective confining stress.
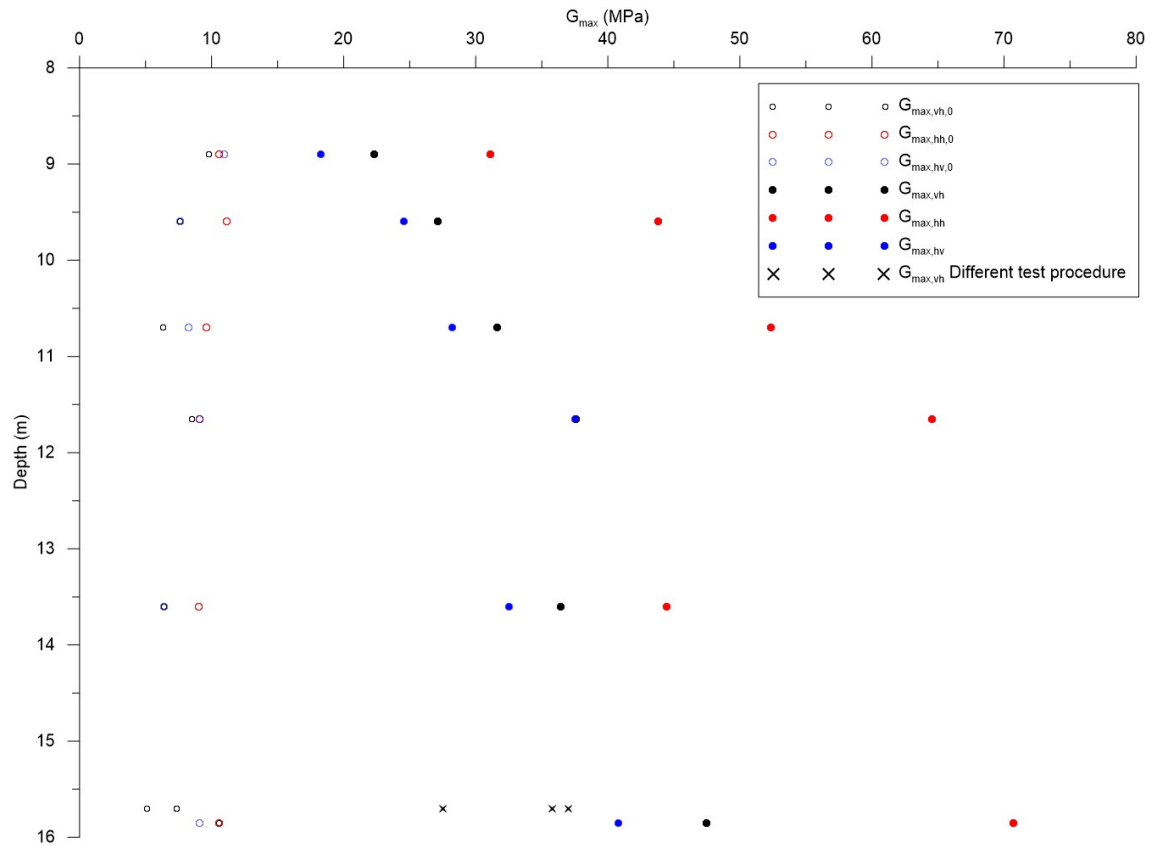
Figure 6.13: Unconfined $G_{max,0}$ results compared with consolidated results

In-situ anisotropy is expected to result from both the stress induced anisotropy and the inherent structural anisotropy, which derives from the structure of the clay. It is known that swelling likely occurs during and after the sampling due to stress relief, which is greater in the vertical direction. If this is the case and since anisotropy is observed in the unconfined samples after sampling, then it is reasonable to assume that anisotropy would be higher in-situ as is seen after consolidation. Since the increase in anisotropy is not huge after consolidation, this suggests that inherent anisotropy plays a significant role.

Regarding the structure of the clay, it is intuitive to suggest that the lateral alignment of clay minerals creates a stiffer reaction in the horizontal direction due to the end-end contacts of the clay particles and the interface van der Waals forces. As such, the relationship between clay content and the degree of anisotropy is analysed and presented in Figure 6.14. Note that the grain size distribution is not considered reliable for 10.70 m.
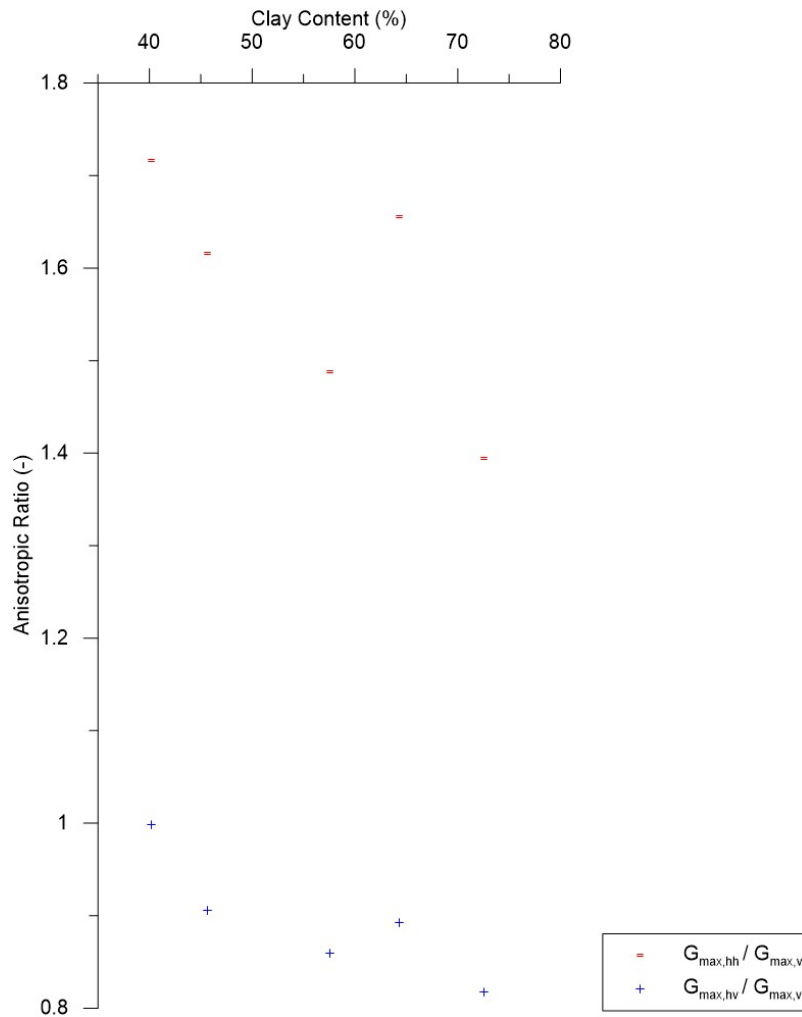
Figure 6.14: Relationship between anisotropic ratios of G_{max} and clay content. Note: 10.70 m not considered reliable.

One would expect anisotropy to increase with increasing clay content. What is seen (when excluding 10.70 m results) is the anisotropy between the shear modulus in the horizontal plane and the vertical plane (G_{hh}/G_{vh}) decreases with increasing clay content. One possible explanation is sample disturbance. More clay content would lead to more swelling from sample unloading such that the flocculated structure would become more symmetric its original deposited state as was discussed in section 2.5 and shown in Figure 2.13. On reloading during consolidation, it is harder to return to its in-situ structure due to the disturbance. Another similar explanation is that during sampling the face-to-face (van der Waals) contacts, which lie in the horizontal plane (affecting G_{hh}) have become weaker on unloading and not returned to their original state. An effect that would be seen in higher clay content clays. This supports the hypothesis that the in-situ clay will show equally high if not higher anisotropy.

We know that according to elastic cross-anisotropic theory discussed in section 2.2.1, G_{hv} should equal G_{vh}. As also discussed in section 6.1.3, the difference seen in the results is

94

likely due to a coupling effect of stiffnesses that comes from the fact that the shear wave does not transfer infinitely in the lateral direction, through the cylindrical sample, and rotation is limited. What is also interesting, in this respect, is that the ratio G_{hv}/G_{vh} increases with increased clay content (Figure 6.14) implying that the coupling effect increases with clay content. This makes sense as more face-to-face contacts increase the shear resistance in the vertical direction.

As such, it seems reasonable to conclude that the anisotropy in the stiffness of the clay is mainly controlled by the structure of the clay and as such there will be some anisotropy present in-situ, possible more so, since sample disturbance may have caused destruction of the flocculated structure. One way to clarify this would be to load the vertical samples to isotropic stress conditions.

It is proposed that in-situ surveys such as cross-hole seismic tests are carried out to investigate this further. Also, it would be interesting to use numerical modelling to study the propagation of shear waves through a cylindrical sample, determine the influence of the stiffness coupling effect to define a monoclinic stiffness matrix, and hence define correct equations for acquiring accurate small-strain shear stiffness moduli (where $G_{hv}=G_{vh}$) from BE measured shear wave velocity.

6.2.3. G_{max} with Average Confining Effective Stress, p'

Since it is known that G_{max} is dependent on effective stress, the BE results are plotted against average confining effective stress (p') in Figure 6.15. There is a clear increase. Results from the top half blocks have been excluded, which is discussed in section 0 and linear best fits are presented. Whilst the data points are limited this presentation also shows that anisotropy increases with effective confining stress. However, these linear fits are not considered reliable due to the minimal data points.
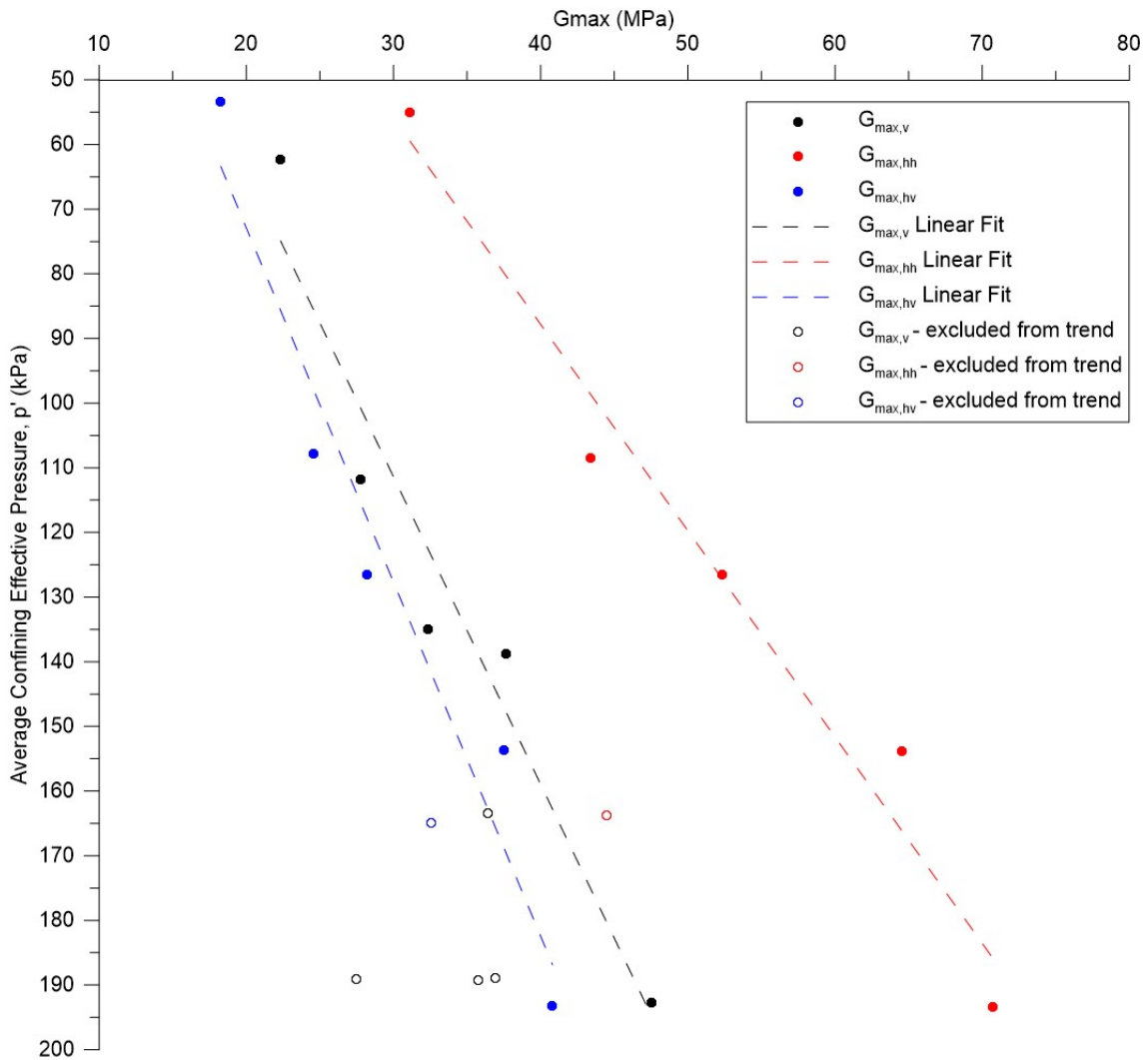
Figure 6.15: Plot of G_{max} against average confining effective stress, p'

There are various proposed relationships between effective confining stress and G_{max} as introduced in section 2.4. The SDMT results are utilised to assess how some of these relationships fit with the data at this site, as illustrated in Figure 6.16.

For the relationship suggested by Janbu (1963) in equation [2.15], a value of m=0.6 seems reasonable (taken from Figure 2.9) for this site and average values from the index test results are used (a plasticity index (I_P) of approximately 7 and liquid limit (w_l) of approximately 32 %). A profile using m=0.5 is also calculated for comparison. These profiles are calculated using K_0 value of 0.7 as have been used for the BE tests in this study. These are then matched to the SDMT data (which has been recalculated with K_0=0.7 and with the measured pore pressure profile) using proportional factors to fit to the data. As such the following are plotted:

$$G_{max} = 6 \cdot p'^{\,0.5}$$

6.3

96

$$G_{max} = 4 \cdot p'^{\,0.6}$$

6.4

This power relationship has then been adjusted to fit the BE results using an average percentage of 48%.

Donohue and Long (2010) and L'Heureux et al. (2013) have shown that the relationship proposed by Leroueil and Hight (2003) in equation [2.14] can be applied to Norwegian clay profiles if one applies values shown in Table 6.5. As such two profiles for S=500 and S=700 have been calculated and are also presented in Figure 6.16.

Table 6.5: Inputs to equation [2.14] for Norwegian clay profiles

Soil characteristic parameter, S	500 and 700
Void ratio function, $F(e)$ (e taken from index tests)	$1/e^{1.3}$
At rest earth coefficient, K_0	0.5
Stress exponent, n	0.25

A profile based on Hardin (1978) relationship in equation [2.13] has also been calculated and plotted using the inputs in Table 6.6.

Table 6.6: Inputs to equation [2.13] for Hardins relationship between G_{max} and p'

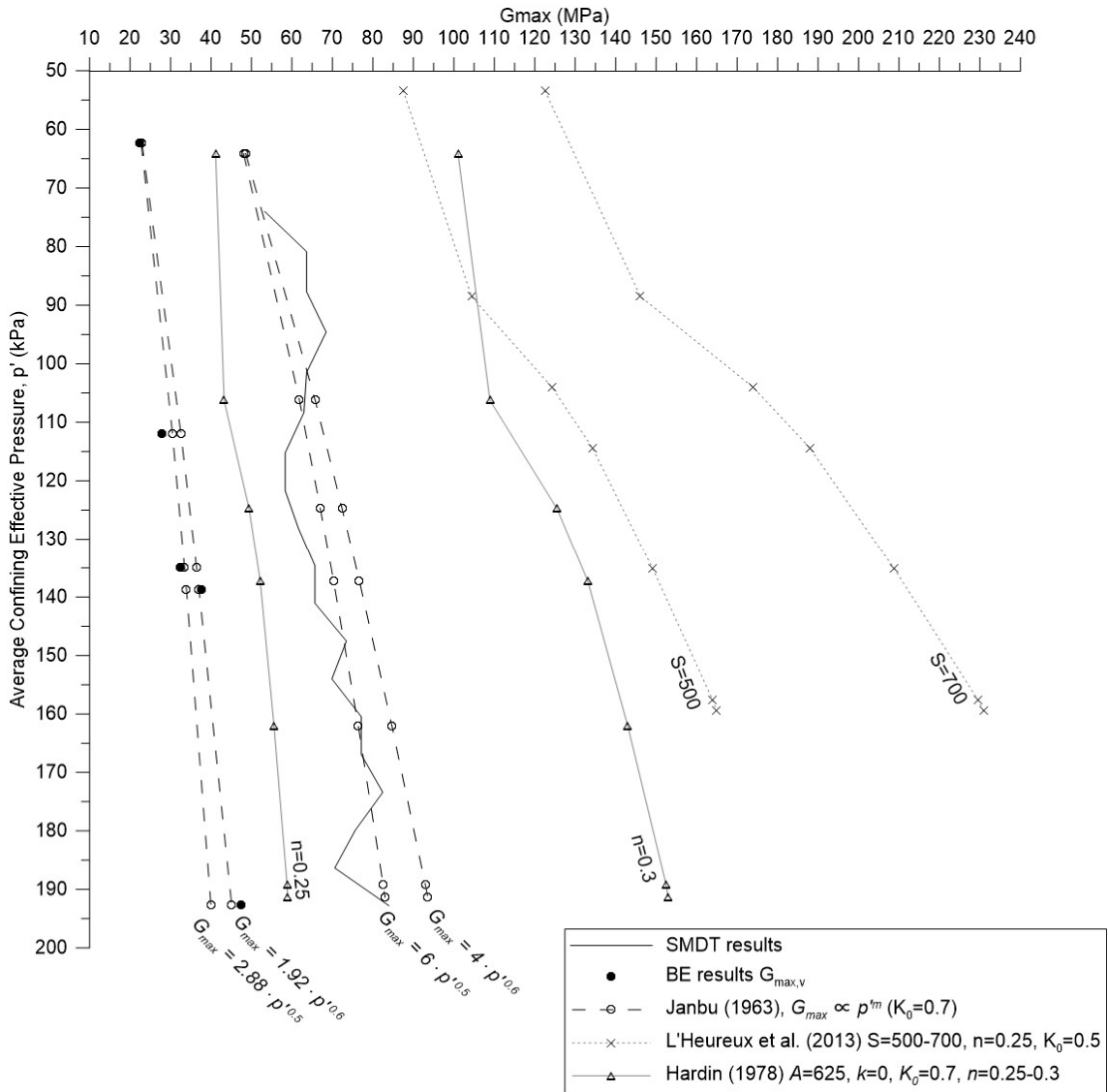| Material constant, A	625
Void ratio function, $F(e)$ (e taken from index tests)	$1/e^{1.3}$
At rest earth coefficient, K_0	0.7
Stress exponent, n	0.25 and 0.3

Figure 6.16: Illustration of the various relationships between G_{max} and effective stress as described in the literature

It is clear that the Janbu (1978) relationship with a power exponent , *m=0.5* gives a very realistic fit to the SDMT data and even though this profile is expected to be somewhat less than the true in-situ G_{max} profile due to its intrusive nature, it can be assumed that a similar shape should be present from another data source such as MASW. When compared to the BE results a power exponent, *m=0.6* gives a better fit and aggress with the suggested exponent based on plasticity and liquid limit (Figure 2.9). Whilst the power relationship describes the trends well, it serves no purpose in predicting results. Overall, determining the power exponent and a factor of proportionality is problematic and this is where other factors such as void ratio, OCR and plasticity need to be accounted for.

Using L'Heureux et al. (2013) relationship with their suggested parameter values results in much higher estimates than the SDMT profile. It also illustrates the influence of the void

ratio, as with Hardin (1978), since the estimate of G_{max} at 8.90 m seems to be out of trend. This is expected to be an error in the index results as was described in section 5.1. Both these relationships illustrate the importance of choosing correct values for *S* and *n.* It would be interesting to look into these factors in more detail but is considered beyond the scope for this study.

6.2.4. G_{max} Relationships with Index Parameters

<u>Clay Content</u>

Since soil type influences stiffness clay content is compared with the shear stiffness results with percentage clay content plotted against depth and against G_{max} in all three orientations in Figure 6.17. It should be noted that the results from 10.70 m are unreliable and G_{max} results for 13.60 m are removed since they are from the top of a block.
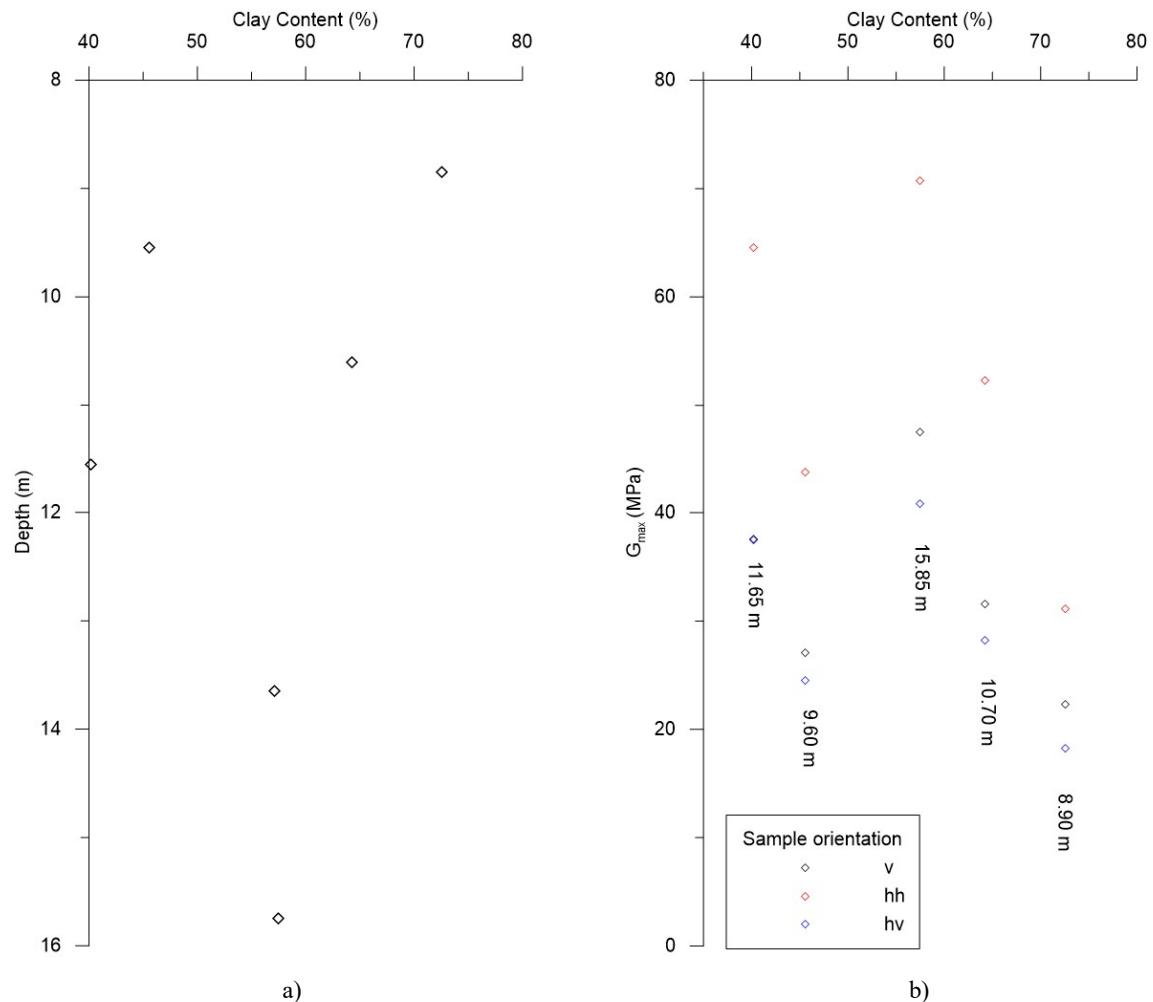
Figure 6.17: Clay content against a) depth and b) $G_{max,v}$, $G_{max,hh}$ and $G_{max,hv}$.

There is no apparent relationship observed in this data and no direct relationships have been reported in that past. It should be noted that perhaps the grain size distribution may not be representative of the triaxial samples, since the sample for hydrometer analysis was taken from offcuts of the mini-block, not necessarily specifically from the depth of the triaxial samples. As such the fact that there is no relationship is not conclusive. We have seen previously that clay content has an influence on the degree of anisotropy.

Water Content

As is seen from the index test results, water content has a general trend of decreasing with depth with the exception of the mini-block sample at 10.45-10.60 m. Since G_{max} increases with depth, there is expected to be a trend between water content and G_{max} as is shown in Figure 6.18.

Figure 6.18: Gmax plotted against water content (w)

There is a clear trend of decreasing shear modulus with increasing water content (when 10.70 m is excluded). This is as expected since water has no shear resistance and therefore reduces the shear stiffness of the whole material. There are not enough data points to determine the trend of relationship.

100

Void Ratio

Void ratio (*e*) is plotted against depth and G_{max} in Figure 6.19. There is a clear trend of decreasing void ratio with depth, which is expected from the increase in pressures on the soil. Again, it is seen that the index test result for mini-block 8.60-8.95 m is out of trend, which is likely to be because this was the first set of index testing to be carried out. This is then excluded from further analysis.
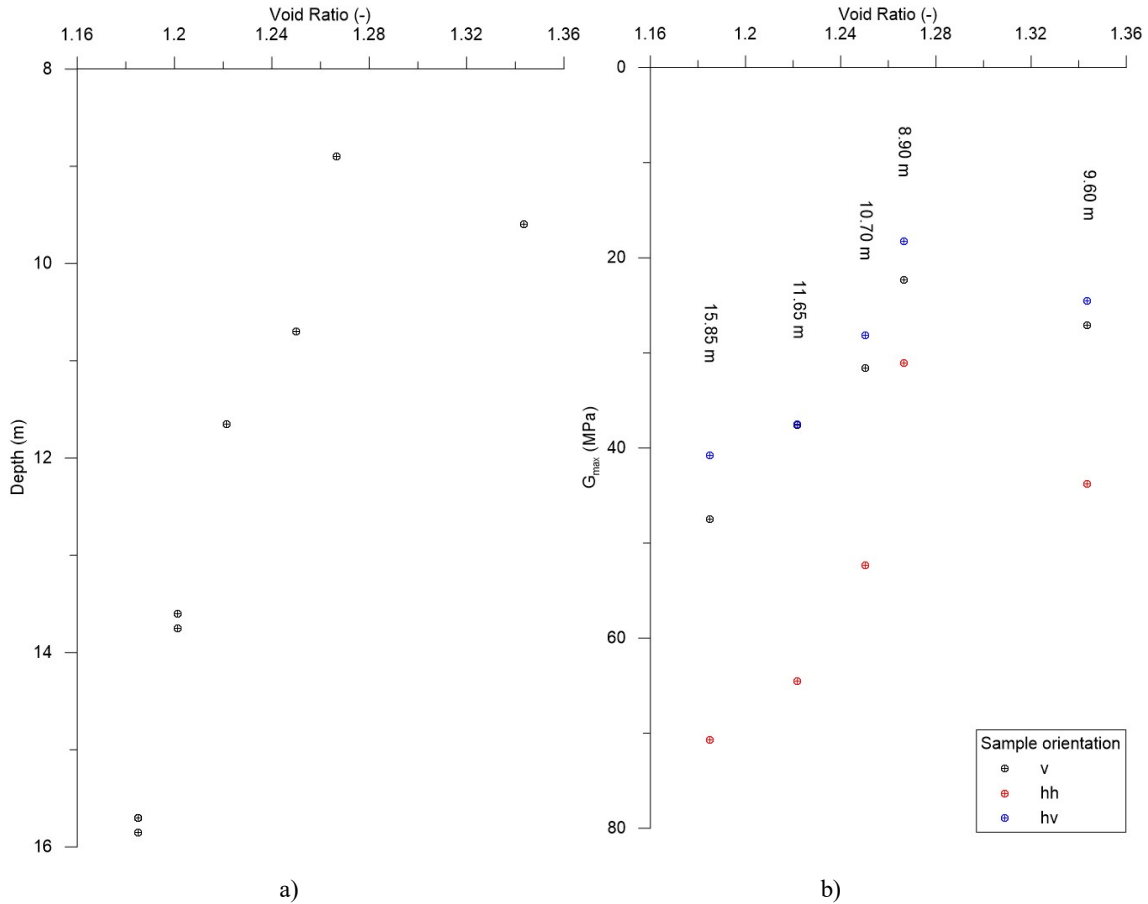
Figure 6.19: Void ratio (e) plotted against a) depth and b) G_{max}

The generally accepted power relationship proposed in the literature (equation [2.16]) and that proposed by Hardin and Richart (1963) (equation [2.17]) are examined and presented in Figure 6.20.
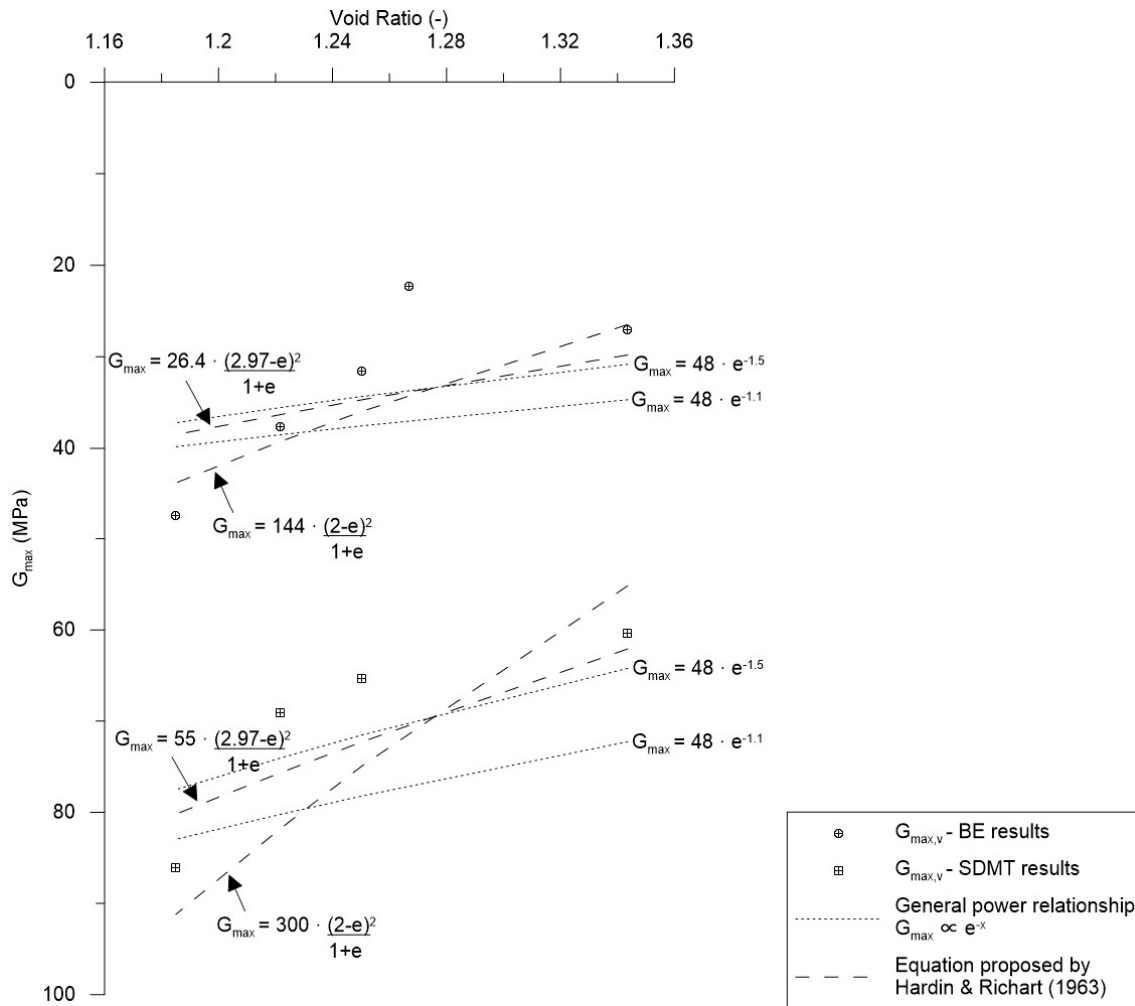
Figure 6.20: Relationships between G_{max} and void ratio proposed in the literature compared with BE results and SDMT results.

It is found that the general power relationship is not a suitable fit to the BE or SDMT data using the exponent (x) in the range suggested by Presti et al. (1993) between 1.1 and 1.5.

However, the Hardin and Richart (1963) equation [2.17] shows a better fit. Using a coefficient of *2.97* does not fit the BE data. Using a higher coefficient as suggested for a clay with high surface activity was found to move further from the trend. As such a coefficient of *2.0* was tested and showed a very good fit with the BE results:

$$G_{max} = 144 \cdot \frac{(2.0 - e)^2}{(1 + e)}$$

<div align="right">*[6.5]*</div>

However, when translated to the SDMT results, *2.97* was a better fit and since these are truer to the expected in-situ values the following relationship seems acceptable:

$$G_{max} = 55 \cdot \frac{(2.97 - e)^2}{(1 + e)}$$

<div align="right">*[6.6]*</div>

102

Of course, this is only based on four test results so is very spurious, but it shows that these relationships are of relevance and could be fine-tuned with more results. It shows that G_{max} is highly influenced by void ratio and should hold a high weighting in the overall estimation of G_{max} from soil properties.

Plasticity Index

The plasticity index (I_P) is expected to show minimal effet on G_{max} since the OCR of the clay is expected to be low. Nonetheless, I_P is plotted against depth and G_{max} in Figure 6.21.
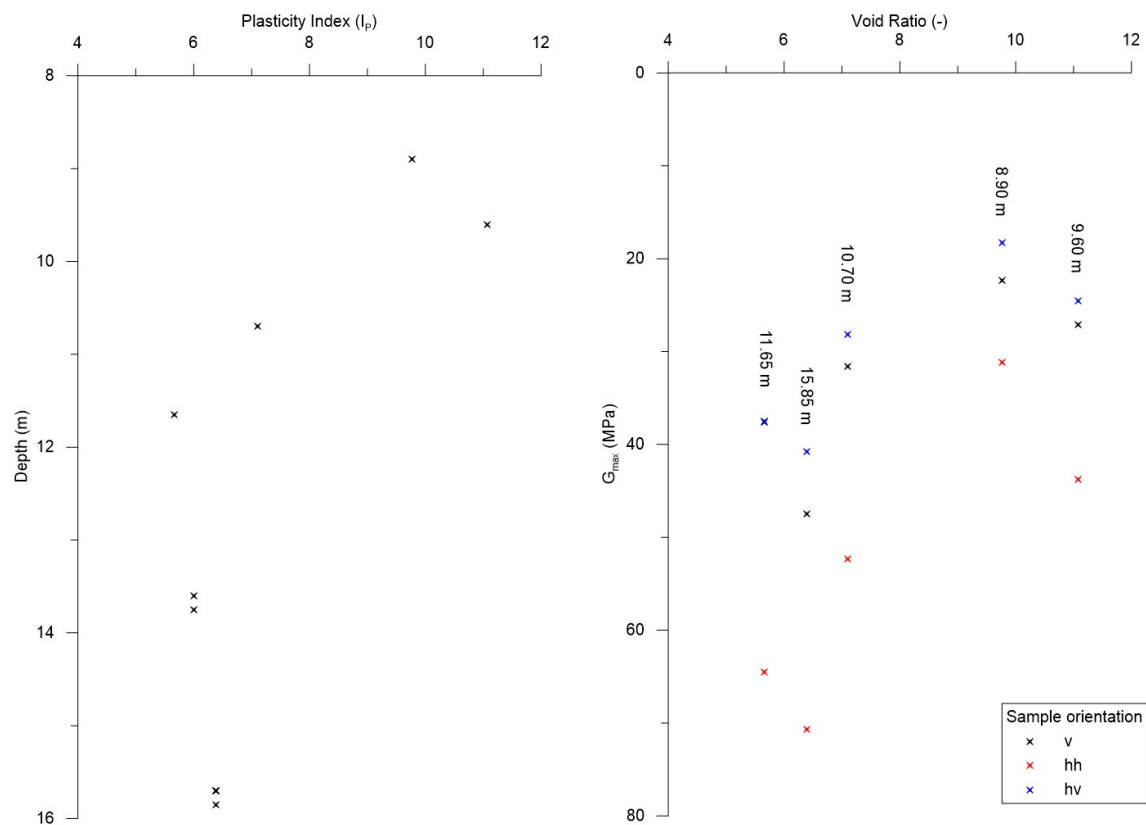
Figure 6.21: Plasticity Index plotted against a) depth and b) G$_{max}$

It seems reasonable to say that there is a reduction of plasticity with depth at shallow depths, where it then evens out, or perhaps that there is slightly higher plasticity in the transition zone from non-sensitive to sensitive clay. But this would be a tentative conclusion. Another tentative conclusion would be that G_{max} reduces with increased plasticity.

6.2.5. Consolidation of the Samples

Examples of plots of G_{max} against applied average pressure are presented in APPENDIX C – Examples of BE Results *Gmax* against Applied Average Confining Pressure, *p*. Note that these

are only applied total stresses and effective stresses are only reached after EOP. Whilst this presentation of results is not very useful it is clear, as with the time plots that the increase in G_{max} is immediate upon application of load via the cell pressure, which is expected as effective stresses start to increase immediately as water is expelled from the sample. As is seen in Figure 5.3 to Figure 5.13 there is also a slight time delay as is expected since it takes time for the water to expel from the clay and the effective pressure to reach its final value at EOP. Effects of the rate of consolidation were discussed in section 6.1.2.

6.2.6. *Variations in Gmax after End of Primary Consolidation (EOP)*

For some samples it is clear there is still a development in stiffness after EOP. For example, 8.90 m (Figure 5.3), 9.60 m (Figure 5.4) and 15.85m (Figure 5.13). Of course, this may be the case for all samples and has lost in the resolution of the BE system. It is likely that this is due to a very small continuation in expelled water and increase in effective stress, but as is seen for sample 890 Shh, water appears to go back into the sample. It is therefore possible that some of this increase is due to ageing effects as was introduced in section 2.4.5.

Ageing Effect

As described by equation [2.18], the difference between in-situ and laboratory G_{max} due to aging effects can be estimated according to the rate of increase in G_{max} after EOP. Since the resolution of the BE system was only overcome for samples at 8.90 m by manual interpretation, this effect can only be analysed for this depth. According to equation [2.19], N_G is found:

$$N_G = 0.027\sqrt{9.77} = 0.26379$$

<div align="right">[6.7]</div>

$(G_{max})_{1000}$ from the G_{max} results after EOP:

$$(G_{max})_{1000} = 22.3\ MPa$$

<div align="right">[6.8]</div>

Therefore, the increase of G_{max} over one log cycle of time:

$$\Delta G_{max} = N_G (G_{max})_{1000} = 5.88\ MPa$$

<div align="right">[6.9]</div>

As was introduced in section 3.2.1 the approximate geological age of the clay at Flotten is expected to be 10,800 years, which equates to approximately 6.94 log cycles in time (after $(G_{max})_{1000}$). Therefore, the expected loss of ageing effect in the sample is approximately 40.8 MPa and the estimated in-situ value is 63.1 MPa. As is seen from the SDMT value of 63.8 MPa, this is a very good approximation. It also suggests that all loss in G_{max} is due to ageing effects,

which is unlikely, and it should be noted that some disturbance is expected using the SDMT method and as such it would be worth acquiring results from a non-intrusive survey to confirm this.

6.2.7. Unloading

As was introduced in section 2.8.3, unloading of a sample creates a reduction of residual effective stress in the sample due to the negative pore pressure gradient, migration of water into the sample and expansion of the pores. This is considered the main cause of sample disturbance. As such, some tests were done to try and imitate unloading conditions with access to water, and some were carried out without access to water to see the affects.

Unloading with open burette

For sample 1570 Sv3, after unloading all the expelled water from the consolidation process was allowed back into the sample as shown in Figure 5.11. In fact, as well as the extra 1.5 ml of water recorded by the burette, it was found after unmounting that only 2 ml of water was in the surrounding filter paper, so in total 2.5 ml extra water was taken into the sample. As such it is seen in Table 6.7 that G_{max} after unloading dropped below the pre-consolidation, unconfined measurement. Whilst pore pressure measurement could not be taken, the rapid drop in G_{max} supports the theory that residual effective stresses in the sample decreases rapidly after unloading.

Table 6.7: Unloading results for samples with access to water (open burette)

Depth (m)			(MPa)		Percentage	Percentage
	Orientation	Pre-Cons $G_{max,0}$	Consolidated G_{max}	Unloaded $G_{max,u}$	> $G_{max,0}$ (%)	of G_{max} (%)
15.70	v	7.4	37.0	3.7	-50	10
13.60	v	6.4	36.5	8.4	31	23

Sample 1360 Sv was also unloaded with access to water, but only half the expelled water was allowed into the sample as shown in Figure 5.7. Even so, the stiffness dropped back almost to its pre-consolidation value. After the burette is closed it is seen that the stiffness gradually increases over the 10 days that the sample is left as shown in Figure 5.8. Pore pressure was measured for this test and it is seen that there is a steep decrease in pore pressure, which correlates with the drop in stiffness. Over approximately 10 hours the pore pressure settles.

There is an increase in pore pressure at approximately 48 hours, which comes from a change in the differential sensor. This cannot be explained.

It would be interesting to carry out more controlled tests than this, ideally in more advanced triaxial cells, that have the means to measure accurate pore pressure and changes in the dimensions of the sample even after unloading.

Unloading with closed burette

Many samples were unloading having been left at the consolidation stresses overnight. After full unloading of pressure, the burette was closed, the water drained from the cell and then a BE measurement was taken almost immediately, with less than 5 minutes between pressure unloading and measurement. Results are summarised in Table 6.8 and it is seen that G_{max} does not return to its original value.

Table 6.8: Summary of unloaded G_{max} values after unloading without access to water

Depth (m)			(MPa)		Percentage	Percentage
	Orientation	Pre-Cons	Consolidated	Unloaded	$> G_{max,0}$	of G_{max}
		$G_{max,0}$	G_{max}	$G_{max,u}$	(%)	(%)
8.90	vh	9.8	22.3	10.7	9	48
Figure 5.3	hh	10.6	31.1	22.3	110	72
	hv	10.9	18.3	14.6	34	80
9.60	vh	7.6	27.1	18.8	147	69
Figure 5.4	hv	7.6	24.5	21.7	186	89
10.70	vh	6.3	31.6	24.2	284	77
Figure 5.5	hh	9.6	52.3	37.4	290	72
	hv	8.3	28.2	19.6	136	70
11.65	vh	8.5	37.6	17.6	107	47
Figure 5.6	hh	9.1	64.5	44.7	391	69
	hv	9.1	44.5	28.1	209	63
13.60	hh	9.0	36.5	24.5	172	67
Figure 5.7	hv	6.4	44.5	19.6	206	44
15.70	v1	7.4	27.5	18.6	151	68
Figure 5.11	v2	5.1	35.8	23.6	363	66
15.85	hh	10.6	70.7	24.9	135	35
Figure 5.13	hv	9.1	40.8	17.2	89	42

There is great variation in the percentage decrease after unloading, which is expected to be due to differences in timing of the unloading. This shows how quickly G_{max} decreases in those first few minutes. Therefore, no quantified conclusions can be made regarding these values. Although, the fact that G_{max} does not return to its original value is interesting. As introduced earlier it has been shown that maintained suction in a sample can induce an increased effective stress, which could explain the remaining stiffness.

What is also interesting for several samples is that G_{max} drops immediately after unloading, but then increases again. For example, samples 1165 Shv and Shh, as shown in Figure 5.6. This is also seen in sample 1570 Sv2, Figure 5.11, which was unloaded after approximately three hours after EOP. The sample was then left to stand for 16 hours and it is seen that G_{max} gradually increased over this time. However, 1570 Sv1, which was unloaded after 22 hours and left for 48 hours, showed a more immediate increase in G_{max} and very slight increase over the 48 hours. For sample 1360 Sv, roughly half the expelled water was allowed back into the sample after unloading and then the burette was closed. Again, there was a gradual increase in G_{max} as seen in the previous section.

Pore pressure was measured for samples 1360 Shv and Shh as shown in Figure 5.7 and shows negative values as would be expected.

The gradual increase in stiffness after the burette is closed, as seen in sample 1360 Sv, 1570 Sv2 and 1570 Sv1, is hard to explain but is thought to be related to micro-structural changes due to suction in the sample. It has been shown that increased matrix suction is analogous to increased effective stress. It would be interesting to look into this further by way of measuring matrix suction after unloading has occurred.

6.2.8. *Constrained Modulus and Bulk Modulus*

The bottom half (~13.75 m) of the mini-block from 13.55-13.90 m was used for the measurement of P-wave velocity and the top half (~13.60 m) for S-wave velocity. The purpose was to try and calculate the constrained and bulk moduli, M and K respectively. As was seen from equations [2.2] to [2.4] in section 2.2, based on Hooke's law for an isotropic elastic material, if any two moduli are known then the Poisson's ratio (v) and Young's modulus (E) can be calculated.

The results are presented in Table 6.9 with limitations and discussions to follow. G and M are taken from the results (in bold), at 13.60 m and 13.75 m, respectively, from the unconfined (pre-consolidated) sample and after EOP (consolidated). Initially, the equations described in section 2.2 are used to calculate K, v and E.

Table 6.9: Summary of attempts to calculate Youngs modulus and Poisson's ratio of the clay

			Calculated using measured G and M			Calculated using K of water (K_w) and measured G			
Vertical	G_{vh} (MPa)	M_v (MPa)	K_v (MPa)	v_{vh} (-)	E_v (MPa)	K_w (MPa)	M (MPa)	v_{vh} (-)	E_v (MPa)
Unconfined	**6.42**	**25.67**	17.11	0.3332	17.1				
Consolidated	**36.45**	**800**	751.4	0.4917	108.7	2193	2241	0.4917	108.7
Horizontal	G_{hh}	M_h	K_h	v_{hh}	E_h	K_w	M	v_{hh}	E_h
Unconfined	**9.0**	**54.3**	42.3	0.4005	25.3				
Consolidated	**44.5**	**1000.0**	940.7	0.4832	132.5	2193	2252	0.4899	132.5

As expected the Youngs modulus and Poisson's ratio of the partially saturated, unconfined, drained sample (pre-consolidation) are low with v~0.3. It can be seen from the results in Figure 5.9 and Figure 5.10 that as pressure is applied to the sample and it approaches it's in-situ conditions with increased saturation, P-wave velocity increases dramatically as expected.

It is also seen that the stiffness resolution (due to the time resolution of 0.05 ms in the BE program, as described in section 6.1.1) is greatly influenced by the steep increase in the constrained modulus (M) as the sample is consolidated and approaches in-situ saturated conditions. This is because as the soil is consolidated to in-situ stresses it becomes closer to its "undrained" in-situ state and we know that the Poisson's ratio is 0.5, since it is controlled by water, which is incompressible. Therefore, theoretically M will be infinite. But since K is limited by the bulk modulus of water one could say that $M = K$ according to equation [2.4] with zero shear stiffness.

Using the values measured in the tests it is seen that the Poisson ratios are less than 0.5 and using the theory to calculate v_{hv} is not possible since it results in a value greater than 0.5.

These problems can be explained because there are several limitations to this technique:

- The constrained modulus, M is not really constrained in this case, since the triaxial sample can deform laterally. It is thought that perhaps in this case the bulk modulus is more appropriately placed in the place of M or a value somewhere between the two.

- In a fully saturated soil the P-wave velocity is controlled by the water in the soil and not the soil skeleton. As such the bulk modulus can be calculated as K=2193 MPa, the constrained modulus from that and the measured shear modulus, as done in last columns of Table 6.9. Even though this increases the Poisson's ratio, the relationships still not represent those outlined in section 2.2.
- It is known that there are different complex types pf P-waves that are dispersed through porous mediums in different ways, which could affect the results.
- It is possible that there is still gas in the sample that has not returned into solution, which would drastically reduce the bulk modulus of the clay.
- As was concluded in section 6.1.3 and 6.2.2 that the application of equations derived from a cross-anisotropic material model are not suitable for wave-propagation from a point source through a cylindrical triaxial sample.

As such, these results are considered inconclusive and require a further investigation beyond the scope of this study.

6.2.9. Stiffness Matrix

As seen in the previous section, whilst it has been possible to determine the anisotropic shear stiffness with some confidence from the SDMT results combined with the anisotropic properties found in the laboratory, the limitations to the P-wave results have deemed it not possible to calculate the vertical and horizontal values for the Youngs modulus or Poisson's ratio. As such this is beyond the scope of this study.

6.2.10. Sample Quality

As was shown in the results section 5.2.3, only the samples from 8.90 m were found to be of good to fair/acceptable quality, whilst the rest were of poor/disturbed quality. Since the samples had been in storage for 3-5 months, poor quality seems reasonable, but the differences are discussed further here. And as Amundsen et al. (2017) states it is the first 10 minutes that unloading effects are most important.

Effects of stress conditions

The only difference between these samples was in the estimation of in-situ stresses. That is, hydrostatic water conditions were used, which would result in lower effective stresses than the other samples which used lower than hydrostatic in-situ measurements. The choice of K_0 would also affect the estimate of stress levels by a significant degree and K_0 is a challenging parameter

to determine. Therefore, one should question the suitability of these sample quality procedures since they are based on quite subjective choices for estimates of applied effective stresses.

Top and bottom of the mini-block

Most of the samples are only just over the limit into poor/disturbed category. Samples from depths 13.60 m and 15.70 m are further over the limit (poorer quality). These were taken from the top of the mini-block samples. It is also clear in the G_{max} results that they show lower stiffness values. This implies that the effects of sample disturbance vary throughout the mini-block sample. Perhaps the sample disturbance reduces slightly from top to bottom since the bottom is slightly more confined by the weight of the sample above. Another possibility is that when the sample is pulled from the ground some pressure is exerted on the bottom of the block and whilst this is expected to directly disturb the bottom few cm of block, it could maintain some of the in-situ pressure in the bottom of the sample a little longer.

6.2.11. Voltage Changes

The amplitude of received voltage reduces drastically on application of pressure as shown in Figure 6.22. It was thought that perhaps the change in voltage of the output signal could give an indication of sample quality, but no correlation was found.

Bender elements are piezoelectric meaning a voltage is created when pressure is applied to the elements. It seems the pressure applied in the triaxial cell is applied to the elements and as such the received signal is masked by the background voltage.

It is apparent that during unloading the voltage immediately returns to its original value if the sample has access to water, whereas remains low if the burette is closed. Also, for sample 1360 Sv the voltage drops again when the burette is closed in a similar trend to the pore pressure. As such it is concluded that there is a relationship with the negative pore water pressure during unloading. It would be an interesting further study to see if there is any use in this voltage measurements in terms of imitating pore pressure behaviour in the clay.
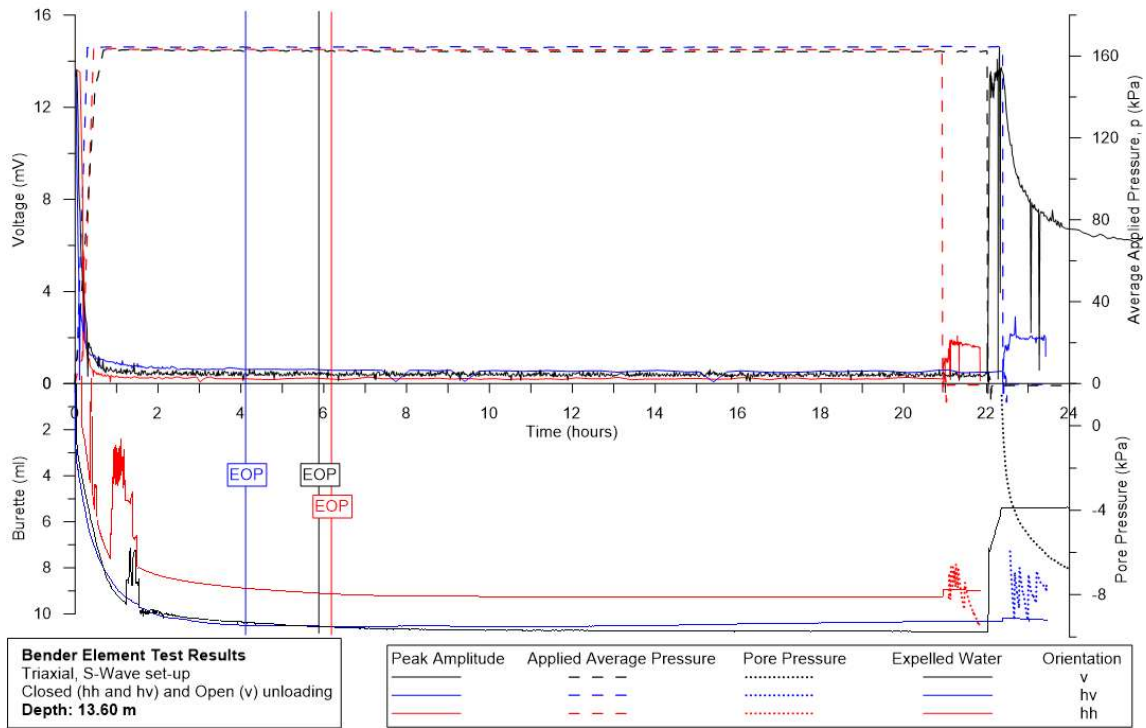
Figure 6.22: Voltage Changes during S-wave testing of Samples 1360 Sv, Shv and Shh.

6.2.12. Salt on BE Contacts

Although the voltage amplitude dropped dramatically during the test there were no problems with signal detection throughout this study. Nonetheless, application of a small amount of salt around the bender elements was tested. As seen in Figure 6.23, there is no apparent affect observed in the amplitude of the received signal.
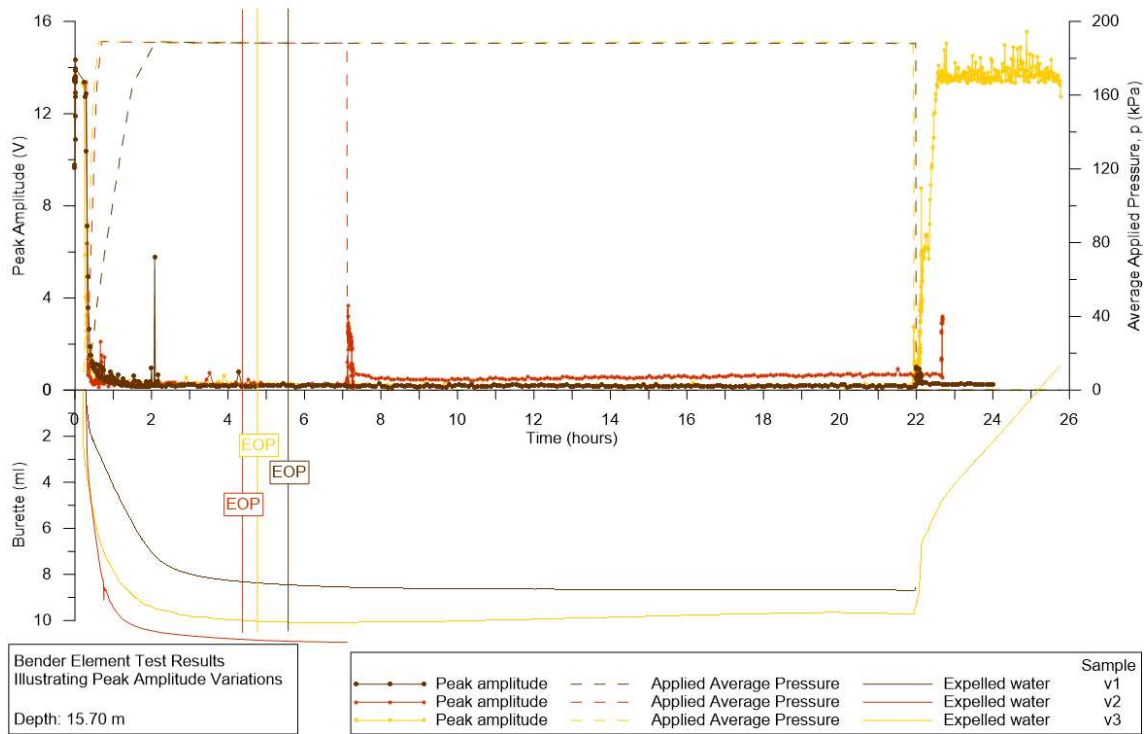
Figure 6.23: Comparison of use of salt on BE contact. Sample v2 has salt applied.

6.3. Results of Stand Alone Bender Element System on Half Mini-block Samples

Four half mini-blocks were tested. Outputs of the signals are presented in APPENDIX B – Details of Individual Bender Element Tests and examples are presented herein. The results are plotted against the pre-consolidation (unconfined) triaxial sample results from the same depth and presented in Figure 6.24 and Table 6.10.
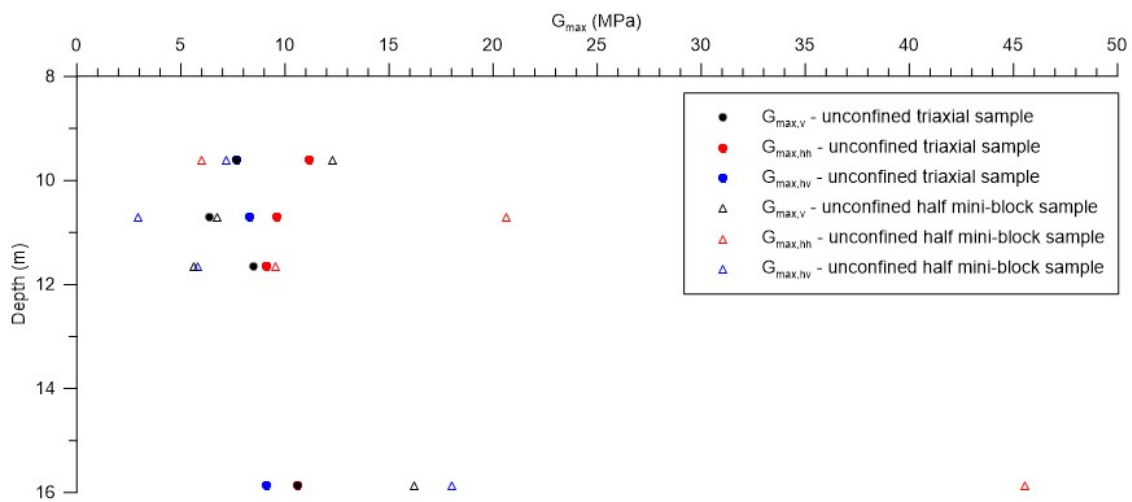
Figure 6.24: Plot of G_{max} from half mini-block samples

Table 6.10: Unconfined G_max measured from half-mini block sample compared to triaxial samples

Depth (m)	Orientation	Unconfined G_{max} (MPa)		Freq (kHz)	Wavelength, λ (mm)	d/λ
		Triaxial	Half Mini-block			
9.6	v	7.6	12.3	1.6	52	2.5
9.6	hh	11.1	6.0	1.6	36	3.7
9.6	hv	7.6	7.2	1.6	40	3.4
10.7	v	6.3	6.8	1.6	38	3.4
10.7	hh	9.6	20.7	1.6	67	2.0
10.7	hv	8.3	3.0	1.6	25	5.3
11.65	v	8.5	5.7	1.6	35	4.0
11.65	hh	9.1	9.6	1.6	45	2.9
11.65	hv	9.1	5.9	1.6	35	3.7
15.85	v	10.6	16.2	1.6	59	2.2
15.85	hh	10.6	45.6	1.6	99	1.4
15.85	hv	9.1	18.1	1.6	62	2.2

In Table 6.10 the calculated sample height to wavelength ratio (d/λ) has been calculated. All apart from one sample were above the suggested limit of d/λ>2 (Sanchez-Salinero et al., 1986) to eliminate the "near-field" effect. However, the first arrivals had to be interpreted manually as there were issues with what appeared to be the interference of P-wave by "near-field" effect. Examples are shown in Figure 6.25.
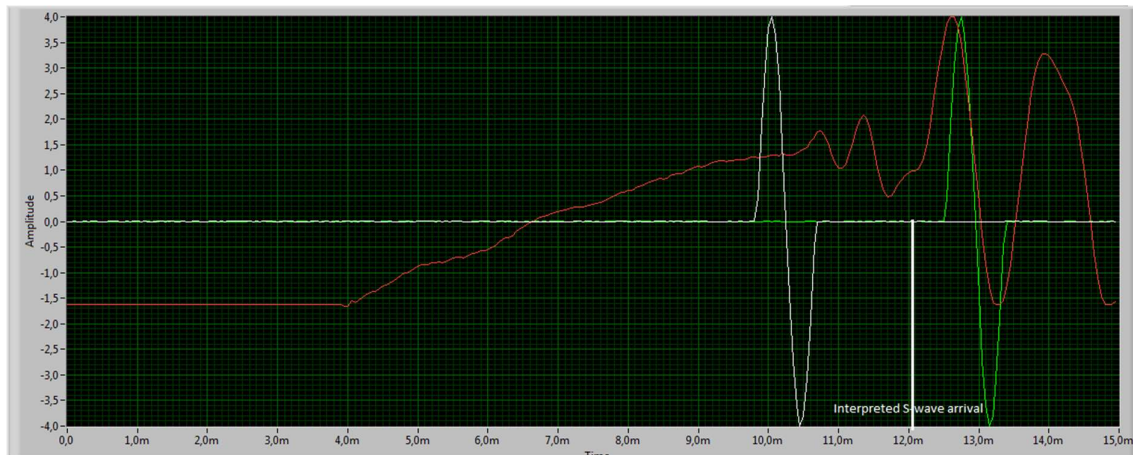
a)
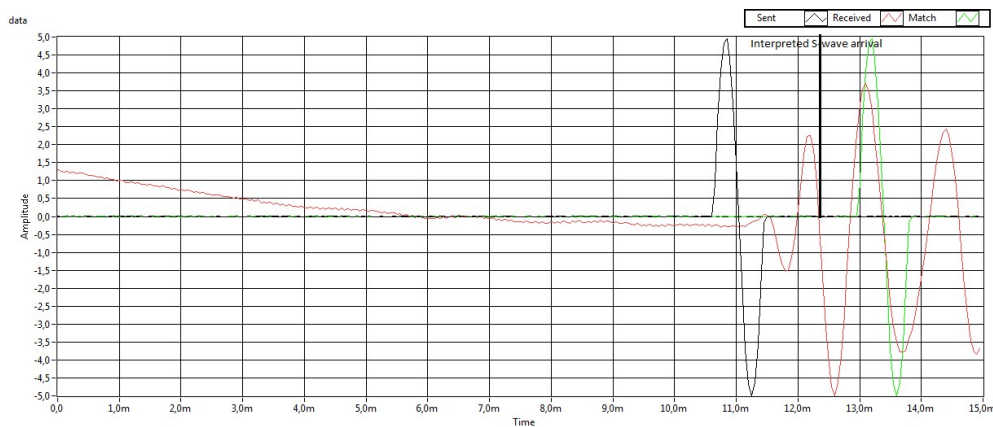
b)

Figure 6.25: Example of "near-field" effect due to P-wave interference from a half mini-block sample. a) 960 Shh and b) 1070 Shh

The results from the half mini-blocks are highly scattered and are considered unusable.

It is considered that since the samples are unconfined that the ratio of P- and S-waves is quite high (V_P/V_S) and that perhaps there is greater influence by the overall proportions of the sample. That is the half-mini block is roughly 1:1 height to width, so the P-wave reaches the receiver ahead or close to the S-wave, whereas in a triaxial sample with a roughly 2:1 ratio, the P-waves have far enough to travel not to interfere.

As such, it is noted here that when the triaxial samples were tested unconfined, the d/λ ratio ranged from 2.0-2.7 and there was no sign of the "near-field" effect. Therefore, it is proposed that the sample dimension ratio has more influence. Since there is no interference observed on the triaxial sample results, it is suggested that a 2:1 ratio is more suitable.

7.   Summary

7.1.   Summary and Conclusions

The stiffness of a soil is of great importance in many areas of geotechnical engineering. It forms the link between strain and stress, which is crucial in incremental numerical modelling. More specific to this study, the maximum shear stiffness (G_{max}) is the primary parameter used in small shear strain models, earthquake engineering and vibration assessments and for immediate working load settlement predictions. G_{max} is also used, in recent studies, to determine sample quality and is an important aspect for understanding what happens to a soil sample when it is unloaded and removed from its in-situ environment. Acquiring accurate values for G_{max} is problematic, particularly in the laboratory. Reduces stiffness is thought to be due to stress relief during unloading, which affects sample quality.

This study utilised mini-block samples taken from the Flotten quick clay at a Norwegian geotechnical test site near Tiller, Trondheim. Seven sample depths were tested with a bender element (BE) triaxial system to determine the shear stiffness properties in both the horizontal and vertical planes. The samples were tested before and during sample consolidation and during unloading to try to imitate the sampling process. Index parameters and grain size distributions were also determined for each mini-block sample. In addition, P-wave velocity was measured for one vertical sample and two horizontal samples from the same depth to determine the constrained modulus and hence elastic parameters of the clay, and S-wave velocity measurements were taken on unconfined half mini-blocks to determine effects of sample proportions. Vertical shear wave velocity results were supplied from a seismic dilatometer test (SDMT) carried out next to the sample hole. During the study many limitations were realised, but strong relationships in the results found.

The main limitation in this study comes from the accuracy of the shear wave and P-wave velocity output from the bender element system. It samples at a rate of 20 kHz, which results in a time resolution of 0.05 ms. The accuracy is studied and found to create maximum errors between 3 and 15 % for the shear modulus and between 7 and 150 % for the constrained modulus, increasing with shear velocity and P-wave velocity respectively. It was found that the errors in the shear modulus were overcome by the trend in the results, whilst the constrained modulus was deemed unusable but still formed some discussions.

The concept of the "near-field" effect was tested using half mini-block samples with a portable bender element set-up for S-wave propagation. The near-field effect is caused by the interference of P-waves due to transverse directivity between the sender and receiver elements.

It was found that even when the ratio between sample height and wavelength (d/λ) was kept below the suggest threshold of 2 (Sanchez-Salinero et al., 1986), there were still strong "near-field" effects deeming the results unusable. This "near-field" effect threshold was also checked for the triaxial samples by varying the input frequency and hence wavelength. It was found that even with a high ratio ($d/\lambda = 3.6$) interference from P-waves was absent. Therefore, a hypothesis is proposed that sample dimension ratio (d/w) has more influence and in this case 2:1 was suitable and 2:2 was not.

The bender element results showed strong anisotropy in the unconfined samples and after consolidation. This increased with consolidation suggesting an increase with effective confining pressure. After consolidation, small-strain shear stiffness in the horizontal plane (G_{hh}) was between 39 % and 72 % higher than in the vertical plane (G_{vh}). The origin of this anisotropy is considered, and it is concluded that whilst there is some influence by sample unloading (stress induced anisotropy) that there is also a relationship with clay content and the structure of the clay (inherent anisotropy) plays a significant role. As such, it seems reasonable to transfer this anisotropy from the BE results to the SDMT results.

The suitability of applying a cross-anisotropic elastic material model to a bender element test is brought into question in this study. In such a model the stiffness in the vertical plane should be equal ($G_{vh} = G_{hv}$) since there is no resistance to rotations in the vertical plane. However, it is found that there is a difference between stiffnesses in these orientations with G_{hv} 7-18 % lower than G_{vh}. It is concluded that since the shear wave comes from a point source and the shear wave is not transferred equally through the cylindrical sample that the cross-anisotropic elastic model is not suitable. A monoclinic material model is proposed which accounts for coupling effects from stiffnesses in other directions. The application of such a model is complex and beyond the scope of this study.

Relationships proposed in the literature between G_{max} with effective stress (p') and index parameters were applied to the BE and SDMT results. Whilst the relationships fit well and confirm high dependence on void ratio, it is challenging to determine correct stress exponents and soil characteristic parameters and as such using these in prediction of stiffness remains problematic. The effect of geological age was applied to the BE results and found to give good approximations to the SDMT results.

Unloading of the samples was carried out to try to imitate the effects of sampling procedures on the clay. One sample was allowed access to water on unloading and returned to its original state as was expected. The sample was allowed to take in more water than was expelled in the consolidation phase and its shear stiffness reduced further. A second sample

was allowed to take in only half the expelled water. Even so the stiffness dropped almost back to its original unconfined value. Several samples were closed to water immediately after unloading and the stiffness was found to remain much higher. This concludes water access during sampling plays a huge role in sample quality.

Sample quality was determined for the triaxial samples in this study based on the three techniques: change in volumetric strain ($\Delta\varepsilon_{vol}$) proposed by Andresen and Kolstad (1979), change in void ratio ($\Delta e/e_0$) proposed by Lunne et al. (2006) and ratio of shear velocity measured on a sample in the field to the in-situ measurement ($v_{S,vh}/v_{SCPTU}$) proposed by Landon et al. (2007). All but three samples were found to be poor to very poor quality. The three samples at 8.90 m were of acceptable quality and were imposed to stress conditions calculated using assumed hydrostatic pore pressure conditions and K_0 of 0.5, as opposed to the in-situ under-hydrostatic pore pressure measurements and K_0 of 0.7 used for other samples. The consolidation rate was also found to influence the amount of water expelled from the clay. It is suggested that since there are many subjective choices in the consolidation phase of a triaxial test that techniques based on expelled water should be used with caution. The technique using shear wave velocities appears more suitable. Samples were also classified as poor using this technique, but the unconfined measurements were taken on trimmed triaxial samples, not straight out of the ground and field measurements were based on seismic dilatometer test results, not seismic cone penetrometer test results. Variation of sample quality was found to be lower for samples taken from the top of a mini-block than those taken from the bottom, which is thought to be due to variations in stress relief throughout the mini-block sample.

P-wave velocity measurements were taken at one sample depth. The limitations from the accuracy of the bender element system and from the complexity of P-wave propagation through the sample deemed the results inconclusive.

7.2.   Recommendations for further work

One of the biggest limitations of this study has been the time resolution in the travel time output by the bender element program. If this set-up is used again, it is recommended that the program is modified with a higher sampling rate. It would also be preferable to use the zero-cross over method, which would eliminate the errors due to frequency change during the consolidation procedure. Although care would have to be taken when other interference from outside sources such as the anti-friction motor.

Since it is clear from the bender element results that the clay at Flotten has inherent anisotropic stiffness properties that relates to the clay content, it would be interesting to investigate to what extent this anisotropic nature is due to unloading of the clay and what is present in-situ. As such an in-situ technique such as a cross-hole seismic survey is suggested along with bender element tests on samples of a younger age than this study. This could be combined with portable bender element tests on samples straight out of the ground.

It is concluded that since the shear wave comes from a point source and the shear wave is not transferred equally through the cylindrical sample that the cross-anisotropic elastic model is not suitable. A monoclinic material model is proposed which accounts for coupling effects from stiffnesses in other directions. This should be investigated further with an attempt to model the propagation of shear waves through a triaxial sample.

The relationships between G_{max} and confining effective pressure (p') seem to be well covered in the literature, and the relationships show trends that fit well to G_{max} profiles. However, in order to use these as estimates of G_{max} for geotechnical engineering problems it is vital that the choice of parameters such as the soil characteristic parameter (S) and the stress exponent (n) are correct. It would be interesting to investigate these parameters with regards to Norwegian clays to see if standard values could be used.

Simulation of sampling conditions has been interesting but would be much more conclusive if accurate measurements of pore pressure and sample dimensions could be taken throughout the tests. As such a study using more advanced triaxial equipment would be advantageous. It is also notices that voltage amplitude recorded by the receiver element has a relationship with pore pressure after unloading of the sample, so further tests could be carried out to see if there is a quantifiable relationship such that voltage amplitude changes can be used to measure pore pressure.

Based on the sample quality findings described in the conclusions it would be interesting to investigate the three techniques of sample disturbance measurements on fresh samples taken at the same site using the same stress calculations used in this study and varying the K_0 value used to see how much influence this has both on supposed sample quality and measured small strain shear modulus. This could incorporate an investigation into the finding that there is variation in sample quality between the top and bottom of the mini-block samples.

Bibliography

Abrahamson, N. A., & Litehiser, J. J. (1989). Attenuation of vertical peak acceleration. *Bulletin of the Seismological Society of America, 79*(3), 549-580.

Amundsen, H. A., Jønland, J., Emdal, A., & Thakur, V. (2017). An attempt to monitor pore pressure changes in a block sample during and after sampling. *Géotechnique Letters, 7*(2), 119-128. doi:10.1680/jgele.16.00176

Andresen, A., & Kolstad, P. (1979). *The NGI 54 - mm samplers for uninterrupted sampling of clays and representative sampling of coarser materials.* Paper presented at the Proceedings of the International Symposium of Soil Sampling, State of the Art on Current Practice of Soil Sampling.

Arroyo, M. (2001). *Pulse tests in soil samples.* University of Bristol UK,

Atkinson, J. H., & Sallfors, G. (1991). *Experimental determination of soil properties.* Paper presented at the 10th ECSMFE.

Benz, T. (2007). *Small-strain stiffness of soils and its numerical consequences* (Vol. 5): Univ. Stuttgart, Inst. f. Geotechnik Stuttgart.

Bjerrum, L. (1967). Engineering Geology of Norwegian Normally-Consolidated Marine Clays as Related to Settlements of Buildings. *Géotechnique, 17*(2), 83-118. doi:10.1680/geot.1967.17.2.83

Bullen, K. E. (1953). An introduction to the theory of seismology, ed. 2. 296.

Chang, F. K., & Krinitzsky, E. L. (1977). *State-of-the-art for assessing earthquake hazards in the United States; Report 8, Duration, spectral content, and predominant period of strong motion earthquake records from Western United States* (Vol. 73-1): U. S. Army Corps of Engineers, Waterways Experiment Station, Soils and Pavement Laboratory, Vicksburg, MS, United States.

Dogangun, A., & Livaoglu, R. (2006). A comparative study of the design spectra defined by Eurocode 8, UBC, IBC and Turkish Earthquake Code on R/C sample buildings. *Journal of Seismology, 10*(3), 335-351. doi:10.1007/s10950-006-9020-4

Donohue, S., & Long, M. (2010). Assessment of sample quality in soft clay using shear wave velocity and suction measurements. *Géotechnique, 60*(11), 883-889. doi:10.1680/geot.8.T.007.3741

Dyvik, R., & Madshus, C. (1985). *Laboratory Measurement ofG max Using Bender Elements.* Paper presented at the Proceedings of ASCE Annual Convention: Advances in the Art of Testing Soils under Cyclic Conditions, Detroit. Google Scholar.

Eiksund, G. (2017). *Response Spectra Lecture. BA8305 Geodynamics, Part 1.*

Emdal, A., Gylland, A., Amundsen, H. A., Kåsin, K., & Long, M. (2016). Mini-block sampler. *Canadian Geotechnical Journal, 53*(8), 1235-1245. doi:10.1139/cgj-2015-0628

Finn, W. D. L. (2000). State-of-the-art of geotechnical earthquake engineering practice. *Soil Dynamics and Earthquake Engineering, 20*(1), 1-15.

GDS. Bender Element Technical Specification.

Griffiths, S. C., Cox, B. R., & Rathje, E. M. (2016). Challenges associated with site response analyses for soft soils subjected to high-intensity input ground motions. *Soil Dynamics and Earthquake Engineering, 85*, 1-10. doi:10.1016/j.soildyn.2016.03.008

Gylland, A., Long, M., Emdal, A., & Sandven, R. (2013). Characterisation and engineering properties of Tiller clay. *Engineering Geology, 164*, 86-100.

Gylland, A. S., Rueslåtten, H., Jostad, H. P., & Nordal, S. (2013). Microstructural observations of shear zones in sensitive clay. *Engineering Geology, 163*, 75-88.

Hanks, T. C., & McGuire, R. K. (1981). The character of high-frequency strong ground motion. *Bulletin of the Seismological Society of America, 71*(6), 2071-2095.

Hardin, B. O. (1978). NATURE OF STRESS-STRAIN BEHAVIOR FOR SOILS. *v*(1), 3-90.

Hardin, B. O., & Drnevich, V. P. (1973). 36. Shear modulus and damping in soils: measurement and parameter effects: B. O. Hardin and V. P. Drnevich.Proceedings of American Society of Civil Engineers, Journal of the Soil Mechanics and Foundations Division. 98 (SM6), 603–624 (1972); 25 ref., 17 fig. *Journal of Terramechanics, 9*(2), 102.

Hardin, B. O., & Richart, J., FE. (1963). Elastic wave velocities in granular soils. *Journal of Soil Mechanics & Foundations Div, 89*(Proc. Paper 3407).

ICBO. (1994). Uniform Building Code, 1991. In *International Conference of Building Officials*. Whittier, California.

ISO. (2004a). Geotechnical investigation and testing - Laboratory testing of soil. In *Part 12: Determination of Atterberg limits*. International Organization for Standardization, Switzerland.

ISO. (2004b). Geotechnical investigation and testing - Laboratory testing of soil. In *Part 9: Consolidated triaxial compression tests on water-saturated soil.* International Organization for Standardization, Switzerland.

ISO. (2014a). Geotechnical investigation and testing - Laboratory testing of soil. In *Part 1: Determination of water content*. International Organization for Standardization, Switzerland.

ISO. (2014b). Geotechnical investigation and testing - Laboratory testing of soil. In *Part 2: Determination of bulk density*. International Organization for Standardization, Switzerland.

ISO. (2015). Geotechnical investigation and testing - Laboratory testing of soil -. In *Part 3: Determination of particle density*. International Organization for Standardization, Switzerland.

ISO. (2017). Geotechnical investigation and testing - Laboratory testing of soil. In *Part 6: Fall cone test*. International Organization for Standardization, Switzerland.

Janbu, N. (1963). *Soil compressibility as determined by odometer and triaxial tests.* Paper presented at the Proc. Europ. Conf. SMFE.

Janbu, N. (1978). *Prinsipper og tolkningsmetoder for in situ måling av jordartsparametre = Principles and methods of interpretation related to in-situ measurement of soil parameters*. Trondheim: Tapir.

Karlsson, M., Emdal, A., & Dijkstra, J. (2016). Consequences of sample disturbance when predicting long-term settlements in soft clay. *Canadian Geotechnical Journal, 53*(12), 1965-1977. doi:10.1139/cgj-2016-0129

Kawaguchi, T., Mitachi, T., & Shibuya, S. (2001). *Evaluation of shear wave travel time in laboratory bender element test.* Paper presented at the Proceedings of the International Conference on Soil Mechanics and Geotechnical Engineering.

Kaynia, A. (2017). *Lecture Notes Part 3, PhD course BA8305, Geodynamics.*: Geotechnical Group, NTNU.

Kramer, S. (2017). *Lecture Notes Part 2, PhD course BA8305, Geodynamics.*: Geotechnical Group, NTNU.

Kramer, S. L. (1996). *Geotechnical Earthquake Engineering*: Prentice Hall, Upper Saddle River, New Jersey.

L'Heureux, J. S., Long, M., Vanneste, M., Sauvin, G., Hansen, L., Polom, U., . . . Janbu, N. (2013). On the prediction of settlement from high-resolution shear-wave reflection seismic data: The Trondheim harbour case study, mid Norway. *Engineering Geology, 167*, 72-83.

L'Heureux, J.-S., & Long, M. (2017). Relationship between Shear-Wave Velocity and Geotechnical Parameters for Norwegian Clays. *Journal of Geotechnical and Geoenvironmental Engineering, 143*(6), 04017013. doi:10.1061/(ASCE)GT.1943-5606.0001645

Landon, M. M., DeGroot, D. J., & Sheahan, T. C. (2007). Nondestructive Sample Quality Assessment of a Soft Clay Using Shear Wave Velocity. *Journal of Geotechnical and Geoenvironmental Engineering, 133*(4), 424-432. doi:10.1061/(ASCE)1090-0241(2007)133:4(424)

Lee, J.-S., & Santamarina, J. C. (2005). Bender Elements: Performance and Signal Interpretation. *Journal of Geotechnical and Geoenvironmental Engineering, 131*(9), 1063-1070. doi:10.1061/(ASCE)1090-0241(2005)131:9(1063)

Leong, E. C., & Cheng, Z. Y. (2016). Effects of Confining Pressure and Degree of Saturation on Wave Velocities of Soils. *International Journal of Geomechanics, 16*(6), D4016013. doi:10.1061/(ASCE)GM.1943-5622.0000727

Leroueil, S., & Hight, D. W. (2003). *Behavior and properties of natural soils and soft rocks.* Paper presented at the International Workshop on Characterisation and Engineering Properties of Natural Soils, Rotterdam, Netherlands.

Lindgård, A., & Ofstad, C. S. (2017). *Field and Laboratory Investigations to Evaluate the Coefficient of Earth Pressure at Rest - NGTS Flotten Quick Clay Test Site.* (Masters), Norwegian University of Science and Technology, (16600)

Lunne, T., Berre, T., Andersen, K. H., Strandvik, S., & Sjursen, M. (2006). Effects of sample disturbance and consolidation procedures on measured shear strength of soft marine Norwegian clays. *Canadian Geotechnical Journal, 43*(7), 726-750. doi:10.1139/t06-040

Newmark, N. M., & Hall, W. J. (1982). *Earthquake spectra and design* (Vol. 3): Earthquake Eng. Res. Inst., Berkeley, CA, United States.

NGF. (2011). Veiledning for symboler og definisjoner i geoteknikk. Identifisering og klassifisering av jord. In *Meldng Nr. 2 utgitt 1982, Revidert 2011*.

NGI. (2017). Norwegian GeoTest Sites (NGTS) Factual Report, Tiller Flotten Research Site. *20160154-19-R*(0 / 2017-03-28).

NGU. (2018). Nasjonal løsmassedatabase dekningoversikt / National soils deposit database coverage map. from Norges geologiske undersøkelse / Geological Survey of Norway

Nordal, S. (2017). *Lecture Notes Part 1, PhD course BA8305 Geodynamics*: Geotechnical Group, NTNU.

Norge, S. (1982). Geoteknisk prøving - Laboratoriemetoder. In *Støtflytegrensen*. Standard Norge, Lysaker.

Norge, S. (1990). Geoteknisk prøving - Laboratoriemetoder. In *Kornfordelingsanalyse av jordprøver*. Standard Norge, Lysaker.

Norge, S. (2004). Eurocode 8: Design of structures for earth quake resistance, Part 1: General rules, seismic acrions and rules for buildings. In.

NTNU. (2015). *MSc Course TBA4110 - Geotechnical Field and Laboratory Investigations*. Trondheim: Geotechnical Division, Norwegian University of Science and Technology.

NVE. (2018). Kvikkleire Riskosoner og Skredhendelser / Quick Clay Hazard Zones and Landslide Events.

Pennington, D. S., Nash, D. F., & Lings, M. L. (2001). Horizontally mounted bender elements for measuring anisotropic shear moduli in triaxial clay specimens. *Geotechnical Testing Journal, 24*(2), 133-144.

Pitilakis, K., Riga, E., & Anastasiadis, A. (2012). Design spectra and amplification factors for Eurocode 8. *Bulletin of Earthquake Engineering, 10*(5), 1377-1400. doi:10.1007/s10518-012-9367-6

PLAXIS (Producer). (2017). Material Models Manual. *Build 8601*.

Presti, D. L., Pallara, O., Lancellotta, R., Armandi, M., & Maniscalco, R. (1993). Monotonic and cyclic loading behavior of two sands at small strains. *Geotechnical Testing Journal, 16*(4), 409-424.

Ridley, A. M., Dineen, K., Burland, J. B., & Vaughan, P. R. (2003). Soil matrix suction: some examples of its measurement and application in geotechnical engineering. *Géotechnique, 53*(2), 241-253. doi:10.1680/geot.2003.53.2.241

Rognlien, P. (2017). *Time Effect in Ordinary Sherbrooke Block Sampler contra Mini-block Sampler.* (Masters), Norwegian University of Science and Technology,

Sanchez-Salinero, I., Roesset, J., & Stokoe, K. (1986). Near-field effects on determination of propagation velocities of body waves. In *SEG Technical Program Expanded Abstracts 1986* (pp. 129-131): Society of Exploration Geophysicists.

Schott, C., & Schwarz, J. (2004). *RELIABILITY OF EUROCODE 8 SPECTRA AND THE PROBLEMS OF THEIR APPLICATION TO CENTRAL EUROPEAN EARTHQUAKE REGIONS*. Paper presented at the 13th World Conference on Earthquake Engineering, Vancouver, B.C., Canada.

Seed, H. B., Ugas, C., & Lysmer, J. (1976). Site-dependent spectra for earthquake-resistant design. *Bulletin of the Seismological Society of America, 66*(1), 221-243.

Shibuya, S., Tatsuoka, F., Teachavorasinskun, S., Kong, X. J., Abe, F., Kim, Y. S., & Park, C. S. (1993). Elastic deformation properties of geomaterials: Shibuya, S; Tatsuoka, F; Teachavorasinskun, S; Kong, X J; Abe, F; Kim, Y S; Park, C S Soils Found V32, N3, Sept 1992, P26–46. *International Journal of Rock Mechanics and Mining Sciences & Geomechanics Abstracts, 30*(4), A214.

Shirley, D. J., & Hampton, L. D. (1978). Shear-wave measurements in laboratory sediments. *The Journal of the Acoustical Society of America, 63*(2), 607-613.

Tanaka, H., Sharma, P., Tsuchida, T., & Tanaka, M. (1996). Comparative study on sample quality using several types of samplers. *Soils and Foundations, 36*(2), 57-68.

Thakur, V., L'Heureux, J.-S., & Locat, A. (2017). Landslide in Sensitive Clays – From Research to Implementation. In V. Thakur, J.-S. L'Heureux, & A. Locat (Eds.), *Landslides in Sensitive Clays: From Research to Implementation* (pp. 1-11). Cham: Springer International Publishing.

Tonouchi, K., Sakayama, T., & Imai, T. (1982). S wave velocity in the ground and the damping factor. *Bulletin of the International Association of Engineering Geology - Bulletin de l'Association Internationale de Géologie de l'Ingénieur, 26*(1), 327-333. doi:10.1007/bf02594237

Torrance, J. K. (2017). Chemistry: An Essential Key to Understanding High-Sensitivity and Quick Clays and to Addressing Landslide Risk. In V. Thakur, J.-S. L'Heureux, & A. Locat (Eds.), *Landslides in Sensitive Clays: From Research to Implementation* (pp. 35-44). Cham: Springer International Publishing.

Towhata, I. (2008). *Geotechnical earthquake engineering*: Springer Science & Business Media.

Verdugo, R., & Peters, G. (2017). *SEISMIC SOIL CLASSIFICATION AND ELASTIC RESPONSE SPECTRA*. Paper presented at the 16th World Conference on Earthquake Engineering, Santiago Chile.

Vucetic, M., & Dobry, R. (1991). Effect of Soil Plasticity on Cyclic Response. *Journal of Geotechnical Engineering, 117*(1), 89-107. doi:10.1061/(ASCE)0733-9410(1991)117:1(89)

Wang, Y., Lo, K., Yan, W., & Dong, X. (2007). Measurement biases in the bender element test. *Journal of Geotechnical and Geoenvironmental Engineering, 133*(5), 564-574.

Yamashita, S., Hori, T., & Suzuki, T. (2006). Anisotropic Stress-Strain Behavior at Small Strains of Clay by Triaxial and Bender Element Tests. *Geomechanics II*. doi:doi:10.1061/40870(216)4

10.1061/40870(216)4

Yang, J. (2000). Influence of water saturation on horizontal and vertical motion at a porous soil interface induced by incident P wave. *Soil Dynamics and Earthquake Engineering, 19*(8), 575-581.

Full List of Figures

127

Full List of Tables

APPENDIX A – Bender Element Specifications

World leaders in the manufacture of laboratory systems for soil & rock

Bender Element System (BES)

The GDS Bender Element system enables easy measurement of the maximum shear modulus of a soil at small strains in a triaxial cell. Measurement of soil stiffness at very small strains in the laboratory is difficult due to insufficient resolution and accuracy of load and displacement measuring devices. The capability exists to regularly carry out measurements of small strain stiffness in the triaxial apparatus using local strain transducers, but this can be expensive and is generally confined to research projects.

The addition of Bender Elements to a triaxial testing system makes the routine measurement of Gmax, maximum shear modulus, simple and cost effective.

Key Features:	Benefits to the User:
USB interface:	Allows the system to be swapped to any PC in the lab with a USB interface.
Titanium element inserts:	Reduces the weight of the top-cap.
Utilising existing products:	Pedestals and top-caps can be made for other manufacturers' cells as well as GDS cells, so upgrading is potentially simple.
The GDS Bender elements are bonded into a standard insert:	This makes the bender element insert a modular device that can then be easily fitted into a suitably modified pedestal/top-cap. Should an element fail, it is simple and quick for the complete insert to be replaced by the customer
2 Mega Samples/Second, 16bit Data Acquisition:	High speed data acquisition is essential as the sample interval provides the resolution for determining wave speeds.
Elements are manufactured to allow S and P wave testing to be performed:	Determining both S & P wave velocities allows additional specimen parameters to be calculated, such as Youngs Molulus, E.
Vertical and horizontal elements are available:	Specimen anisotropy can be studied with the use of both vertical and horizontal elements on the sample.

Tests that can be Performed:

Determination of Shear Wave Velocity, determination of P-Wave Velocity, vertically propogating horizontally polarised (vertical elements), horizontally propogating horizontally polarised (horizontal elements), horizontally propogating vertically polarised (horizontal elements).

Upgrade Options:

- Combined pedestals for unsaturated testing and bender elements (ie with bonded high air entry porous disc).

Technical Specification:

Data acquisition speed:	2,000,000 samples/second, simultaneous sampling of both source and received signals.
Resolution of data acquisition (bits):	16
Computer Interface:	USB
Available gain ranges for data acquisition:	From x10 to x500
Operating Temperature:	-10°C to 50°C
Sample Sizes:	Up to 300mm

www.gdsinstruments.com

APPENDIX B – Details of Individual Bender Element Tests

Described by block, roughly in the order carried out. Correct order was shown in Table 4.4.

Mini-block 8.75-9.05 m

On initial inspection this mini-block contained several silt layers as illustrated in Figure C.1.

Figure C.1: Mini-block showing dark, silt layers

The bottom half, approximately 8.85-8.95 m was used for testing S-wave velocities (v_{Sv}, v_{Shh} and v_{Shv}). The mini-bock was not tested with the stand-alone bender element system.

<u>*Index Tests*</u>

Results are presented in Table C.1. The properties highlighted in bold indicate behaviour of a quick clay. However, the remoulded shear strength (s_r) is only slightly greater than 0.5 kPa, the definition by NGF (2011), it is not strictly defined as a quick clay, which may be since it is just below the transition zone. It should be noted that these were the first index tests to be carried out, so there may have been some human errors, which is likely to be the reason for the erroneous value of degree of saturation (S_r).

Table C.1: Index test results for mini-block depth 8.85-9.05 m

Density, ρ (g/cm3)	1.83
Unit weight, γ (kN/m3)	17.98
Water Content, w (%)	**47.2**
Plastic Limit, w_P (%)	24.9
Liquid Limit, w_L (%)	**34.6**
Plasticity, I_P (%)	9.8
Porosity, n (%)	55.9
Degree of saturation, S_r (-)	1.05*
Salt content, S (g/l)	**1.0**
Falling Cone - Undrained shear strength, s_u (kPa)	38.7
Falling Cone - Remoulded shear strength, s_u (kPa)	0.7
Sensitivity, S_t (-)	**59.0**

Sample 890 Sv

This vertically cut triaxial sample was consolidated to anisotropic conditions. Since this test was carried out before index test results were complete, a unit weight of 19 kN/m³ was used for the stress calculations, which was higher than later samples. Also, a K_0 value of 0.5 was used to calculate the in-situ horizontal stresses, which was later reviewed after reading of literature (Lindgård & Ofstad, 2017). Discussions with supervisors at the Geotechnical Departments at NTNU also led to the conclusion that 0.5 may lead to higher shear levels than would really exist in-situ.

The sample was consolidated at a rate of 2 kPa every 2 minutes to a cell pressure of 53.4 kPa and added vertical pressure of 26.7 kPa. This cell pressure was too much and should have been 40.1 kPa in order to give comparable average applied pressure to the other two tests. The sample was then left to consolidate overnight. According to the ISO standards (ISO, 2004b) EOP was reached after 5.5 hours. After 23 hours the cell pressure was reduced to zero and the vertical load removed. The burette was closed immediately and the triaxial software was stopped. The triaxial cell was then drained and a final unloaded measurement was taken.

At this stage in the study program the bender element software only allowed velocity readings to be taken manually, so readings were taken at approximately four-minute intervals during application of pressure, then intervals were lengthened. It was also necessary to take

snapshots of the readings/waveforms. This was both for quality control and to be able to manually pick the first arrivals. Manual picks were carried out for this test and the next two. It was then realised that this was too big a task for whole project.

Sample 890 Shh

- Horizontally cut, BE perpendicular to the bedding planes
- Consolidated to isotropic average stress conditions.
- Silt layer through the centre as seen in Figure C.2.

Figure C.2: Photos of Sample 890 Shh

- Consolidated at a rate of 2 kPa every 2 minutes
- Cell pressure of 53.4 kPa
- Vertical pressure of 5 kPa to maintain good contacts with the bender elements
- EOP 5.9 hours
- Unloaded 23 hours
- Burette closed immediately after unloading
- Triaxial software was stopped.
- final unloaded measurement was taken.

Sample 890 Shv

- Horizontally cut, BE parallel to the bedding planes
- Consolidated to isotropic average stress conditions.

- No obvious layering

- Consolidated at a rate of 2 kPa every 2 minutes

- Cell pressure of 53.4 kPa

- Vertical pressure of 5 kPa to maintain good contacts with the bender elements

- EOP 5.8 hours

- Unloaded 23 hours

- Burette closed immediately after unloading

- Triaxial software was stopped.

- final unloaded measurement was taken.

Figure C.3: Photos of Sample 890 Shv

Mini-block 9.40-9.75 m

On initial inspection this mini-block contained some silt layers. The bottom half, approximately 9.55-9.65 m was used for testing S-wave velocities (v_{Sv}, v_{Shh} and v_{Shv}) both on half a mini-block and then triaxial sample were trimmed and tested.

Half Mini-block Results

The mini-bock was tested with the stand-alone bender element system. Resulting output signals are presented in Figure C.4. Some results were manually interpreted. It is though that the output image for the vertical test is actually from the previous triaxial test so is not included in the results.

a)

b)

c)

Figure C.4: Output results for half mini-block test at 9.60m for a) S_v b)S_{hh} and c) S_{hv}.

B.V

Index tests were carried out after the block had been sub-divided and are presented in Table C.2. The properties highlighted in bold indicate behaviour of a quick clay.

Table C.2: Index test results for mini-block depth 9.40-9.75 m

Density, ρ (g/cm3)	1.78
Unit weight, γ (kN/m3)	17.43
Water Content, w (%)	**46.2**
Plastic Limit, w_P (%)	24.5
Liquid Limit, w_L (%)	**35.6**
Plasticity, I_P (%)	11.1
Porosity, n (%)	57.3
Degree of saturation, S_r (-)	0.98
Salt content, S (g/l)	**0.9**
Falling Cone - Undrained shear strength, s_u (kPa)	52.6
Falling Cone - Remoulded shear strength, s_u (kPa)	**0.4**
Sensitivity, S_t (-)	**124.3**

Sample 960 Sv

- Vertically cut
- One silt layer at the base
- Consolidated to anisotropic average stress conditions using K_0= 0.7 and γ=18 kN/m^3. Cell pressure of 106.2 kPa, vertical pressure of 16.6 kPa. Some slight mistake with proportion of stresses but led to similar average stress to the other 2 samples.
- Consolidation rate 2 kPa / min
- EOP 5.2 hours
- Unloaded 21 hours
- Burette closed immediately after unloading
- Triaxial software was stopped.
- Final unloaded measurement was taken.
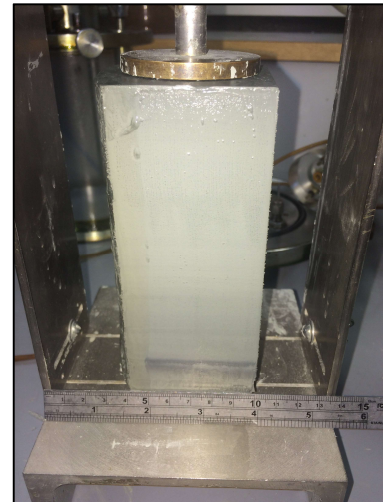
Sample 960 Shh

- Horizontally cut, BE perpendicular to the bedding planes
- Consolidated to isotropic average stress conditions.
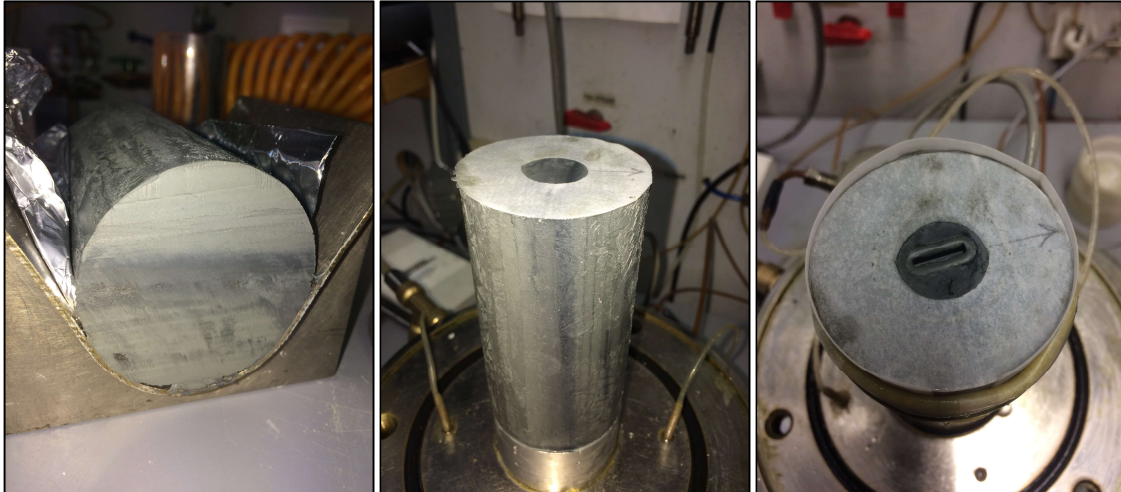- One silt layer at the edge
- Consolidated at a rate of 2 kPa every 2 minutes
- Cell pressure of 106.2 kPa, vertical pressure of 5 kPa to maintain good contacts with the bender elements
- EOP 4.8 hours
- Unloaded 22 hours
- Burette closed immediately after unloading
- Triaxial software was stopped.
- No final unloaded measurement was taken.
- NOTE: Triaxial software crashed at 12:56, but files were recovered and combined.
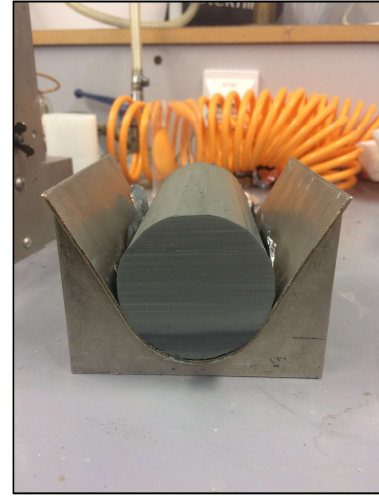
Sample 960 Shv

- Horizontally cut, BE parallel to the bedding planes
- No obvious silt layers
- Consolidated as above
- EOP 4.4 hours
- Unloaded 22 hours
- Burette closed immediately after unloading
- Triaxial software was stopped.
- Final unloaded measurement was taken.
- NOTE: The bender element software was updated to automatically take measurements as regular intervals and output images of the output signal.
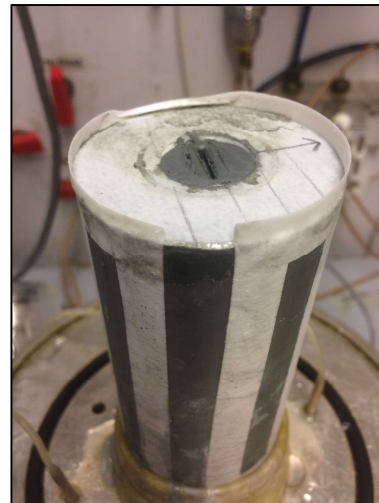
Mini-block 10.45-10.80 m

On initial inspection this mini-block contained some silt layers. The bottom half, approximately 10.65-10.75 m was used for testing S-wave velocities (v_{Sv}, v_{Shh} and v_{Shv}) both on half a mini-block and then triaxial sample were trimmed and tested.

Half Mini-block Results

The mini-bock was tested with the stand-alone bender element system. Resulting output signals are presented in Figure C.5. These were very hard to interpret but first arrivals of S-waves are interpreted as shown from the change in wave form.
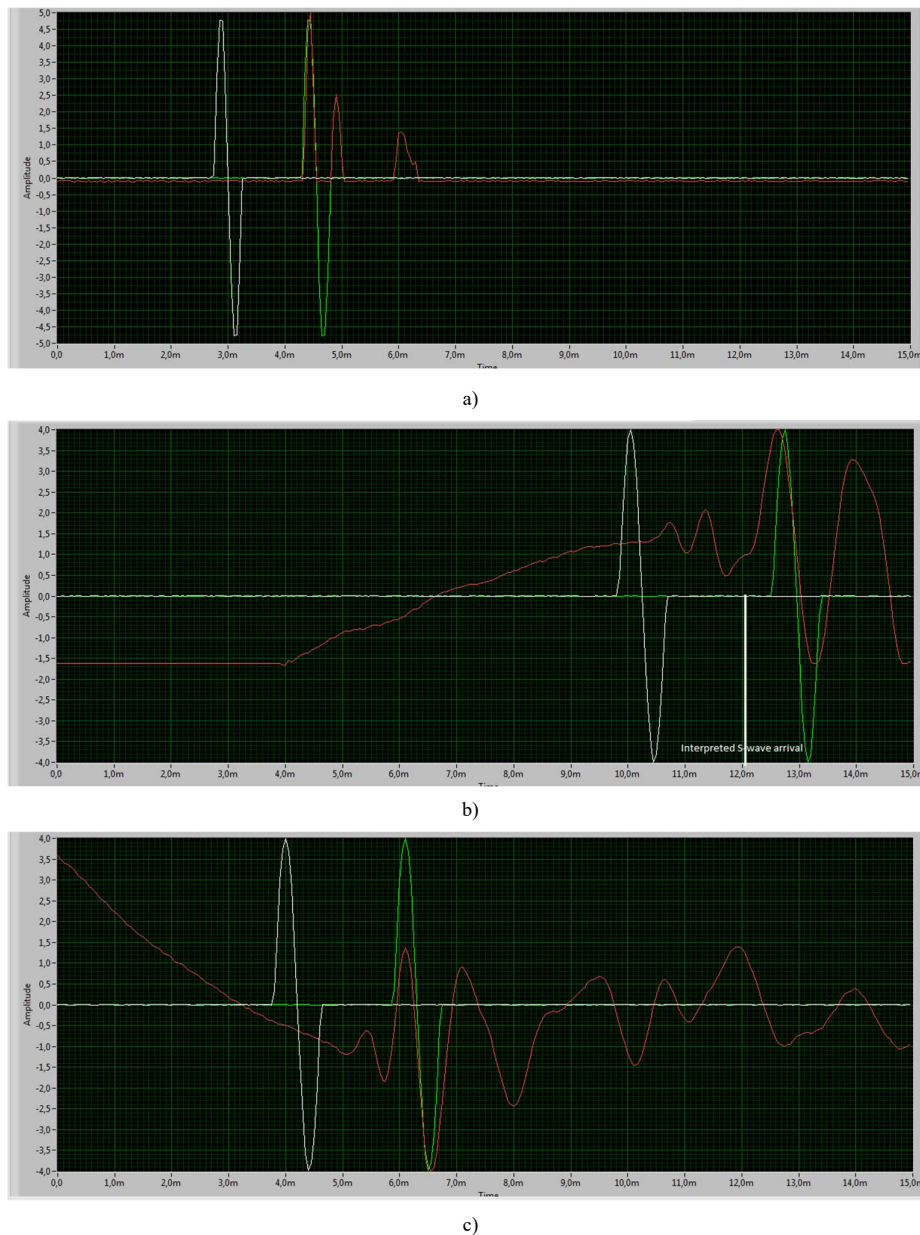

Figure C.5: Output results for half mini-block test at 10.70m for a) S_v b)S_{hh} and c) S_{hv}.

Index tests were carried out after the block had been sub-divided and are presented in Table C.3. The properties highlighted in bold indicate behaviour of a quick clay.

Table C.3: Index test results for mini-block depth 10.45-10.80 m

Density, ρ (g/cm3)	1.80
Unit weight, γ (kN/m3)	17.65
Water Content, w (%)	**40.9**
Plastic Limit, w_P (%)	25.2
Liquid Limit, w_L (%)	**32.3**
Plasticity, I_P (%)	7.1
Porosity, n (%)	55.6
Degree of saturation, S_r (-)	0.94
Salt content, S (g/l)	**1.3**
Falling Cone - Undrained shear strength, s_u (kPa)	49.7
Falling Cone - Remoulded shear strength, s_u (kPa)	**0.3**
Sensitivity, S_t (-)	**169.6**

Sample 1070 Sv

- Vertically cut
- One silt layer at the base as shown in Figure C.6
- Consolidated to anisotropic average stress conditions using K_0= 0.7 and γ=18.5 kN/m³. Cell pressure of 124.8 kPa, vertical pressure of 30.7 kPa. A slight mistake with proportion of stresses, which led to a slightly higher average stress to the other 2 samples.
- Consolidation rate 2 kPa / min
- EOP 6.4 hours
- Unloaded after 21.5 hours
- Burette closed immediately after unloading
- Triaxial software was stopped.
- Final unloaded measurement was taken.

Figure C.6: Photos of Sample 1070 Sv

Sample 1070 Shh

- Horizontally cut, BE perpendicular to the bedding planes

- Consolidated to isotropic average stress conditions.

- One silt layer across the sample as shown in Figure C.7

- Consolidated at a rate of 2 kPa every 2 minutes

- Cell pressure of 124.8 kPa, vertical pressure of 5 kPa to maintain good contacts with the bender elements

- EOP 6.4 hours

- Unloaded after 22 hours

- Burette closed immediately after unloading

- Triaxial software was stopped.

- Final unloaded measurement was taken.

- NOTE: The sample was disturbed during unmounting so out of interest another reading was taken after this.
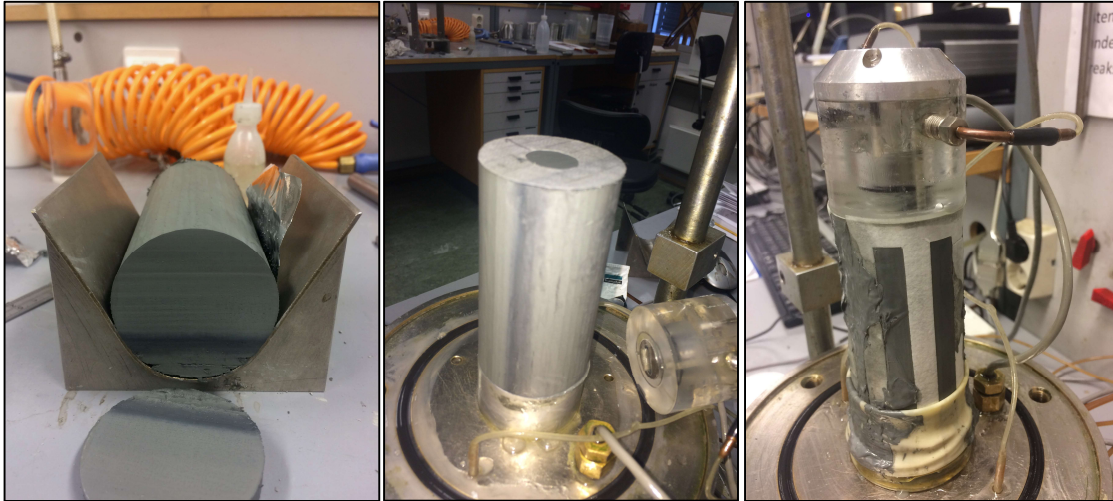
Figure C.7: Photos of Sample 1070 Shh

<u>Sample 1070 Shv</u>

- Horizontally cut, BE parallel to the bedding planes
- No obvious silt layers
- Consolidated as above
- EOP 6.1 hours
- Unloaded 23 hours
- Burette closed immediately after unloading
- Triaxial software was stopped.
- Final unloaded measurement was taken.
- NOTE: the edge of the disturbed zone of the mini-block is observed in Figure C.8. This was removed during cutting to 100 mm length.
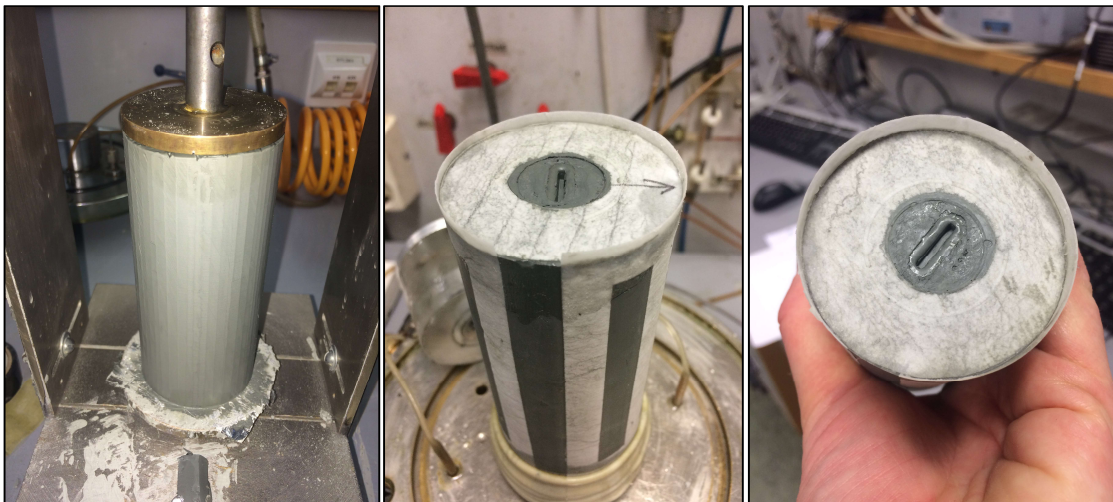
Figure C.8: Photos of Sample 1070 Shv

Mini-block 15.60-15.95 m

On initial inspection this mini-block contained some silt layers.

Figure C.9: Mini-block sample 15.60-15.95m

The whole of this block was utilised. The bottom half, approximately 15.80-15.90 m was used for testing S-wave velocities (v_{Sv}, v_{Shh} and v_{Shv}) both on half a mini-block and then triaxial sample were trimmed and tested. The top half, approximately 15.65-15.75 m was used to test various techniques on 3 vertical samples, such as the use of salt on the BE contacts and changes in the rate of consolidation.

Half Mini-block Results

The mini-bock was tested with the stand-alone bender element system. Resulting output signals are presented in Figure C.10. The program seemed to manage to pick the first arrivals well, although it is noted that there is no apparent P-wave interference, so it is hard to know if the S or P wave has been picked.
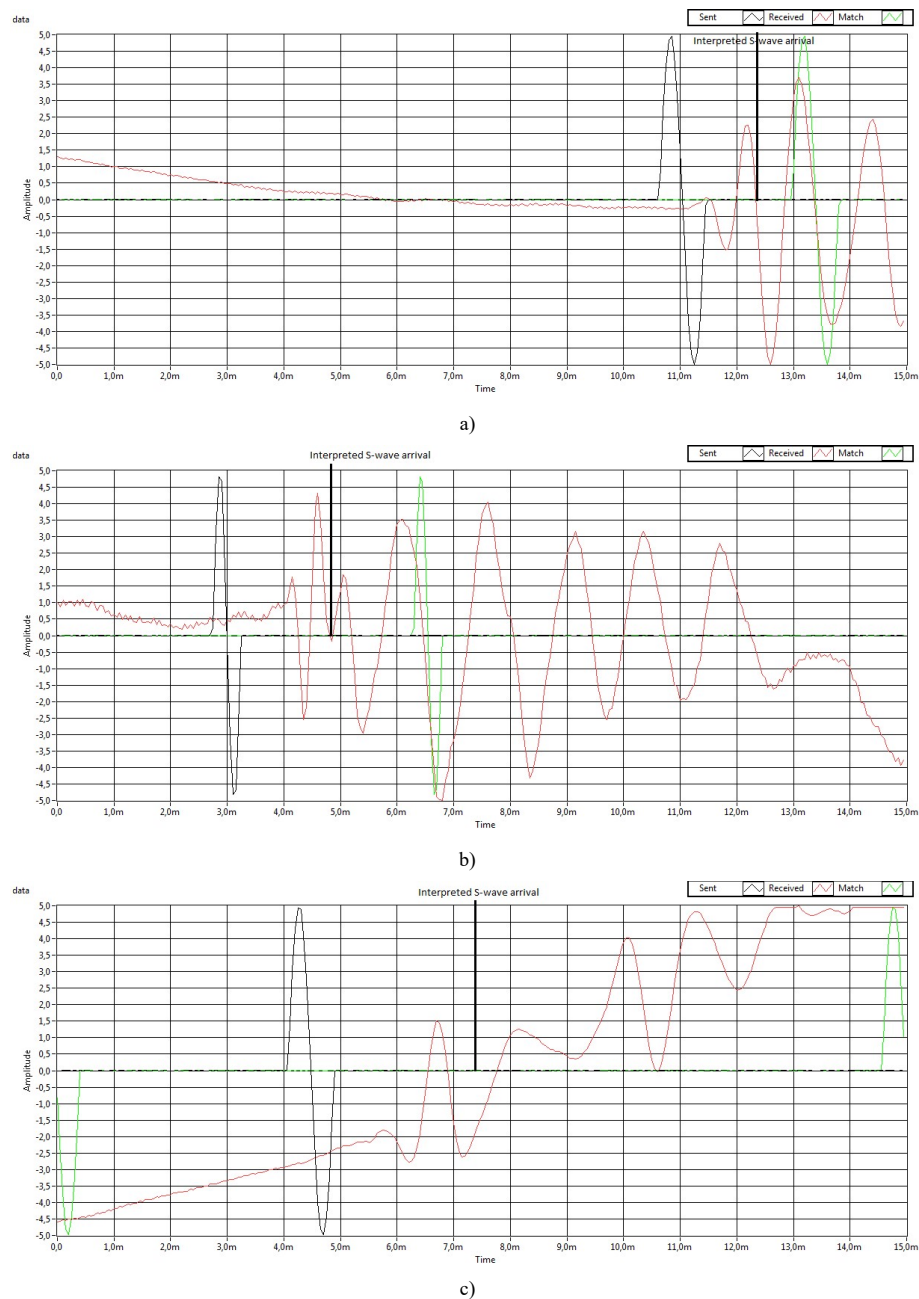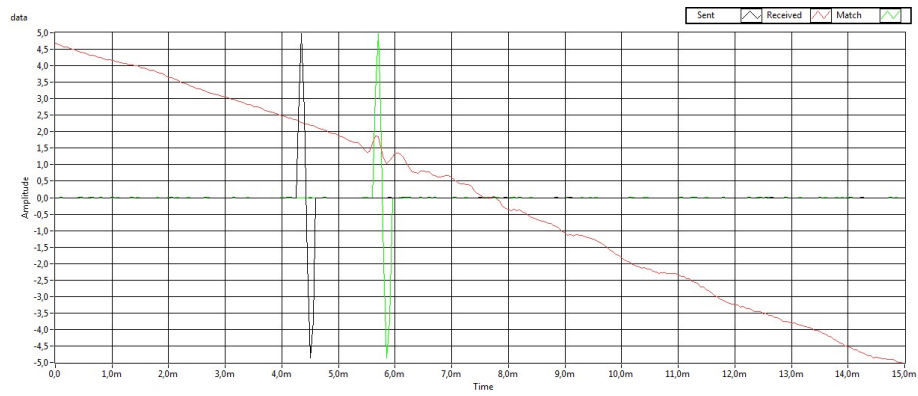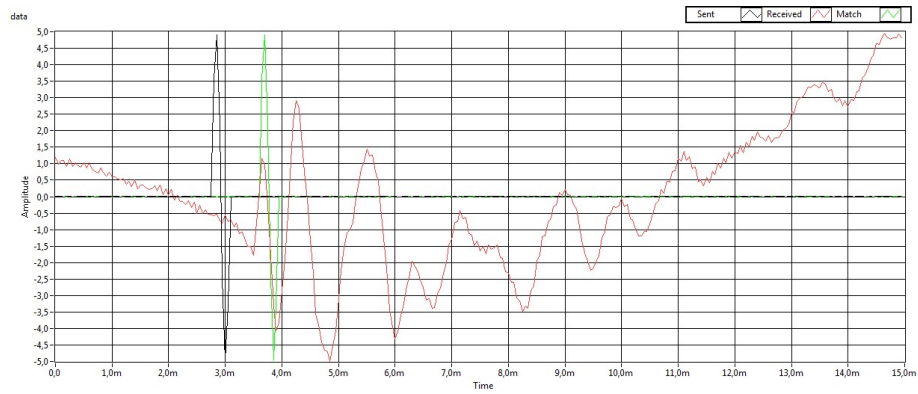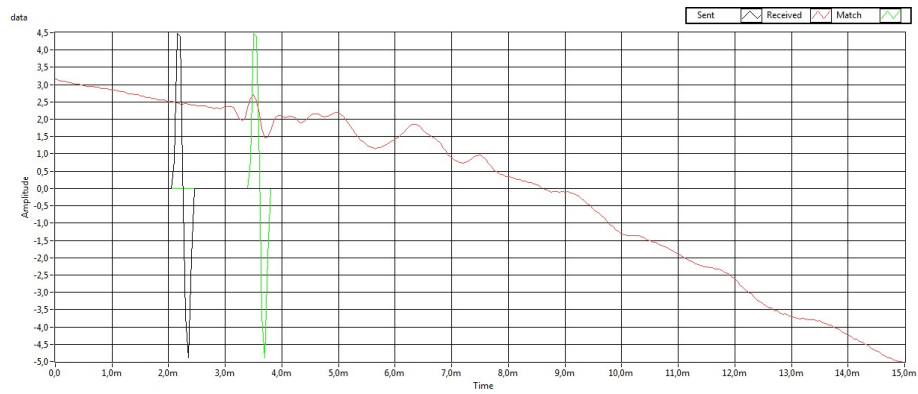
Figure C.10: Output results for half mini-block test at 15.85m for a) S_v b)S_{hh} and c) S_{hv}.

<u>*Index Tests*</u>

Index tests were carried out after the block had been sub-divided and are presented in Table C.4. The properties highlighted in bold indicate behaviour of a quick clay. The remoulded shear strength (s_r) is only slightly greater than 0.5 kPa, the definition by NGF (2011).

Table C.4: Index test results for mini-block depth 15.60-15.95 m

Density, ρ (g/cm3)	1.83
Unit weight, γ (kN/m3)	17.98
Water Content, w (%)	**39.8**
Plastic Limit, w_P (%)	25.5
Liquid Limit, w_L (%)	**31.8**
Plasticity, I_P (%)	6.4
Porosity, n (%)	54.2
Degree of saturation, S_r (-)	0.96
Salt content, S (g/l)	**1.3**
Falling Cone - Undrained shear strength, s_u (kPa)	40.5
Falling Cone - Remoulded shear strength, s_u (kPa)	**0.6**
Sensitivity, S_t (-)	**72.8**

Sample 1585 Sv

- Vertically cut
- Relatively large silt layer near the top of the sample and another dark layer at the bottom.
- Consolidated to anisotropic average stress conditions using K_0= 0.7 and γ=18.5 kN/m^3. Cell pressure of 167.5 kPa, vertical pressure of 76.7 kPa.
- Consolidation rate 2 kPa / min
- EOP 7.5 hours
- Unloaded after 21.5 hours
- Burette closed immediately after unloading
- Triaxial software was stopped.
- NOTE: No unloading measurement recorded.
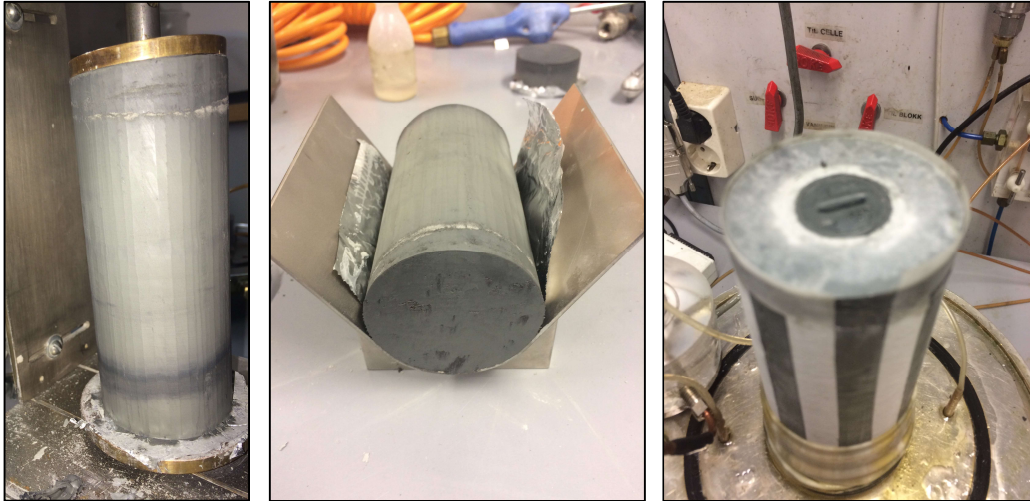
Figure C.11: Photos of Sample 15.85 Sv

<u>Sample 1585 Shh</u>

- Horizontally cut, BE perpendicular to the bedding planes
- Consolidated to isotropic average stress conditions.
- Significant silt layer at the edge of the sample
- Consolidated at a rate of 2 kPa every 2 minutes
- Cell pressure of 191.5 kPa, vertical pressure of 5 kPa to maintain good contacts with the bender elements
- EOP 6.7 hours
- Unloaded after 22.5 hours
- Burette closed immediately after unloading
- Triaxial software was stopped.
- Measurements were taken at small intervals during unloading.

Figure C.12: Photos of Sample 15.85 Shh

<u>Sample 1585 Shv</u>

- Horizontally cut, BE parallel to the bedding planes

- Dark silt layer across the sample

- Consolidated as above

- EOP 6.5 hours

- Unloaded 25 hours

- Burette closed immediately after unloading

- Triaxial software was stopped.

- Measurements were taken at small intervals during unloading.
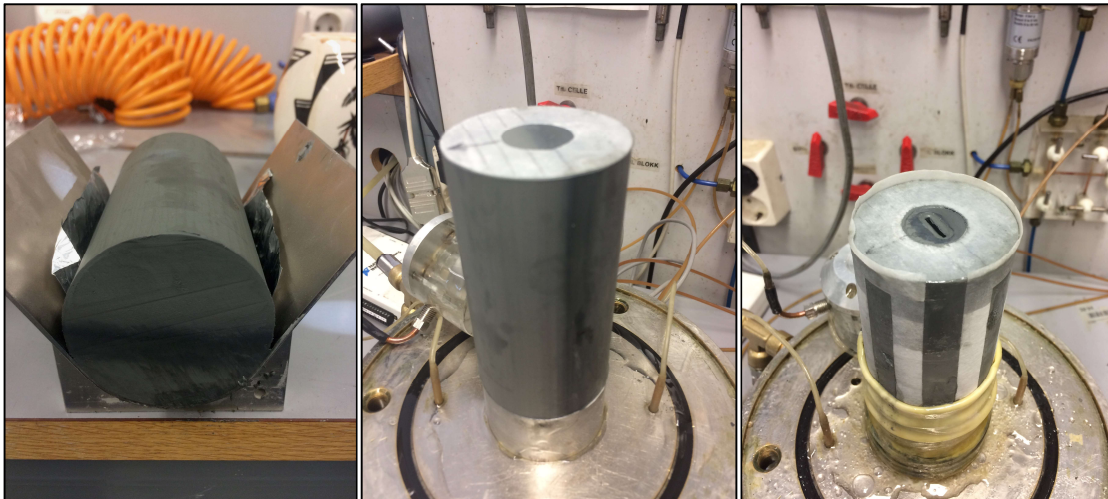
Figure C.13: Photos of Sample 1558 Shv

(NOTE: The following 3 were carried out after 11.40 m samples, so the half block sat in the storage room for three extra days)

- Vertically cut

- Silt layers seen in Figure C.14 at top and bottom removed on cutting to 100 mm.

- Consolidated to anisotropic average stress conditions using K_0= 0.7 and γ=18.5 kN/m^3. Cell pressure of 165.6 kPa, vertical pressure of 71 kPa.

- Consolidation rate 2 kPa / min

- EOP 5.7 hours

- Unloaded after 22 hours

- Burette closed immediately after unloading

- Triaxial software was stopped.

- NOTE: The sample was left over a weekend with measurements automatically taken at intervals. Some data was lost.
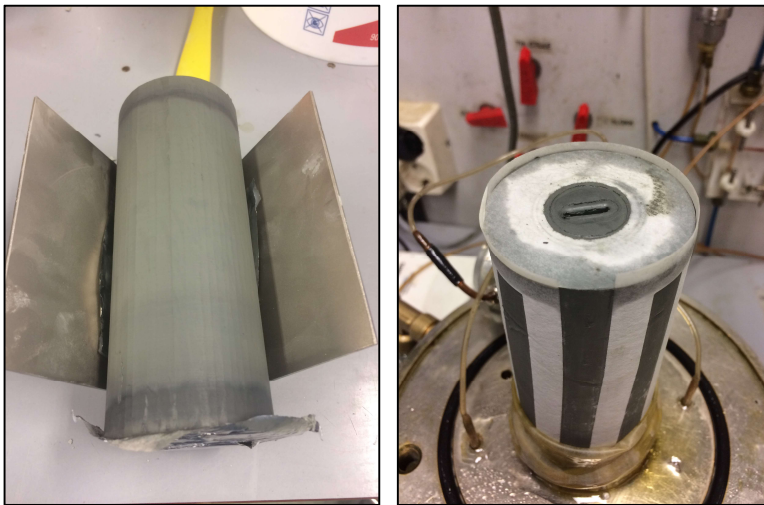
Figure C.14: Photos of Sample 15.70 Sv1

Sample 1570 Sv2

- Vertically cut

- Silt layers at top and bottom removed on cutting to 100 mm.

- Consolidated to anisotropic average stress conditions using K_0= 0.7 and γ=18.5 kN/m^3. Cell pressure of 165.6 kPa, vertical pressure of 71 kPa.

- Consolidation rate 10 kPa / min

- EOP 4.4 hours

- Unloaded after 7 hours

- Burette closed immediately after unloading

- Triaxial software was stopped.

- NOTE: The sample was left overnight with measurements automatically taken at intervals. The filter paper was seen to be almost dry in the morning and the sample length was 93mm so the sample swelled from a deformation of 4.21mm to 2mm. The deformation between these values is therefore calculated by interpolation in excel.
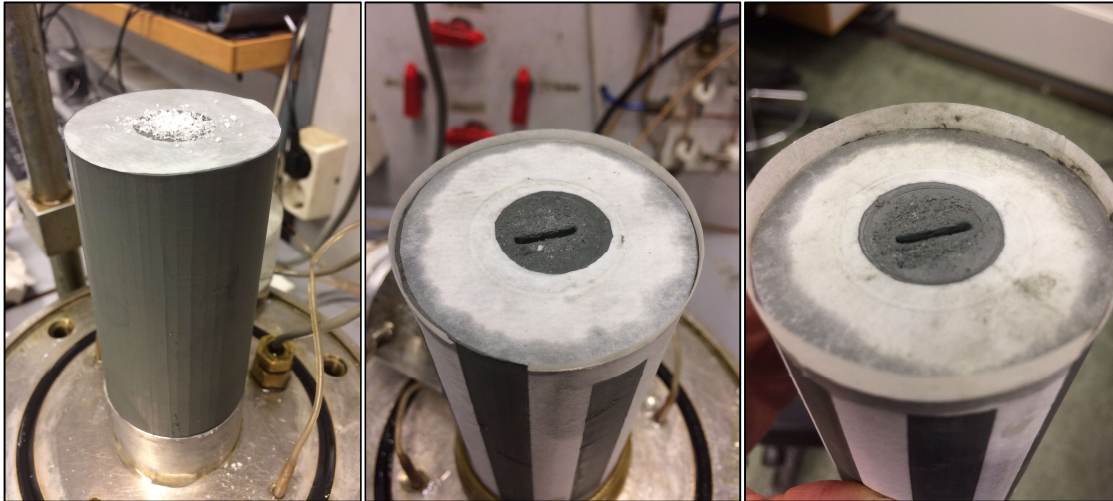
Figure C.15: Photos of Sample 15.70 Sv2 showing salt application before and after at both elements

Sample 1570 Sv3

- Vertically cut

- Silt layers removed on cutting to 100 mm.

- Consolidated to anisotropic average stress conditions using K_0= 0.7 and γ=18.5 kN/m^3. Cell pressure of 165.6 kPa, vertical pressure of 71 kPa.

- Consolidation rate 10 kPa / min

- EOP 4.8 hours

- Unloaded after 22 hours

- NOTE: The burette was left open and the triaxial program was left to run until all the water had returned to the sample. Approximately 1.5 ml of extra water went into the sample. Measurements were automatically taken at intervals during this time. The paper was wet on unmounting but no excess water runn-off.
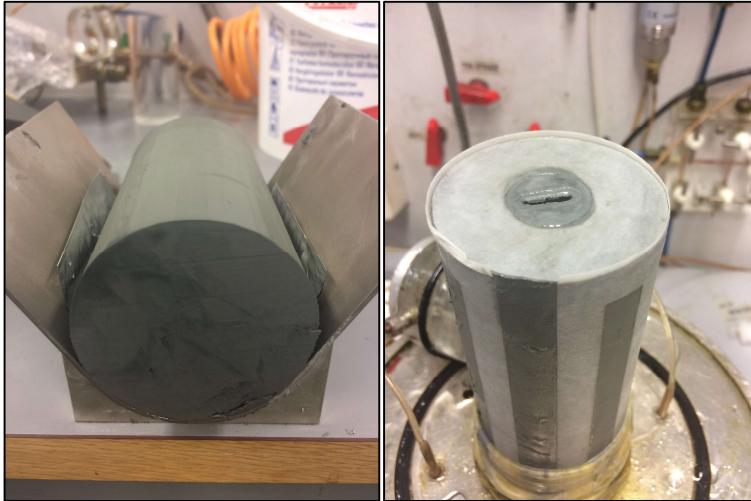
Figure C.16: Photos of Sample 15.70 Sv3 showing saturation of filter paper after test.

Mini-block 11.40-11.75 m

On initial inspection this mini-block contained some silt layers. The bottom half, approximately 11.60-11.70 m was used for testing S-wave velocities (v_{Sv}, v_{Shh} and v_{Shv}) both on half a mini-block and then triaxial sample were trimmed and tested.

Half Mini-block Results

The mini-bock was tested with the stand-alone bender element system. Resulting output signals are presented in Figure C.17. Although hard to distinguish, the first arrivals of S-waves are interpreted as shown from the change in wave form.
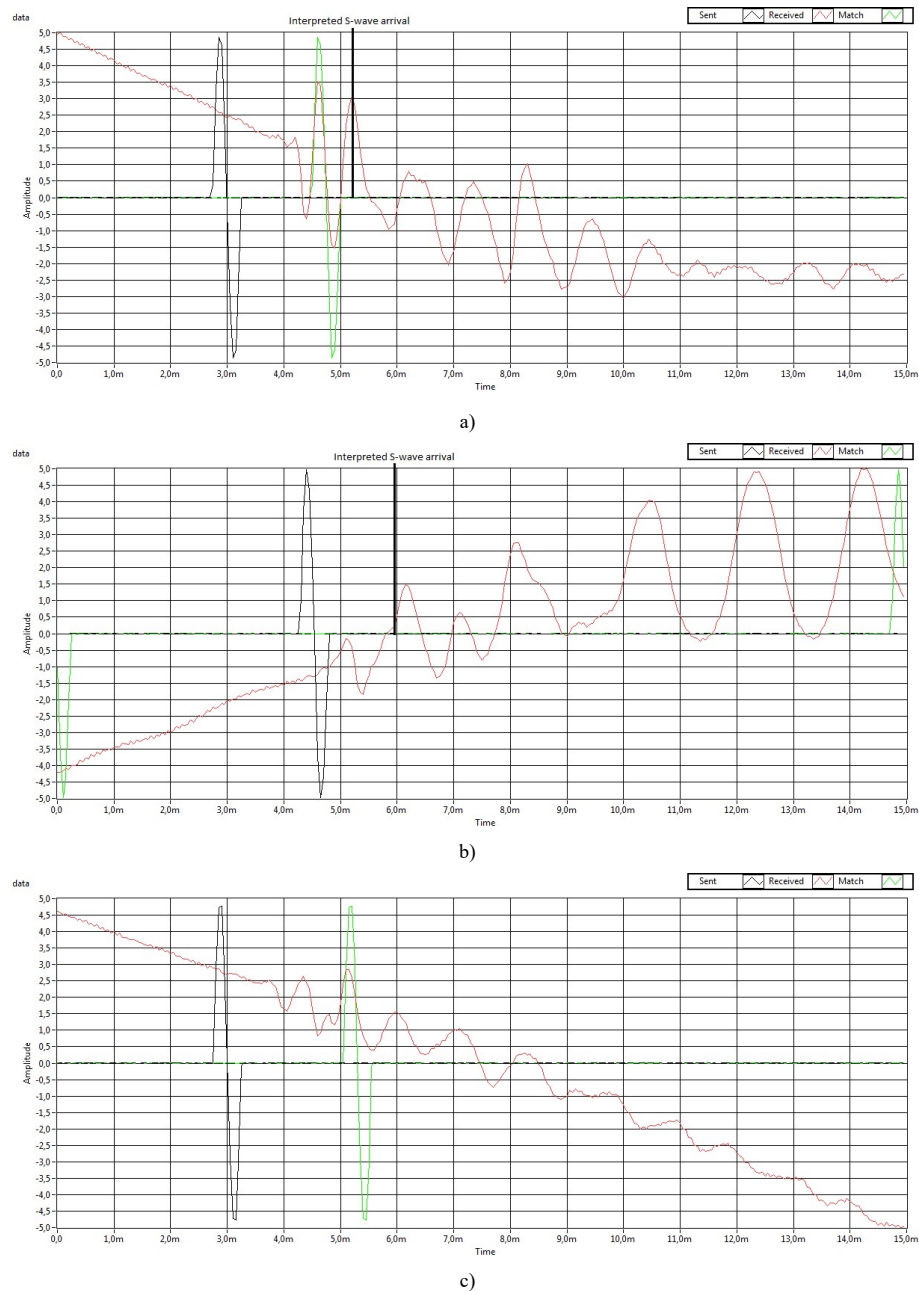
Figure C.17: Output results for half mini-block test at 11.65m for a) S_v b) S_{hh} and c) S_{hv}.

Index Tests

Index tests were carried out after the block had been sub-divided and are presented in Table C.5. The properties highlighted in bold indicate behaviour of a quick clay.

Table C.5: Index test results for mini-block depth 11.40-11.75 m

Density, ρ (g/cm3)	1.84
Unit weight, γ (kN/m3)	18.01
Water Content, w (%)	**42.5**
Plastic Limit, w_P (%)	25.4
Liquid Limit, w_L (%)	**31.1**
Plasticity, I_P (%)	3.0
Porosity, n (%)	55.0
Degree of saturation, S_r (-)	1.00
Salt content, S (g/l)	**0.8**
Falling Cone - Undrained shear strength, s_u (kPa)	54.0
Falling Cone - Remoulded shear strength, s_u (kPa)	**0.3**
Sensitivity, S_t (-)	**186.1**

Sample 1165 Sv

- Vertically cut
- One silt layer
- Consolidated to anisotropic average stress conditions using K_0= 0.7 and γ=18.5 kN/m³. Cell pressure of 119.9 kPa, vertical pressure of 56.6 kPa. A slight mistake with proportion of stresses, which led to a slightly higher average stress to the other 2 samples.
- Consolidation rate 2 kPa / min
- EOP 3.6 hours
- Unloaded after 18.5 hours
- Burette closed immediately after unloading
- Triaxial software was stopped.
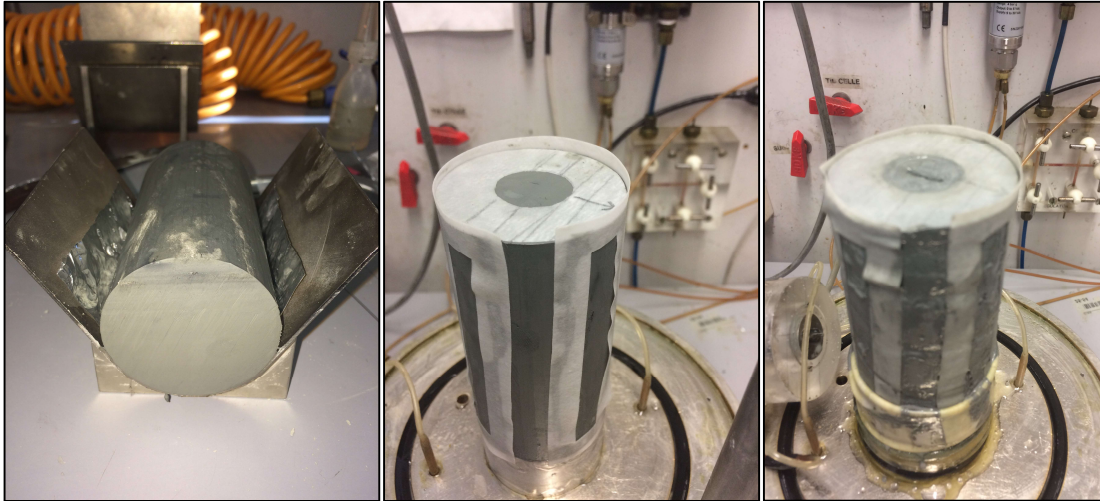- NOTE: Measurements were taken at small intervals during unloading.
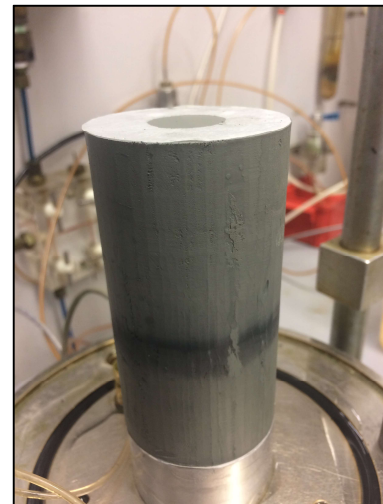
Sample 1165 Shh

- Horizontally cut, BE perpendicular to the bedding planes
- Consolidated to isotropic average stress conditions.
- No obvious silt layers
- Consolidated at a rate of 2 kPa every 2 minutes
- Cell pressure of 119.9 kPa, vertical pressure of 5 kPa to maintain good contacts with the bender elements
- EOP 6.8 hours
- Unloaded after 22.5 hours
- Burette closed immediately after unloading
- Triaxial software was stopped.
- Measurements were taken at small intervals during unloading.
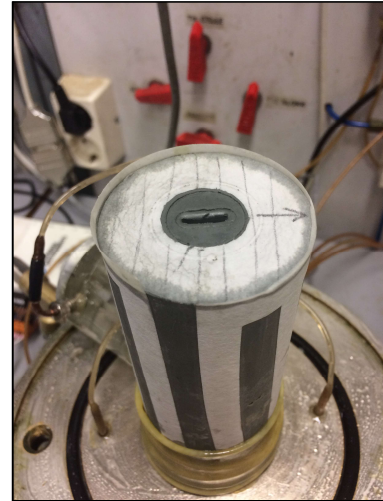
Sample 1165 Shv

- Horizontally cut, BE parallel to the bedding planes
- No obvious silt layers
- Consolidated as above
- EOP 5.6 hours
- Unloaded 23 hours
- Burette closed immediately after unloading
- Triaxial software was stopped.
- Final unloaded measurement was taken.
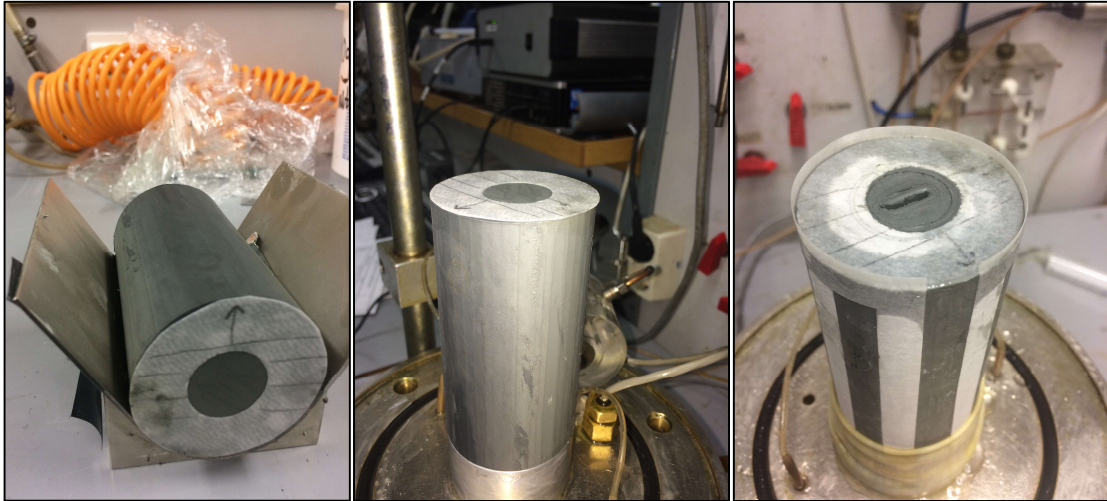
Figure C.18: Photos of Sample 1165 Shv

Mini-block 13.50-13.85 m

On initial inspection this mini-block contained some silt layers. The top half this time, approximately 13.55-13.65 m was used for testing S-wave velocities (v_{Sv}, v_{Shh} and v_{Shv}). No tests were carried out on the half mini-block. The bottom half, approximately 15.70-15.80 m was used to test P-waves velocities to determine the bulk modulus of the clay.

<u>Index Tests</u>

Index tests were carried out after the block had been sub-divided and are presented in Table C.6. The properties highlighted in bold indicate behaviour of a quick clay.

Table C.6: Index test results for mini-block depth 11.40-11.75 m

Density, ρ (g/cm3)	1.82
Unit weight, γ (kN/m3)	17.86
Water Content, w (%)	**41.6**
Plastic Limit, w_P (%)	25.0
Liquid Limit, w_L (%)	**31.0**
Plasticity, I_P (%)	6.0
Porosity, n (%)	54.6
Degree of saturation, S_r (-)	0.98
Salt content, S (g/l)	**0.8**
Falling Cone - Undrained shear strength, s_u (kPa)	40.8
Falling Cone - Remoulded shear strength, s_u (kPa)	**0.3**
Sensitivity, S_t (-)	**157.1**

<u>Sample 1375 Pv</u>

- Vertically cut
- No obvious silt layers
- Consolidated to anisotropic average stress conditions using K_0= 0.7 and γ=18.5 kN/m³. Cell pressure of 143.7 kPa, vertical pressure of 61.8 kPa.
- Consolidation rate 10 kPa / min
- EOP 3.9 hours
- Unloaded after 19 hours
- Burette left open after unloading until volume of water expelled was back in and readings were taken during and after the triaxial program was stopped.
- The sample was left over a weekend.
- There were errors in the burette readings. The burette was checked and fine, so the error was in the sensor.

B.XXIV

Figure C.19: Photos of Sample 1375 Pv

<u>*Sample 1375 Ph1*</u>

- Horizontally cut, BE perpendicular to the bedding planes (this should not matter).

- One silt layer at the edge of the sample

- Consolidated at a rate of 5 kPa/min

- Consolidated to isotropic average stress conditions. A cell pressure of 164.7 kPa, vertical pressure of 5 kPa to maintain good contacts with the bender elements

- EOP 6.6 hours

- Unloaded in 2 steps after 22 hours

- Burette left open during and after unloading until volume of water expelled was back in and readings were taken during.

- Burette was closed and triaxial software was left running for an hour and pore pressure measurements were taken

- There were errors in the burette readings. The burette was checked and fine, so the error was in the sensor
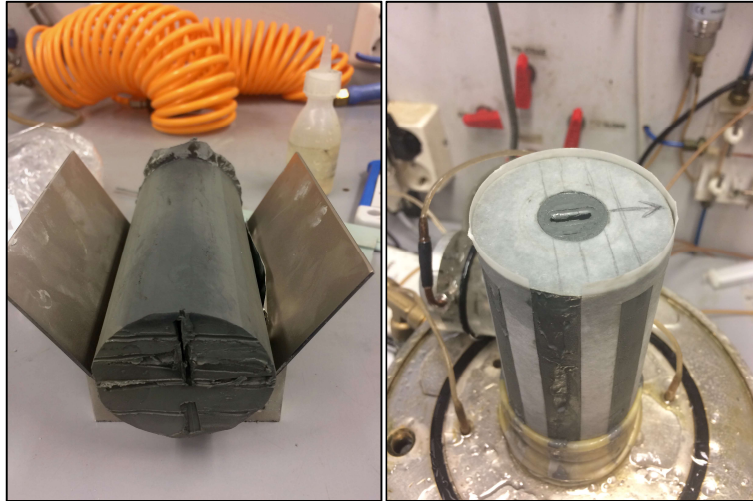
Figure C.20: Photos of Sample 1375 Ph1

Sample 1375 Ph2

- Horizontally cut, BE parallel to the bedding planes (this should not matter)
- No obvious silt layers, but what looked like a dried crack was notices after insertion of the BE as shown in Figure C.21
- Consolidated as above
- EOP 4.9 hours
- Unloaded 21 hours
- Burette closed immediately after unloading
- Triaxial software was left to run for ~1.5 hours to try to measure pore pressure
- There were errors in the burette readings in the first few hours. The burette was checked and fine, so the error was in the sensor.
- There was a drop in the cell pressure at approximately 8 hours, which coincided with an increase in vertical pressure. There was also a drop in the burette level. All levels went back to normal. There was no presence in the lab at this time, so the cause is not known.
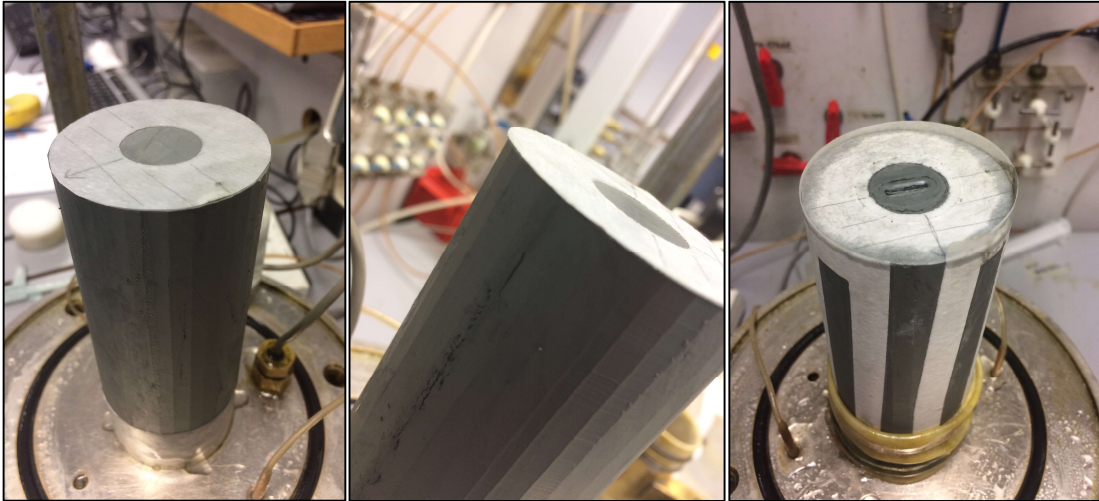
Figure C.21: Photos of Sample 1375 Ph2

<u>Sample 1360 Sv</u>

- Vertically cut

- One dark silty layer across the middle

- Consolidated to anisotropic average stress conditions using $K_0 = 0.7$ and $\gamma = 18.5$ kN/m^3. Cell pressure of 141.8 kPa, vertical pressure of 64.1 kPa.

- Consolidation rate 5 kPa / min

- EOP 5.9 hours

- Unloaded after 22 hours

- The burette was left open after unloading and half the volume of expelled water was allowed back into the sample before being closed

- The triaxial software was left to run for 10 days so pore pressure variations could be determined

- NOTE: On unmounting the filter paper was still wet but could not be removed.
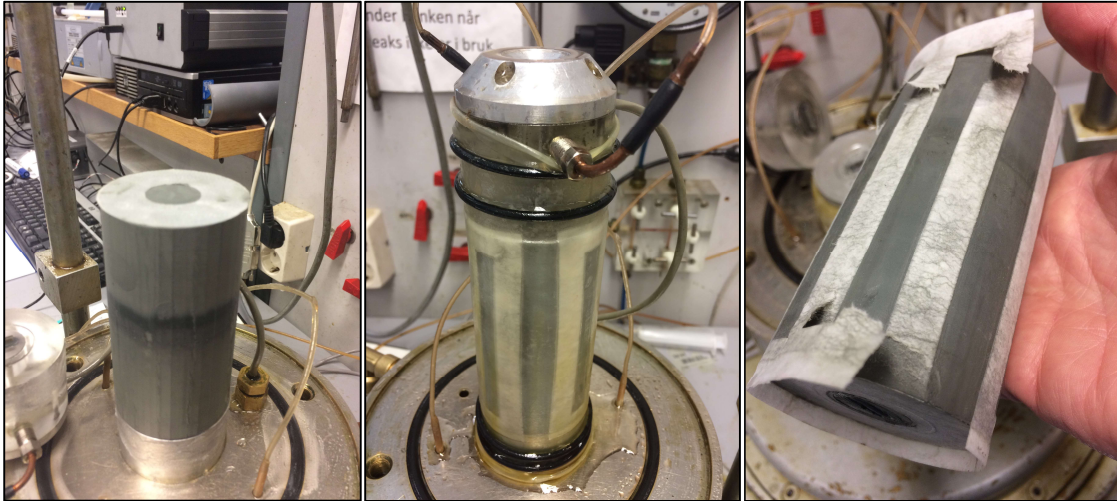
Figure C.22: Photos of Sample 1360 Sv

Sample 1360 Shh

- Horizontally cut, BE perpendicular to the bedding planes

- Consolidated to isotropic average stress conditions.

- One dark silty layer at the edge of the sample

- Consolidated at a rate of 10 kPa/min

- Cell pressure of 162.5 kPa, vertical pressure of 5 kPa to maintain good contacts with the bender elements

- EOP 6.3 hours

- Unloaded after 21 hours

- Burette closed immediately after unloading

- Triaxial software continued to determine pore pressure changes for 1 hour.
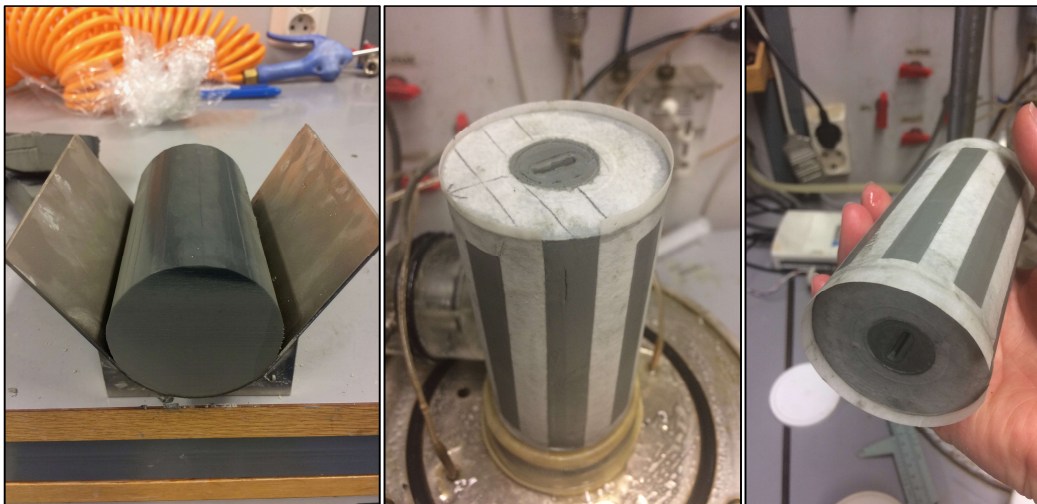
Figure C.23: Photos of Sample 1360 Shh

Sample 1360 Shv

- Horizontally cut, BE parallel to the bedding planes

- No obvious silt layers

- Consolidated as above

- EOP 4.1 hours

- Unloaded 22.5 hours

- Burette closed immediately after unloading

- Burette closed immediately after unloading

- Triaxial software continued to determine pore pressure changes for 1.5 hours.
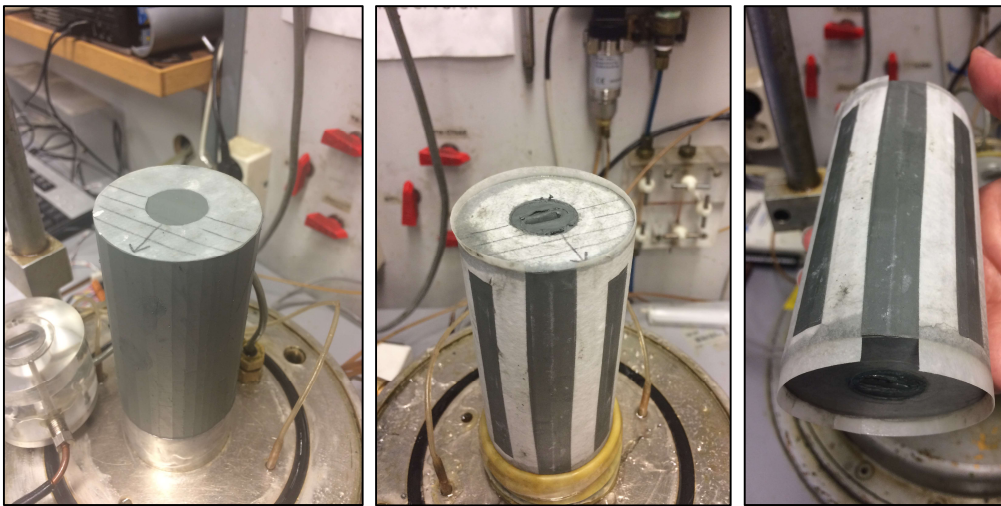
Figure C.24: Photos of Sample 1360 Shv

B.XXX

APPENDIX C – Examples of BE Results G_{max} against Applied Average Confining Pressure, p

APPENDIX D – SDMT Results

SEISMIC DILATOMETER TEST (S D M T)
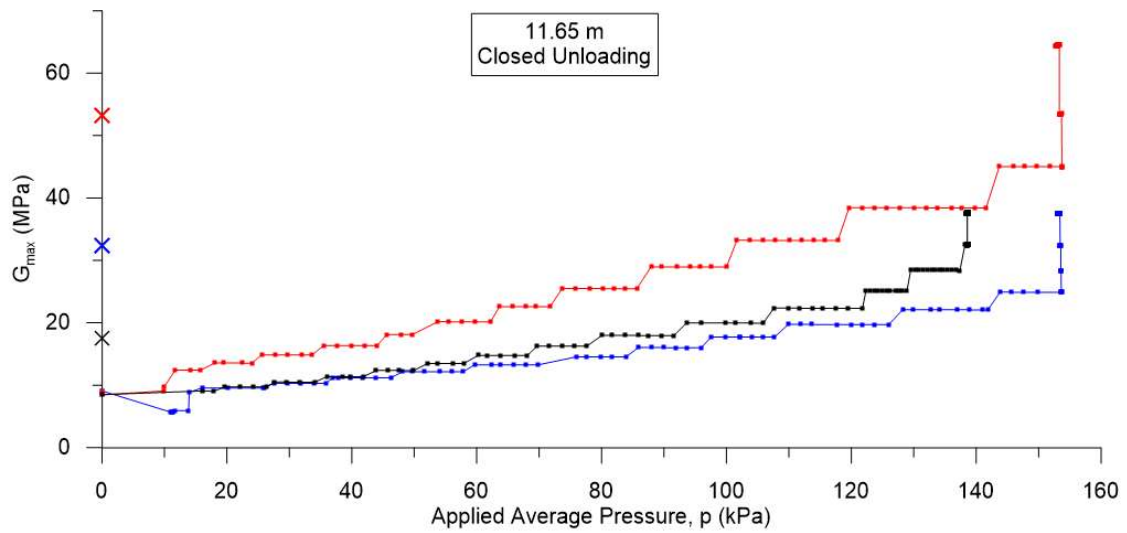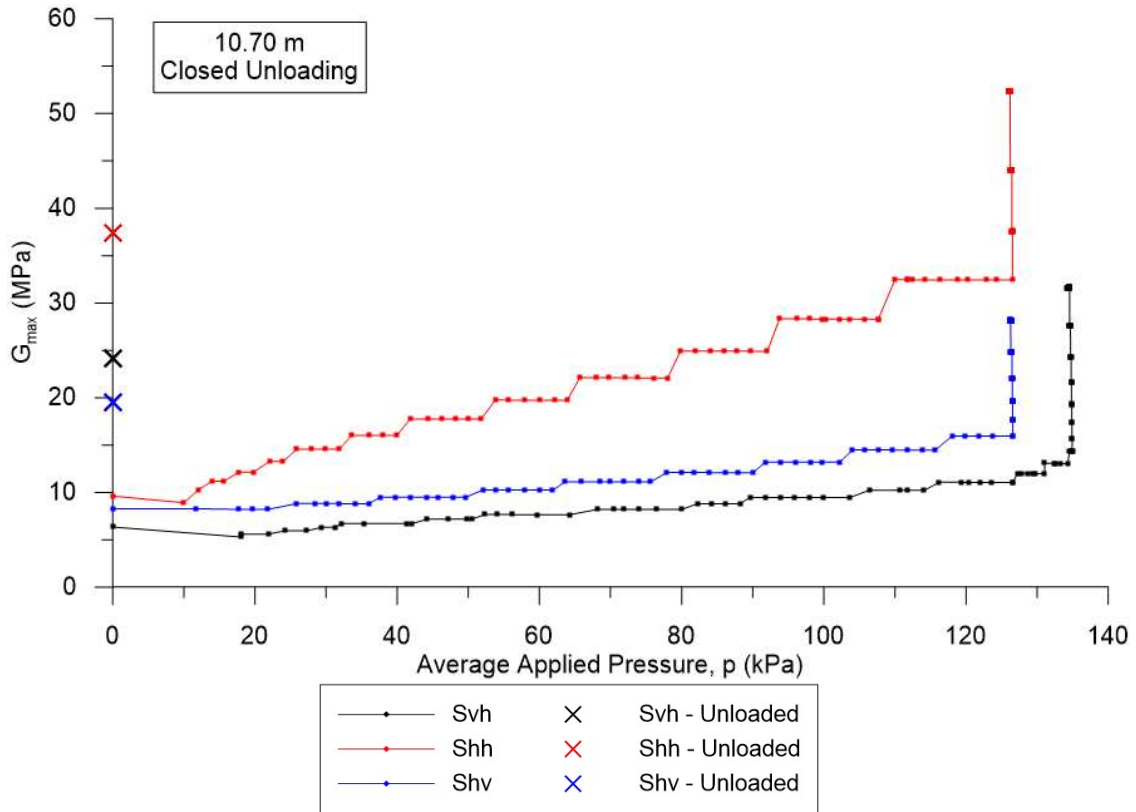
NGI
Tiller-Flotten

NRC
Quick Clay

TEST
T-F 1
13 FEB 2017

D.II
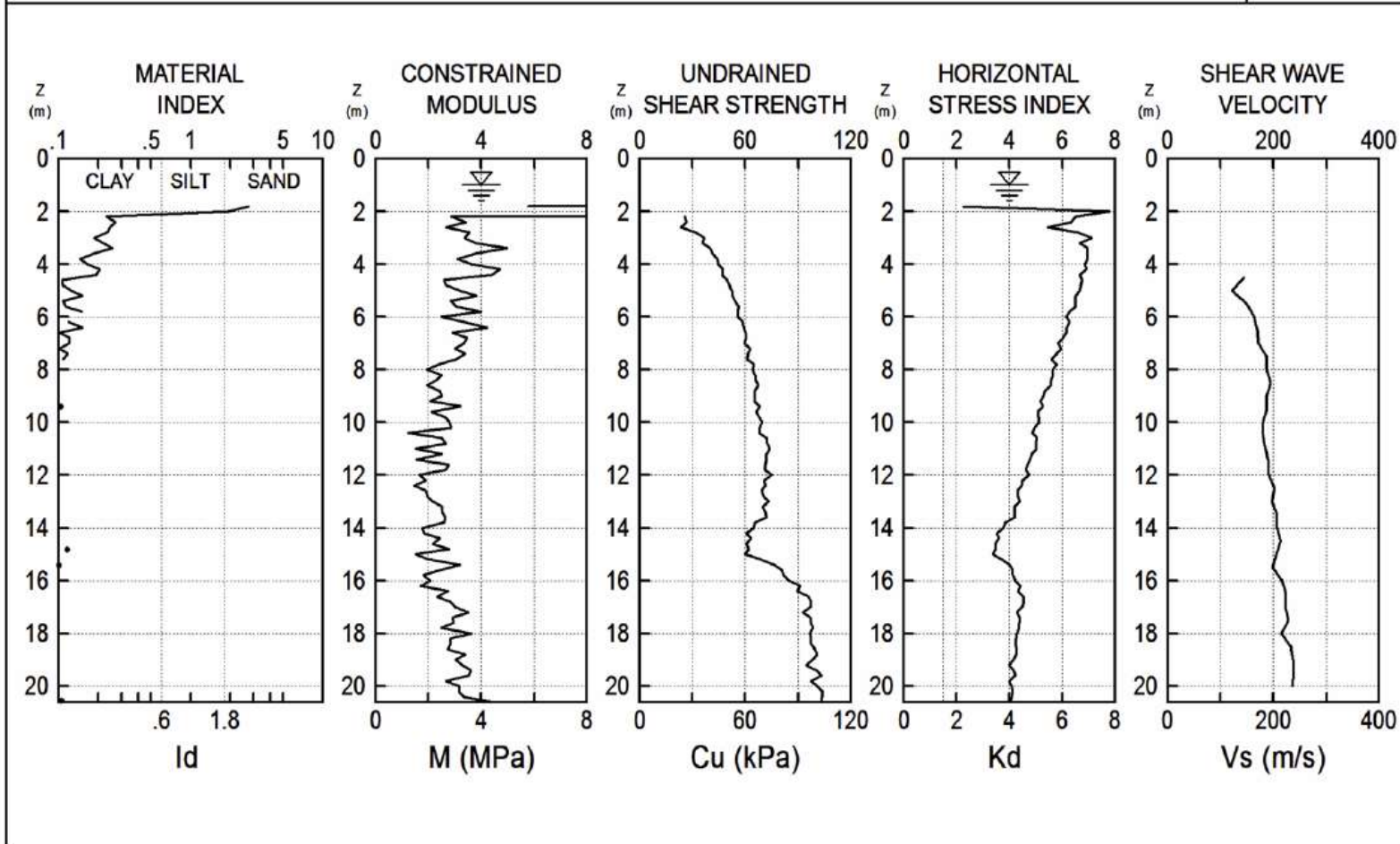
	T-F 1
LEGEND	**INTERPRETED PARAMETERS**	**GENERAL PARAMETERS**

T-F 1

13 FEB 2017

NGI

NRC

Tiller-Flotten

Quick Clay

LEGEND
Z = Depth Below Ground Level
Po,P1,P2 = Corrected A,B,C readings
Id = Material Index
Ed = Dilatometer Modulus
Ud = Pore Press. Index = (P2-Uo)/(Po-Uo)
Gamma = Bulk unit weight
Sigma' = Effective overb. stress
Uo = Pore pressure

INTERPRETED PARAMETERS
Phi = Safe floor value of Friction Angle
Ko = In situ earth press. coeff.
M = Constrained modulus (at Sigma')
Cu = Undrained shear strength
Ocr = Overconsolidation ratio
(OCR = 'relative OCR'- generally
realistic. If accurate independent OCR
available, apply suitable factor)

GENERAL PARAMETERS
DeltaA = 8 kPa
DeltaB = 76 kPa
GammaTop = 17.0 kN/m^3
FactorEd = 34.7
Zm = 0.0 kPa
Zabs = 123.44 m
Zw = 1.0 m

WaterTable at 1.00 m
Reduction formulae according to Marchetti, ASCE Geot.Jnl.Mar. 1980, Vol.109, 299-321; Phi according to TC16 ISSMGE, 2001

| Z (m)	A (kPa)	B (kPa)	C (kPa)	Po (kPa)	P1 (kPa)	P2 (kPa)	Gamma (kN/m^3)	Sigma' (kPa)	Uo (kPa)	Id	Kd	Ed (MPa)	Ud	Ko	Ocr	Phi (Deg)	M (MPa)	Cu (kPa)	T-F 1 DESCRIPTION
1.8	58	276		59	200		19.5	23	8	2.73	2.3	4.9				33	5.8		SILTY SAND
2.0	212	650		202	574		19.4	25	10	1.93	7.8	12.9				39	29.2		SILTY SAND
2.2	179	301		185	225		19.4	27	12	0.23	6.5	1.4		1.4	6.3		2.9	26	CLAY
2.4	189	319		195	243		19.4	29	14	0.27	6.3	1.7		1.4	6.1		3.4	27	CLAY
2.6	176	299		182	223		19.3	30	16	0.25	5.5	1.4		1.2	4.8		2.7	24	CLAY
2.8	225	356		231	280		19.3	32	18	0.23	6.6	1.7		1.4	6.4		3.5	32	CLAY
3.0	257	384		263	308		19.3	34	20	0.19	7.1	1.6		1.5	7.2		3.4	37	CLAY
3.2	257	391		263	315		19.2	36	22	0.22	6.7	1.8		1.4	6.6		3.8	36	CLAY
3.4	284	432		289	356		19.2	38	24	0.25	7.0	2.3		1.5	7.0		5.0	40	CLAY
3.6	297	430		303	354		19.2	40	26	0.19	6.9	1.8		1.5	7.0		3.8	42	CLAY
3.8	313	437		319	361		19.2	42	27	0.14	7.0	1.5		1.5	7.0		3.1	44	CLAY
4.0	323	454		329	378		19.1	44	29	0.16	6.9	1.7		1.4	6.9		3.6	45	CLAY
4.2	342	487		347	411		19.1	46	31	0.20	6.9	2.2		1.5	7.0		4.7	47	CLAY
4.4	344	486		349	410		19.1	47	33	0.19	6.7	2.1		1.4	6.6		4.4	47	CLAY
4.6	362	480		368	404		19.0	49	35	0.11	6.8	1.2		1.4	6.7		2.6	50	CLAY
4.8	373	492		379	416		19.0	51	37	0.11	6.7	1.3		1.4	6.6		2.7	51	CLAY
5.0	385	511		391	435		19.0	53	39	0.13	6.6	1.5		1.4	6.5		3.2	52	CLAY
5.2	392	527		397	451		18.9	55	41	0.15	6.5	1.9		1.4	6.3		3.8	53	CLAY
5.4	404	526		410	450		18.9	57	43	0.11	6.5	1.4		1.4	6.3		2.8	54	CLAY
5.6	419	544		425	468		18.9	58	45	0.11	6.5	1.5		1.4	6.3		3.1	56	CLAY
5.8	420	558		425	482		18.9	60	47	0.15	6.3	2.0		1.4	6.0		4.0	55	CLAY
6.0	425	543		431	467		18.8	62	49	0.09	6.2	1.2		1.3	5.8		2.5	56	CLAY
6.2	445	574		451	498		18.8	64	51	0.12	6.3	1.6		1.4	6.0		3.3	58	CLAY
6.4	453	595		458	519		18.8	66	53	0.15	6.2	2.1		1.3	5.8		4.2	59	CLAY
6.6	463	587		469	511		18.7	67	55	0.10	6.1	1.5		1.3	5.8		2.9	60	CLAY
6.8	469	601		475	525		18.7	69	57	0.12	6.0	1.7		1.3	5.6		3.5	61	CLAY
7.0	467	598		473	522		18.7	71	59	0.12	5.8	1.7		1.3	5.3		3.3	59	CLAY
7.2	488	614		494	538		18.6	73	61	0.10	6.0	1.5		1.3	5.5		3.0	63	CLAY
7.4	488	620		494	544		18.6	74	63	0.12	5.8	1.7		1.3	5.3		3.4	62	CLAY
7.6	487	615		493	539		18.6	76	65	0.11	5.6	1.6		1.3	5.0		3.1	61	CLAY
7.8	512	630		518	554		18.6	78	67	0.08	5.8	1.2		1.3	5.3		2.4	65	CLAY
8.0	512	624		519	548		18.6	80	69	0.07	5.6	1.0		1.3	5.1		2.0	64	MUD AND/OR PEAT
8.2	525	645		531	569		18.6	82	71	0.08	5.6	1.3		1.3	5.1		2.5	66	CLAY
8.4	531	648		537	572		18.6	83	73	0.07	5.6	1.2		1.3	5.0		2.3	66	CLAY
8.6	542	654		549	578		18.6	85	75	0.06	5.6	1.0		1.3	5.0		1.9	67	MUD AND/OR PEAT
8.8	534	654		540	578		18.7	87	77	0.08	5.3	1.3		1.2	4.6		2.4	65	CLAY
9.0	541	662		547	586		18.7	89	78	0.08	5.3	1.3		1.2	4.6		2.5	66	CLAY
9.2	542	657		548	581		18.7	90	80	0.07	5.2	1.1		1.2	4.4		2.1	65	MUD AND/OR PEAT
9.4	563	695		569	619		18.7	92	82	0.10	5.3	1.7		1.2	4.6		3.2	68	CLAY
9.6	555	671		561	595		18.7	94	84	0.07	5.1	1.2		1.2	4.3		2.1	66	MUD AND/OR PEAT
9.8	569	693		575	617		18.7	96	86	0.09	5.1	1.5		1.2	4.3		2.6	68	CLAY
10.0	582	708		588	632		18.7	97	88	0.09	5.1	1.5		1.2	4.4		2.8	70	CLAY
10.2	577	705		583	629		18.7	99	90	0.09	5.0	1.6		1.2	4.1		2.9	68	CLAY

Z (m)	A (kPa)	B (kPa)	C (kPa)	Po (kPa)	P1 (kPa)	P2 (kPa)	Gamma (kN/m^3)	Sigma' (kPa)	Uo (kPa)	Id	Kd	Ed (MPa)	Ud	Ko	Ocr	Phi (Deg)	M (MPa)	Cu (kPa)	T-F 1 DESCRIPTION
10.4	578	681		585	605		18.7	101	92	0.04	4.9	0.7		1.1	4.0		1.2	68	MUD AND/OR PEAT
10.6	608	730		614	654		18.7	103	94	0.08	5.1	1.4		1.2	4.3		2.5	72	CLAY
10.8	614	739		620	663		18.7	105	96	0.08	5.0	1.5		1.2	4.2		2.7	72	CLAY
11.0	625	732		632	656		18.7	106	98	0.05	5.0	0.8		1.2	4.2		1.5	74	MUD AND/OR PEAT
11.2	619	742		625	666		18.7	108	100	0.08	4.9	1.4		1.1	4.0		2.5	72	CLAY
11.4	622	730		629	654		18.8	110	102	0.05	4.8	0.9		1.1	3.9		1.5	72	MUD AND/OR PEAT
11.6	622	750		628	674		18.8	112	104	0.09	4.7	1.6		1.1	3.8		2.8	71	CLAY
11.8	625	752		631	676		18.8	114	106	0.09	4.6	1.6		1.1	3.7		2.7	71	CLAY
12.0	651	761		658	685		18.8	115	108	0.05	4.8	0.9		1.1	3.9		1.6	75	MUD AND/OR PEAT
12.2	629	744		635	668		18.8	117	110	0.06	4.5	1.1		1.1	3.5		1.9	71	MUD AND/OR PEAT
12.4	637	745		644	669		18.8	119	112	0.05	4.5	0.9		1.1	3.5		1.5	72	MUD AND/OR PEAT
12.6	626	742		632	666		18.8	121	114	0.06	4.3	1.2		1.0	3.3		1.9	69	MUD AND/OR PEAT
12.8	640	757		646	681		18.8	123	116	0.07	4.3	1.2		1.0	3.3		2.0	71	CLAY
13.0	657	777		663	701		18.8	124	118	0.07	4.4	1.3		1.1	3.4		2.2	73	CLAY
13.2	642	769		648	693		18.8	126	120	0.09	4.2	1.6		1.0	3.2		2.5	70	CLAY
13.4	654	781		660	705		18.8	128	122	0.08	4.2	1.6		1.0	3.2		2.5	71	CLAY
13.6	663	792		669	716		18.8	130	124	0.09	4.2	1.6		1.0	3.2		2.6	72	CLAY
13.8	626	757		632	681		18.9	132	126	0.10	3.8	1.7		0.96	2.8		2.6	66	CLAY
14.0	625	741		631	665		18.9	133	128	0.07	3.8	1.2		0.94	2.7		1.8	65	MUD AND/OR PEAT
14.2	601	720		607	644		18.9	135	129	0.08	3.5	1.3		0.90	2.4		1.8	61	CLAY
14.4	620	750		626	674		18.9	137	131	0.10	3.6	1.7		0.91	2.5		2.4	63	CLAY
14.6	607	733		613	657		18.9	139	133	0.09	3.5	1.5		0.88	2.4		2.2	60	CLAY
14.8	621	759		626	683		18.9	141	135	0.12	3.5	2.0		0.89	2.4		2.8	62	CLAY
15.0	610	724		616	648		18.9	142	137	0.07	3.4	1.1		0.86	2.3		1.5	60	MUD AND/OR PEAT
15.2	666	787		672	711		18.9	144	139	0.07	3.7	1.3		0.93	2.6		2.0	68	CLAY
15.4	721	861		726	785		18.9	146	141	0.10	4.0	2.0		0.99	3.0		3.2	77	CLAY
15.6	749	875		755	799		18.9	148	143	0.07	4.1	1.5		1.0	3.1		2.4	81	CLAY
15.8	757	872		763	796		18.9	150	145	0.05	4.1	1.1		1.0	3.1		1.8	82	MUD AND/OR PEAT
16.0	783	902		789	826		18.9	152	147	0.06	4.2	1.3		1.0	3.2		2.1	85	CLAY
16.2	822	934		829	858		18.9	153	149	0.04	4.4	1.0		1.1	3.5		1.7	91	MUD AND/OR PEAT
16.4	815	945		821	869		19.0	155	151	0.07	4.3	1.7		1.0	3.3		2.7	89	CLAY
16.6	857	979		863	903		19.0	157	153	0.06	4.5	1.4		1.1	3.6		2.3	96	CLAY
16.8	871	1001		877	925		19.0	159	155	0.07	4.5	1.7		1.1	3.6		2.8	97	CLAY
17.0	873	1006		879	930		19.0	161	157	0.07	4.5	1.8		1.1	3.5		3.0	97	CLAY
17.2	850	993		855	917		19.0	162	159	0.09	4.3	2.1		1.0	3.3		3.5	93	CLAY
17.4	880	1012		886	936		19.0	164	161	0.07	4.4	1.7		1.1	3.4		2.9	97	CLAY
17.6	885	1018		891	942		19.0	166	163	0.07	4.4	1.8		1.1	3.4		3.0	97	CLAY
17.8	894	1019		900	943		19.0	168	165	0.06	4.4	1.5		1.1	3.4		2.5	98	CLAY
18.0	888	1033		893	957		19.0	170	167	0.09	4.3	2.2		1.0	3.3		3.6	97	CLAY
18.2	895	1027		901	951		19.0	172	169	0.07	4.3	1.7		1.0	3.3		2.8	97	CLAY
18.4	899	1031		905	955		19.0	174	171	0.07	4.2	1.7		1.0	3.2		2.8	97	CLAY
18.6	916	1046		922	970		19.0	175	173	0.06	4.3	1.7		1.0	3.3		2.7	100	CLAY
18.8	925	1066		930	990		19.1	177	175	0.08	4.3	2.1		1.0	3.3		3.4	100	CLAY
19.0	916	1052		921	976		19.1	179	177	0.07	4.2	1.9		1.0	3.1		3.0	98	CLAY
19.2	897	1039		902	963		19.1	181	179	0.08	4.0	2.1		0.98	3.0		3.3	95	CLAY
19.4	934	1080		939	1004		19.1	183	181	0.09	4.1	2.3		1.0	3.1		3.6	100	CLAY
19.6	957	1101		962	1025		19.1	185	182	0.08	4.2	2.2		1.0	3.2		3.5	103	CLAY
19.8	924	1055		930	979		19.1	186	184	0.07	4.0	1.7		0.98	3.0		2.7	97	CLAY
20.0	950	1089		955	1013		19.1	188	186	0.08	4.1	2.0		1.0	3.1		3.2	101	CLAY
20.2	971	1109		976	1033		19.1	190	188	0.07	4.1	2.0		1.0	3.1		3.1	104	CLAY
20.4	971	1113		976	1037		19.1	192	190	0.08	4.1	2.1		1.0	3.1		3.3	103	CLAY
20.6	973	1135		977	1059		19.1	194	192	0.10	4.0	2.8		0.99	3.0		4.5	103	CLAY

D.IV

T-F 1 - Tabular data: Vs, Go, Ed, Vs Repeatability

Each Vs value in the 'Vs Repeatability' column corresponds to a distinct energization.

Z	Vs	Go	Rho	Ed	Go/Ed	Id	Kd	Vs Repeatability	Var Coeff.
[m]	[m/s]	[MPa]	[kg/m^3]	[MPa]				[m/s]	[%]
4.50	144	40.3	1942	1.68	24.03	0.15	6.7	148,141,144	2.00
5.00	122	28.8	1934	1.53	18.81	0.13	6.6	127,104,134	10.51
5.50	149	42.8	1927	1.44	29.72	0.11	6.5	149,150,149	0.39
6.00	164	51.6	1919	1.24	41.66	0.09	6.2	153,171,168	4.80
6.50	169	54.6	1911	1.79	30.58	0.13	6.2	175,166,167	2.39
7.00	172	56.3	1904	1.71	32.89	0.12	5.8	175,170,170	1.38
7.50	188	67.0	1896	1.68	39.98	0.11	5.7	188,189,186	0.69
8.00	188	67.1	1898	1.02	65.76	0.07	5.6	191,187,187	1.02
8.50	195	72.3	1900	1.11	65.02	0.07	5.6	195,194,197	0.66
9.00	188	67.2	1902	1.35	49.87	0.08	5.3	188,185,191	1.30
9.50	187	66.6	1904	1.46	45.69	0.09	5.2	182,190,190	2.02
10.00	180	61.8	1906	1.53	40.36	0.09	5.1	184,184,172	3.14
10.50	180	61.8	1908	1.04	59.54	0.06	5.0	180,180,179	0.32
11.00	185	65.4	1910	0.84	78.02	0.05	5.0	186,184,185	0.44
11.50	191	69.8	1912	1.24	56.32	0.07	4.7	186,192,196	2.16
12.00	191	69.8	1914	0.95	73.72	0.05	4.8	193,189,191	0.85
12.50	202	78.2	1916	1.02	76.65	0.06	4.4	201,201,203	0.50
13.00	197	74.5	1918	1.31	56.76	0.07	4.4	198,198,194	0.97
13.50	207	82.3	1920	1.60	51.33	0.09	4.2	205,208,208	0.68
14.00	207	82.4	1923	1.17	70.66	0.07	3.8	209,209,204	1.15
14.50	214	88.1	1925	1.60	54.98	0.09	3.5	221,212,209	2.38
15.00	205	81.0	1927	1.09	74.07	0.07	3.4	201,209,205	1.59
15.50	198	75.6	1929	1.79	42.35	0.09	4.1	190,199,204	2.93
16.00	216	90.1	1931	1.28	70.64	0.06	4.2	221,209,217	2.31
16.50	224	97.0	1933	1.53	63.37	0.06	4.4	229,219,224	1.82
17.00	222	95.4	1935	1.79	53.41	0.07	4.5	222,224,220	0.74
17.50	228	101	1937	1.77	56.98	0.07	4.4	230,225,230	1.04
18.00	215	89.6	1939	2.22	40.32	0.09	4.3	220,212,214	1.59
18.50	233	105	1941	1.71	61.53	0.07	4.3	239,235,226	2.34
19.00	237	109	1943	1.89	57.60	0.07	4.2	244,236,231	2.26
19.50	238	110	1945	2.22	49.57	0.08	4.2	243,240,230	2.34
20.00	236	108	1947	2.00	54.11	0.08	4.1	231,239,237	1.45

APPENDIX E – Theory of Geotechnical Earthquake Engineering

E.1   Theory of Dynamics

The theory of dynamics lies behind site response analysis and soil-structure interaction, and therefore the development of response spectra. It is based on a single degree of freedom (1-DOF) system with an applied load (motion).

E.1.1 Single Degree of Freedom System

As (Kaynia, 2017) states it is beneficial to idealise structures, objects and isolated systems as simple 1-DOF systems consisting of a mass, spring and damper as shown in Figure E.1. In such a way, it is possible to model the response of the system when subjected to an impact, noise or vibration such as an earthquake.
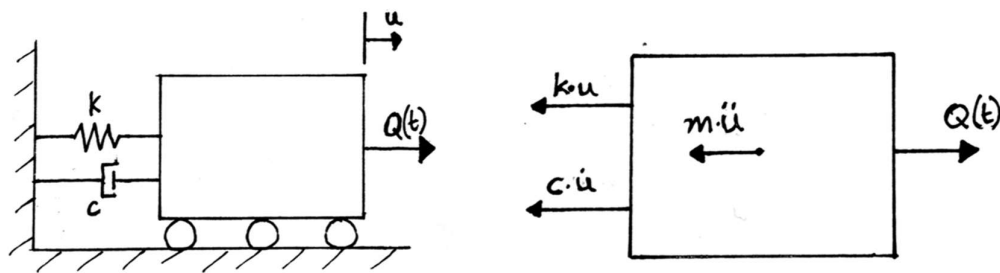

Figure E.1: A sketch of a simple single degree of freedom system illustrating dynamic equilibrium (taken from Figure 1.5, (Nordal, 2017)).

The theory of 1-DOF systems is outlined by Nordal (2017), where the response of the system and the applied load can be assumed as having a harmonic motion as shown in Figure E.2
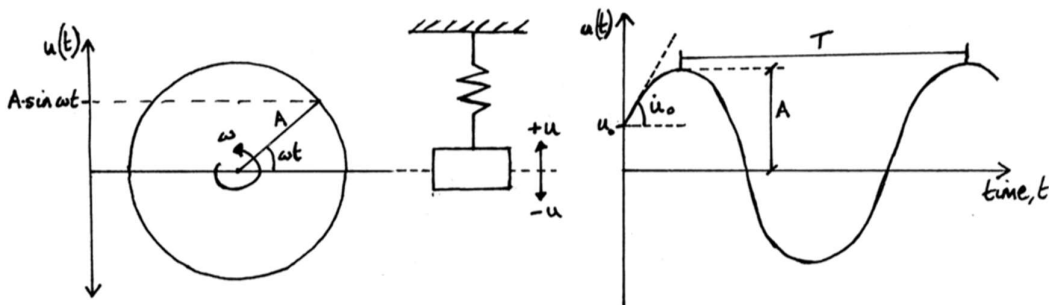

Figure E.2: Illustration of harmonic oscillation and the terminology used (modified from Figure 1.1, (Nordal, 2017)).

In **Error! Reference source not found.**, the response of the system is displayed as the displacement, u, which varies with time. From this the velocity and acceleration can be found by integration over time:

Displacement, $u = A\,sin\,\omega t$

Velocity, $\dot{u} = \frac{dz}{dt} = A\omega\,cos\,\omega t$

Acceleration, $\ddot{u} = \frac{dz^2}{d^2 t} = -A\,sin\,\omega t$

where A is the displacement amplitude from a mean position, ω is the angular frequency ($=2\pi/T$), T is the time period for a full cycle and f is the frequency ($=1/T$).

E.1.2 Dynamic equilibrium

Newton's second law defines dynamic equilibrium such that the forces on the system should be equal to the product of the mass and acceleration of the system. This is illustrated in Figure E.1, where the applied force is assumed as a harmonic load, $Q(t) = Q_0\,sin\,\bar{\omega}t$. As such, dynamic equilibrium of the system can be written:

$$m\ddot{u}(t) + c\dot{u}(t) + ku(t) = Q_0\,sin\,\bar{\omega}t$$

where m is the mass of the system, k is the stiffness of the system, c is the viscous damping coefficient and $\bar{\omega}$ is the angular frequency of the applied loaE.

Before presenting the solution of the dynamic equilibrium equation (the response of the system), it is first necessary to define a few more properties of a 1-DOF system. Dynamic equilibrium is only satisfied when the system is in its natural state of free vibration ((Nordal, 2017)) at a particular frequency called the undamped natural angular frequency:

$$\omega_n = \sqrt{\frac{k}{m}}$$

When a load is applied and the angular frequency of that load is equal to the natural angular frequency of the system $\omega_n = \bar{\omega}$, then the system will be at resonance. The ratio between these frequencies is called frequency ratio:

$$\beta = \frac{\bar{\omega}}{\omega_n}$$

where resonance is defined by $\beta = 1$. In such undamped cases, resonance means the response of the system (displacement) will reach infinity. However, such undamped systems do not exist ((S. L. Kramer, 1996)).

E.1.3 Damping

It is generally the case that after a load is applied to a system, the response attributed to that load will gradually diminish with time and the system will return to its natural equilibrium (free vibration) state. S. L. Kramer (1996) states that in real systems, this reduction in energy can be

due to friction, heat generation, air resistance or other physical mechanisms. In particular in real materials such as soils, through which a wave is travelling, part of the elastic energy is converted to heat resulting in a decrease in amplitude of the wave, known as material damping. The various mechanisms are not fully understood in order to be modelled separately, so are usually lumped together in one convenient damping mechanism. The effect of damping and can be defined by the viscous damping ratio, D:

$$D = \frac{c}{c_{cr}}$$

which is the ratio between the viscous damping coefficient, c and the critical damping, c_{cr}:

$$c_{cr} = 2m\omega_n = 2\sqrt{mk}$$

When $c = c_{cr}$ ($D=1$) this is the definition of critical damping, which is when no actual vibration arises and there is a simple asymptotic decay back to static equilibrium ((Nordal, 2017)). Over critical damping occurs when $D>1$. Both these situations are not relevant to earthquake engineering where critical underdamping ($D<1$) is of concern ((S. L. Kramer, 1996)). An example of this is presented in Figure E.3.
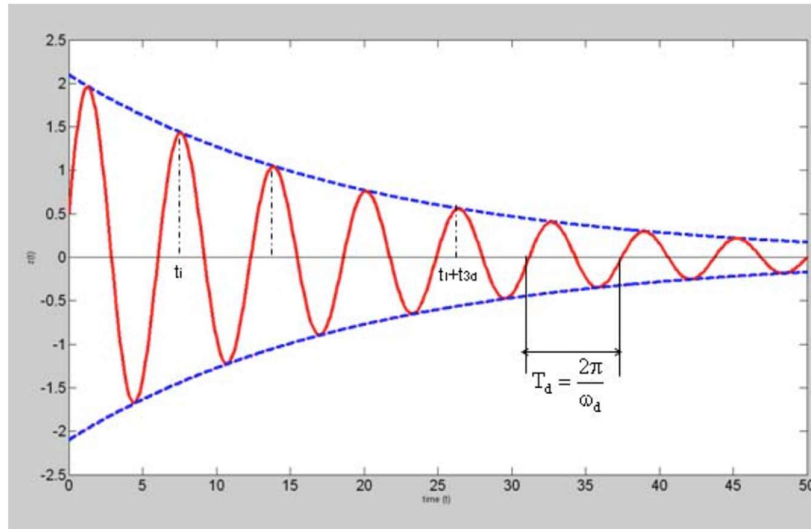

Figure E.3: Undercritical damping (Figure 1.11, (Nordal, 2017))

Due to the damping in a system, the natural angular frequency of the system will be modified as such ((Nordal, 2017)):

$$\omega_d = \omega_n\sqrt{1 - D^2}$$

where ω_d is the damped natural angular frequency and consequently there is a damped natural period:

$$T_d = \frac{2\pi}{\omega_d}$$

For a small value of damping there is only a very small change to the natural frequency. For example, a damping ratio of 5% results in $\omega_d = 0.9987 \cdot \omega_n$. The damping ratio can be measured by the ratio between neighbouring amplitudes over several oscillations, known as the logarithmic decrement, which is a function of D ((Nordal, 2017)):

$$\nabla = 2\pi \frac{D}{\sqrt{1 - D^2}}$$

E.1.4 Energy dissipation

As described above in section E.1.3, viscous damping is used to represent the loss of elastic energy in a system. It is possible to determine the energy loss per cycle of the 1-DOF system from the force displacement hysteresis loop ((S. L. Kramer, 1996) and (Nordal, 2017)) as shown in Figure E.4.
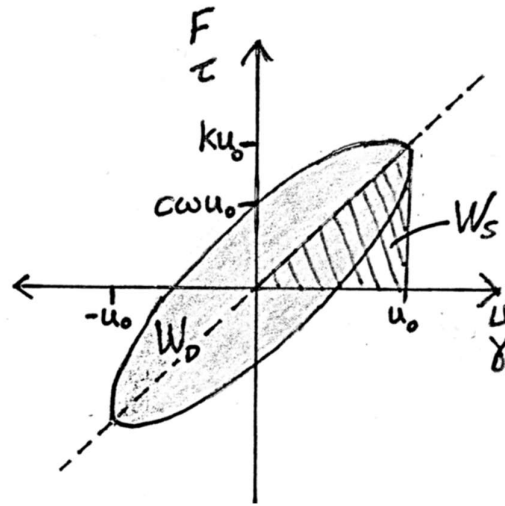

Figure E.4: Hysteresis loop illustrating energy loss per cycle due to viscous damping (W_D) and stored energy (W_S) of a 1-DOF system from a measured hysteresis loop (combination of Figures B.15 and B.16, (S. L. Kramer, 1996)).

With harmonic displacement:

$$u\,(t) = u_0 \sin \omega t$$

the net force is balanced by the dashpot and the spring:

$$F(t) = ku(t) + c\dot{u}(t) = ku_0 \sin \omega t + c\omega u_0 \cos \omega t$$

The energy loss of one cycle between time $t_0 = 0$ and $t_0 + 2\pi/\overline{\omega} = T$ can be found from the area of the ellipse:

$$W_D = \int_0^T F \frac{du}{dt} dt = \pi c \omega u_0^2$$

The dashed line in Figure E.4 represents an undamped system, giving a linear elastic stress-strain behaviour and hence zero energy loss.

As illustrated in Figure E.4, the strain energy stored in the system is found from the maximum displacement and force:

$$W_s = \frac{1}{2} k u_0^2$$

One finds:

$$D = \frac{W_D}{4\pi W_S}$$

which concludes that the damping ratio can be determined from the measured hysteresis loop of a 1-DOF system.

E.1.5 Solution of the dynamic equilibrium equation

It is now possible to present the solution to the dynamic equilibrium equation. Solving the equation in two parts; the homogeneous part for the free vibration response of a 1-DOF system and the particular part for the response due to the applied load, the total solution for the equation of motion for a damped system subjected to forced vibration, can be obtained by combining these parts and is written as ((S. L. Kramer, 1996) and (Nordal, 2017)):

$$u(t) = e^{-D\omega_n t} \left(\frac{\dot{u}_0 + D\omega_n u_0}{\omega_d} \sin \omega_d t + u_0 \sin \omega_d t \right) +$$

$$\frac{Q_0}{k} \frac{1}{(1-\beta^2) + (2D\ )^2} [(1-\beta^2) \sin \overline{\omega} t - 2D\beta \cos \overline{\omega} t]$$

where u_0 and $\dot{u}_0$ are the displacement and velocity, respectively, at the initial conditions. As S. L. Kramer (1996) points out, there are several important characteristics of the equation above that can describe the systems response. The homogeneous part (first part), which represents the effect of the initial conditions, is controlled by an exponential function and therefore dies out with time, leaving the particular part, which represents the steady state response of the system. This steady state response is out of phase with the applied load but occurs at the same frequency. Figure E.5 illustrates the relationship between the homogeneous, particular and total solutions (where z is the displacement).
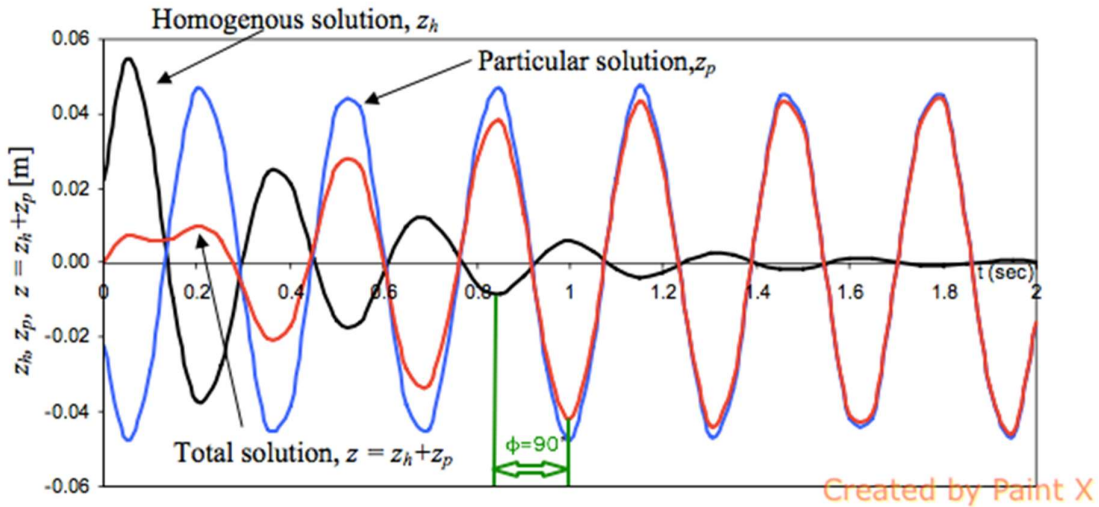
Figure E.5: Response of a damped 1-DOF system subjected to forced vibration (z=u). (Taken from an exercise on the course BA8305 Geodynamics ((Nordal, 2017)).)

In order to understand the phase difference, it is possible to introduce two new constants; an amplitude, R and phase angle, ϕ. Using trigonometric rules, it is possible to rewrite the equation above as:

$$u(t) = e^{-D\omega_n t} R_h \cos(\omega_d t - \phi_h) + R_p \sin(\overline{\omega} t - \phi_p)$$

where,

$$R_h = \sqrt{(R_h \sin \phi)^2 + (R_h \cos \phi)^2}$$

$$\phi_h = \arctan\left(\frac{R_h \sin \phi}{R_h \cos \phi}\right)$$

$$R_p = \frac{Q_0}{k} \frac{1}{(1 - \beta^2) + (2D\beta)^2}$$

$$\phi_p = \arctan\left(\frac{2D\beta}{(1 - \beta^2)}\right)$$

where the subscripts, h and p refer to the homogeneous and particular parts of the equation, respectively. It is perhaps easier to visualise this relationship with illustrations using an argand diagram or by looking at the harmonic relationships as shown in Figure E.6 and Figure E.7, respectively. Note that the phase angle in Figure E.5 is 90°.
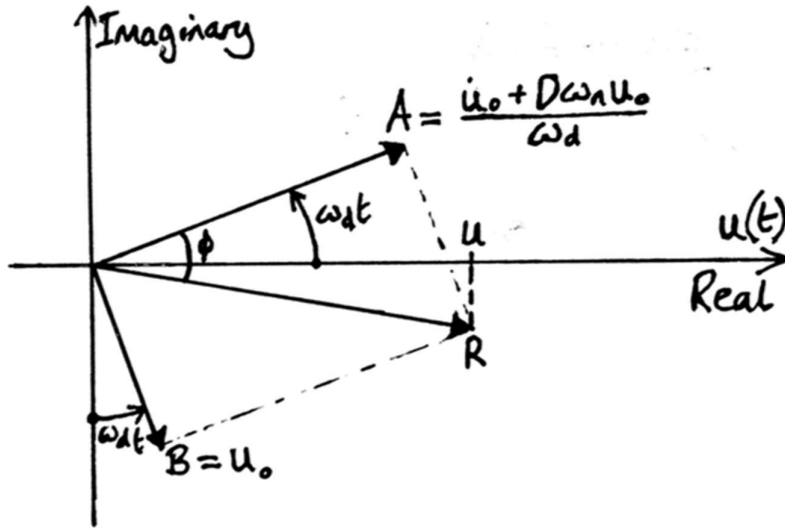
Figure E.6: Illustration of the relationship between R, φ and ω in an Argand diagram.
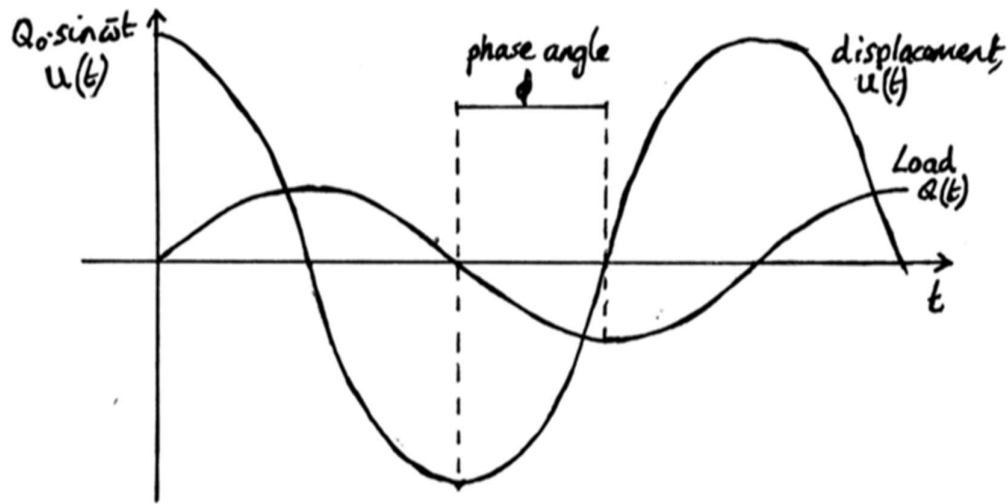

Figure E.7: Illustration of the harmonic relationships between the applied load, displacement (response) and φ.

Another important feature of the equation is the magnification of the amplitude due to the particular part of the equation (the steady state response). This is called the dynamic magnification factor ((Nordal, 2017)):

$$M = \frac{Q_0}{k} \frac{1}{\sqrt{(1-\beta^2)^2 + (2D\beta)^2}}$$

Two more important relationships to illustrate are the relationships that the magnification factor and phase angle both have with the frequency ratio. These relationships are illustrated inFigure E.8.
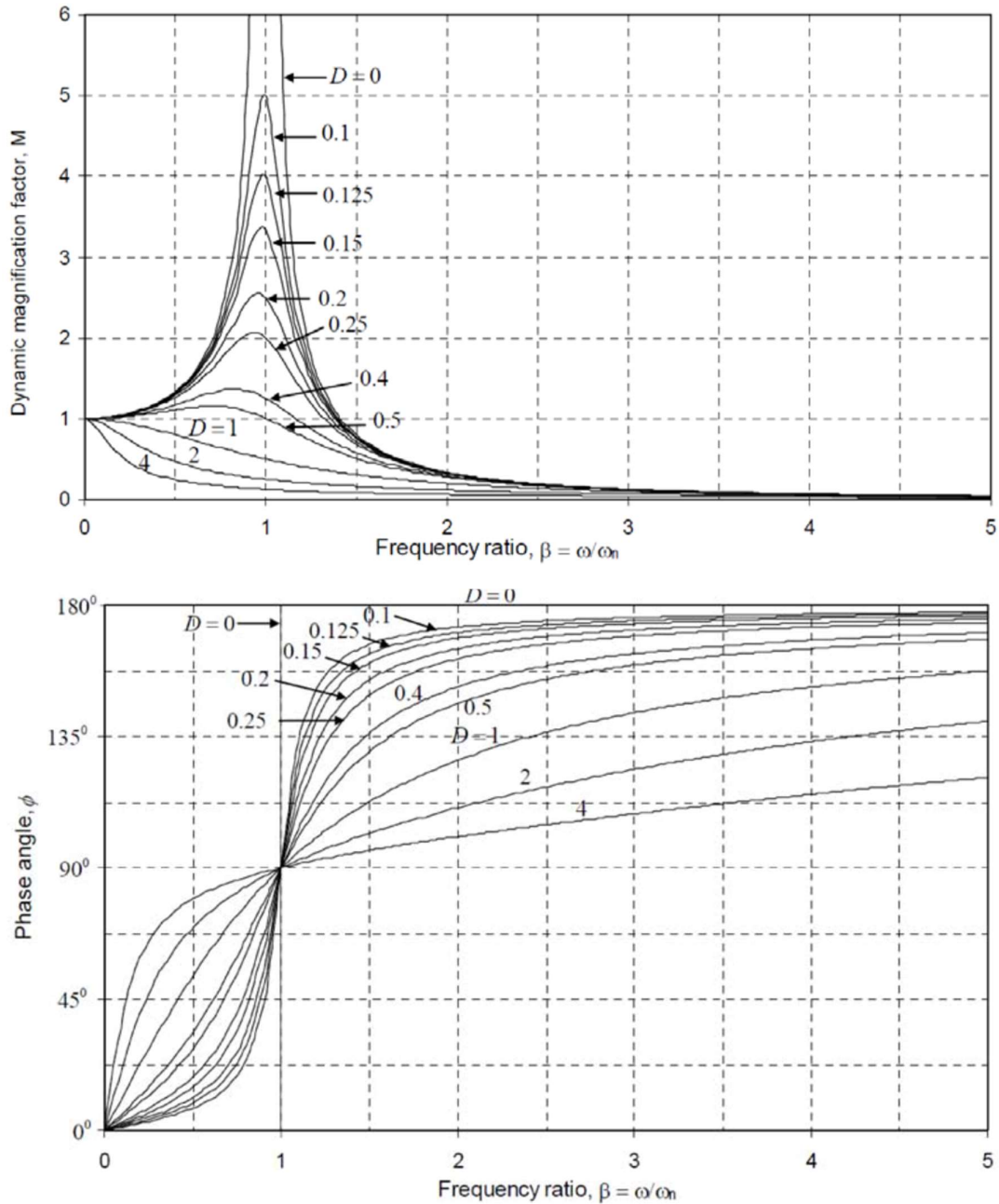
Figure E.8: Magnification factor and phase angle as a function of the frequency ratio (Figure 1.15, (Nordal, 2017))

It is important to note that the amplitudes are greatly magnified when the system is at or close to resonance ($\bar{\omega} \approx \omega_n$). When the angular frequency of the applied load is less than the natural angular frequency of the 1-DOF system ($\bar{\omega} < \omega_n$) then the response will still be amplified to some degree. On the other hand, when the angular frequency of the applied load is more than the natural angular frequency of the 1-DOF system ($\bar{\omega} > \sim 1.4\ \omega_n$) then the response will have a smaller amplitude than the applied loaE.

E.1.6 Transfer Functions

To conclude the importance of this background theory of dynamics, the concept of a transfer function is introduceE. As S. L. Kramer (1996) states, a transfer function may be thought of as a filter, which allows computation of the response to complicated loading patterns. An example of how such a function works is illustrated in Figure 2.1. In the case of a simple 1-DOF system that is accelerated due to external loading, the transfer function can be written:

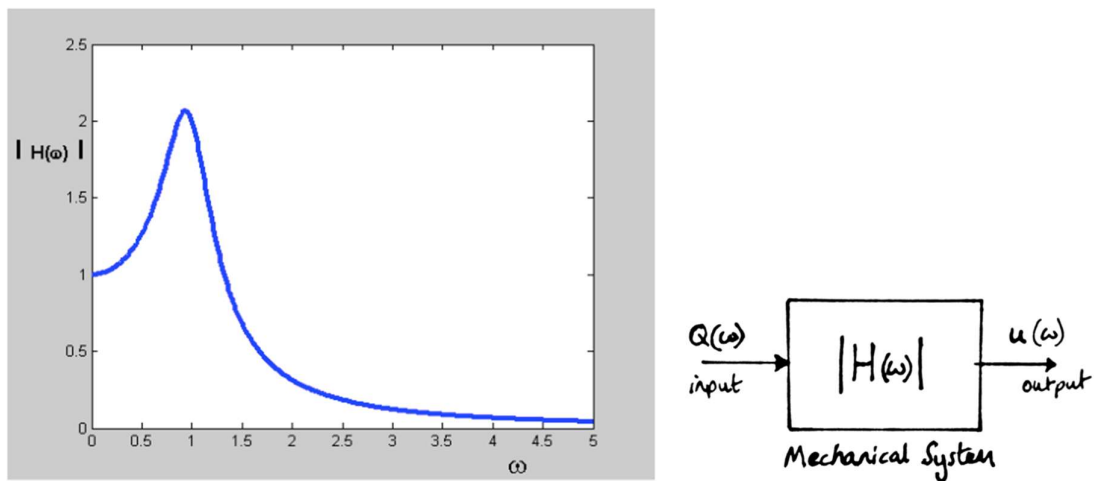$$|H(\omega)| = \frac{1/k}{\sqrt{(1-\beta^2)^2 + (2D\beta)^2}} = \frac{1}{k}M \qquad [A.1]$$

Figure 2.1: An illustration of how a transfer function works (Figure 1.18, (Nordal, 2017))

E.2 Earthquakes and Seismic Waves

It is well understood that earthquakes are related to plate tectonics and tend to occur due to movement along plate boundaries. There are three main types of plate boundaries; a spreading ridge; a subduction zone and a transform boundary ((S. Kramer, 2017)). Shear stresses build up at or near these plate boundaries and are stored as elastic strain energy, until the shear strength of the rock is reacheE. The accumulated strain energy is then released along associated faults. This process is known as elastic rebound theory. There are three main types of faults; normal; reverse and strike slip as shown in Figure E.10.
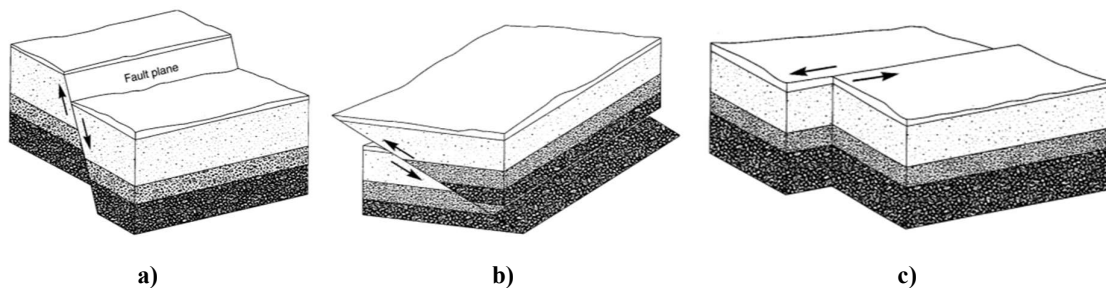

a)   b)   c)

Figure E.10: Three main types of fault movement ((S. L. Kramer, 1996)). a) Normal fault, b) Reverse fault and c) Strike Slip fault.

Seismic moment is one way of measuring the size, or more accurately, the energy released (work done) by an earthquake and is defined by

$$M_0 = \mu \cdot A \cdot D$$

where μ is the rupture strength of the material, A is the rupture area and D is the average amount of slip. Earthquake size (magnitude) is not necessarily relevant for earthquake engineering. Other relevant parameters are discussed later in Section E.2.6, but it is first important to outline how the energy is dispersed from an earthquake hypocentre in the form of seismic waves.

The epicentre of an earthquake is located on the earth surface above the hypocentre, which is the mean centre of the rupture surface/fault. It is from the hypocentre (source) that the energy originates and is propagated by seismic waves. There are four types of seismic waves; Primary waves (P-waves); Secondary waves (S-waves); Love waves and Rayleigh waves. P- and S-waves are known as body waves and originate at the source. Love and Rayleigh waves are known as surface waves as they are a result of body waves interacting with the ground surface, and their effects die out with depth. A summary of the wave types is shown in Figure E.11. It is illustrated by the squares in the figure that P-waves involve no shear movement as the rectangles remain rectangular, also the particle motion is parallel to the propagation direction of the wave. S-waves involve perpendicular motion of the particles to the direction of propagation and the rectangles are sheared without any volume change.
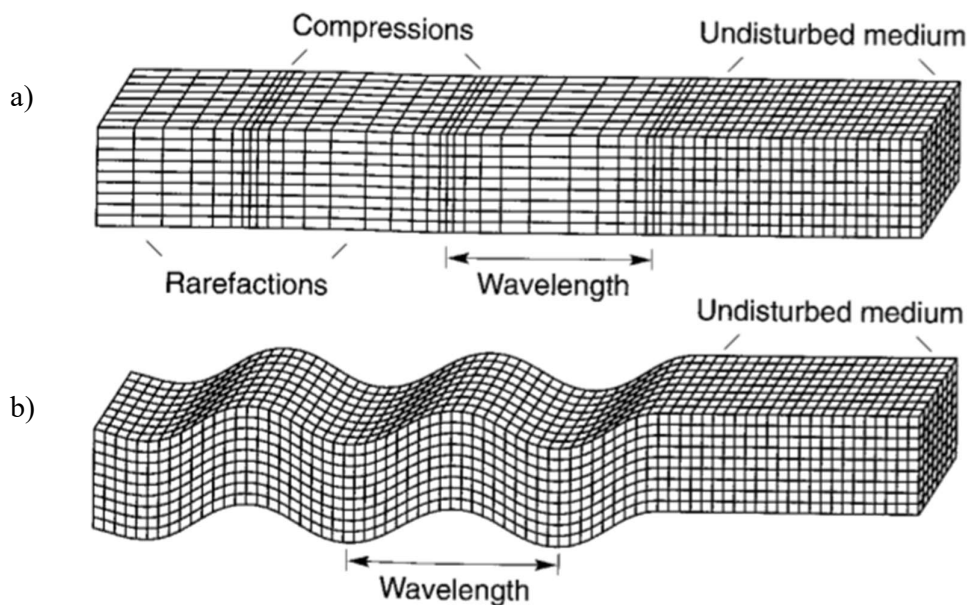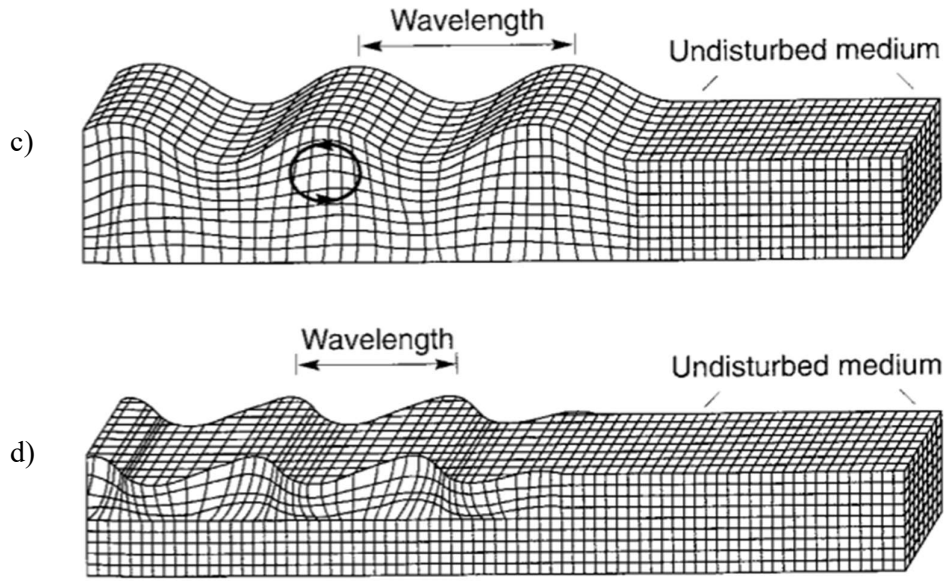
Figure E.11: Seismic wave types ((S. L. Kramer, 1996)). a) P-waves (compressional), b) S-waves, c) Rayleigh waves and d) Love waves.

E.2.1 Wave Propagation

The theory of wave propagation that is applied in geotechnical earthquake engineering, comes from looking at waves in an infinitely long elastic bar. It is found that the general form of a one-dimensional wave is given by the equation:

$$\frac{\delta^2 u}{\delta t^2} = v_c^2 \, \frac{\delta^2 u}{\delta x^2}$$

and the general form of the solution is:

$$z(t, x) = f(v_c t + x) + h(v_c t + x)$$

where z is displacement, t is time, x is distance and V_c is the velocity of the wave given by:

$$V_c = \sqrt{\frac{E}{\rho}}$$

where E is the Young's modulus and ρ the density of the elastic bar.

For the purposes of body waves, it is necessary to apply this relationship to an elastic 3-D body where the same relation exists, but using shear wave velocity and compressional wave velocity for S-waves and P-waves, respectively:

$$v_s = \sqrt{\frac{G}{\rho}}$$

$$v_p = \sqrt{\frac{M}{\rho}}$$

Where G is the shear modulus of the material the wave is travelling through, and M is the constrained modulus. Both are elastic parameters that are commonly used to describe the stiffness of soils.

E.2.2 Elastic Half-space and Surface Waves

As S. L. Kramer (1996) states, for earthquake analysis it is idealistic to consider the earth as a semi-infinite body with a planar free surface, referred to as an elastic half-space by Nordal (2017). Therefore, it is necessary to understand the effects of a free surface on seismic wave behaviour. Since the surface of the earth is also formed of layers of rock and soil, with different stiffness properties, it is also important to understand these effects on the behaviour of seismic waves.

At the surface, the elastic half-space conditions favour the existence of surface waves and it is Rayleigh waves that dominate the surface motion. As previously mentioned (Figure E.11) Rayleigh waves are a combination of P- and S-waves where the particles have an ellipsoidal movement and they are strongly limited by depth. The velocity of a Rayleigh wave is slightly slower than an S-wave for all Poisson ratios except 0.5 ((S. L. Kramer, 1996)). A comparison of the P-wave and Rayleigh wave velocities to the velocity of an S-wave is presented in Figure E.12.
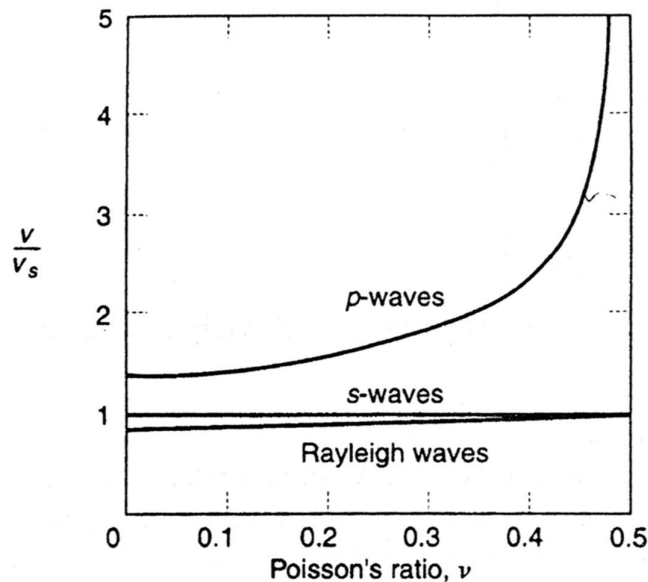
Figure E.12: Variation of Rayleigh wave and body wave velocities with Poisson's ratio (Figure 5.9, (S. L. Kramer, 1996))

Since Rayleigh waves come from a combination of P- and S- waves and interaction with the free surface, they tend to have horizontal and vertical components as illustrated in Figure E.13. S. L. Kramer (1996) presents the equations which define these components and it is seen that they are out of phase by 90°, and hence the horizontal displacement will be zero when the vertical is maximum and vice versa. Rayleigh waves are thought to be significant from approximately a few tens of kilometres from the epicentre.

Amplitude at Depth z / Amplitude at Surface

Horizontal Component

$\nu = 0.25$
$\nu = 0.33$
$\nu = 0.40$
$\nu = 0.50$

Vertical Component

$\nu = 0.25$
$\nu = 0.33$
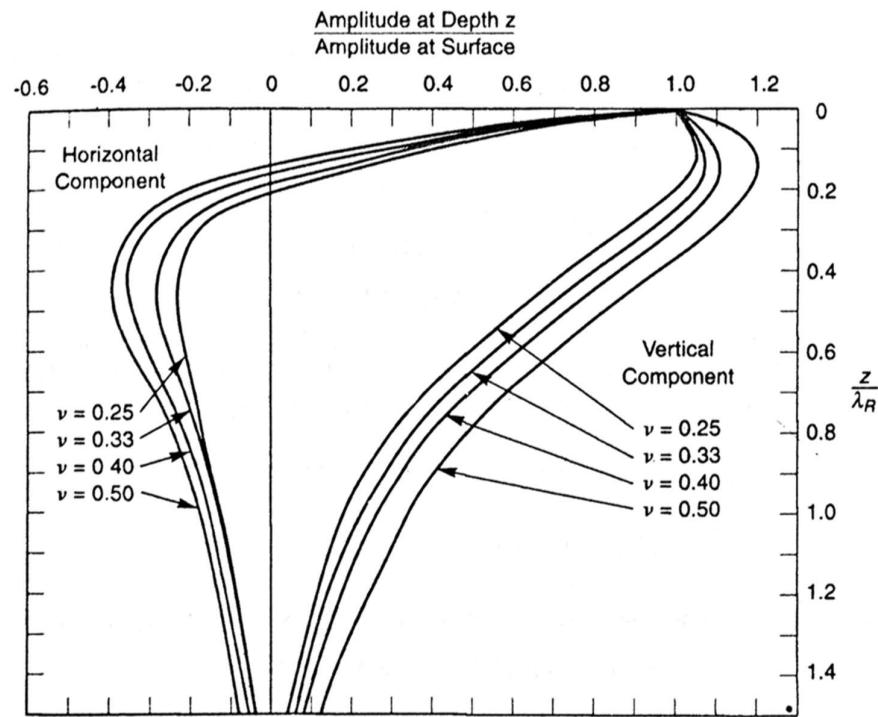$\nu = 0.40$
$\nu = 0.50$

$\frac{z}{\lambda_R}$

Figure E.13: Variation of the horizontal and vertical components of a Rayleigh wave with depth (Figure 5.10, (S. L. Kramer, 1996))

Love waves tend to only exist if the elastic half-space is overlain by a surficial layer with a lower body wave velocity. Therefore, these are likely to be significant when looking at soft soil over a stiff soil or elastic rock for example. Again these waves are a result of the interaction of P- and S- waves with a free surface, and are often described as horizontal shear motions that become trapped by multiple reflections within the soft layer ((S. L. Kramer, 1996)). This effect is illustrated in Figure E.14. The love wave particle displacement amplitude (denoted v in this diagram) varies sinusoidally within the soft layer then decays exponentially in the elastic half space.

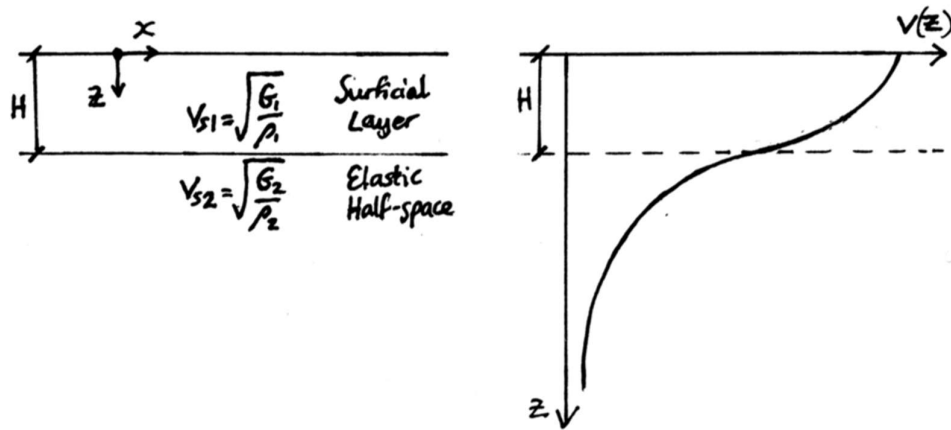*Figure 2.2: The variation of Love wave particle displacement amplitude for a surficial soft layer overlying an elastic half-space where $G_1/\rho_1 << G_2/\rho_2$ (taken from Figure 5.11 and 5.12, (S. L. Kramer, 1996))*

Figure E.15 indicates that the Love waves are dispersive. That is to say that they travel at different velocities depending on the frequency (wavelength) ((S. L. Kramer, 1996)). Love waves are also frequency dependant with velocities equal to S-wave velocity in the elastic half-space (v_{s2}), at low frequencies, and velocities equal to S-wave velocity in the surficial layer (v_{s1}).
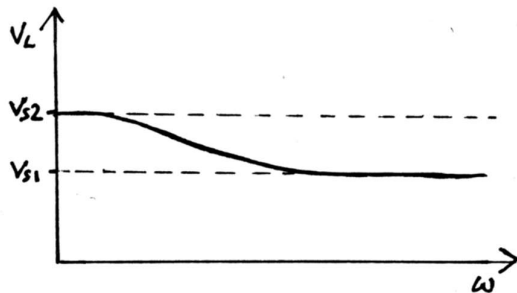

Figure E.15: Frequency dependant velocity of Love waves (taken from Figure 5.13, (S. L. Kramer, 1996))

Rayleigh waves are nondispersive in a homogenous elastic half-space, although they are dispersive in real heterogeneous materials such as the earth's crust where the stiffness of soils and rock increase with depth ((S. L. Kramer, 1996)). In fact, the dispersion of Rayleigh waves is used as one of the main field techniques for determining subsurface stiffness'.

E.2.3 Material Boundaries

It is briefly necessary to return to an infinite elastic bar model to describe material boundary effects on the propagation of seismic waves. At a free boundary (earth's surface), the polarity of the reflected wave is opposite that of the incident wave ((S. Kramer, 2017)) and thus the stresses will cancel each other out, whilst the displacement is momentarily doubled. This is well illustrated in Figure E.16. This figure also illustrates what happens at a fixed boundary, where no displacement can occur and therefore the stress is doubled, and a wave of equal amplitude

and polarity is reflected. A fixed end situation does not occur within the earth's crust as there are no infinitely stiff materials. It is somewhere between these two extremes that needs to be considered for layered materials such as the subsurface of the earth.
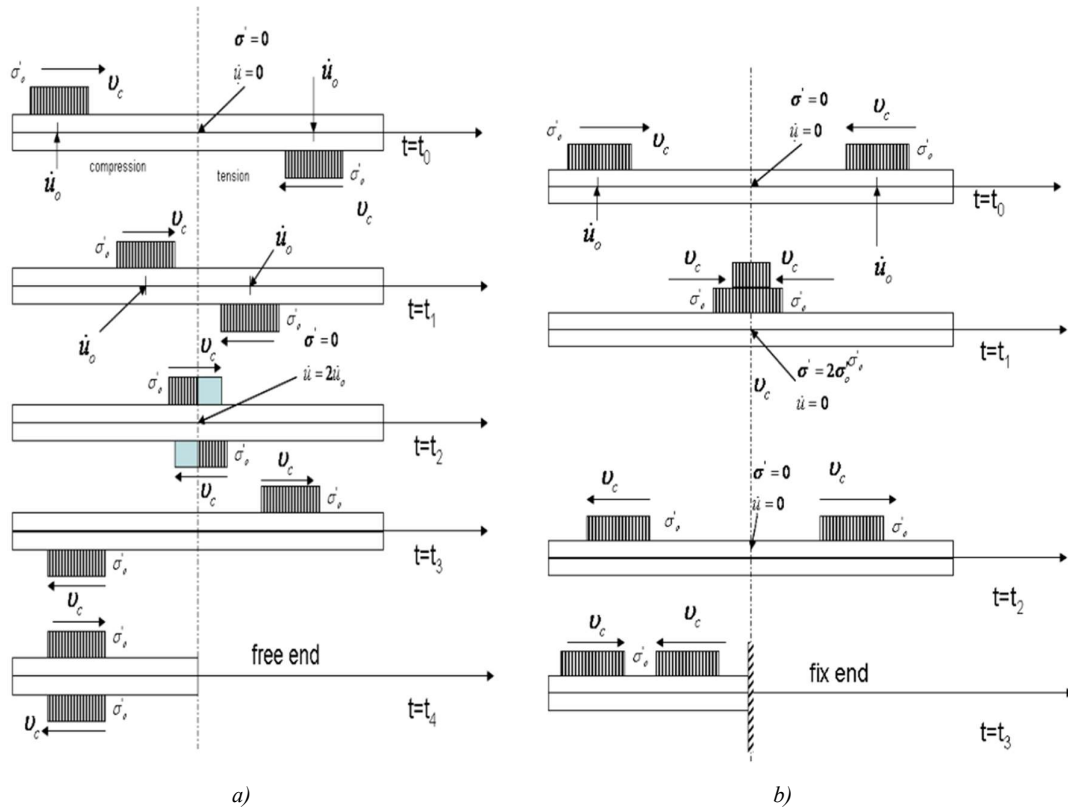

Figure E.16: a) Free-end - A compression wave meets an identical tension wave in an infinite bar. b) Fixed-end - A compression wave meets an identical compression wave in an infinite bar. (Figure 2.5 and 2.7, (Nordal, 2017)).

At a material boundary with two differing material properties, as shown in Figure E.17, equilibrium, compatibility of displacements and continuity of stresses must be satisfied ((S. L. Kramer, 1996)). This dictates that the sum of incident and reflected displacement amplitudes must equal the displacement amplitude of the transmitted wave. The same relationship applies to stresses.

$$A_i + A_r = A_t$$
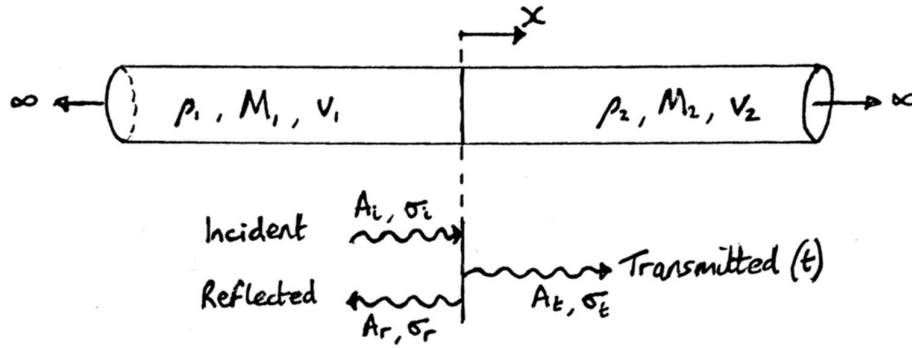
$$\sigma_i + \sigma_r = \sigma_t$$

Figure E.17: One dimensional wave propagation between two different materials (taken from Figure 5.14, (S. L. Kramer, 1996)).

As such it is possible to define an impedance ratio ((S. L. Kramer, 1996)):

$$\alpha_z = \frac{\rho_2 v_2}{\rho_1 v_1}$$

which applies to displacement amplitudes:

$$A_r = \frac{1 - \alpha_z}{1 + \alpha_z} A_i$$

$$A_t = \frac{2}{1 + \alpha_z} A_i$$

and stresses:

$$\sigma_r = \frac{\alpha_z - 1}{1 + \alpha_z} \sigma_i$$

$$\sigma_t = \frac{2\alpha_z}{1 + \alpha_z} \sigma_i$$

It is worth noting that the impedance ratio is a function of material density and stiffness modulus. Since densities of soils very by only approximately 1.5 and shear moduli vary much more ((S. Kramer, 2017)), impedance can be said to be much like a stiffness ratio. The impedance ratio also clearly shows that at a free end, $\alpha_z = 0$ and therefore the transmitted stress will be zero ($\sigma_t = 0$). Thus, the displacement amplitude at the free boundary will have twice the amplitude of the incident wave ($A_t = 2A_i$). Also, the reflected wave will have an equal displacement amplitude but with opposite polarity ($\sigma_r = -\sigma_i$). The fixed boundary conditions defined earlier can also be proven in the same way using $\alpha_z = \infty$, but are less important in this case. For materials with the same stiffness (and density), $\alpha_z = 1$ and there will be no reflected wave, with all energy being transmitted. For a layered body of soil with reducing stiffness towards the surface, at each layer boundary the impedance ratio will be expected somewhere between ($0 < \alpha_z < 1$). As such, at each boundary the displacement amplitude of the reflected

wave will be reduced and the displacement amplitude of the transmitted wave will increase. Therefore, there is an overall increase in the displacement amplitude of the transmitted wave, and a decrease in the stress amplitude ((S. L. Kramer, 1996)).

E.2.4 Refraction

It is now necessary to look at a 3-D elastic body to determine the behaviour of inclined waves. Snell's law, as illustrated in Figure E.18, states the angle of incidence reduces each time the velocity (function of stiffness and density) of the material decreases. A process known as refraction. Therefore, by the time the wave path from an earthquake reaches the surface, the wave propagation is more or less vertical. This concept is important when looking at ground motions for site response analysis.
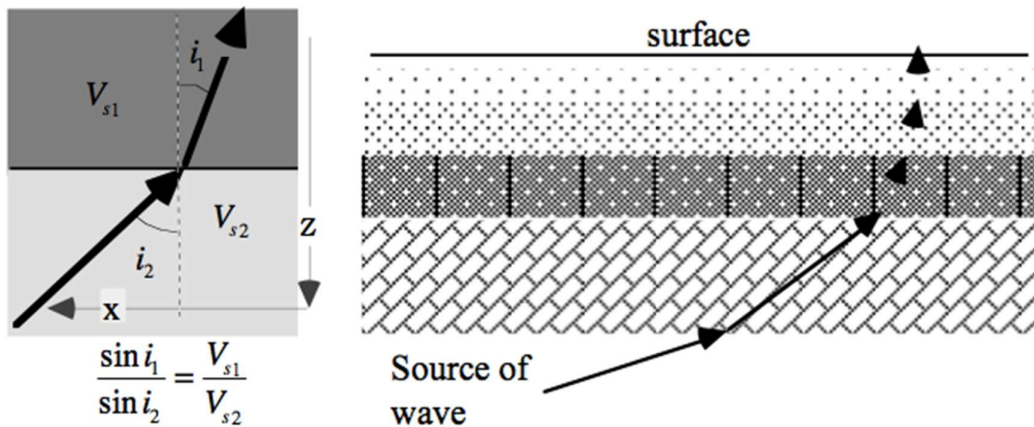

Figure E.18: Snell's law of wave refraction at an interface and wave path in a layered material (Figure 4.7 and 4.8, (Towhata, 2008)).

E.2.5 Attenuation

The boundary effects described previously involve loss of energy in the form of the reflected wave, resulting in an attenuation of the transmitted wave. There are two other forms of loss of energy that cause attenuation of waves, described by S. Kramer (2017) as material damping and radiation damping (also referred to as geometrical damping ((Nordal, 2017)), which will be used hereon). Material damping was touched on previously in Section D.1.3, when looking at how the response of a simple 1-DOF system will eventually return to its equilibrium state. In a real system, this reduction in energy can be due to friction, heat generation, air resistance or other physical mechanisms. Particular to soils, part of the elastic energy is converted to heat due to hysteresis type behaviour caused by slippage of grains relative to one another. S. L. Kramer (1996) states that the damping ratio, D can be related to the force-displacement (or stress-strain) loop as was discussed in Section E.1.4 (Figure E.4).

Geometric damping is described by Nordal (2017) as the reduction in amplitude of the waves, with distance from the source, due to increased surface area or volume for the same energy to be dissipated over. As S. L. Kramer (1996) states this geometric damping is found to cause the amplitude to decrease at a rate of 1/r, when analogous to a point source with spherical wave fronts. It was also shown by Bullen (1953) that the geometric attenuation of surface waves reduces the amplitude by 1/√r, which is slower and therefore explains the domination of surface waves at larger distances from the epicentre. It is also found ((Nordal, 2017) and (Tonouchi, Sakayama, & Imai, 1982)) that material damping of S-waves varies with epicentral distance, with the reduction of amplitude by:

$$e^{-\alpha \cdot r}$$

where

$$\alpha = \frac{\omega D_m}{v}$$

The relationship between material and geometric damping with distance is illustrated in Figure E.19 where it is shown that geometric damping has the greatest effect.
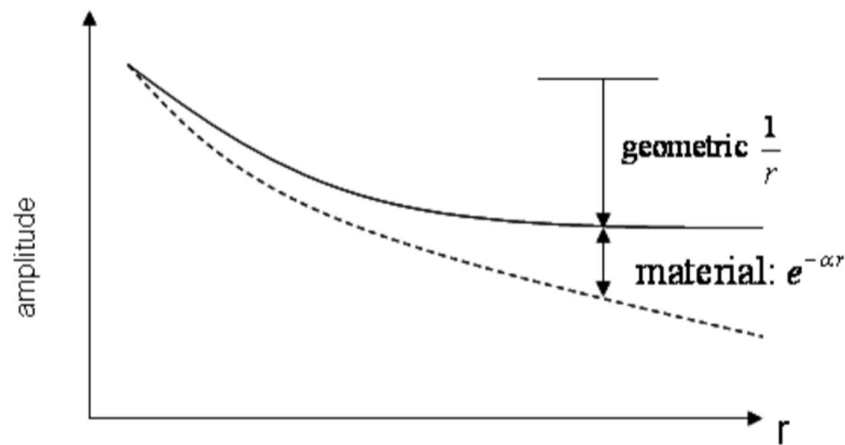

Figure E.19: Amplitude reduction with distance due to geometric and material damping (Figure 2.18, (Nordal, 2017)).

E.2.6 Ground motions

As described earlier it is possible to quantify the amount of energy released by an earthquake as its moment magnitude, but this gives us little information on the movement of the ground in terms of displacement, velocity or acceleration. There are other measure of intensity and magnitude but again these are not terribly useful for earthquake engineering design. As S. L. Kramer (1996) states there are a number of relevant ground motion parameters that are required to adequately describe ground motion for engineering purposes. In practice, at least one or more of these is required. These are:

1. amplitude
2. frequency content
3. duration of the motion

Amplitude can be acquired from the time history of an earthquake. Time histories of strong ground motions are readily available from a number of sources (eg. The U.S. Geological Survey) ((S. L. Kramer, 1996)). One of the motion parameters, displacement, velocity or acceleration is measured (most commonly acceleration) and the remaining can be computed, as shown in Figure E.20. This shows that each integration step from acceleration results in a reduced frequency.
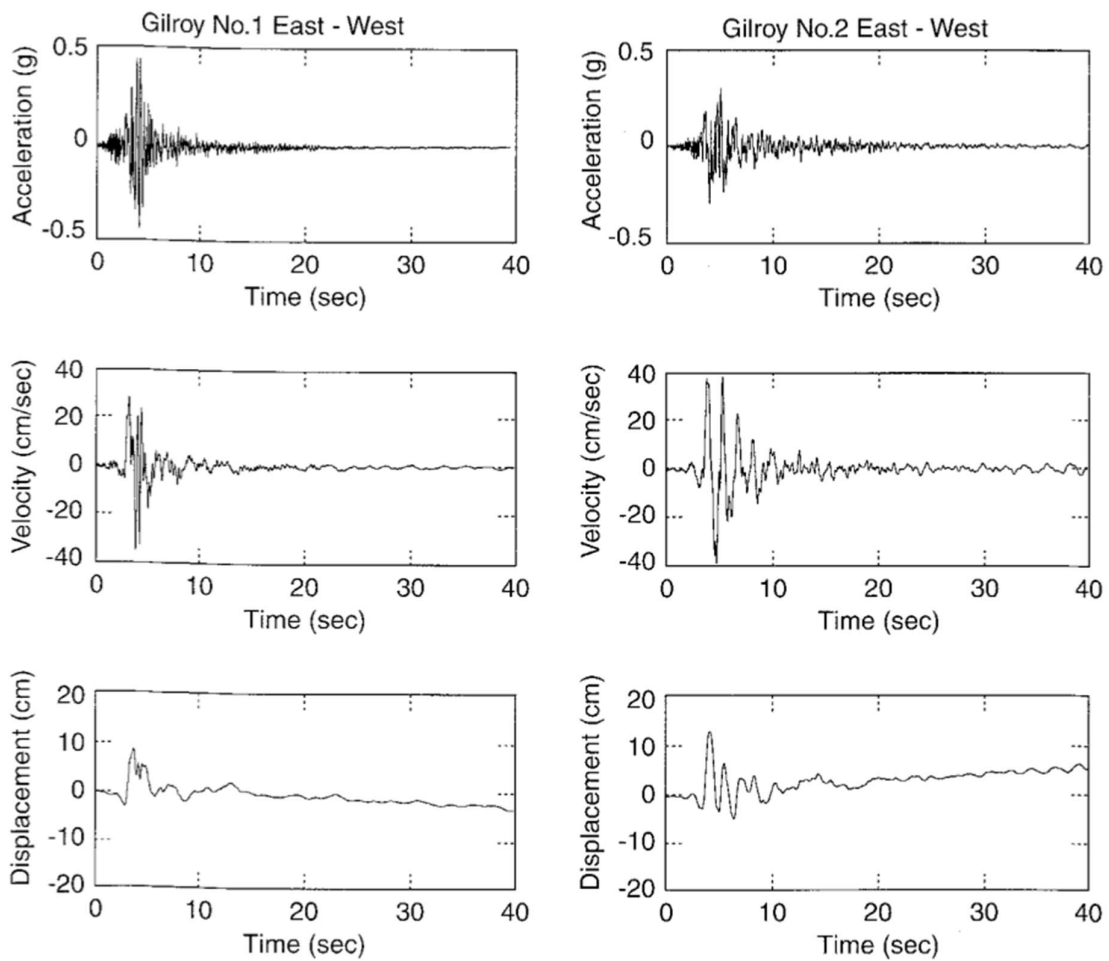

Figure E.20: Acceleration, velocity and displacement time histories for the E-W components of the Gilroy No.1 (rock) and Gilroy No. 2 (soil) strong motion records. (Figure 3.10, (S. L. Kramer, 1996))

Peak ground acceleration (PGA or a_g) is the largest absolute value of acceleration during a ground motion record. The peak horizontal acceleration (PHA) is often used in geotechnical engineering design since it has as natural relationship to inertia forces ((S. L. Kramer, 1996)) and is taken from the horizontal component of a record. The peak vertical acceleration (PVA)

is considered to be approximately 2 thirds of PHA ((Newmark & Hall, 1982)) but is variable with distance ((Abrahamson & Litehiser, 1989)). As S. L. Kramer (1996) remarks destructive motions are usually those with higher peak accelerations, but destruction is also very dependent on frequency and duration, so PGA is of very little use on its own and should be supplemented with other parameters to characterise the ground motion.

The frequency content of a ground motion is imperative for engineering design since the response of the system, be it soil or structure, is highly dependent on the load frequency as we saw from Section E.1.5 (i.e. the response is greatly amplified $\beta \approx 1$). Frequency content describes how the amplitudes of a ground motion are distributed among different frequencies ((S. L. Kramer, 1996)). There are three main techniques for determining the frequency content:

1. Fourier Spectra, which is based on the Fourier series that is the sum of a series of simple harmonic terms of different frequency, amplitude and phase:

$$x(t) = c_0 + \sum_{n=1}^{\infty} c_n \, sin(\omega_n t + \phi_n)$$

The motion can be recovered by the inverse Fourier series and therefore provides a complete description of the ground motion ((S. L. Kramer, 1996)).

2. Power Spectra, which is based on the power spectral density function and is useful to estimate the statistical properties of a ground motion and to characterise the earthquake as a random process ((S. L. Kramer, 1996)).

3. Response Spectra is the technique usually used in earthquake engineering practice. It based on the response of a 1-DOF system subjected to a load (motion) as a function of the natural frequency (or period) and damping ratio of the system. This process is the basis of building standards, such as Eurocode 8 and is described in more detail in Section 0.

The duration of a ground motion also influences the amount of destruction because a variation in the number of loading and unloading cycles effects many factors, such as stiffness and strength of a material or structure, or the build-up of pore pressure in loose saturated sands ((S. L. Kramer, 1996)). The duration can be related to the earthquake magnitude, since the amount of accumulated energy stored along the rupture is related to the length or area of the rupture surface and how long it will take to rupture. Therefore, increased earthquake magnitude will increase duration. This relationship has been quantified by Hanks and McGuire (1981), where the duration is shown to be proportional to the cube root of the seismic moment. The duration can be expressed using a threshold limit of acceleration, where the duration is defined

within the exceedance of this threshold. For example, Chang and Krinitzsky (1977) used a threshold of 0.05g for epicentral distances less than 10km to find a relationship between magnitude and duration for soil and rock sites. Duration can also be expressed in terms of number of equivalent stress cycles.

E.3   Response Spectra

A response spectrum is a tool used in earthquake engineering practice to predict response of a structure to ground motion. It based on the response of a 1-DOF system subjected to a load (ground motion) as a function of the natural frequency (or period) and damping ratio of the system. This process is the basis of building standards, such as Eurocode 8, where the building (structure) is modelled as the 1-DOF system. The response spectra used in such standards are discussed further in Section E.0. The response spectrum does not show amplification of the ground motion itself, but the amplification of spectral acceleration at different periods of the structure. For example, in Figure E.21, the time history (a) is broken down, using Fourier series, to find the maximum displacement, known as the spectral displacement S_d, at several natural periods for the 1-DOF system with 2% damping (b). In (c) the peak values are then plotted against the natural period, T_n to form the response spectrum.
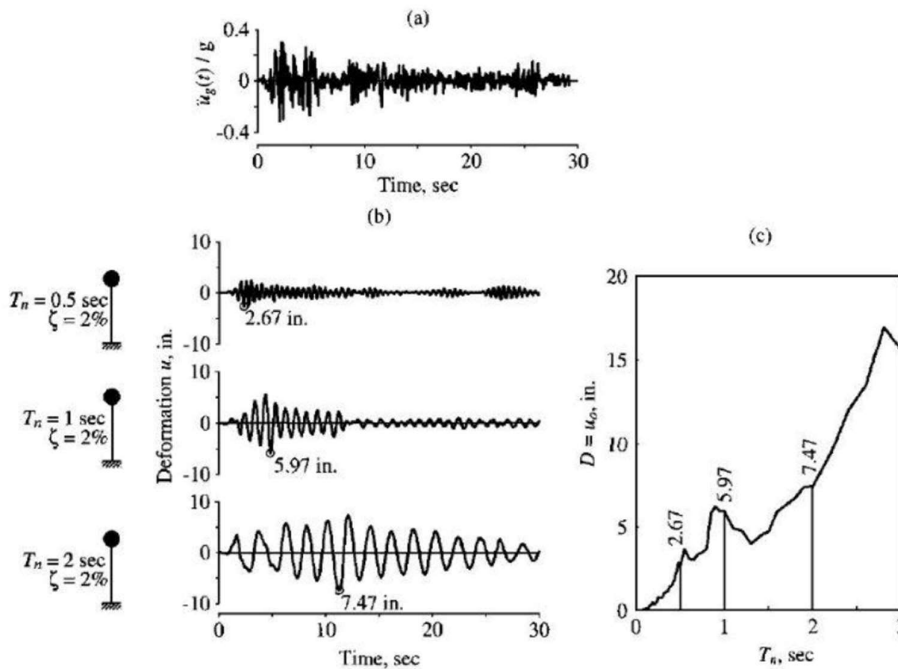

Figure E.21: Steps in creating a response spectrum ((Eiksund, 2017))

The same can be done for velocity and acceleration for the same time series to give the spectral velocity, S_v and spectral acceleration, S_a, respectively. On the other hand, the approximate relationships below can be used to find the equivalent maximum values referred to as

pseudospectral velocity (PSV) and pseudospectral acceleration (PSA). These relationships are considered good enough approximations for use in practice ((S. L. Kramer, 1996)) and come from the application of the Duhamel integral to a linear elastic 1-DOF system.

$$S_d = |z|_{max}$$

$$S_v = |\dot{z}|_{max} \approx \omega_n S_d = PSV$$

$$S_a = |\ddot{z}|_{max} \approx \omega_n^2 S_d = \omega_n \cdot PSV = PSA$$

One characteristic of a response spectrum is that the peak acceleration, velocity and displacement occur at different frequencies (or periods).

It can be beneficial to view spectra in tripartite plots as shown in Figure E.22. It is then possible to divide the spectra in to regions of acceleration-controlled, velocity-controlled and displacement-controlled.
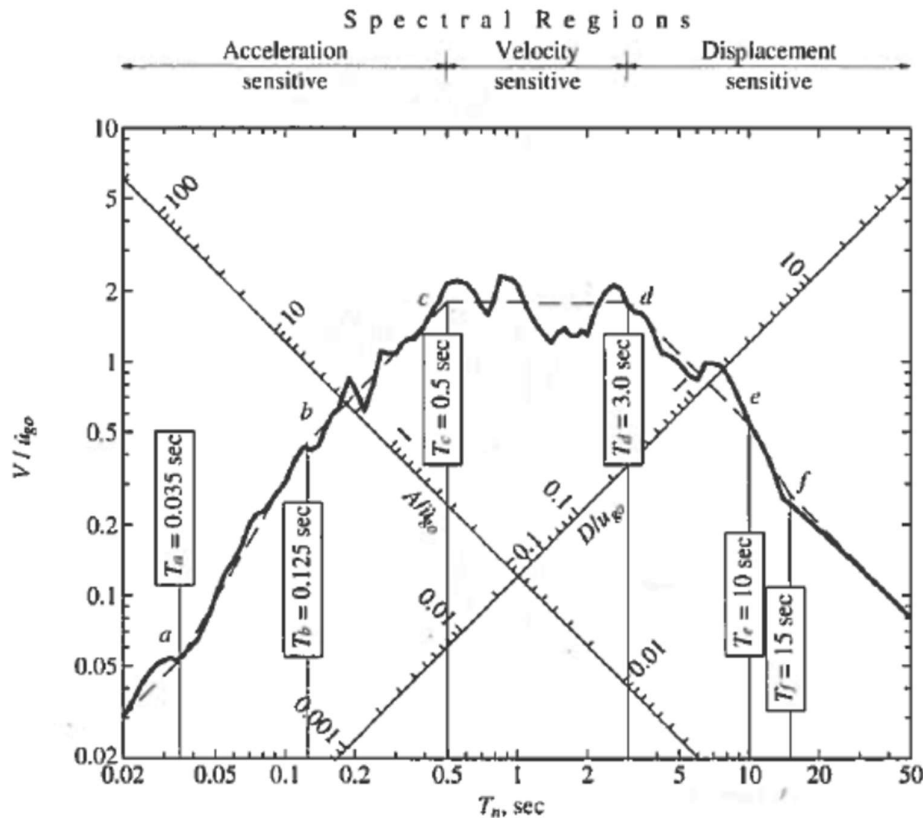

Figure E.22: Response spectra for El Centro ground motion shown by a solid line together with an idealised version shown by a dashed line, D=5% ((Eiksund, 2017))

Elastic response spectra apply to structures with assumed linear force-displacement behaviour, which is not realistic. Inelastic response spectra (also referred to as design spectra,

S. L. Kramer (1996)) can be used to account for more realistic non-linear force-displacement behaviour of a structure, by the use of a ductility factor ((S. L. Kramer, 1996)):

$$\mu = \frac{u_{max}}{u_y}$$

where u_{max} is the maximum allowable displacement and u_y is the yield displacement. It is shown that whilst total displacements increase, spectral accelerations of a system decrease with increasing ductility as shown in Figure E.23.
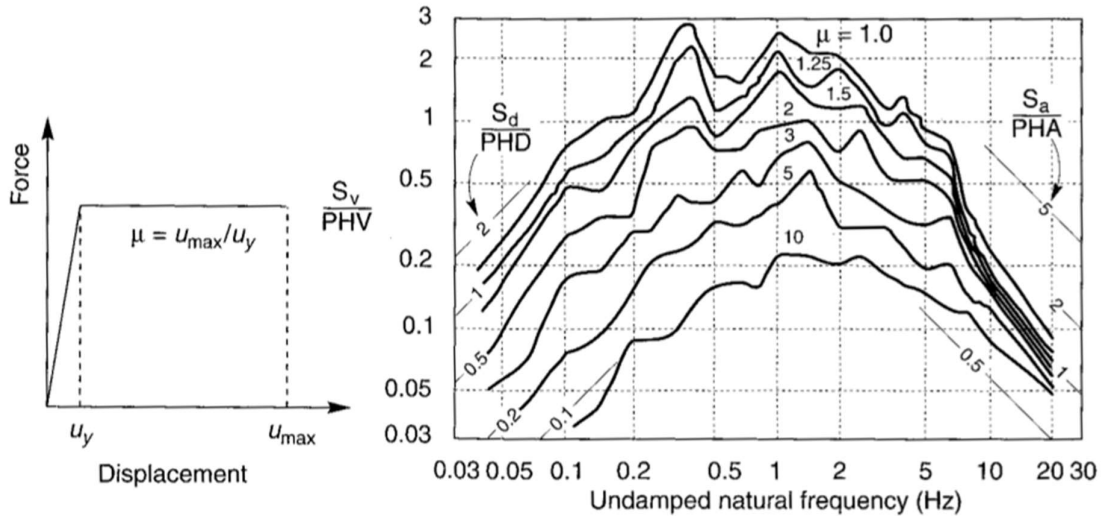

Figure E.233: Inelastic response spectra for the El Centro N-S component of the 1940 Imperial Valley earthquake. …… (Figure 3.16, (S. L. Kramer, 1996) after (Newmark & Hall, 1982))

For design purposes response spectra are often smoothed or separated into a series of straight lines such as the dashed line in Figure E.22. These idealised, straight lines are used in the buildings standards as they provide convenient equations for calculations.

In summary, the procedure for constructing a response spectrum as outlined by Eiksund (2017) is as follows:

1. Select representative ground motion records
2. Select relevant periods (T) and damping ratios (D)
3. Calculate the relative deformation response z(t)
4. Determine peak displacement z_0
5. Calculate pseudo-velocity and pseudo-acceleration
6. Repeat 2-3 for all relevant periods and damping ratios
7. Select another ground motion record and repeat steps 1-5

E.3   Design Standards for Earthquake Loads

Building standards around the world have been developed to give guidelines for the design of structures to withstand potential earthquake loads. Examples of such building standards (that are referred to in this report) are the Uniform Building Code (UBC) and the American Society of Civil Engineers (ASCE7), which are used in the US, the International Building Code (IBC), the Chilean design standards (DS-61) and Eurocode 8, which is used in Europe. It is apparent that more local codes in Europe have or are being developed, for example the Turkish Earthquake Code (TEC), which is described and compared with the previously mentioned by (Dogangun & Livaoglu, 2006).

It is response and design spectra that forms the basis of the design procedures in all of these standards, with the aim of determining the response of the structure, along with the aim of calculating the base shear that will be imposed on a building due to an applied seismic load. For such purposes there are several steps that must be carried out as described by Kaynia (2017):

1. Specify the Peak Ground acceleration (PGA/a_g)
2. Introduce the effect of structural type for ULS design
3. Compute total lateral earthquake force (base shear)
4. Distribute the load along the height of the structure to compute internal forces to be used for design

This procedure is described in more detail the next section, which is based on Eurocode 8.

E.3.1 Eurocode 8 Requirements and Procedure

In Europe, the Eurocode standards have been developed for design safety purposes. In particular Eurocode 8 deals with "Design of Structures for Earthquake Resistance". The standard ((Standard Norge, 2004)) stipulates that structures in seismic regions shall be designed and constructed in such a way that to an adequate degree of reliability the following requirements are met:

- No collapse requirement – that the structure shall be designed and built to withstand the design seismic action without local or global collapse.

- Damage limitation requirement – the structure should be designed and built to withstand seismic action having a larger probability of occurrence than the design seismic action without damaging or limiting the use of the structure for its intended purposes. Building types are classed based on importance and consequence of failure, and an importance factor is applied accordingly.

It stipulates that appropriate ground investigations must be carried out to classify the ground type in accordance to the 7 ground types defined, based on the geotechnical properties of the top 30m of ground, as shown in Table E.3.1 for 5 of these ground types, response spectra have been developed, which predict how a building with a particular natural period will respond to ground surface motion. These are presented in Figure with the appropriate values presented in Table E.3.2.

Table E.3.1: Ground Types defined by Eurocode 8 ((Standard Norge, 2004))

| Ground type	Description of stratigraphic profile	Parameters		
		$v_{s,30}$ (m/s)	N_{SPT} (blows/30cm)	c_u (kPa)
A	Rock or other rock-like geological formation, including at most 5 m of weaker material at the surface.	>800	-	-
B	Deposits of very dense sand, gravel, or very stiff clay, at least several tens of metres in thickness, characterised by a gradual increase of mechanical properties with depth.	360 – 800	>50	>250
C	Deep deposits of dense or medium- dense sand, gravel or stiff clay with thickness from several tens to many hundreds of metres.	180-360	15-50	70-250
D	Deposits of loose-to-medium cohesionless soil (with or without some soft cohesive layers), or of predominantly soft-to-firm cohesive soil.	<180	<15	<70
E	A soil profile consisting of a surface alluvium layer with vs values of type C or D and thickness varying between about 5 m and 20 m, underlain by stiffer material with vs > 800 m/s.			
S1	Deposits consisting, or containing a layer at least 10 m thick, of soft clays/silts with a high plasticity index (PI 40) and high water content	<100 (indicative)	-	10-20
S2	Deposits of liquefiable soils, of sensitive clays, or any other soil profile not included in types A – E or S1			
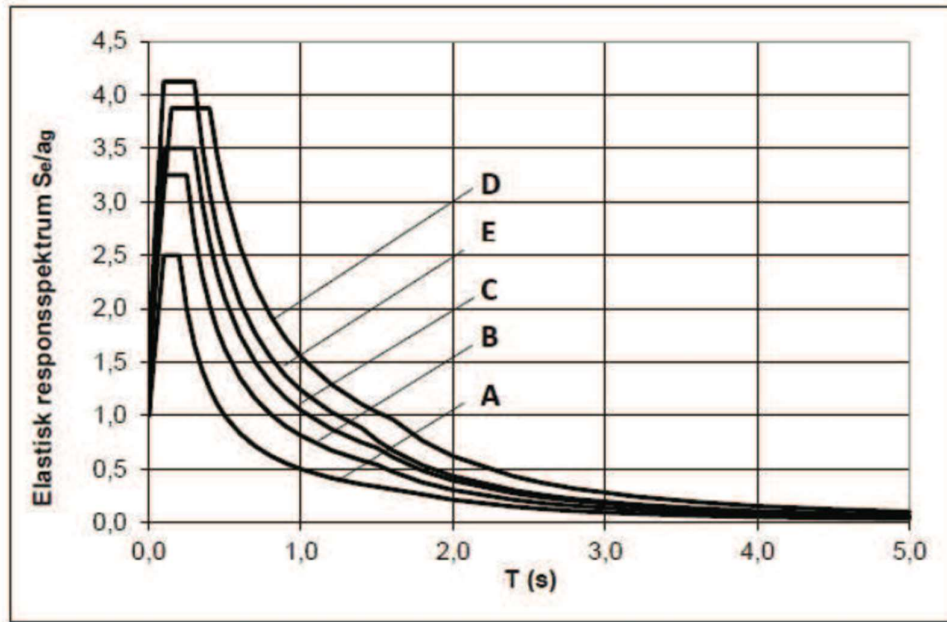
Figure E.3.1: Horizontal elastic response spectra for use in Norway for ground types A to E (Figure NA.3(903), (Standard Norge, 2004))

Table E.3.2: Values of the parameters describing the recommended elastic response spectra in Eurocode 8 ((Standard Norge, 2004)).

Ground Type	S	TB (s)	TC (s)	TD (s)
A	1.0	0.10	0.20	1.7
B	1.3	0.10	0.25	1.5
C	1.4	0.10	0.30	1.5
D	1.55	0.15	0.40	1.6
E	1.65	0.10	0.30	1.4

There are 2 ground types, S1 and S2 that call for "special studies for the definition of the seismic action" (Standard (Norge, 2004)). Ground type S1 is defined by deposits consisting, or containing a layer at least 10m thick, of soft clays/silts with a high plasticity index (PI>40) and high water content. Parameters of such soils are a shear velocity <100m/s and undrained shear strength of 10-20 kPa. How to carry out these special studies, for a type S1 soil type, will be covered in Chapter E.4.

As is apparent from Figure E.3.1, the amplification of the response is greater at lower periods (higher frequencies) as the ground gets softer (A-E). This is as expected from the theory covered in Chapter E.1 and is accounted for the in Eurocode 8 by the soil factor, S. Amplification of

soft soils (type S1) is too varied to be predicted by one soil factor, hence the requirement for a specific study (site response analysis).

For soil types A to E, the base shear on the structure can be calculated using the relevant response spectra and the procedure outlined in the standard. The elastic response spectrum, S_e, is calculated for the natural period of the structure using the equations given in the code and the values for the ground type as given in Figure E.3.1.

$$0 \leq T \leq T_B : S_e(T) = a_g \cdot S \cdot \left[1 + \frac{T}{T_B} \cdot (\eta \cdot 2{,}5 - 1) \right] \qquad (3.2)$$

$$T_B \leq T \leq T_C : S_e(T) = a_g \cdot S \cdot \eta \cdot 2{,}5 \qquad (3.3)$$

$$T_C \leq T \leq T_D : S_e(T) = a_g \cdot S \cdot \eta \cdot 2{,}5 \left[\frac{T_C}{T} \right] \qquad (3.4)$$

$$T_D \leq T \leq 4s : S_e(T) = a_g \cdot S \cdot \eta \cdot 2{,}5 \left[\frac{T_C T_D}{T^2} \right] \qquad (3.5)$$

where

$S_e(T)$	is the elastic response spectrum;
T	is the vibration period of a linear single-degree-of-freedom system;
a_g	is the design ground acceleration on type A ground ($a_g = \gamma_I . a_{gR}$);
T_B	is the lower limit of the period of the constant spectral acceleration branch;
T_C	is the upper limit of the period of the constant spectral acceleration branch;
T_D	is the value defining the beginning of the constant displacement response range of the spectrum;
S	is the soil factor;
η	is the damping correction factor with a reference value of $\eta = 1$ for 5% viscous damping, see (3) of this subclause.

Figure E.3.2: Equations for the elastic response spectrum S_e(T) ((Standard Norge, 2004))

The design ground acceleration, a_g is calculated using the supplied seismic zonation map for the country (Figure E.3.3), and the importance factor, γ_I depending on importance class, which is based on the structure type (Table E.3.3).
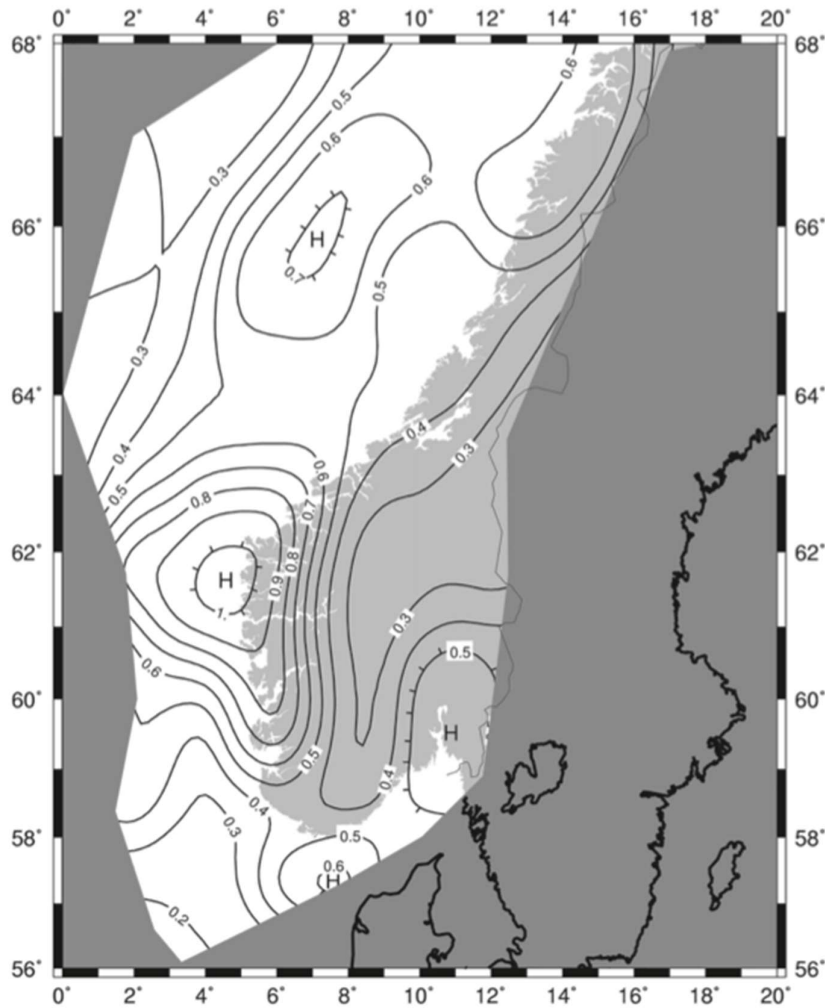
Figure E.3.3: Seismic Zonation Map for Norway ((Standard Norge, 2004))

Table E.3.3: Importance Class – building type ((Standard Norge, 2004))

Importance class	Buildings
I	Buildings of minor importance for public safety, e.g. agricultural buildings, etc.
II	Ordinary buildings, not belonging in the other categories.
III	Buildings whose seismic resistance is of importance in view of the consequences associated with a collapse, e.g. schools, assembly halls, cultural institutions etc.
IV	Buildings whose integrity during earthquakes is of vital importance for civil protection, e.g. hospitals, fire stations, power plants, etc.

Table E.3.4: Importance Factors Specific for Norway ((Standard Norge, 2004))

Importance class	γ_I
I	0.7
II	1.0
III	1.4
IV	2.0

In order to account for the non-linear nature of the structure response due to its ductile behaviour, the behaviour factor, q is introduced. This is equivalent to the ductility factor, μ defined by S. L. Kramer (1996) as described in Section 0. The design spectrum can then be determined for the structure and using the equations from the standard as shown in Figure E.3.4 ((Standard Norge, 2004))

$$0 \leq T \leq T_B : S_d(T) = a_g \cdot S \cdot \left[\frac{2}{3} + \frac{T}{T_B} \cdot \left(\frac{2,5}{q} - \frac{2}{3} \right) \right] \qquad (3.13)$$

$$T_B \leq T \leq T_C : S_d(T) = a_g \cdot S \cdot \frac{2,5}{q} \qquad (3.14)$$

$$T_C \leq T \leq T_D : S_d(T) \begin{cases} = a_g \cdot S \cdot \frac{2,5}{q} \cdot \left[\frac{T_C}{T} \right] \\ \geq \beta \cdot a_g \end{cases} \qquad (3.15)$$

$$T_D \leq T : \quad S_d(T) \begin{cases} = a_g \cdot S \cdot \frac{2,5}{q} \cdot \left[\frac{T_C T_D}{T^2} \right] \\ \geq \beta \cdot a_g \end{cases} \qquad (3.16)$$

where

a_g, S, T_C and T_D are as defined in **3.2.2.2**;

$S_d(T)$ is the design spectrum;

q is the behaviour factor;

β is the lower bound factor for the horizontal design spectrum.

NOTE The value to be ascribed to β for use in a country can be found in its National Annex. The recommended value for β is 0,2.

Figure E.3.4: Equations for the design response spectrum $S_d(T)$ ((Standard Norge, 2004))

From the design spectrum, the seismic base shear, F_b can be calculated for the structure and from the this, be designed sufficiently:

$$F_b = S_d(T_1) \cdot m \cdot \lambda$$

where T_1 is the fundamental period of the vibration of the building for lateral motion in the direction considered, m is the total mass of the building, above the foundation or above the top of a rigid basement, λ is the correction factor, the value of which is equal to 0.085 if $T_1 \leq 2T_c$ and the building has more than two storeys of $\lambda = 1.0$ otherwise.

It is then possible to determine the distribution of the forces between each storey.

E.3.2 Limitations of Building Standards

When using a building standard, there come several assumptions and generalisations that should be considered and accepted. In particular that all the building standards are likely to be conservative and thus it may be beneficial to carry out a specific site response analysis depending on the requirements of the project. Dogangun and Livaoglu (2006) carried out a comparison of four building standards; Eurocode 8, UBS, IBS and TEC. They found that there were many subtle variations in the results, but mainly that Eurocode 8 was most conservative giving the maximum displacements and largest base shears.

Verdugo and Peters (2017) compare the ASCE7, Eurocode 8 and DS-61 design standards and highlight that there are differences in the soil classifications that should be considered, as shown in Figure E.3.5. They also showed that all standards were conservative.
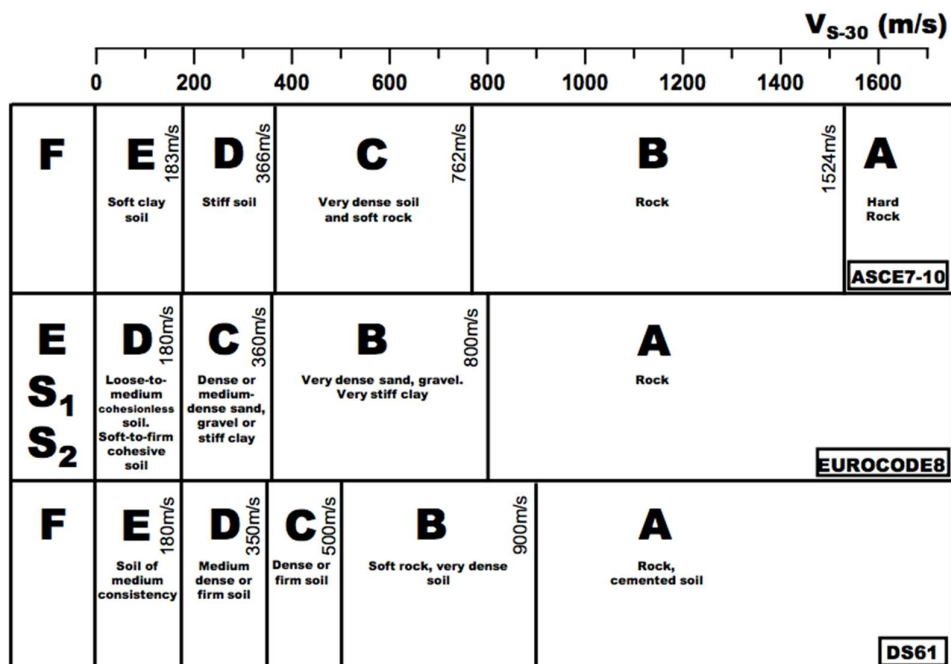
Schott and Schwarz (2004) and Pitilakis, Riga, and Anastasiadis (2012) both suggest variations to Eurocode 8 based on the control periods of the response spectra, T_B, and T_C along with the soil amplifications factors. In particular Pitilakis et al. (2012) concludes that the soil amplification factors for soil types D and E may need refining based on differences in spectral shape against empirical data. This highlights the fact that the ground motions are somewhat less predictable as the soil get softer and softer, and reaffirms Eurocode 8's specification that special studies should be carried out for soil type S1.

E.4 Site Response Analyses

The building standards described in Chapter 0 all refer to soil types that require site specific evaluations. The Uniform Building Code (UBC) recommends this for soil type F. This group includes liquefiable soils, peat or highly organic clays, clays with very high plasticity and very thick soft to medium stiff clays ((ICBO, 1994)). In Eurocode 8 ((Standard Norge, 2004)), soil types S1 and S2 are recommended for special studies. Type S2 refers to soils that are liquefiable or consist of sensitive clays. These are not considered in this report. Soil type S1, which refers to layers more than 10m thick of soft clays or silts, with high plasticity index and high water content. The procedures and various approaches to such studies are outlined in this chapter along with the particular challenges that come from soft soil sites. In order to carry out the analyses one needs to consider first the ground motions without any structure, known as free surface motion, and the soil-structure interaction (SSI).

E.4.1 Free Surface Motions

When an earthquake occurs in bedrock, it sends energy in the form of seismic body waves. Due to refraction, the propagation of the seismic waves in the surficial layers is near vertical as illustrated in Figure E.4.1.
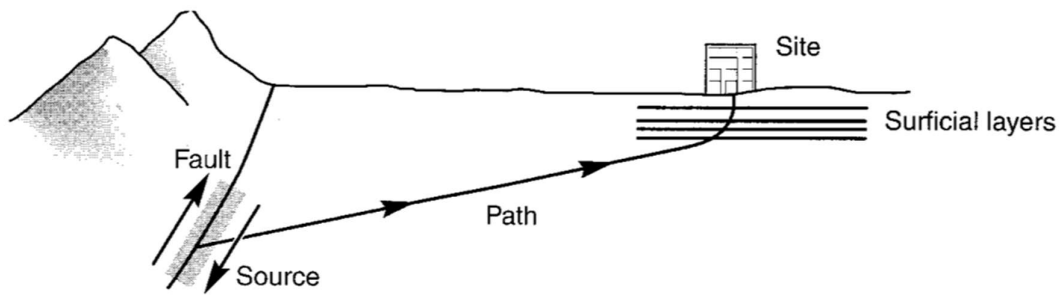

Figure E.4.1: Refraction process that causes near vertical wave propagation near the ground surface (Figure 7.1, (S. L. Kramer, 1996))

Although the nature of the rupture mechanism at the source is complex, it is possible to predict the motion characteristics of the bedrock at a site using empirical methods, based on recorded earthquakes, and seismic hazard analysis ((S. L. Kramer, 1996)). Figure E.4.2 illustrates the nomenclature used when referring to bedrock motions and free surface (field) motions. As discussed Section E.2, the amplitude of the displacement, at ground surface, depends greatly on the layering and stiffness of the surficial soils. That is the displacement amplitude increases with reducing stiffness. It is the variation in the soil that causes complications when it comes to determining the ground shaking motions at the site and the interaction with the structure.

As illustrated in Figure E.4.2, the overall steps when it comes to carrying out a site response analysis ((Kaynia, 2017)) are:

1. Take an acceleration time history that represents the bedrock ground motions at the site

2. Perform a site response analysis and compute the acceleration time history at the surface

3. Compute a response spectrum of the acceleration time history.
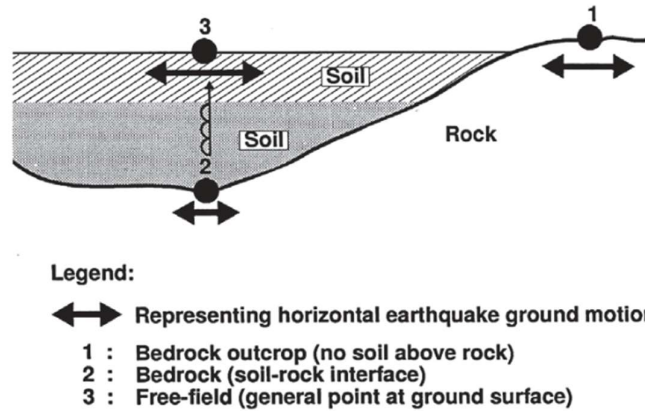

Figure E.4.2: Illustration of steps in a site response analysis and the nomenclature ((Kaynia, 2017)).

The various techniques of ground response analyses, depend on the number of dimensions the technique addresses. All techniques are generally based on the 1-dimensional approach, which can be carried out in a linear, equivalent linear or non-linear manor.

E.4.1.1   One-Dimensional Linear approach

The 1-D approaches assume that all boundaries are infinitely horizontal and the response of the soil is determined by horizontal S-waves propagating vertically from the bedrock. This technique has been shown to predict reasonable results when compared to measured responses ((S. L. Kramer, 1996)). It also assumes that stiffness and damping in the soil have a linear relationship with shear strain as shown in Figure E.4.3.
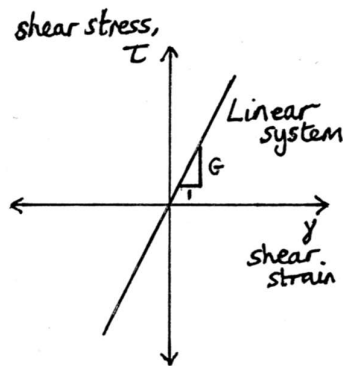

Figure E.4.3: Linear stress-strain relationship. Stiffness is the gradient and therefore constant.

The linear approach is based on the use of a transfer function that was briefly introduced in Section E.1.6 in regard to a 1-DOF system. It is because the transfer function is based on the principle of superposition that it is limited to linear systems.

The transfer function approach is based on a number of steps ((S. L. Kramer, 1996)) that are illustrated in Figure E.4.4:

1. The time history of the bedrock is represented as a Fourier series in the frequency domain

2. Each term of the Fourier series is multiplied by the transfer function to produce a time series of the ground surface motion in the frequency domain

3. The inverse Fourier transform is then carried out to create the ground surface motion in the time domain.
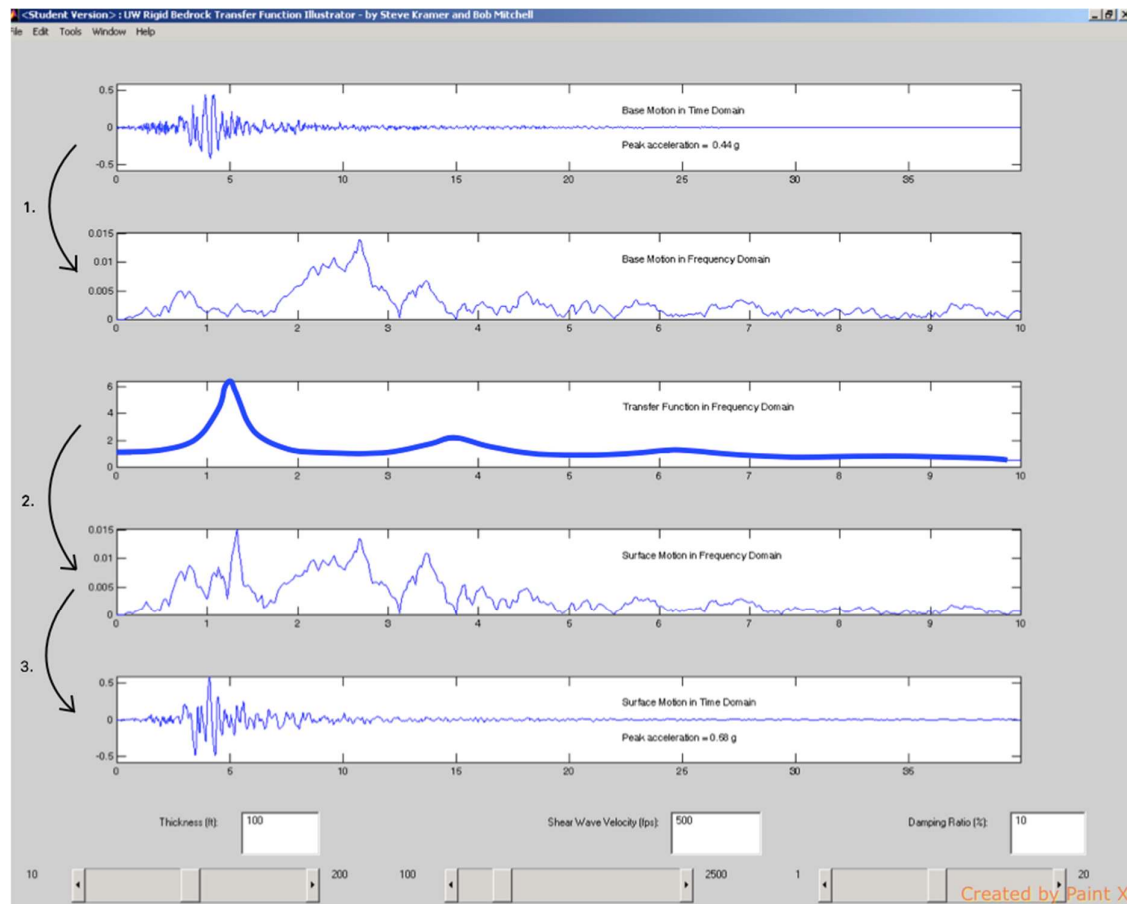
Figure E.4.4: Illustration of the use of a transfer function in a 1D ground response analysis, using SHAKE ((S. Kramer, 2017)).

Thus, the evaluation of the transfer function is key to this technique. The basis of the function comes from looking at an undamped soil layer on rigid rock as illustrated in Figure E.4.5. This is of course unrealistic but illustrates the effects of the soil layer.
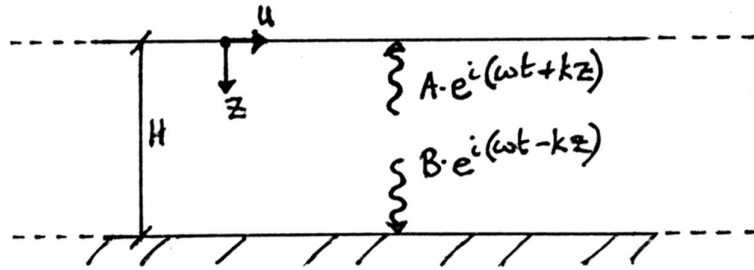
Figure E.4.5: Linear elastic deposit of thickness H underlain by rigid bedrock (taken from Figure 7.3, (S. L. Kramer, 1996))

Using complex notation of or the solution of a propagating wave the resulting displacement can be written ((S. L. Kramer, 1996)):

$$u(z,t) = Ae^{i(\omega t + \quad)} + Be^{i(\omega t - k \quad)}$$

where ω is the frequency of the ground shaking, k is the wave number ($=\omega/v_s$) and A and B are the amplitude of the wave travelling in the upward and downward directions, respectively ((S. L. Kramer, 1996)). This equation can be solved for the soil layer using the condition of the free surface, where shear stress will be zero ($\tau = 0$), to give the displacement in the layer. From this it is shown that the displacement follows the form of a standing wave, since there is full reflection from the rigid bedrock and constructive interference:

$$u(z,t) = 2A \cos kz \, e^{i\omega t}$$

the transfer function is the ratio between the free surface motion amplitude (at z=0) and the bedrock motion amplitude (at z=H) ((S. L. Kramer, 1996)):

$$H\,(\omega) = \frac{u_{max}(0,t)}{u_{max}(H,t)} = \frac{1}{\cos(\frac{\omega H}{v_s})}$$

and the modulus is the amplification function:

$$|H(\omega)| = \frac{1}{\left|\cos(\frac{\omega H}{v_s})\right|}$$

Resonance occurs when the denominator of the equation above reaches zero, as illustrated in Figure E.4.6, and this highlights how sensitive the response of the soil layer is to the frequency of the base motion (load). It is also known that natural angular frequency of the soil layer depends on its geometry and material parameters (velocity and stiffness).
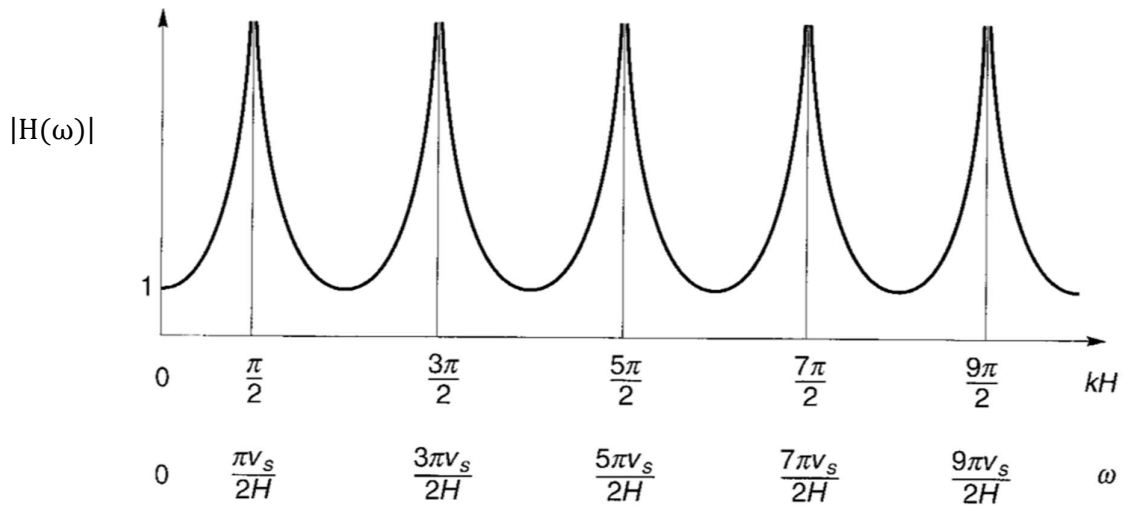
Figure E.4.6: Influence of frequency on steady-state response of undamped linear elastic layer. (Figure 7.4, (S. L. Kramer, 1996)).

In the more realistic case of a damped soil layer (note, the rigid bedrock is still not realistic), the transfer function will be ((S. L. Kramer, 1996)):

$$H(\omega) = \frac{1}{\cos\left[\frac{\omega H}{v_s}(1 + iD)\right]}$$

and the amplification factor will be:

$$|H(\omega)| = \frac{1}{\sqrt{\cos^2\left(\frac{\omega H}{v_s}\right) + \left[D\left(\frac{\omega H}{v_s}\right)\right]^2}}$$

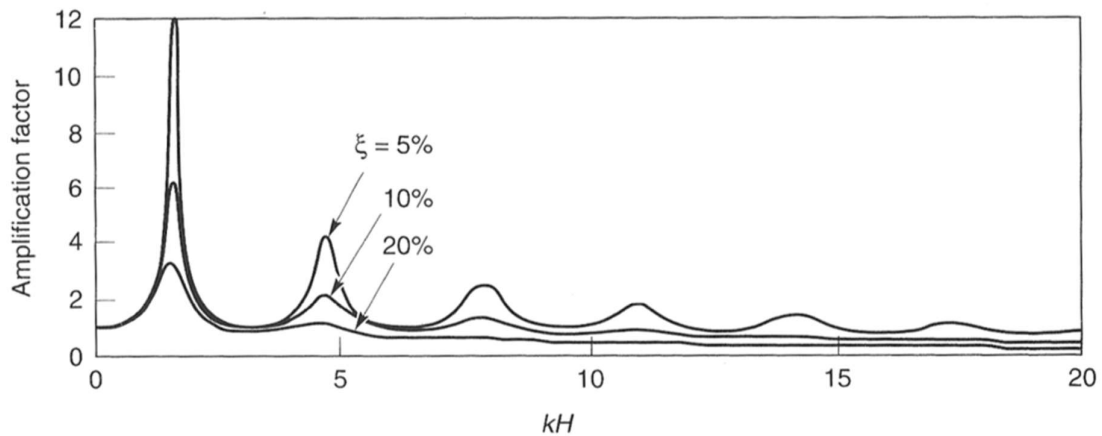which is illustrated in Figure E.4.7 for various values of damping.

Figure E.4.7: Influence of frequency on steady-state response of undamped linear elastic layer on rigid rock. (Figure 7.5, (S. L. Kramer, 1996))

The denominator will always be greater than zero and therefore the amplification will never reach infinity. However, the peaks in the amplitude will still correspond to the natural frequencies of the soil deposit, with the greatest amplitude factor at the lowest natural frequency, known as the fundamental frequency ((S. L. Kramer, 1996)):

$$\omega_0 = \frac{\pi v_s}{2H}$$

and the corresponding period of vibration is called the characteristic site period:

$$T_s = \frac{2\pi}{\omega_0} = \frac{4H}{v_s}$$

As can be seen, since this is simply a function of the thickness of the soil layer and its velocity, it is a very useful tool for determining the period of vibration for which the highest amplification can be expected.

At the natural frequencies standing waves are produced, and the shape of these standing waves, known as the mode shapes, can be determined as shown in Figure E.4.8. It is clear that at the higher frequencies (mode 1 and 2), the soil profile will be displaced in different directions. It is important to consider this in the evaluation of inertial forces within the soil mass ((S. L. Kramer, 1996)).
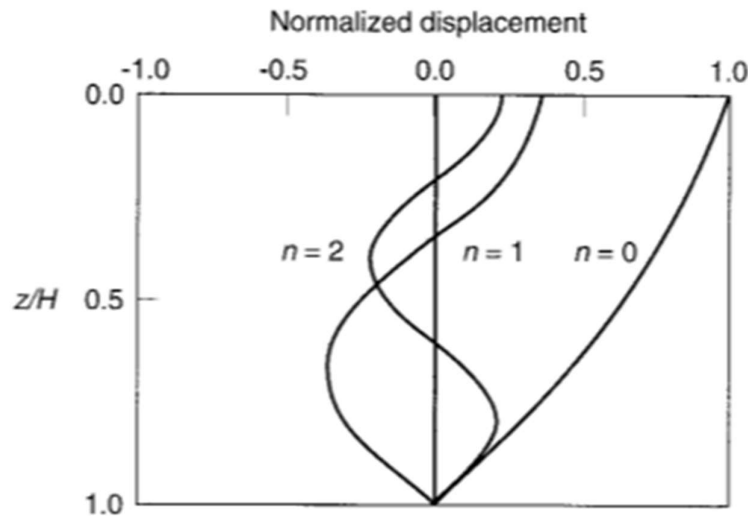

Figure E.4.8: Displacement patterns for standing waves at fundamental (n=0), second (n=1) and third (n=2) natural frequencies for a soil layer with damping ratio, D=5%. Displacements are normalised by the maximum displacement at eh fundamental frequency (Figure 7.6, (S. L. Kramer, 1996))

In a more realistic situation, the rock will be elastic, such that the downward travelling waves will be partially reflected and partially transmitted into the rock, as illustrated in Figure E.4.9. If the rock continues to such a depth without any more layers of differing velocity then this elastic energy is effectively lost from the soil layer ((S. L. Kramer, 1996)). Thus, the amplitude

of the motions at the ground surface will be smaller than those of the rigid bedrock case considered before.
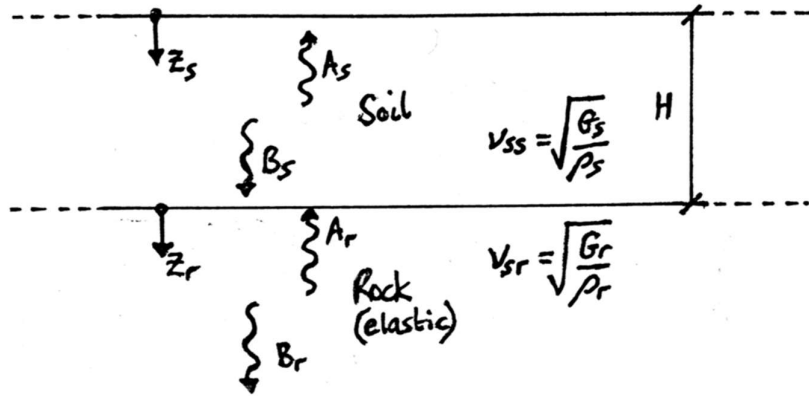

Figure E.4.9: Soil layer overlying an elastic half-space of rock (taken from Figure 7.7, (S. L. Kramer, 1996))

Using the free surface effect, the compatibility of displacements and continuity of stresses at the soil-rock boundary, the following transfer function is found ((S. L. Kramer, 1996)):

$$H\left(\omega\right) = \frac{1}{cos\left(\frac{\omega H}{v_{ss}^*}\right) + i\alpha_z^* \, sin\left(\frac{\omega H}{v_{ss}^*}\right)}$$

where α_z^* is the complex impedance ratio. The solution for the amplitude factor for a damped soil is not simple or compact, so in order to illustrate the effects of the elastic rock boundary the amplitude factor for an undamped soil can be written:

$$|H(\omega)| = \frac{1}{\sqrt{cos^2 k_s H + \alpha_z^2 \, sin^2 k_s H}}$$

The function is illustrated in Figure E.4.10, along with the effects of the impedance ratio, which like damping, prevents the denominator from reaching zero and therefore the stiffness of the bedrock has similar significance to the damping of the soil.
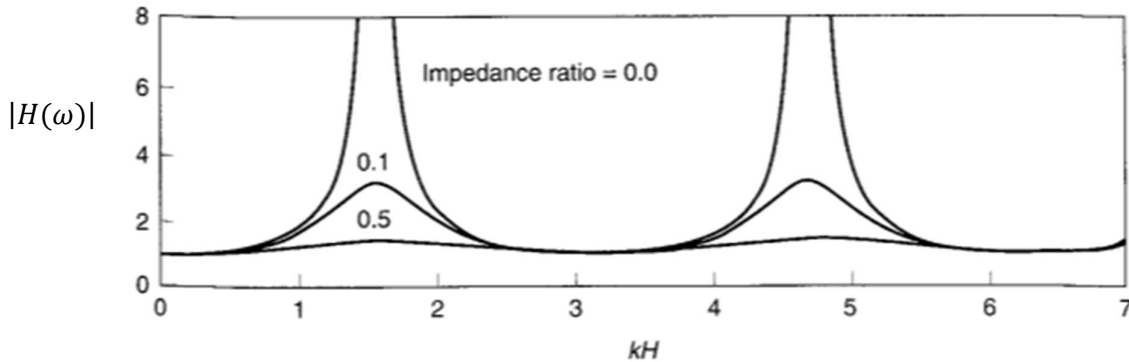

Figure E.4.10: Effect of impedance ratio on amplification factor for a case of undamped soil (Figure 7.8, (S. L. Kramer, 1996))

Of course, it is also likely that the soil at a site will be layered and as such, it is useful to have a transfer function that can be applied to such cases.
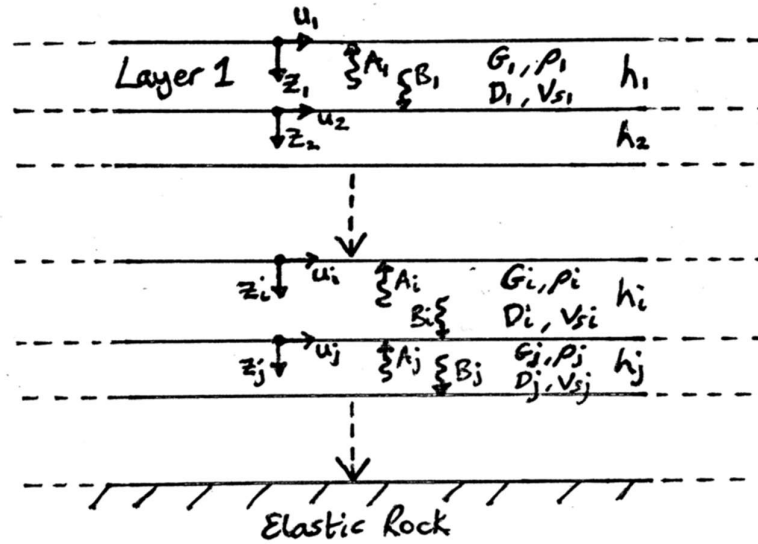
Figure E.4.11: Layered soil deposit on elastic bedrock (modified from Figure 7.9, (S. L. Kramer, 1996))

Satisfying the free surface condition, the compatibility of displacements and continuity of stresses between soil boundaries, the following transfer function between 2 layers can be produced:

$$H_{ij}(\omega) = \frac{|u_i|}{|u_j|} = \frac{a_i(\omega) + b_i(\omega)}{a_j(\omega) + b_j(\omega)}$$

where a and b are the ratios between the amplitude in the layer to the amplitude in the top layer (i.e. $a_i(\omega) = \frac{A_i}{A_1}, etc$). This equation shows that if the motion in any one layer is known, one can directly determine the motion in the adjacent layer. This process is known as deconvolution ((S. L. Kramer, 1996)) and is used in the following technique of equivalent linear analysis.

E.4.1.2 One-Dimensional Equivalent Linear approach

Since soils are in fact nonlinear with regards to their stiffness, one needs to modify this approach, and as such the equivalent linear (EL) approach was developed in the 1970s ((Finn, 2000)) and is still often used for such analysis. The non-linear behaviour of soil is illustrated in Figure E.4.12. The shape of the hysteresis loop created by cyclic loading and can be described by 2 parameters ((S. L. Kramer, 1996)). The gradient is the stiffness, where $G_{sec} = \frac{\tau_c}{\gamma_c}$ is the average gradient of the loop, G_{tan} is the gradient at any point and G_{max} is the gradient at the minimum shear strain. The breadth of the loop is related to the work done (energy dissipated) and energy stored, and is therefore a direct measurement of the damping ratio. Thus, both stiffness and damping have a non-linear relationship with shear strain.
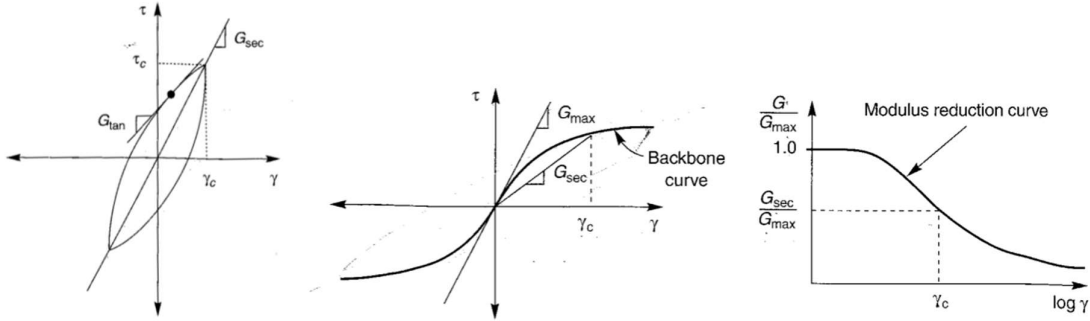
Figure E.4.12: Cyclic hysteresis loop and typical relationship between shear strain, shear stress and stiffness (Figures 6.39 and 6.40, (S. L. Kramer, 1996))

The linear equivalent approach involves the following steps ((S. L. Kramer, 1996)) as are illustrated in Figure E.4.13:

1. Initial estimates of G and D for each layer

2. These are input and used to compute time histories for each layer, including a time history of shear strain for which the maximum shear strain is used to calculate the effective shear strain $\gamma^i_{eff\,j} = R_\gamma \gamma^i_{max\,j}$. Where $R_\gamma \approx 0.65$ is often used ((S. Kramer, 2017))

3. From this strain, new values of G and D are input to the next iteration.

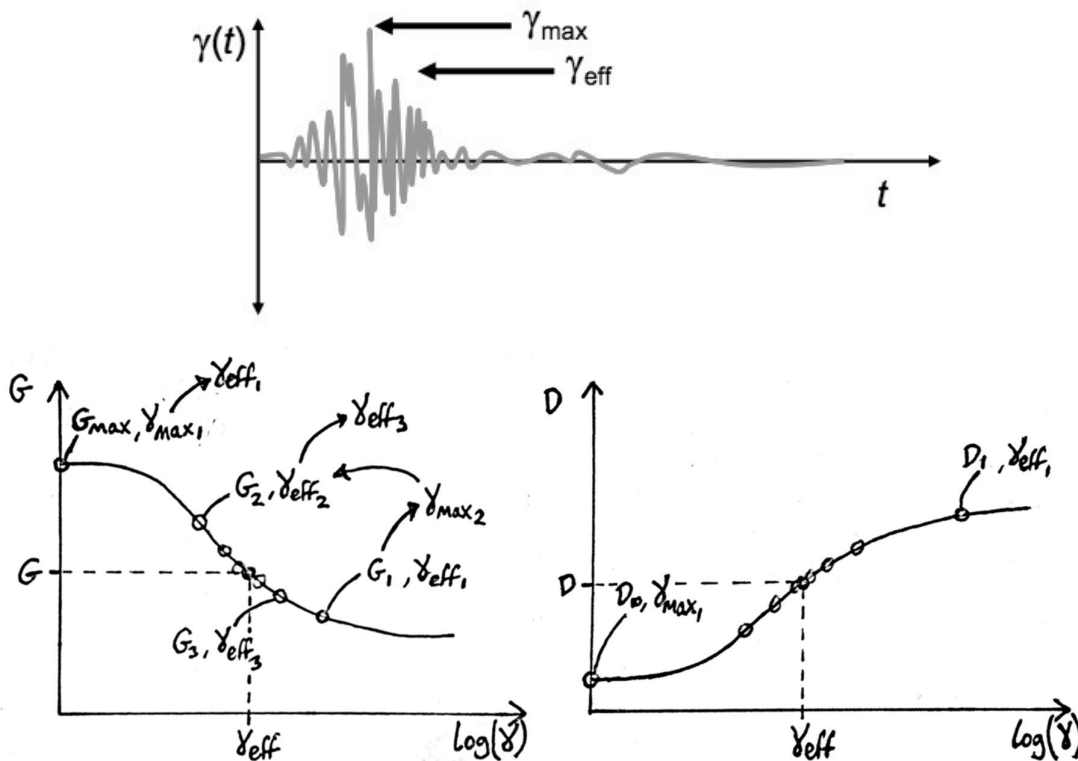4. Several iterations are carried out until suitable convergence is achieved.

Figure E.4.131: Procedure of the linear equivalent approach (modified from Figure 7.11, (S. L. Kramer, 1996))

E.XL

This approach is beneficial since it can compute a transfer function in relatively few number of steps in the frequency domain (i.e. not at every time step as for the non-linear technique described next). This approach produces reasonable results for many practical problems ((S. L. Kramer, 1996)). However, there are several disadvantages to the EL approach that can be overcome by using the non-linear approach:

- It is only an approximation of non-linear soil behaviour.

- It can result in spurious resonances at certain frequencies since it does not account for changes in stiffness as an earthquake develops (after each load cycle) and therefore overestimates the amplification.

- The use of peak shear strain to estimate effective shear strain can result in an over-softened, overdamped system if the peak is much larger than the remainder of the shear strains, or an under-softened, underdamped system if the shear strains are uniform over time.

- At high strain levels (soft soils or high ground shaking) the non-linear behaviour of a soil is more noticeable, which is when the results of this approach may not be suitably accurate.

E.4.1.3   One-Dimensional Non-Linear approach

The non-linear (NL) approach keeps true to the non-linear behaviour of the soil and is carried out in the time domain. It involves the integration of the equation of motion for small time steps to determine the stress-strain behaviour and thereon the appropriate soil properties for that particular time step. The process is carried out as follows ((S. L. Kramer, 1996)):

1. The particle velocities and displacements for each layer are known at the start of each time step, t_i.

2. The particle displacement is used to determine the shear strain within each layer and thereon the shear stress based on the chosen stress-strain model. Often a linear relationship is good enough especially when small time steps are chosen as shown in Figure E.4.14. The more steps the better.

3. The input motion is used to determine the motion at the soil-rock boundary at time t_{i+1} by satisfying the boundary conditions.

4. The process of deconvolution (as described in the previous approach) is used within each time step to determine the displacement within each layer at time t_{i+1}.

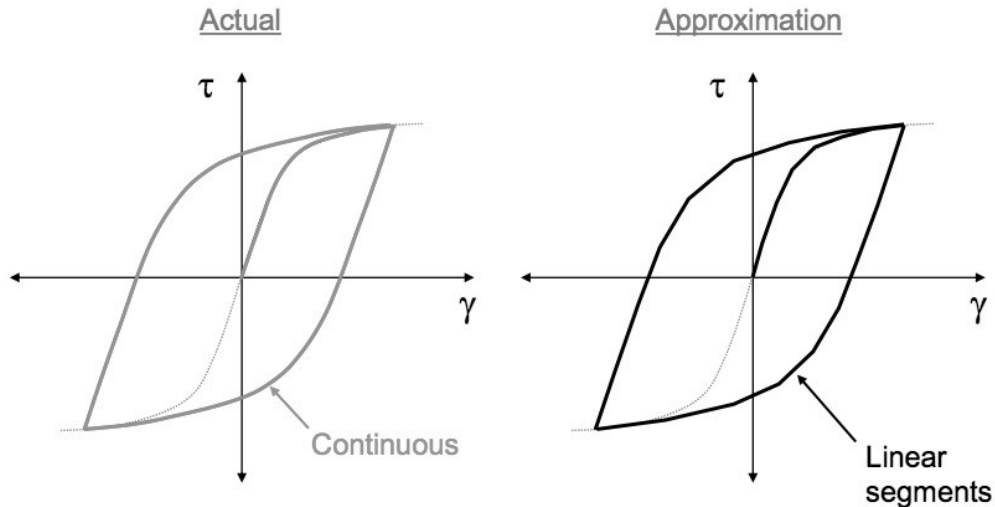5. The values at the end of the time step are used as the starting values for the next time step.

Figure E.4.14: Approximation of the non-linear behaviour with an incremental linear stress-strain behaviour, often used in the non-linear approach ((S. Kramer, 2017))

The advantages of this approach to the EL approach are that:

- it models non-linearity much more accurately.

- since the model can be formulated in terms of effective stresses it can compute pore pressure changes including dissipation, therefore being very advantageous for identifying liquefaction potential.

- it can compute permanent deformations.

- it does not create spurious resonances (over amplification) that the EL model can do at certain frequencies

- the results at high strain levels (soft soils or high ground shaking), where the non-linearity of the soil becomes most significant, are more accurate.

The disadvantages are that:

- it takes many more computations.

- it requires a reliable stress-strain model or constitutive model of which the parameters are not as well established as those in the EL approach. It may therefore require significantly thorough field and laboratory investigation ((S. L. Kramer, 1996)).

E.4.1.4   *Two and Three-Dimensional approaches*

In most cases boundaries cannot be assumed infinitely horizontal and 1-D analyses cannot be used. For example, soil basins, retaining structures, dams, tunnels, etc. In these cases, 2-D approximations are suitable in the form of plane strain problems (where changes in strain in the 3rd dimension are zero). In some cases, the problem can be more complicated with boundaries

varying in 3 dimensions. For example, localised structures (eg. dams in narrow canyons), complex soil conditions or multiple structures. In these cases, 3D analyses are required.

Both 2-D and 3-D approaches follow roughly the same basis. The most common approach is the finite element method (FEM). This involves the discretisation of the problem into elements. Dynamic loading is applied to the elements and displacements, strains, and stresses are calculated for each element using matrix functions, boundary conditions and the input stress-strain relationships. The elements are then reassembled for the overall problem. The process can be carried out using the linear, equivalent linear or non-linear approaches as described in the 1-D approaches previously ((S. L. Kramer, 1996)).

E.4.2 Soft Soil Site Response

In general, it is known that soft soil site will create complex responses, hence the inability to create one response (design) spectrum for the building standards.

Some general rules for soft soil response is that the soil will have relatively low stiffness, therefore velocity and therefore relatively high particle velocity. Thus, an amplification of low frequencies (high periods). This is illustrated by S. L. Kramer (1996) in Figure E.4.19, where 2 soil elastic types with differing stiffness' overlay rigid bedrock and produce the resulting amplitude factors.
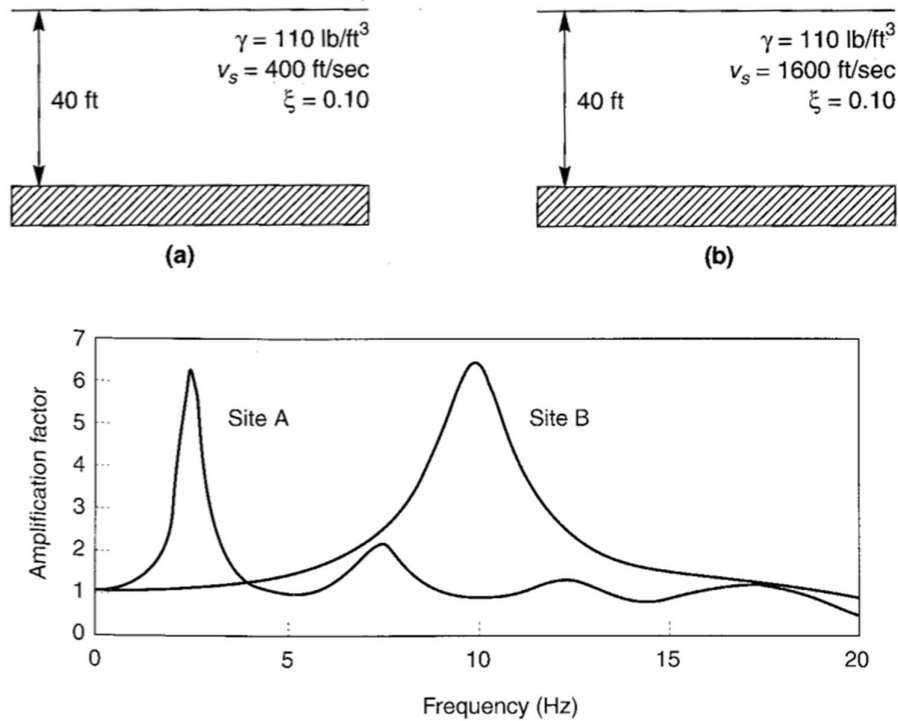

Figure E.4.19: Two soil types with differing velocity (stiffness) overlying rigid bedrock: (a) site A (soft soil) shows amplification of low frequency inputs, (b) site B (stiff soil) shows amplification of high frequency inputs. (Figures 8.1 and 8.2, (S. L. Kramer, 1996))

S. L. Kramer (1996) also refers to research carried out by Seed, Ugas, and Lysmer (1976), where they compared the computed response spectra of four site conditions, one of them being soft to medium-stiff clay deposits. The study found the response spectrum of such deposits was much more varied over larger period ranges and with amplification at higher periods (lower frequency) as shown in Figure E.4.20.
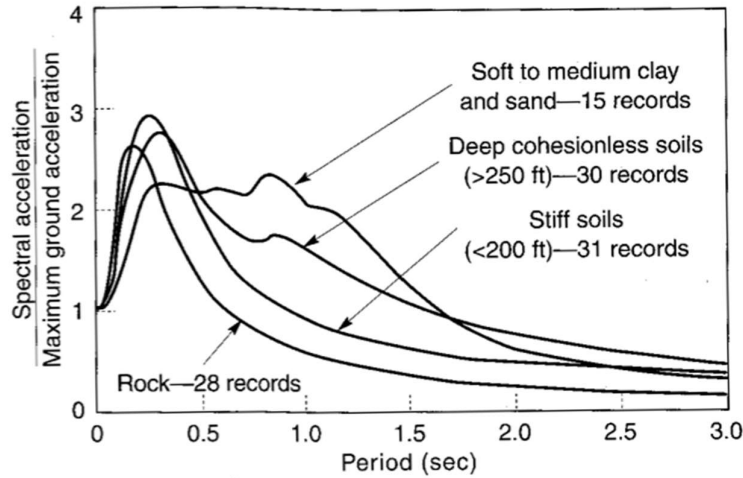

Figure E.4.20: Average normalised response spectra (5% damping) for different local site conditions (after (Seed et al., 1976), Figure 8.12, (S. L. Kramer, 1996))

Griffiths, Cox, and Rathje (2016) consider high intensity ground motions at a well-known soft-soil site, Treasure Island. They recognise and prove that high strain levels created in soft soils are best analysed by non-linear approaches. However, they found the non-linear model still did not characterise the ground shaking for high frequency (low period) motions (see Figure E.4.21) and that the non-linear approach should still be used with caution.
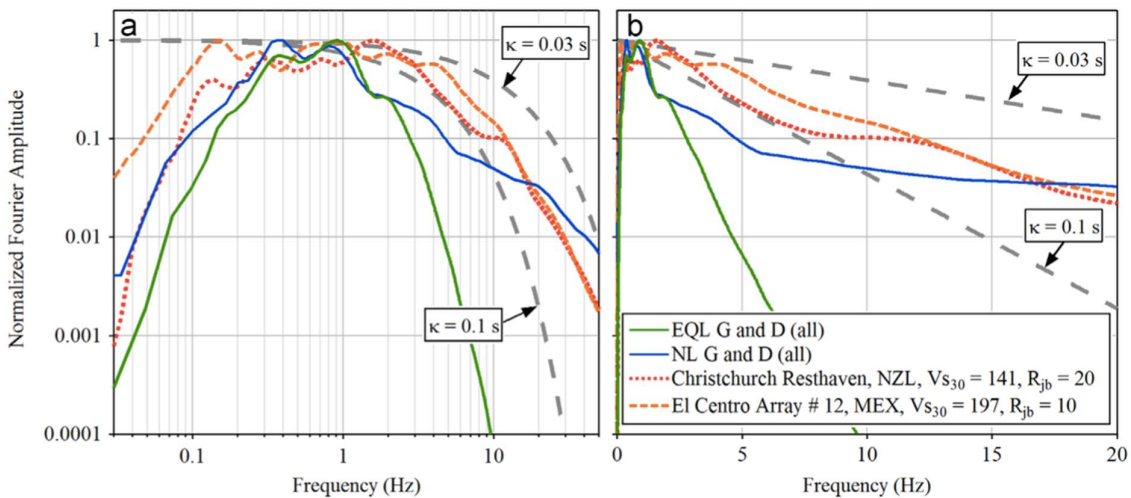

Figure E.4.21: Normalised Fourier amplitude spectra for the EQL and NL fully-modified site response analyses at the TI site along with recorded time histories from two soft soil sites that recorded high-intensity ground motions during previous earthquakes and the expected shapes of FAS using kappa (κ) values of 0.03 and 0.1 s. (Figure 15, (Griffiths et al., 2016)

Figure E.4.21 shows an example of site response analysis carried out for an example soft soil site with the layer properties as shown in Table E.4.2. Proshake uses the EL approach. It is seen that for 3 ground motion inputs, the response spectra are similar and amplify higher period motions as expected. It would be reasonable to assumes an average spectrum for this site, although this is only based on the EL approach. From conclusions of studies outlined above, it would be sensible to compare with other techniques, such as NL, and if possible with sites that have similar properties and measured responses.
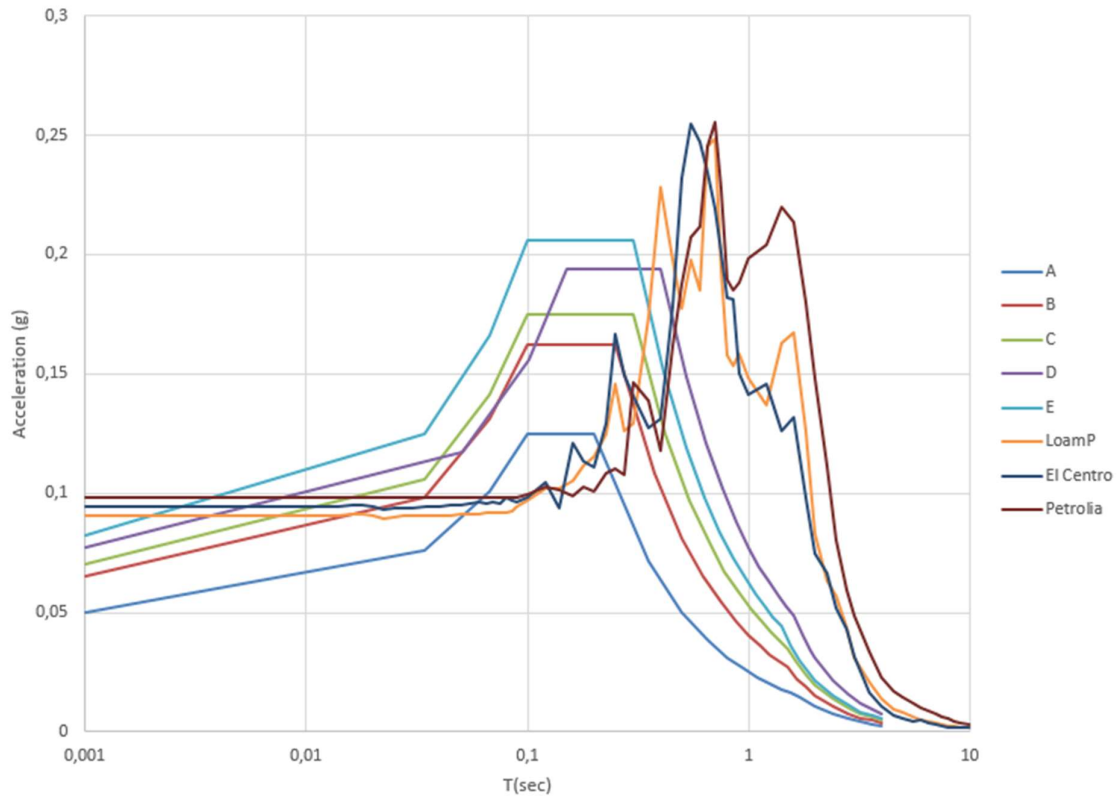

Figure E.4.22: Comparison of response spectra using soft soil site parameters with Eurocode 8 response spectra for ground types A-E using the ProShake program (taken from an exercise for B!8305 Geogynamics at NTNU)

Table E.4.2: Layer properties for Proshake example of a soft soil site.

Layer	Depth (m)	Unit weight (kN/m³)	v_s (m/s)	PI (%)
1	0-10	18	60	40
2	10-20	18	100	30
3	20-30	18	120	20
4	30-∞	24	1500	0
$v_{s,30}$ = 85.7 m/s				